https://doi.org/10.15388/vu.thesis.998
https://orcid.org/0000-0001-8109-7286

VILNIUS UNIVERSITY
CENTER FOR PHYSICAL SCIENCES AND TECHNOLOGY

Kernius Vilkevičius

Femtosecond Laser Nanoengineering of Noble-Metal Gratings for Plasmonic Applications

DOCTORAL DISSERTATION

Technological Sciences,
Materials Engineering (T 008)

VILNIUS 2026

The dissertation was prepared between 2022 and 2026 at the Center for Physical Sciences and Technology. The research was partly supported by the Research Council of Lithuania.

Academic Supervisor – Dr. Evaldas Stankevičius (Center for Physical Sciences and Technology, Technological Sciences, Materials Engineering, T 008).

This Doctoral Dissertation will be defended in a Public Meeting of the Dissertation Defence Panel:

Chairman – Prof. Dr. Mangirdas Malinauskas (Vilnius University, Technological Sciences, Materials Engineering, T 008).
Members:
Prof. Dr. Saulius Juodkazis (Swinburne University of Technology, Technological Sciences, Materials Engineering, T 008),
Prof. Habil. Dr. Arūnas Ramanavičius (Vilnius University, Natural Sciences, Chemistry, N 003),
Prof. Habil. Dr. Kęstutis Staliūnas (Universitat Politècnica de Catalunya, Natural Sciences, Physics, N 002),
Prof. Dr. Tomas Tamulevičius (Kaunas University of Technology, Technological Sciences, Materials Engineering, T 008).

The dissertation will be defended at a public meeting of the Dissertation Defence Panel at 2 p.m. on 30th of October 2026, in meeting room A140 of the Institute of Physics, Center for Physical Sciences and Technology.

Address: Savanorių Ave. 231, 02300 Vilnius, Lithuania
Tel. +370 645 15557; e-mail: info@ftmc.lt

https://doi.org/10.15388/vu.thesis.998
https://orcid.org/0000-0001-8109-7286

VILNIAUS UNIVERSITETAS
FIZINIŲ IR TECHNOLOGIJOS MOKSLŲ CENTRAS

Kernius Vilkevičius

Tauriųjų metalų gardelių nanoinžinerija femtosekundiniu lazeriu ir jų plazmoniniai taikymai

DAKTARO DISERTACIJA

Technologijos mokslai,
Medžiagų inžinerija (T 008)

VILNIUS 2026

Disertacija rengta 2022–2026 metais Fizinių ir technologijos mokslų centre, Lazerinių technologijų skyriuje, Plazmonikos ir nanofotonikos laboratorijoje. Mokslinius tyrimus dalinai rėmė Lietuvos mokslo taryba.

Mokslinis vadovas – dr. Evaldas Stankevičius (Fizinių ir technologijos mokslų centras, technologijos mokslai, medžiagų inžinerija, T 008).

Gynimo taryba:
Pirmininkas – prof. dr. Mangirdas Malinauskas (Vilniaus universitetas, technologijos mokslai, medžiagų inžinerija, T 008).
Nariai:
prof. dr. Saulius Juodkazis (Svinburno technologijos universitetas, technologijos mokslai, medžiagų inžinerija, T 008),
prof. habil. dr. Arūnas Ramanavičius (Vilniaus universitetas, gamtos mokslai, chemija, N 003),
prof. habil. dr. Kęstutis Staliūnas (Katalonijos politechnikos universitetas, gamtos mokslai, fizika, N 002),
prof. dr. Tomas Tamulevičius (Kauno technologijos universitetas, technologijos mokslai, medžiagų inžinerija, T 008).

Disertacija ginama viešame Gynimo tarybos posėdyje 2026 m. spalio mėn. 30 d. 14 val. Fizinių ir technologijos mokslų centro Fizikos instituto A140 salėje.

Adresas: Savanorių pr. 231, 02300 Vilnius, Lietuva
Tel. +370 645 15557; el. paštas: info@ftmc.lt

TABLE OF CONTENTS

LIST OF ABBREVIATIONS

1D – one-dimensional
1H – 1st harmonic
2D – two-dimensional
2H – 2nd harmonic
3D – three-dimensional
3H – 3rd harmonic
4-MBA – 4-mercaptobenzoic acid
AOI – angle of incidence
BFAST – broadband fixed angle source technique
CCD – charge-coupled device
DLW – direct laser writing
DMC – Direct Machining Control
DP – diagonal plane
EBL – electron beam lithography
EF – enhancement factor
EM – electromagnetic
FDTD – finite-difference time-domain
FEM - finite element method
FIB – focused ion beam
FOM – figure of merit
fs - femtosecond
FWHM – full width at half maximum
HLPR – hybrid lattice plasmon resonance
IR – infrared
LIFT / LIBT - laser-induced forward/backward transfer
LIPSS – laser-induced periodic surface structures
LoD – limit of detection
LSP – localized surface plasmon
MQ-factor, MQF – modified quality factor
NA – numerical aperture
PDMS – polydimethylsiloxane
PL – photoluminescence
PML – perfectly matched layer
PI – plane of incidence
PP – perpendicular plane
Q-factor, QF – quality factor
RI – refractive index

SEM – scanning electron microscope
SERS – surface-enhanced Raman spectroscopy
SLR – surface lattice resonance
SP – surface plasmon
SPP – surface plasmon polariton
SPR – surface plasmon resonance
TIR – total internal reflection
TMDC - transition metal dichalcogenide
TTM – two-temperature model
UV – ultraviolet
Vis-NIR – visible and near-IR

INTRODUCTION

Plasmonic micro- and nanostructures have attracted significant attention over the past decades because of their ability to confine light and enhance electromagnetic (EM) fields at sub-wavelength scales through the excitation of surface plasmons (SPs) [1-3]. While the field of plasmonics primarily utilizes noble metals due to their strong free-electron response, a broader range of plasmonic materials can be used, including heavily doped semiconductor nanocrystals [4, 5], two-dimensional (2D) materials [6], and conductive polymers [7]. Each material class relies on distinct mechanisms: semiconductors utilize free holes, 2D materials combine electron-hole interactions, and polymers operate via polaronic charge carriers. However, noble metals such as gold (Au) and silver (Ag) remain the primary media for high-performance plasmonic applications due to the complexity of doping semiconductors, the fabrication challenges of 2D materials, and the high defect densities in conductive polymers [8].

In noble metal systems, light-matter interactions are governed by collective oscillations of conduction electrons and are characterized as localized surface plasmons (LSPs) in individual nanoparticles and as propagating surface plasmon polaritons (SPPs) at metal-dielectric interfaces. A large number of free electrons, excited at surface plasmon resonance (SPR) frequency, causes amplified scattering and absorption of incident radiation, as well as great enhancement of the near-field [9]. Arranging such metallic structures in periodic arrays on thin metal films introduces additional diffractive coupling mechanisms that enable interaction between these modes. Such coupling leads to hybridization of LSPs and SPP, resulting in stronger interactions, reduced radiative losses, and improved properties [10-12].

These unique properties enable a wide range of applications, including contamination detection [13], label-free biomedical diagnostics [3, 14], environmental monitoring [15], photonic devices [16], energy harvesting [17], and nanolasing [18, 19]. The strong field localization within structures provides a basis for highly sensitive detection platforms and compact photonic instruments. As global demand for advanced analytical and diagnostic tools is steadily growing, plasmonic platforms have attracted considerable attention for their high sensitivity, rapid response, accuracy, and compatibility with integrated systems.

The traditional fabrication of such structures relies on top-down lithographic methods, often combined with metal deposition and lift-off techniques [20, 21]. While precise, these multi-step processes are limited by

either low throughput, high fabrication costs, or moderate repeatability and controllability. Consequently, direct laser writing (DLW) has emerged as a rapid, single-step, and cost-effective alternative for fabrication [22-25]. The use of ultrafast femtosecond pulses for material structurization and nanoengineering offers a new way to increase production rates and improve the tunability of fabricated structures and their properties. An accurate variation of the resonance position, quality factor, or efficiency of the near-field enhancement can be manipulated by several parameters [26, 27]. Despite the potential of DLW, several challenges still remain in this methodology. Precise control of the structures is essential to ensure stable, repeatable output properties; thus, the in-depth analysis of the main laser system, sample, and grating parameters is required to understand the management capabilities. Also, the understanding of the complex, multidirectional coupling in 2D gratings remains unexplored, as do their abilities to exhibit one-dimensional (1D) properties. Therefore, the research presented in this thesis investigates the femtosecond-laser nanoengineering of noble metals and the fabrication of large-scale plasmonic gratings for advanced plasmonic applications.

The main aim of the research covered in this thesis is to investigate and optimize the single-step fabrication of morphologically tunable noble-metal nanostructures for large-scale gratings using femtosecond (fs) direct laser writing technology, to experimentally and theoretically characterize their plasmonic properties, and to examine their applicability for plasmon-related areas, including surface-enhanced Raman spectroscopy (SERS) detection and refractive index (RI) sensing.

In order to achieve the aim of the thesis, **the following tasks** were defined:

1. To develop a fast and scalable direct laser writing method for the single-step fabrication of large-scale 1D and 2D gratings composed of metallic nanostructures with tunable morphology.
2. To investigate the morphological control provided by the DLW process and optimize the fabrication parameters for the formation of each specific shape structure.
3. To characterize the plasmonic properties of the produced gratings with both experimental and theoretical investigations and establish their relationship with the resulting morphology and grating geometry.
4. To investigate the applicability of periodic nanostructures in the field of surface-enhanced Raman spectroscopy (SERS).
5. To investigate the applicability of periodic nanostructures for metallic plasmonic RI-based sensors.

Scientific novelty and relevance of the work

A fast femtosecond direct laser writing technique for single-step structurization of thin metallic films and the fabrication of large-scale, free-form gratings with wavelength-sized periods was presented and systematically investigated. This research presents, for the first time, a detailed analysis of the DLW-produced gold nanostructures, their period-induced morphological changes, and the overlapping effect that influences formation parameters. Furthermore, this work introduces quasi-1D arrays produced via DLW, which provide a unique platform possessing 2D physical geometry but exhibiting high-quality 1D-like spectral characteristics. This work also provides a combined theoretical-experimental analysis of plasmonic resonances in symmetric gratings, highlighting the interplay between the main and diagonal diffraction lattices and demonstrating dual-angular tuning of the resonances. Finally, the research demonstrates a scalable route toward large-area plasmonic structures with application-specific morphology and functionality. This potential was demonstrated through the development of compact and high-throughput analytical platforms for SERS detection and refractive-index sensing.

Statements to defend

1. Using a constant-NA objective, decreasing fs laser wavelength from 1030 nm to 343 nm expands the energy-dependent nanostructure formation fluence window by 3 times and reduces the achievable grating period down to 450 nm, while control of film thickness and an increase in spatial pulse overlap provide additional morphological tuning with a lower modification threshold.

2. Plasmonic resonances in 2D arrays exhibit morphology-dependent spectral behavior, as increasing nanostructure height leads to a redshift of the out-of-plane resonance, while manufactured quasi-1D gratings enable spectral-mode isolation by suppressing diagonal resonances.

3. Grating-coupled resonances in symmetric 2D arrays possess the highest quality when excited along the high-symmetry axes (0°, 45°, and 90°), while their spectral positions across the whole Vis-NIR (400-1600 nm) range can be tuned through double-angular control by changing azimuthal (0°-90°) and incidence (8°-30°) angles.

4. Morphological engineering of laser-fabricated plasmonic nanostructures provides application-specific functionality of large-scale gratings: high-aspect-ratio nanojets maximize SERS enhancement factor up to 2.73×10^7, while Ag-Au bimetallic nanobump gratings offer stability and tunable sensitivities exceeding 850 nm/RIU, sufficient for RI sensing.

List of Publications

The main results of the thesis were published in 6 peer-reviewed scientific journals [P1-P6], 1 patent [T1], and presented at 26 conferences [C1-C26].

Scientific papers directly related to the thesis (peer-reviewed and indexed in Clarivate Analytics Web of Science (WoS)):

[P1] **K. Vilkevičius**, A. Selskis, E. Stankevičius, "Femtosecond Laser Wavelength-Dependent Formation of Plasmonic Gold Nanostructures", *Appl. Surf. Sci.* 617, 156629 (2023). DOI: 10.1016/j.apsusc.2023.156629

[P2] **K. Vilkevičius**, G. D. Tsibidis, A. Selskis, E. Stratakis, E. Stankevičius, "Formation of Highly Tunable Periodic Plasmonic Structures on Gold Films Using Direct Laser Writing", *Adv. Opt. Mater.* 12(20), 2400172 (2024) + Front Inside Cover. DOI: 10.1002/adom.202400172

[P3] **K. Vilkevičius**, K. Čepaitis, A. Selskis, E. Stankevičius, "Ultrafast Laser Ablation and Modification of Thin Metal Film for Quasi-1D Array Formation", *Opt. Laser Technol.* 183, 112330 (2025). DOI: 10.1016/j.optlastec.2024.112330

[P4] **K. Vilkevičius**, L. A. Letelier, L. Grinevičiūtė, E. Stankevičius, "Grating-Coupled Plasmonic Resonances in Symmetric 2D Gold Nanobump Grating: Theory Meets Experiments", *ACS Appl. Mater. Interfaces* 18(23), 33007-33023 (2026) + Cover. DOI: 10.1021/acsami.6c04043

[P5] **K. Vilkevičius**, I. Ignatjev, A. Selskis, G. Niaura, E. Stankevičius, "Tuning SERS Performance Through the Laser-induced Morphology Changes of Gold Nanostructures", *Appl. Surf. Sci.* 660, 160003 (2024). DOI: 10.1016/j.apsusc.2024.160003

[P6] **K. Vilkevičius**, T. Rakickas, E. Stankevičius, "High-quality plasmonic Ag-Au bilayer nanobump grating sensor", *Adv. Mater. Technol.* 10(20), e01199 (2025) + Back Cover. DOI: 10.1002/admt.202501199

Lithuanian patents:

[T1] **K. Vilkevičius**, E. Stankevičius, "Plasmonic sensor and method of its formation", Nr. LT 7152 B (2025).

Scientific papers directly related to the thesis (conference proceedings):

[P7] **K. Vilkevičius**, T. Rakickas, E. Stankevičius, "Direct laser writing of Ag-Au thin films for plasmonic sensing platform", *Proc. 16th Int. Conf. META 2026*, 1549-1551 (2026).

[P8] **K. Vilkevičius**, I. Ignatjev, G. Niaura, E. Stankevičius, "Gold nanostructure gratings produced using direct laser writing with pulse energy-

dependent morphology for SERS substrates", *Proc. 15th Int. Conf. META 2025*, 1701-1702 (2025).

[P9] **K. Vilkevičius**, E. Stankevičius, "Wettability of fs-laser produced periodic gold nanostructures", *Proc. 7th Int. Conf. OPAL 2024*, 97-98 (2024).

Other scientific papers (peer-reviewed and indexed in Clarivate Analytics Web of Science (WoS)):

[OP1] R. Liudvinavičius, **K. Vilkevičius**, E. Stankevičius, "High-quality grating-coupled surface plasmon resonances in silver and gold bumps arrays fabricated in thin metallic films using the third harmonic of femtosecond laser", *Appl. Surf. Sci.* 711, 164127 (2025).

[OP2] J. Anulytė, E. Bužavaitė-Vertelienė, E. Stankevičius, **K. Vilkevičius**, Z. Balevičius, "High Spectral Sensitivity of Strongly Coupled Hybrid Tamm-Plasmonic Resonances for Biosensing Application", *Sensors* 22, 9453 (2022).

[OP3] J. Anulytė, E. Bužavaitė-Vertelienė, V. Vertelis, E. Stankevičius, **K. Vilkevičius**, Z. Balevičius, "Influence of a gold nano-bumps surface lattice array on the propagation length of strongly coupled Tamm and surface plasmon polaritons", *J. Mater. Chem. C* 10, 13234-13241 (2022).

[OP4] E. Stankevičius, **K. Vilkevičius**, M. Gedvilas, E. Bužavaitė-Vertelienė, A. Selskis, Z. Balevičius, "Direct Laser Writing for the Formation of Large-Scale Gold Microbumps Arrays Generating Hybrid Lattice Plasmon Polaritons in Vis-NIR Range", *Adv. Opt. Mater.* 9(12), 2100027 (2021) + Front Inside Cover.

Other scientific papers (conference proceedings):

[OP5] R. Liudvinavičius, **K. Vilkevičius**, E. Stankevičius, "Laser-induced formation of plasmonic nanostructures", *Proc. 16th Int. Conf. META 2026*, 763 (2026).

[OP6] **K. Vilkevičius**, R. Liudvinavičius, K. Čepaitis, E. Stankevičius, "Gold Film Treatment using a Tightly Focused Femtosecond Laser Beam", *Proc. 7th Int. Conf. OPAL 2024*, 145-146 (2024).

[OP7] **K. Vilkevičius**, V. Petrikaitė, R. Liudvinavičius, E. Stankevičius, "Laser-based techniques for micro-optics and photonics", *Proc. SPIE* 12012, 1201204 (2022).

[OP8] **K. Vilkevičius**, E. Stankevičius, "Formation of gold microbumps in thin gold films using femtosecond laser", *Proc. 17th Int. Conf. CYSENI 2021*, 791-795 (2021).

List of Conference Presentations

Conferences directly related to the thesis:

[C1] **K. Vilkevičius**, L. A. Letelier, L. Grinevičiūtė, E. Stankevičius, Plasmonic excitation management in symmetric 2D metallic gratings produced with direct laser writing, 18th International Conference on Laser Ablation "COLA 2026", Vilnius, Lithuania, 14-18 09 2026 (Poster presentation).

[C2] **K. Vilkevičius**, A. Karnilavičius, E. Stankevičius, Geometrically Controlled Plasmonic Laser-Written 2D Arrays of Gold Nanostructures and Their Potential Applications, 28th International Conference - School "Advanced Materials and Technologies 2026", Palanga, Lithuania, 24-28 08 2026 (Poster presentation).

[C3] **K. Vilkevičius**, T. Rakickas, E. Stankevičius, Direct Laser Writing of Ag-Au Thin Films for Plasmonic Sensing Platform, 16th International Conference on Metamaterials, Photonic Crystals and Plasmonics "META 2026", Dublin, Ireland, 14-17 07 2026.

[C4] **K. Vilkevičius**, T. Rakickas, E. Stankevičius, Rapid femtosecond-laser fabrication of a plasmonic sensor for glycerol detection, 69th International Conference for Students of Physics and Natural Sciences "Open Readings 2026", Vilnius, Lithuania, 27-30 04 2026 (Oral presentation – Best presentation award).

[C5] **K. Vilkevičius**, E. Stankevičius, Efektyvus lazerinis aukso dangų apdirbimas kuriant multifunkcines plazmonines gardeles, 14th Conference for Young Scientists "Fizinių ir technologijos mokslų tarpdalykiniai tyrimai", Vilnius, Lithuania, 17 04 2026 (Oral presentation – Best presentation award).

[C6] **K. Vilkevičius**, T. Rakickas, E. Stankevičius, Hibridinės sidabro-aukso bimetalinės nanogardelės, skirtos plazmonų rezonanso sensorikai, 15th Conference for Students and Young Scientists of the Center for Physical Sciences and Technology "FizTeCh 2025", Vilnius, Lithuania, 21-22 10 2025 (Oral presentation).

[C7] **K. Vilkevičius**, I. Ignatjev, G. Niaura, E. Stankevičius, Surface-enhanced Raman spectroscopy platform featuring variable morphology of periodic gold nanostructures, 46th Lithuanian National Physics Conference "LNFK 2025", Kaunas, Lithuania, 08-10 10 2025 (Oral presentation).

[C8] **K. Vilkevičius**, I. Ignatjev, A. Selskis, E. Stankevičius, Gold nanostructure gratings produced using direct laser writing with pulse energy-dependent morphology for SERS substrates, 15th International Conference on Metamaterials, Photonic Crystals and Plasmonics "META 2025", Torremolinos, Spain, 22-25 07 2025 (Oral presentation).

[C9] **K. Vilkevičius**, T. Rakickas, E. Stankevičius, The periodic bimetallic nanobumps for plasmonic sensing of glycerol concentration, Summer School on Ultra-short Pulse Lasers Applications in Material Processing "UPLAMP 2025", Vilnius, Lithuania, 7-11 07 2025 (Oral & Poster presentation).

[C10] **K. Vilkevičius**, I. Ignatjev, E. Stankevičius, Fast formation of high-quality periodic SERS platforms using direct laser writing, 9th International Congress on Laser Advanced Materials Processing "LAMP 2025", Ise-city, Mie-prefecture, Japan, 10-13 06 2025 (Oral presentation).

[C11] **K. Vilkevičius**, I. Ignatjev, E. Stankevičius, Direct laser writing fabrication of morphologically tunable SERS structures, 10th Symposium on Optical Coatings for Laser Applications "OCLA 2025", Vilnius, Lithuania, 08 05 2025 (Poster presentation).

[C12] **K. Vilkevičius**, I. Ignatjev, E. Stankevičius, Lazeriu suformuotų nanodarinių morfologinis valdymas paviršiumi sustiprintai Ramano spektroskopijai, 14th Conference for Students and Young Scientists of the Center for Physical Sciences and Technology "FizTeCh 2024", Vilnius, Lithuania, 15-17 10 2024 (Oral presentation - Best oral award).

[C13] **K. Vilkevičius**, G. D. Tsibidis, A. Selskis, E. Stratakis, E. Stankevičius, Ultrashort laser pulse induction of diverse morphology nanostructures on thin films, 17th International Conference on Laser Ablation "COLA 2024", Hersonissos, Crete, Greece, 29 09 – 04 10 2024 (Oral presentation).

[C14] **K. Vilkevičius**, E. Stankevičius, The periodic plasmonic nanostructures with tunable morphology produced using femtosecond pulses, 8th Venice International School on Lasers in Materials Science "SLIMS 2024", Venice, Italy, 14-20 07 2024 (Oral & Poster presentation).

[C15] **K. Vilkevičius**, E. Stankevičius, The periodic plasmonic nanostructures with tunable morphology produced using femtosecond pulses, Summer School on Ultra-short Pulse Lasers Applications in Material Processing "UPLAMP 2024", Vilnius, Lithuania, 1-6 07 2024 (Oral & Poster presentation).

[C16] **K. Vilkevičius**, I. Ignatjev, E. Stankevičius, Morphological tunability of periodic SERS structures generated by single fs pulses, The 25th International Symposium on Laser Precision Microfabrication "LPM 2024", San Sebastian, Spain, 11-14 06 2024 (Oral presentation).

[C17] **K. Vilkevičius**, E. Stankevičius, Wettability of fs-laser produced periodic gold nanostructures, 7th International Conference on Optics, Photonics and Lasers "OPAL 2024", Palma de Mallorca (Balearic Islands), Spain, 15-17 05 2024 (Poster presentation).

[C18] **K. Vilkevičius**, I. Ignatjev, E. Stankevičius, Fs-laser microprocessing for SERS substrates of periodic metallic structures, 67th International Conference for Students of Physics and Natural Sciences "Open Readings 2024", Vilnius, Lithuania, 23-26 04 2024 (Oral presentation).

[C19] **K. Vilkevičius**, E. Stankevičius, Laser-Induced Wavelength-Dependent Periodic Gold Nanostructures Exhibiting Hybrid Plasmon Resonance, 6th Nanophotonics and Micro/Nano Optics International Conference 2023 "NANOP2023: Functional Nanophotonics", Barcelona, Spain, 27-29 11 2023 (Poster presentation).

[C20] **K. Vilkevičius**, E. Stankevičius, Morphological Changes in Thin Gold Films for Plasmon Resonance Control, 45th Lithuanian National Physics Conference "LNFK 2023", Vilnius, Lithuania, 25-27 10 2023 (Oral presentation).

[C21] **K. Vilkevičius**, E. Stankevičius, Aukso nanodarinių gamyba, naudojant skirtingas femtosekundinio lazerio harmonikas, 13th Conference for Students and Young Scientists of the Center for Physical Sciences and Technology "FizTeCh 2023", Vilnius, Lithuania, 18-19 10 2023 (Poster presentation).

[C22] **K. Vilkevičius**, E. Stankevičius, Shape-Dependent Plasmon Resonance of Laser-Fabricated Gold Nanostructures, 25th International Conference - School "Advanced Materials and Technologies 2023", Palanga, Lithuania, 21-25 08 2023 (Poster presentation - Best poster award).

[C23] **K. Vilkevičius**, E. Stankevičius, Femtosecond Laser-Induced Formation of Wavelength-Dependent Periodic Gold Nanostructures, 19th International Conference of Young Scientists on Energy and Natural Sciences Issues "CYSENI", Kaunas, Lithuania, 23-26 05 2023 (Oral presentation).

[C24] **K. Vilkevičius**, E. Stankevičius, Femtosecond Laser Wavelength Influence on the Formation of Single-Shot Gold Nanostructures, 66th International Conference for Students of Physics and Natural Sciences "Open Readings 2023", Vilnius, Lithuania, 18-21 04 2023 (Oral presentation - Best oral award).

[C25] **K. Vilkevičius**, E. Stankevičius, Periodinių aukso nanodarinių formavimas bei jų plazmoninės savybės, 11th Conference for Young Scientists "Fizinių ir technologijos mokslų tarpdalykiniai tyrimai", Vilnius, Lithuania, 23 03 2023 (Oral presentation).

[C26] **K. Vilkevičius**, E. Stankevičius, Pavieniais femtosekundinio lazerio impulsais suformuoti periodiniai aukso mikrogumbeliai, žadinantys hibridinę plazmoninę modą, 12th Conference for Students and Young Scientists of the Center for Physical Sciences and Technology "FizTeCh 2022", Vilnius, Lithuania, 19-20 10 2022 (Poster presentation).

Contribution of the author and others

The author has personally designed and conducted the majority of the experimental work, from sample preparation and metal deposition to the laser setup and DLW-based fabrication. The author conducted all experimental measurements, characterization, data analysis, theoretical Comsol simulations and calculations, and result representations that are not attributed to co-authors in the following paragraph. The author prepared the manuscripts for all publications [P1]-[P6], incorporating comments and suggestions from co-authors. Also, the author prepared the cover designs, which were published together with [P2], [P4], and [P6].

Dr. Evaldas Stankevičius proposed the idea and supervised the whole study and work. ***Dr. Algirdas Selskis*** performed all SEM measurements. ***Dr. George D. Tsibidis*** performed thermal simulations using TTM for [P2]. ***Dr. Emmanuel Stratakis*** provided the equipment for [P2] and consulted on the fabrication and simulation results described in [P2]. ***Kipras Čepaitis***, under the author's supervision, fabricated the gratings and performed their optical measurements described in [P3]. ***Dr. Lina Grinevičiūtė*** consulted on diffraction grating simulations and calculations performed for [P4]. ***PhD student Lucciano A. Letelier*** performed FDTD spectral and near-field simulations using Ansys Lumerical for [P4]. ***Dr. Ilja Ignatjev*** performed SERS measurements described in [P5]. ***Dr. Gediminas Niaura*** consulted on SERS experimental results for [P5]. ***Tomas Rakickas*** prepared and provided liquids for RI sensing analysis and performed ellipsometric measurements for [P6].

1. LITERATURE REVIEW

1.1. Nanophotonics and plasmonic excitations in metallic nanostructures

Nanophotonics and rapid development in this area have led to increasing interest in controlling light and light-matter interactions at subwavelength scales. Here, plasmonics has emerged as one of the main research fields, combining physics and materials engineering. **Surface plasmons** (SPs) are collective oscillations of conduction electrons in metals that are excited under specific resonant conditions by external electromagnetic (EM) radiation. They are described as the displacement of the electron cloud from its equilibrium position relative to the positive ions. Because excitation occurs only at particular resonant frequencies, the process itself is referred to as plasmon resonance [9].

Plasmonic excitation is accompanied by increased optical extinction, near-field enhancement, and strong EM-field localization, enabling efficient light coupling and confinement below the diffraction limit. During resonance, incident radiation is attenuated by two mechanisms: scattering (Mie scattering) and absorption. Scattering occurs when excited plasmons re-emit photons of the same frequency, while absorption results from non-radiative energy dissipation through inelastic processes within the lattice. The combined contribution of scattered and absorbed radiation produces an extinction band in the optical spectrum, which is observed as a resonance peak [28]. Generally, plasmonic properties are related to two physical phenomena: optical extinction and enhanced near-field effects. Optical extinction reaches a maximum at the plasmon resonance excitation frequency. Additionally, during resonance, nanoparticles behave as nanolenses, and the EM field is significantly amplified around the particle surface, while it rapidly weakens as it moves away from the particle. These two effects form the basis for plasmonic applications [2].

The interaction between metallic systems and the EM field is classically described by Maxwell's equations, which relate the electric and magnetic fields to the material's dielectric response [29]. Here, the complex dielectric function is the primary parameter governing the metal's optical response. To achieve plasmonic effects, the real part of this function has to be negative. A widely used model for describing metal-dielectric response is the Drude model, which treats conduction electrons as a free-electron gas. In this approximation, the dielectric function depends on the plasma frequency and

electron damping rate, below which metals exhibit negative permittivity. The plasma frequency is expressed as [29]:

$$\omega_p = \sqrt{\frac{ne^2}{\varepsilon_0 m}}, \quad (1)$$

where n is the electron number density, e is the electron charge, ε_0 is the vacuum permittivity, and m is the effective optical mass of the electron.

Surface plasmon resonance (SPR) occurs when the EM wave frequency matches the natural electron plasma frequency, thereby causing the incident radiation to be absorbed. The main factors influencing this phenomenon are environmental properties (dielectric permittivity, absorption), particle size (absorption and scattering cross-section), and shape (morphology), as well as their concentration (distribution, dimer formation) and composition (material properties, doping, core-shell structures) [30]. Plasmonic oscillations are limited by losses associated with either radiative or non-radiative origins. Non-radiative losses originate from intrinsic electron scattering within the material, while radiative losses arise from the coupling of plasmonic oscillations to the far field [2, 31].

Among plasmonic metals, gold and silver are the most commonly used due to their favorable optical responses in the visible and near-infrared (near-IR) spectral range. Silver exhibits lower intrinsic losses, resulting in sharper and more intense resonances. However, it is less chemically stable and more prone to oxidation. Gold, in contrast, offers excellent chemical stability and biocompatibility, although it exhibits higher metallic losses [32]. Meanwhile, aluminum is often used in the ultraviolet (UV) range [33]. Although pure metals are usually used, the choice among these materials, or their combination in alloys or bimetallic systems, involves a compromise between optical performance and environmental stability and resistivity.

1.2. Plasmonic modes

Optical properties of plasmonic nanostructures heavily depend on the plasmonic modes they support. Metallic structures exhibit two fundamental surface plasmon modes, as well as other modes arising from interactions and their hybridization. Plasmonic interactions can be near-field, when the distances between metal structures are shorter than the resonant wavelength, or far-field, when this distance is exceeded [34].

1.2.1. Localized surface plasmons

The first fundamental mode is the **localized surface plasmon** (LSP), which occurs in individual metallic nanoparticles with dimensions smaller than the incident photon's wavelength. Under EM excitation, free electrons collectively oscillate throughout the nanoparticle volume at the radiation frequency. As a result, an oscillating dipole is formed across the entire nanoparticle, aligned parallel to the EM field. Such nanoparticles exhibit strong radiative damping, leading to broad resonant spectra [11, 28].

Commonly, LSP systems are described using the classical harmonic oscillator model. In the case of spherical nanoparticles, the oscillation of the electron cloud induced by interaction with the electric field can be described through the polarizability of the metal, from which the extinction cross-section is derived [29]:

$$\sigma_{ext} = \frac{18\pi\varepsilon_d^{3/2}}{\lambda} V_{NP} \frac{\mathrm{Im}\varepsilon_m}{(\mathrm{Re}\varepsilon_m + 2\varepsilon_d)^2 + (\mathrm{Im}\varepsilon_m)^2}, \tag{2}$$

where ε_m and ε_d are the dielectric constants of the metal and the surrounding dielectric medium, respectively, and V_{NP} is the nanoparticle volume. From this expression, it can be seen that plasmonic properties strongly depend on the material itself through its dielectric function, while the extinction increases with increasing volume, and the maximum value is achieved when the denominator reaches its minimum value – LSP is excited at frequency [2]:

$$\mathrm{Re}\big(\varepsilon_m(\omega)\big) \approx -\chi\varepsilon_d(\omega), \tag{3}$$

where χ is the geometrical factor, equal to 2 for spherical nanoparticles. Generally, this mode is observed in homogeneous spherical nanoparticles with dimensions below 100 nm and is called the dipole surface plasmon.

The presented relations demonstrate that LSPs are strongly dependent on nanoparticle size, shape, material, and the surrounding medium. However, these expressions are valid only for spherical nanoparticles, while for other geometries, LSPs exhibit different characteristics due to the presence of multiple polarization modes. Consequently, non-spherical nanoparticles exhibit several resonant peaks; for example, rod-shaped structures can be polarized along two principal axes, resulting in two distinct absorption peaks corresponding to transverse and longitudinal resonances [29].

1.2.2. Propagating surface polariton

The second fundamental plasmonic mode is the **surface plasmon polariton** (SPP), which occurs at the interface between a conductor (metal)

and a dielectric due to the interaction of the EM field with plasma oscillations in the metal. SPP at the metal-dielectric interface cannot be excited directly by incident radiation, because the wavevector of light (more specifically, its in-plane component along the interface) is always smaller than the polariton wavevector, resulting in the absence of phase-matching conditions (Figure 1.1a). The SPP wavevector is commonly expressed as [33]:

$$k_{SPP} = k_0 \sqrt{\frac{\varepsilon_m \varepsilon_d}{\varepsilon_m + \varepsilon_d}}, \tag{4}$$

where k_{SPP} and k_0 are the SPP and the incident light wavevectors.

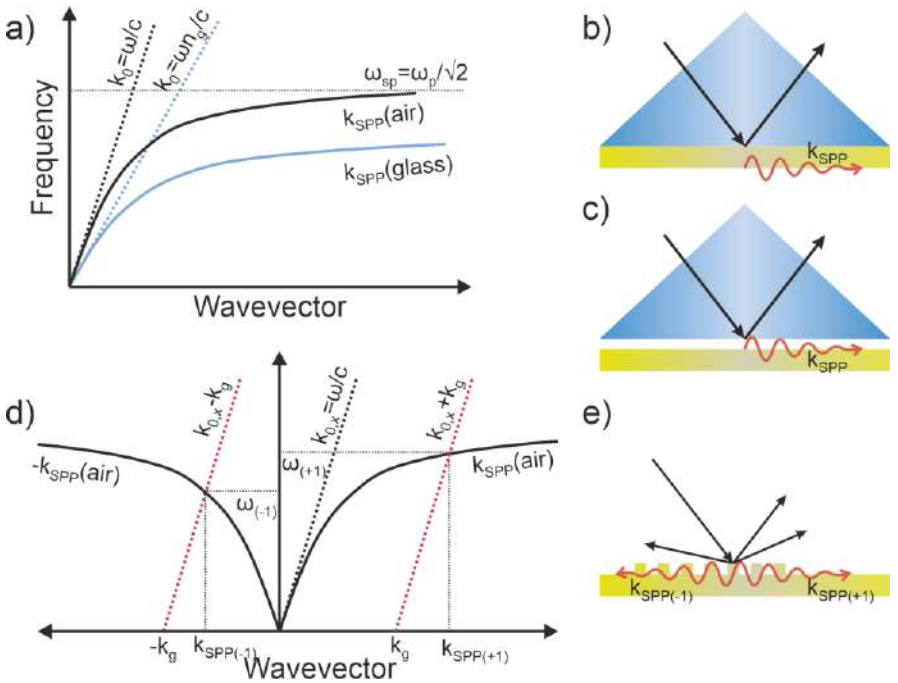

Figure 1.1. a) SPP dispersion relation and phase-matching using a glass prism. SPP excitation using b) Kretschmann and c) Otto configurations. d) SPP dispersion relation and phase-matching using a grating. e) SPP excitation using a grating.

To achieve wavevector matching and excite SPPs, several methods are used. The most common is the **glass prism-based excitation**, which requires three media: a conductor (metal) and two different dielectrics (air and prism). The principle is based on total internal reflection (TIR) within the prism, in which the reflected light acquires an in-plane wavevector component $k_{SPP} = k_0\sqrt{\varepsilon_d}\sin\theta$, thereby enabling SPP excitation at the metal-air interface [35, 36]. These propagating polaritons are not excited at the metal-prism interface because the prism wavevector intersects the SPP propagation dispersion only at the metal-air interface and does not satisfy the condition for the metal-prism

boundary (Figure 1.1a). Depending on the prism arrangement relative to the thin metal film, two excitation geometries can be distinguished: Kretschmann and Otto configurations. The more common Kretschmann configuration [35] uses a metal layer deposited directly onto the prism surface (or in contact without a gap), with SPPs excited on the opposite side of the metal (Figure 1.1b). In this case, light propagating in the prism at an angle exceeding the critical angle tunnels through the metallic film. In the Otto configuration [37], an air gap is present between the prism and the metal surface. Under TIR conditions, the evanescent field tunnels through the air gap and excites SPPs at the upper film surface Figure 1.1c. This configuration is advantageous when direct contact with the metal must be avoided.

An alternative method for SPP excitation, intended to eliminate the need for an additional optical element (a prism), is **grating-based coupling**. This is achieved by structuring the metal surface into periodic arrays of grooves, holes, or nanostructures [38, 39]. The periodic arrangement enables SPP excitation due to the grating compensation for the light wavevector (Figure 1.1d), when the matching condition can be expressed as [40]:

$$k_{SPP} = k_0 \sin\theta \pm \frac{2\pi n}{s}, \tag{5}$$

where θ is the angle of incidence, n is the diffraction order, and s is the grating period. In this type of excitation, the plasmonic response strongly depends on the array period, morphology, and angle of incidence. Both one-dimensional and two-dimensional gratings may be employed for SPP excitation (Figure 1.1e). This diffraction-based excitation can be described either by a complex two-dimensional (2D) diffraction grating or by a simplified one-dimensional (1D) formula [41].

Although the aforementioned methods are suitable for SPP excitation, they are not suitable for localized excitation at specifically selected positions, and more precise approaches have been developed. One such method employs a **tightly focused beam** with a high numerical aperture objective (NA > 1) together with an immersion oil. The large NA provides a broad distribution of incident angles, ensuring wavevector matching and SPP excitation [42]. This methodology enables excitation not at a single wavelength, but also using a broadband white-light source continuum.

Another excitation technique is **near-field excitation**, enabling polariton generation within an area smaller than the diffraction limit. In this approach, a tapered aperture, commonly fabricated from an optical fiber, acts as a point-like source, directing radiation onto the sample. Since photons propagate through an aperture smaller than the SPP wavelength, an efficient excitation

of the plasmonic mode becomes possible. Also, such precise positioning enables localized excitation at specific points on the sample [43].

The near-field decay length of SPP modes is approximately 40-50 times larger than that of LSPs, so SPP-based structures provide higher bulk sensitivity. Also, such SPP waves can propagate along a plasmonic surface over distances ranging from tens to hundreds of nanometers [1]. However, the use of fundamental (LSP or SPP) plasmonic modes limits the practical applicability of the structures, so hybrid plasmonic modes are commonly employed. Coupling between different plasmonic modes can provide nanostructures with additional optical properties, thus improving their performance and broadening their range of applications [44].

1.2.3. Hybrid plasmonic modes

Periodic metallic nanostructures can function not only as platforms for SPP excitation but also as light-scattering and diffractive elements, giving rise to hybrid plasmonic modes. One of these is **surface lattice resonance** (SLR), which emerges from the coupling between diffracted light and LSPs supported by metallic nanoparticles within a periodic array [45-47]. If individual nanoparticles are arranged in an array with a period comparable to the wavelength of light, the LSPs couple diffractively via the Rayleigh anomaly, thereby producing a hybrid plasmonic-photonic mode. In this case, the light is scattered by each nanoparticle while maintaining phase-matching with the diffracted light and the adjacent structures' resonance, thus reducing radiative losses and increasing the coherence of the collective response. This SLR results in narrower resonance linewidths and higher quality factors than those of isolated nanoparticles [48].

The spectral position and characteristics of the SLR can be tailored by adjusting the nanoparticle size, morphology, and array periodicity. Efficient excitation of SLR requires both strong localized plasmonic resonances and long-range diffractive coupling. If the structural dimensions are too small, the collective dipolar interaction may be insufficient to compensate for radiative damping, thereby preventing the effective formation of the SLR. Furthermore, out-of-plane plasmonic modes can enhance coupling and generate high-quality resonances [49-51].

Additionally, when periodic metallic nanostructures are produced on the metallic film, both SLR and SPP modes can be excited [10, 52], and diffractively coupled **hybrid lattice plasmon resonance** (HLPR) can be achieved [22, 53], which will be referred to as grating-coupled resonance. Since this excitation is, as well, diffraction-based, the theoretical resonant

wavelength for a squared grating can be determined from the 2D diffraction formula in plasmonic gratings [54]:

$$\lambda_{res,2D} = \frac{s}{(m^2+n^2)}\left(-m\sin\theta \pm \sqrt{\frac{\varepsilon_m\varepsilon_d}{\varepsilon_d+\varepsilon_m}(m^2+n^2) - n^2\sin^2\theta}\right), \quad (6)$$

where m and n are diffraction orders in the plane of incidence and the perpendicular plane. From this formula, simplified 1D-type diffraction can be derived as a special case [22].

1.3. Control of plasmonic properties

Surface structuring modifies both the properties of individual nanostructures and enables control over the interaction of EM radiation with the material, thereby altering the properties of the entire plasmonic system. The properties are determined by the characteristics of the fabricated structures, including their size, shape, composition, degree of aggregation, and concentration. These parameters govern the most important functional properties – their ability to absorb EM radiation, transport the generated charge carriers, and emit light [55].

Among the parameters, the **size of nanostructures** is particularly important in determining their optical response. As discussed previously, LSPs are excited in particles with dimensions lower than the wavelength of incident radiation. An increase in nanoparticle size leads to a redshift of the resonant peak [56]. However, when the size becomes comparable to or exceeds the wavelength, the electric field distribution within the particle is no longer spatially uniform. Consequently, the polarization of the electron cloud becomes non-uniform, leading to the excitation of higher-order multipolar plasmonic modes. This transition from dipolar to multipolar behavior leads to broadening and a shift of plasmonic resonances toward longer wavelengths [2, 28].

Changes in the optical response are also observed when the **shape of the nanostructures** is modified. Symmetry reduction of a particle is a widely used approach for tailoring the spectral position and intensity of plasmonic resonances. For example, spherical gold nanoparticles exhibit a single resonant peak near 520 nm, whereas cylindrical or more complex structures support two or more distinct modes. In the case of gold nanorods, two peaks are observed, corresponding to transverse and longitudinal plasmonic modes [57, 58]. The transverse mode is relatively weak and appears within the visible spectral range, while the longitudinal mode is stronger and occurs in the near-IR region. Also, an increase in the aspect ratio of these nanorods results in a

redshift of the longitudinal mode [8]. Meanwhile, structures with more complex geometries (nanocubes, nanoprisms) [59, 60] exhibit more intricate interactions with radiation, leading to broader LSP resonances that span a wider spectral range. Such structures often provide stronger near-field enhancement, particularly at sharp corners and edges, where the EM field becomes highly concentrated.

The properties are also strongly influenced by the **material composition**. Noble metals, including gold, silver, and copper, dominate in plasmonic applications due to their resonances appearing in the visible and near-IR spectral regions. In contrast, aluminum, indium, and gallium possess higher plasma frequencies and are therefore employed in UV plasmonics. Other metals, such as lithium, could support resonances over a broader range, but practical applications are limited by their high chemical activity [2, 8]. Such structures are not only limited to pure metals but can also be fabricated from hybrid materials consisting of metal-dielectric or metal-metal combinations [61]. Surface chemical properties can be modified by coating nanostructures with a secondary material, thereby improving their stability and oxidation resistance. The optical response of multimetallic nanostructures can generally be categorized into three regimes: optical properties of individual components remain distinguishable; intermediate optical characteristics of both constituent metals are obtained; entirely new optical properties emerge. This behavior primarily depends on whether the components produce a distinct phase or a homogeneous alloy. In the case of noble metal alloys (Au, Ag, Cu), the optical response is dominated by the metal possessing larger interband electronic transitions [62], while the resonant wavelength also linearly depends on the relative concentration of the metals [63]. Core-shell nanostructures depend on the thicknesses – as the shell thickness increases, the resonance associated with the core becomes suppressed, while the shell mode dominates the optical response. By adjusting the relative dimensions of the core and shell, the plasmonic resonance can be continuously tuned [64]. In addition, noble metal combinations with magnetic materials are used to produce magnetoplasmonic nanostructures [65].

Plasmonic properties are further affected by the **number and density** of nanostructures, as well as the degree of aggregation. As discussed previously in the context of SLRs, the LSP modes of closely spaced nanoparticles interact via EM coupling, thereby modifying their optical response [45]. The simplest example is a dimer composed of two metallic nanospheres. Here, LSP coupling results in a decrease in the resonant frequency for excitation along the dimer axis and an increase for excitation perpendicular to it [66, 67]. More complex agglomerates containing tens of nanoparticles exhibit two dominant

spectral bands: one near the resonant wavelength of an isolated nanoparticle, and a second one shifted toward longer wavelengths [68]. In contrast, periodic arrays exhibit collective optical responses. When the spacing is close to the LSP mode wavelength, the far-field interference between neighboring structures narrows the resonance linewidth [44]. Additional arrangements in which periodic nanoparticle arrays are organized into larger periodic superlattices can support multiple narrow resonant peaks [11, 45, 69].

1.4. Fabrication techniques of plasmonic gratings

Metallic micro- and nanostructures for plasmonics and nanophotonics are in high demand for their scalability, repeatability, and uniformity; therefore, various fabrication techniques have been developed to produce plasmonic gratings. Methodologies are generally categorized into two approaches: top-down, which relies on traditional lithographic methods to process bulk material into specific structures, and bottom-up, which utilizes the interaction of atoms and molecules to assemble nanostructures [70, 71]. Here, the main fabrication techniques for plasmonic structures and their arrays are presented.

1.4.1. Lithography-based techniques

Electron beam lithography (EBL) is one of the main top-down techniques that uses a sharply focused electron beam to scan thin resist layers, thereby modifying areas to become more or less soluble in organic solvents. The process follows three stages: coating the substrate with a resist, electron-beam exposure to alter its chemical structure, and chemical development [72]. Depending on the structure shape, positive resist is more commonly used for metal structures, while negative resist is used to create holes in the sample [73]. Once the required pattern has been formed, the resist is used as a mask during etching or deposition processes to produce micro- or nanostructures with the desired geometries [11]. The main advantage of EBL is its high resolution and extremely small feature sizes (5-10 nm), achieved because the electron wavelength is significantly smaller than that of photons, thereby bypassing the diffraction limit [74]. Despite its precision, EBL faces significant throughput challenges because the small beam is scanned point-by-point, limiting its use to small-area research. Additionally, the proximity effect, caused by electron scattering in the resist, can lead to unintended exposure of areas near the beam, resulting in rounded-edge structures. Also, this method is limited to film thicknesses below 100 nm due to the limited electron penetration depth [72]. The periodic nanostructures produced with EBL can be of any complex shape, from dual nanostars with tips of 50 nm

[75] or nanoprisms with a period of 225 nm [76] to C-shaped [77] or chiral and hierarchical arrays [78].

Focused ion beam (FIB) lithography employs ions (usually Ga^+) for the additive or subtractive structuring of materials. In FIB milling, high-mass ions directly remove material from the substrate surface without a mask (Figure 1.2a). The material removal and penetration depth of ions can be precisely controlled by adjusting the ion energy [72]. This dry, single-step process has a major advantage over EBL: it eliminates the need for resist coating, development, or pattern transfer. FIB can achieve a resolution of approximately 5 nm and can fabricate structures with vertical sidewalls, as ions have a much shorter wavelength and lower scattering probability than electrons [55]. However, FIB systems are expensive and, similar to EBL, have low throughput, making them unsuitable for large-scale production. Also, Ga^+ ions can contaminate the surface, as they can be implanted in the processed zone. Structures fabricated using FIB are usually holes milled in metallic films, with the narrowest zones reaching around 15 nm [79]. More complex structures include chiral spirals with 80 nm wide strips [80] or cylindrical arrays [81]. The fabrication of isolated structures requires removing the surrounding film, making the process extremely slow and practical only for small arrays. Also, a combination of EBL and FIB is used to improve resolution and minimize defects, when after fabrication of the primary nanostructure with EBL, FIB is used to finalize the structural shape [82].

To overcome throughput and cost limitations, **soft lithography** has emerged as a high-efficiency alternative for large-area modification. It relies on a soft elastomeric polydimethylsiloxane (PDMS) stamp, which is favored for its mechanical strength, chemical inertness, transparency in the visible range, and reusability. Typically, a stamp is produced from a master fabricated using slower EBL or FIB techniques [83]. This method is significantly cheaper than previously described beam-based methods, as it eliminates the need for expensive optics and vacuum systems. Also, its high throughput makes it ideal for mass production of large-scale samples and for implementation in roll-to-roll systems [72]. A major drawback is that stamp fabrication is costly, and a new master must be created for every design change. Additionally, the elastomeric nature of PDMS can lead to pattern distortion or deformation, and it cannot replicate complex structures with high precision [71]. A similar method is **nanoimprint lithography**, in which a rigid master is pressed into a resist to produce polymerized structures [55] (Figure 1.2b). The most common morphologies are periodic hole arrays or cylinders [14, 84]. Also, linear gratings with diameters on the order of tens of nanometers can be achieved with a few-nanometer interstructural spacing [85]. As an extension

of this technique, soft-lithography stamps can be used to self-assemble colloidal nanoparticles into ordered arrays exhibiting high-quality resonances [86, 87].

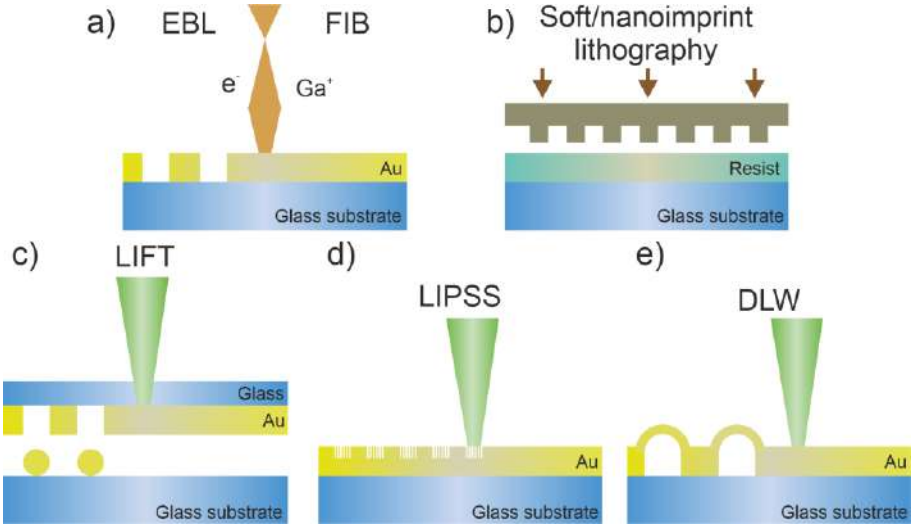

Figure 1.2. Metallic nanostructure fabrication methods: a) EBL and FIB, b) Soft nanoimprint lithography, c) LIFT, d) LIPSS, and e) DLW.

1.4.2. Laser-assisted fabrication techniques

Alternative techniques for periodic structure formation rely on laser processing, in which the material can be either completely removed or partially modified to produce plasmonic arrays via laser-metal interaction. Ultrashort laser pulses enable precise, clear structuring of various materials, from metals to ceramics and dielectrics. When the material is exposed to nanosecond pulses, the dominant process is melting, whereas with femtosecond pulses, surface ablation and deformation occur without heat diffusion and with a minimal heat-affected zone [88].

One such laser-based method is **laser-induced forward/backward transfer** (LIFT/LIBT), which enables localized deposition of donor material onto a substrate, called an acceptor, via melting and ablation of the donor. In the case of LIFT, a laser illuminates a transparent donor substrate, partially vaporizing and ejecting donor material, which is then deposited onto the acceptor substrate (Figure 1.2c). The main difference in LIBT is that the laser illuminates through a transparent acceptor [89]. The key feature of this method is that the donor material is melted and remains in the liquid phase throughout the transfer process until it reaches the substrate, where it forms spherical nanoparticles [90]. However, even slight inhomogeneity in laser absorption significantly affects the size and position deviations of printed structures [91].

Laser pulses can also be used to produce periodic ripples on a metal surface across the entire beam spot area. These **laser-induced periodic surface structures** (LIPSS) manifest as periodic lines ranging in size from a few micrometers to 100 nm, with the period and orientation depending on the wavelength and polarization of the light (Figure 1.2d). The formation mechanism is still under discussion: whether it is based on interference between incident and scattered radiation, or on self-organization and absorption-related atomic diffusion and hydrodynamic motion of the melt, leading to spontaneous surface modifications [92]. Since the LIPPS period is close to the wavelength of light, such gratings are used to alter wettability, create a self-cleaning surface, or produce surface coloration [93].

Finally, **direct laser writing** (DLW) can be used to form metallic nanostructures. Frequently, such a technique, when a laser beam is tightly focused within the polymeric sample, is used to create three-dimensional (3D) polymerized structures in a transparent material via multiphoton absorption [94, 95]. However, such a method can also be used to modify thin metallic film surfaces. By implementing single femtosecond pulses to structure metals characterized by a high elastic modulus, surface modifications with varying morphologies can be produced [96-98]. Laser-induced modification of thin films includes mechanical and thermodynamic processes. Upon irradiation, the deposited energy is transferred to the metal, resulting in rapid heating and melting within the central area of the beam. At relatively low pulse energies, adhesion between the film and substrate is weakened, leading to metal delamination and expansion away from the substrate (Figure 1.2e). The final morphology and height are governed by the balance among surface tension forces, cooling, and the material's solidification rate. At higher energies, mass redistribution occurs, resulting in the formation of differently shaped structures [99, 100]. Heat dissipation begins at the substrate, causing the molten material in the central part to rise due to the momentum gained, producing a high, narrow, jet-like tip [101].

1.5. Applications of plasmonic grating structures

Advanced fabrication techniques used to produce plasmonic structures and their periodic arrays have enabled convenient tunability of structural parameters and resulting plasmonic responses. This opportunity greatly expands the usability of such structures in various fields, as the parameters can be tailored to each specific application. In the following section, the main applications of plasmonic gratings are presented.

1.5.1. Surface-enhanced Raman spectroscopy

As mentioned previously, one of the two main phenomena observed in plasmonic structures is near-field enhancement. Due to this amplification, plasmonic particles are used in surface-enhanced Raman spectroscopy (SERS). By measuring inelastic Raman scattering, it is possible to obtain the exact molecular fingerprint of its vibrations. However, such a scattering signal is relatively weak and requires a large concentration of molecules to be detected. Meanwhile, by utilizing plasmonic structures near the investigated molecules, the signal can be greatly amplified and detected at low molecular concentrations, or even at single-molecule levels. Structures with sharp tips or several nanometer spacings create hot spots with extreme signal enhancement, reaching up to 10 orders of magnitude [102, 103]. The strongest SERS signals are obtained when the excitation is close to the resonant wavelength of the used structures [104]. The periodic arrangement increases signal intensity and enables tunability of the resonance via variations in size or period [105, 106]. Also, a high uniformity of the enhancing structures is required, which can be achieved in metallic gratings.

Owing to its high sensitivity and molecular specificity, plasmonic grating-based SERS is applied to low-level detection in chemical analysis, environmental monitoring, and food safety [13, 107]. It has been successfully employed for the detection of chemical traces of dye molecules, food allergens and contaminants, explosives, and other hazardous substance traces [108, 109]. This method is also used for bioanalysis. Accurate detection of proteins and biomolecules, as well as infectious diseases and tumors, can be performed using such structures [110, 111].

1.5.2. Refractive index sensing

Another major application is based on the observed absorption peaks and SPR sensitivity to changes in the local refractive index (RI) around the plasmonic structure. When biological molecules or chemical analytes bind to the surfaces of the structures, the RI changes, thereby modifying the SPP excitation conditions and the spectral resonance position. Since this shift is directly dependent on the surrounding medium RI, it enables the identification of attached molecules or changes in concentration [38, 50, 112]. The sensitivity of such platforms and their performance highly depend on the linewidth of the resonant peak, which is determined by radiative and nonradiative losses. Narrow resonance peaks enable the detection of smaller spectral shifts and improve detection resolution; therefore, loss reduction is highly desirable in this area. A considerable amount of research has focused

on developing structures that support ultranarrow plasmonic modes, leading to the use of metallic arrays [113].

Such RI-based grating sensors are investigated for chemical and biological sensing. Periodic hole arrays, nanoparticle arrays, and hybrid plasmonic gratings have demonstrated the ability to label-free detect cancer cells, bacteria, and biochemical markers [14, 114]. Beyond this, such sensors are employed for gas sensing, liquid analysis, and real-time detection of molecular adsorption processes [15, 115]. Their compatibility with microfluidic systems makes them attractive for integrated sensing platforms. Recent advances have also improved RI-sensing performance through the combination of plasmonic nanostructures and gain materials with the nanolasing concept. Such coupling leads to ultranarrow linewidths and responses several hundred times larger than those of a typical SPR sensor [116, 117].

1.5.3. Other applications

The enhancement of the near-field in plasmonic nanoparticles can be applied not only to SERS but also to photoluminescence, absorption, and nonlinear interaction amplification. The 2D transition metal dichalcogenide (TMDC) monolayers, such as MoS_2 and WS_2, typically exhibit weak light-matter interaction, with low-intensity **photoluminescence** (PL) emission. Metallic nanostructures combined with these TMDCs can greatly enhance the signal due to SPR coupling with excitons. The PL intensity can be enhanced several hundredfold for MoS_2 [118, 119] and WS_2 [120], as well as for quantum dot emission [121]. Similar gratings are used to enhance nonlinear phenomena (second harmonic generation) [122, 123] and nanolasing [18].

Finally, the strong EM field localization at the metallic arrays enables the use of such samples as **perfect light absorbers**, consisting of an array-dielectric-metal configuration. Due to the interaction between the top metallic grating and the bottom metallic film, perfect absorption can be achieved. The efficiency, absorbed wavelength, and intensity are controlled and tuned by accurate array engineering [124], thereby achieving both narrowband [125] and broadband [126] absorbing platforms.

2. ANALYSIS AND EXPERIMENTAL METHODOLOGY

Experimental methodology will be divided into two parts. The first will describe the preparation of the sample, its microstructuring, and the fabrication of nanostructures. The second will describe the equipment used for the investigation of the samples (structural and plasmonic properties).

2.1. Materials and sample preparation

2.1.1. Thin film deposition

The experiments were carried out on thin metallic films deposited on 1 mm thick microscopic soda-lime glass substrates (Biosigma VBS653). The films were deposited using a magnetron sputter coater (Quorum Q150T). Most of the samples investigated in [P1]-[P6] were prepared using a gold target, at a deposition rate of 0.26 nm/s. Meanwhile, for the sensing-related studies reported in [P6], additional silver films were deposited at a rate of 0.59 nm/s. For the same study, a silver-gold bilayer sample was prepared by sequentially depositing silver and gold layers. In some experiments, prior to metal deposition, an additional 3 nm-thick titanium adhesion layer was deposited at a rate of 0.175 nm/s to enhance metal adhesion to the substrate. A summary of the coatings used is provided in Table 1.

Table 1. Thin films used for the experiments.

Material	Thickness, nm	Deposition time, s	Publications
Au	25	94	[P2]
	50	188	[P1]-[P3],[P5],[P6]
	75	283	[P2], [P5]
	100	377	[P2],[P4],[P5]
	125, 150, 175, 200	472, 566, 660, 755	[P5]
Ag	50	84	[P6]
Ag-Au	25-25	42-94	[P6]
Ti	3	17	[P3],[P6]

2.1.2. Sample fabrication

Plasmonic nanostructures on thin metal films were fabricated using direct laser writing with a tightly focused femtosecond (fs) laser to locally modify the layer. In this method, a laser beam induces melting, modification, or ablation of the metal surface, thereby enabling the formation of periodic structures via direct microfabrication. The Yb:KGW based fs-laser (Pharos, Light, Conversion) beam was focused onto the sample using a high-NA objective (Mitutoyo Plan Apo Infinity Corrected 100x/0.5NA), while the sample was mounted on a translation stage. The laser source provided linear polarization. Depending on the research, three fs laser harmonics were used for fabrication: 1030 nm, 515 nm, and 343 nm. Laser parameters are listed in Table 2. The wavelength, pulse duration, and beam quality parameter M^2 were specified by the laser manufacturer in the parameter sheet. A typical fabrication setup (Figure 2.1) consists of a laser source, mirrors for guiding the beam, an attenuator, a beam reducer made as a Galilean telescope from bi-convex and bi-concave lenses (f = 100 mm and f = -50 mm), a high-NA objective, and a movable translational stage. An additional charge-coupled device (CCD) camera was mounted in the system's 3rd-harmonic path to visualize the magnified sample and enable real-time monitoring of the fabrication process. An additional objective (Olympus UPlanFL N 20x/0.5NA) was used for CCD visualization at 1030 nm and 515 nm fabrication, whereas for 343 nm, the same objective as for DLW was used. The sample along the x and y axes was moved using linear stages (Aerotech), while the focus position in the z direction was changed by moving a stage on which the telescope with an objective was mounted. The laser and scanning stages were controlled using the Direct Machining Control (DMC) software.

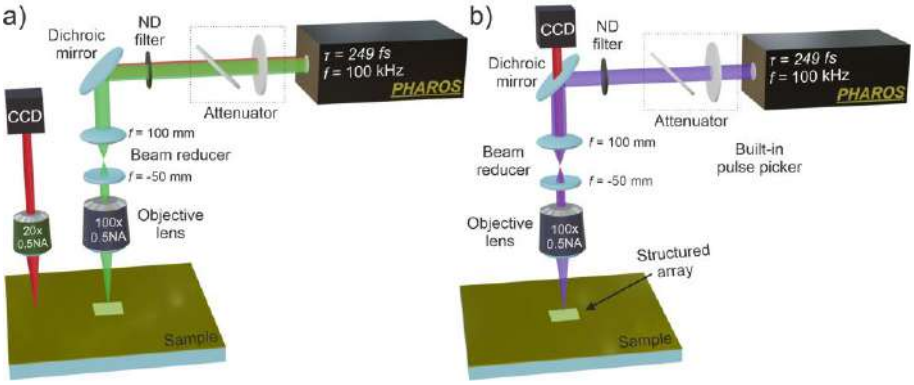

Figure 2.1. Laser fabrication setup scheme for a) 1030 nm and 515 nm wavelengths and b) 343 nm wavelength.

Table 2. Laser parameters used for the experiments.

Laser source	Pharos, Light Conversion		
Wavelength	1030 nm	515 nm	343 nm
Pulse duration	249 fs		
M^2	1.1	1.07	1.06
Base rep. rate	100 kHz		
Pulse picker rep. rate	7 kHz	7 kHz	7 kHz / 20 kHz
Objective	Mitutoyo Plan Apo NIR 100x		Mitutoyo Plan Apo NUV 100x
Focused beam spot size	2.2 µm	1.1 µm	0.8 µm
Pulse energy	7.5 – 10 nJ	0.2 – 1.9 nJ	0.3 – 4.0 nJ
Fluence	0.4 – 0.507 J/cm^2	0.043 – 0.4 J/cm^2	0.126 – 1.68 J/cm^2
Scanning speed	0.7 – 14.7 mm/s		
Publications	[P1]	[P1], [P3]	[P1], [P2], [P4]-[P6]

Periodic 2D gratings were fabricated using the DLW technique by unidirectionally scanning a focused laser beam along the sample surface according to a predefined template. Since only a single fs pulse is required for the formation, a pulse picker was implemented to separate pulses at a specific rate matched to the scanning speed. The in-line period of the scanned line, as well as the pulse overlap, was adjusted by varying the translation speed or the pulse picker rate (Figure 2.2a). Mainly, this rate was maintained constant at 7 kHz, with the translation speed being adjusted according to the period by:

$$v = s \cdot f_{PP}, \tag{7}$$

where s is the in-line period, and f_{PP} is the pulse picker repetition rate. The distance along the perpendicular axis was determined in the software by defining the spacing d between the scanning lines. To produce a uniform array at all edges, additional acceleration and deceleration were implemented before and after the fabrication zone. Pulse energy control was achieved using an attenuator. The average power was measured using a Centauri (Ophir) power meter with a silicon photodiode sensor (PD300-TP) for 1030 nm and 515 nm, and PD300-UV for 343 nm, with an in-built filter. The power was measured at a constant laser base repetition rate (100 kHz), and the single-pulse energy was calculated by dividing the average power by this base repetition rate.

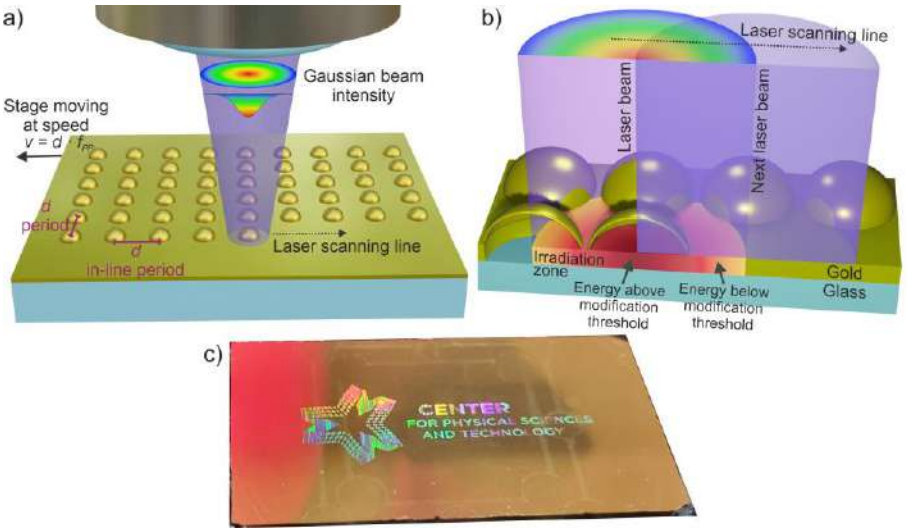

Figure 2.2. a) Direct laser writing formation scheme. b) Overlapping effect of the laser beam and layer modification zone. c) Free-form array produced on gold film.

The formation of the nanostructures is driven by thermal stresses induced in the film by the laser pulse. After irradiation, either plastic deformation or melting and subsequent resolidification results in morphologically distinct structures. Due to the Gaussian intensity distribution of the laser beam, most of the pulse energy is concentrated in the central region, where the modification threshold is exceeded first. Therefore, working at the threshold, structures can be produced only in the central region of the beam (Figure 2.2b), resulting in dimensions smaller than the focal spot and enabling structure fabrication with pulse overlap. In this way, an array of any free-form shape can be produced (Figure 2.2c).

The periodic square-shaped arrays of 100×100 μm^2 dimensions were fabricated for structural analysis and SERS measurements, while larger arrays (3×3 mm^2) were produced for optical properties measurements.

2.2. Instrumentation and analysis

2.2.1. Morphological characterization

After fabrication, structural characterization was primarily performed using an optical microscope (Nikon Eclipse LV100D) to study large-area uniformity, periodicity, and defect localization.

Afterward, an investigation was conducted using a scanning electron microscope (SEM) (Helios NanoLab 650) to determine the morphology of the obtained structures and measure their feature sizes. The SEM micrographs were obtained in two regimes: a top view (0°) and at angles of 52° in [P6] and

57° in [P1]-[P5]. Magnification was 35000x and 100000x. Additionally, in [P2], [P4], and [P6], the cross-sections of the structures were prepared by sputtering a thin Pt layer to enhance contrast, followed by cutting the structures with focused Ga ions.

The morphology of the structures was determined from their height-to-diameter ratio. Structures of hemispherical shape with a diameter greater than their height were called bumps; structures with similar dimensions were cones; and jets were structures with a high, narrow protrusion in the central part. Structural diameters and heights were measured from SEM micrographs using ImageJ analysis software.

2.2.2. Optical and spectral characterization

The spectral characterization and reflection measurements were performed using a spectrophotometer (EssentOptics Photon RT). The responses were measured for both perpendicular s- and p-polarizations in the 400-1600 nm range with a 4 nm step for [P1]-[P3] and a 1 nm step for [P4], and in the 600-2000 nm range with a 1 nm step for [P6]. The angle of incidence (AOI) was set to 8°, with additional measurements at 15°, 30°, 45°, and 60°. The samples were measured at two azimuthal angles: φ = 0°, when the plane of incidence (PI) is parallel to the laser scanning lines (Figure 2.3a), and φ = 90°, when the PI is perpendicular to the laser scanning lines (Figure 2.3b). Additional azimuthal rotation from φ = 0° to φ = 180° in 15° increments by manual rotation of the sample was performed for [P4]. For all measurements, a 2 mm-diameter circular aperture was placed at the light source to enhance the signal and ensure that the signal was obtained solely from the structured array.

The resonant peaks observed in the spectra were qualitatively investigated for relative comparison. For comparison with other articles, the quality factor (Q-factor, QF) was expressed as:

$$QF = \frac{\lambda_{res}}{FWHM}, \tag{8}$$

where λ_{res} is the central resonance wavelength, and $FWHM$ is the width of the peak at half its height. We introduced an additional parameter that accounts for both the peak width and its depth, as the latter parameter shows the light-plasmon coupling efficiency. This modified quality factor (MQ-factor, MQF) was described as:

$$MQF = \frac{\lambda_{res} \cdot h}{FWHM \cdot 100\%}, \tag{9}$$

where h is the depth of the peak. However, in the literature, only the Q-factor is used; therefore, this MQ-factor is only suitable for internal comparisons of resonances in this work. Because the spectral peaks were asymmetric, the

calculations were performed by measuring depth from the lower-reflection side (usually, lower-wavelength), as depicted in Figure 2.3c.

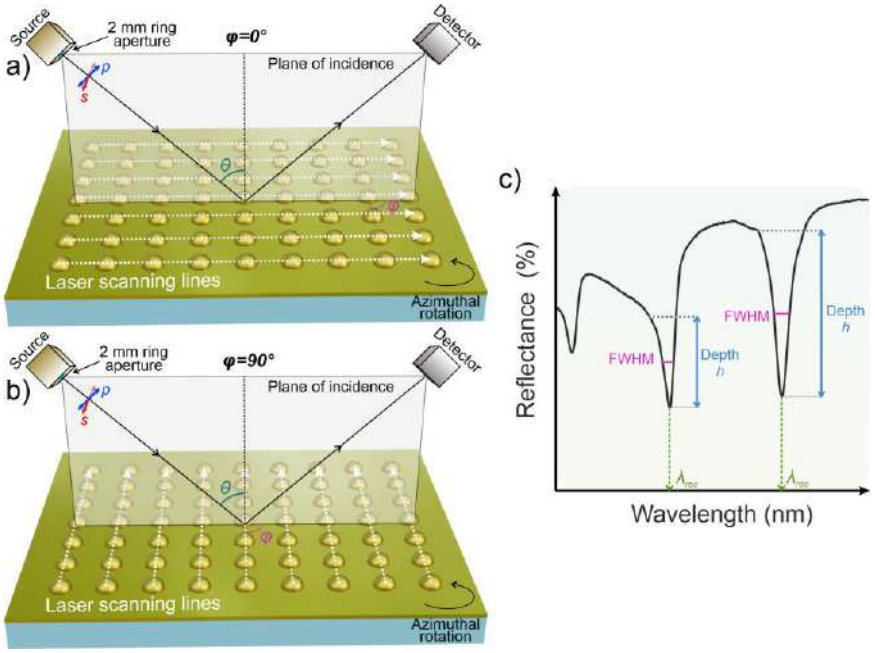

Figure 2.3. Spectrophotometer measurement scheme for a) φ = 0° and b) φ = 90° azimuthal angles. c) Analysis and determination of the depth and width of the resonant peaks.

2.2.3. Simulation of plasmonic properties

EM field distribution and reflection spectra for gold nanostructures were calculated using the finite element method (FEM) in the COMSOL Multiphysics solver. In [P2], linearly polarized light ranging from 800 to 1600 nm in 5 nm steps was used to irradiate the structures at an AOI of 8°. For [P5], linearly polarized 785 nm radiation was used for excitation at normal incidence. A rectangular domain containing a single nanostructure was used, with Floquet periodic boundary conditions (1 µm period) and two perfectly matched layers (PMLs) applied below and above the domain. The gold dielectric function was based on Johnson and Christy's data [127]. The surrounding medium was air (n = 1), and the substrate was soda-lime glass on which a thin 100 nm gold film was deposited. The air domain thickness was determined to be twice the wavelength used. Structures were described as hollow ellipsoids, cones, and truncated cones with solid spikes. The dimensions of the structures were taken from SEM micrographs.

Theoretical reflection spectra and near-field distributions for a 2D symmetric nanobump grating analyzed in [P4] were computed using

Lumerical finite-difference time-domain (FDTD) solver. Here, the structure was described using a unit cell with Bloch boundary conditions in the grating directions and PMLs in the light-propagation direction. Unit cell with a 1 μm period consisted of dielectric (n = 1.51 at 900 nm) covered with a 100 nm gold film. Oblique-incidence results were simulated using the Broadband Fixed Angle Source Technique (BFAST) with a source from 400 nm to 1600 nm and 1 nm spectral resolution. During the simulations, AOIs of θ = 8°, 15°, 30° and azimuthal angles of φ = 0°, 15°, 30°, 45° were chosen.

2.2.4. SERS measurements

Raman spectroscopy and SERS measurements were performed to investigate local electromagnetic field enhancement at the structures and to evaluate their SERS performance, as described in [P5]. The 4-mercaptobenzoic acid (4-MBA) self-assembled monolayer was used as a reporter in the SERS experiment. The gold samples, with thicknesses ranging from 50 to 200 nm in 25 nm increments, were immersed in a 1 mM 4-MBA isopropanol solution for 6 hours. Subsequently, they were rinsed with isopropanol solution and dried under N_2 gas.

The SERS spectra were measured using an inVia Raman spectrometer (Renishaw) equipped with a thermoelectrically cooled (-70°C) CCD camera and a 50x/0.5NA objective with a long working distance. Meanwhile, the Raman measurements were performed using a 5x/0.12NA objective with a 14 mm working distance and a grating (1200 lines/mm). For these Raman measurements, a 0.25 M (250 mol/m^3) MBA in isopropanol solution was analyzed. The excitation source was a 785 nm diode laser with an average power of 0.8 mW. The spectra were recorded at the focus of the integrated confocal microscope (Leica), with an accumulation time of 9 s. The Raman scattering wavenumber axis was calibrated by the Si-Si vibrational mode at 520.7 cm^{-1}. During SERS measurements, the beam was focused to a 1.2 μm spot, thereby covering and recording the response from a single metal nanostructure. The signal was registered over time and then normalized to 1 second. Additionally, a mapping of the sample was performed over a 5×5 μm^2 surface area with a step of 1 μm.

One of the main parameters used in SERS, an enhancement factor (EF), was calculated using the formula:

$$EF = \frac{I_{SERS} \cdot N_R}{I_R \cdot N_{SERS}}, \tag{10}$$

where I_R and I_{SERS} are the intensities of Raman and SERS spectral bands, while N_R and N_{SERS} correspond to the average number of excited molecules in Raman

and SERS experiments. Since Raman measurements were performed in a solution, the following formula was used for the number of excited molecules:

$$N_R = V_R \cdot C_R \cdot N_A \tag{11}$$

where N_A is the Avogadro constant, C_R is the analyte concentration, and V_R is the Raman probe volume. For the latter probe volume, the 785 nm wavelength was used with a 7.7 mm unfocused beam diameter and a focal length of 1.75 mm. Therefore, the calculated probe volume was 8.38×10^{-17} m^3, resulting in an excited-molecule count of 1.26×10^{10} in the Raman measurements.

Meanwhile, for SERS measurements, the laser beam was focused to a 1.2 μm-diameter spot on the surface, corresponding to a 1.13 μm^2 spot area. The gold nanostructure grating surface was covered with 4-MBA molecules at a density of 5×10^{-6} mol/m^2. Therefore, the total number of excited molecules in SERS was calculated by multiplying the product of these by Avogadro's number and the surface roughness. Such a number is $N_{SERS} = 3.404\times10^6\times R$. The roughness factor R was calculated from the following formula:

$$R = \frac{S_{real}}{S_{geom}} \tag{12}$$

where S_{real} is the actual illuminated area of the surface (Figure 2.4a), and S_{geom} is the area of the focused laser beam on the surface (1.13 μm^2). The illuminated structure area S_{real} was determined from SEM images by calculating surface areas of bumps, cones, and jets. This calculation method is depicted in Figure 2.4b.

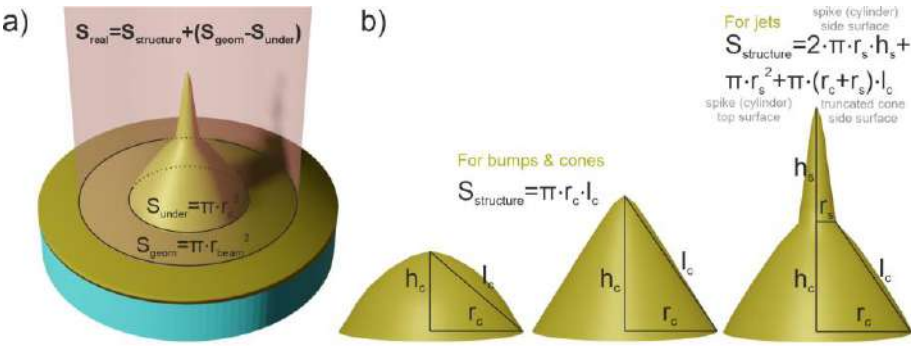

Figure 2.4. a) Calculation of real irradiated surface area. Geometrical area S_{geom} is the spot size into which the beam is focused. S_{under} is the area under the structure (base area), while $S_{structure}$ is the surface area of the structure. b) Calculation of the structure surface area. The subscript *c* marks the height, radius, and slant height for the conical base, while the subscript *s* marks the height and radius for the spike.

2.2.5. Sensing measurements

After metal surface structuring, an adhesive chamber (HybriWell-FL) was attached to the surface to investigate sensing capabilities. A spectrum was measured for reference resonances in air; compared with the spectrum without the adhesive chamber, it was almost identical, with only a few percent drop in signal intensity. Then, a syringe with a needle was used to infuse the liquid into the chamber to cover the entire structured array, and the spectrum was measured again. After each measurement, the liquid was blown out using high-pressure air, and the infusion-extrusion procedure, along with the measurements, was repeated 3 times for each investigated liquid. The full measurement scheme is depicted in Figure 2.5a.

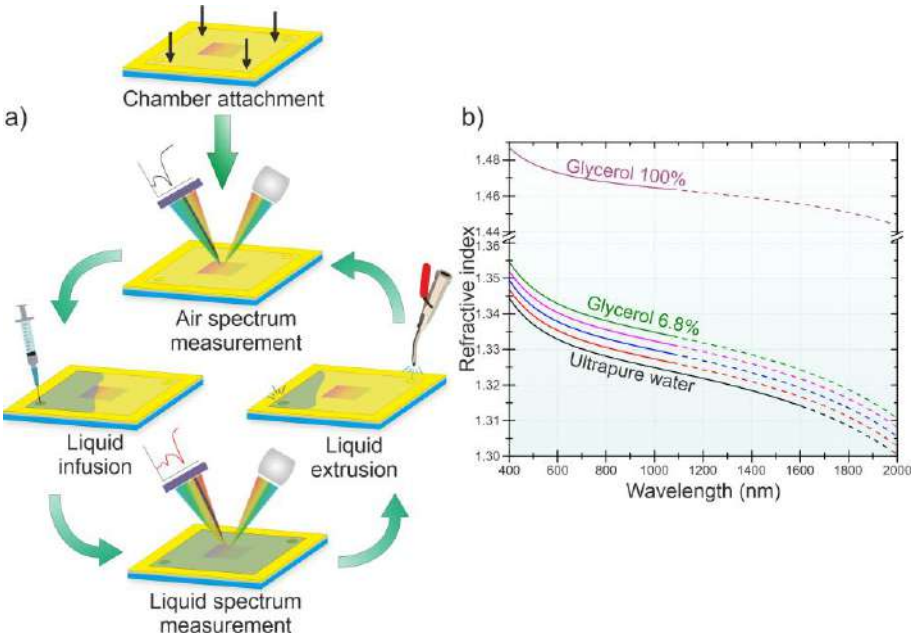

Figure 2.5. a) Sensing platform preparation and measurement scheme. b) Dispersion curves of ultrapure water (black line) and glycerol of 1.7% (red), 3.4% (blue), 5.1% (magenta), 6.8% (green), and 100% (purple) concentrations. Solid lines depict the experimentally obtained values, and dashed lines indicate the values calculated using the Sellmeier dispersion formula.

Measurements were performed using five liquids: ultrapure water and four different concentrations of glycerol in water. Ultrapure water (resistivity 18.2 MΩ×cm at 25°C) was obtained from a Synergy UV (Merck, USA) water purification system, while glycerol (86 wt%) was obtained from Carl Roth GmbH, Germany. An imaging null ellipsometer (Accurion Nanofilm EP3) equipped with a Kinetics/SPR cell and a BK7 prism was used to determine the RIs of the liquids at 658 nm. In the beginning, the TIR angle was determined

for ultrapure water injected into a cell, and the glass RI was obtained using the water RI (n_{658} = 1.3314 at 658 nm) from Kedenburg et al. [128]. Then, glycerol in ultrapure water solutions was injected into the cell, and TIR angles were measured, which determined the RI and concentration of 1.7% (n_{658} = 1.3339), 3.4% (n_{658} = 1.3364), 5.1% (n_{658} = 1.3389), and 6.8% (n_{658} = 1.3414) glycerol solutions. For additional limit of detection (LoD) measurements, glycerol solutions of 0.84% (n_{658} = 1.3327), 0.4% (n_{658} = 1.332), and 0.2% (n_{658} = 1.3316) were used. The RI dispersions of the liquids were calculated using a Sellmeier equation, with constants taken from the literature [128, 129]. The dispersion for the 400-2000 nm range is depicted in Figure 2.5b.

The sensing platform was evaluated and characterized in terms of resonance quality (Q-factor and MQ-factor), sensitivity, and figure of merit (FOM). Sensitivity, describing the ability of the resonance to respond to changes in the surrounding refractive index, was defined as:

$$S = \frac{\Delta\lambda_{res}}{\Delta n}, \tag{13}$$

where $\Delta\lambda_{res}$ is the change in resonant wavelength, and Δn is the change in the environment RI. Here, the exact RI values at each specific resonant wavelength were obtained from the corresponding dispersion curves. Since sensitivity is a platform parameter, the calculated value was averaged across all investigated liquids. Meanwhile, the FOM characterizes overall sensing efficiency by combining sensitivity with the spectral resolution of the resonance. It describes how well a shift can be resolved and is defined as:

$$FOM = \frac{S}{FWHM} \tag{14}$$

A higher FOM indicates a greater sensing performance, as it reflects both a strong spectral response to RI changes and a narrow resonance profile. This value differed across liquids, and averaging was performed only for consecutive measurements.

Finally, to assess durability, the samples were stored in unsealed plastic Petri dishes in a dark, dry box at room temperature for 6 months. During this period, the relative humidity ranged from 20% to 50%, and the adhesive chamber was attached to the sample, which served as a protective layer.

3. RESULTS AND DISCUSSION

This chapter presents and discusses the results reported in publications [P1]-[P6]. The findings are organized to reflect the progression of the research, starting with the fundamental parameters governing femtosecond-laser-based nanostructure formation and progressing to application-oriented plasmonic devices. Therefore, this chapter is divided into two parts. The first part focuses on DLW-based fabrication of nanostructures under varying conditions and the resulting effects on plasmonic properties. These results are supported by [P1]-[P4]. The second part addresses the functional performance and practical applicability of the described plasmonic gratings. These results are supported by publications [P5]-[P6].

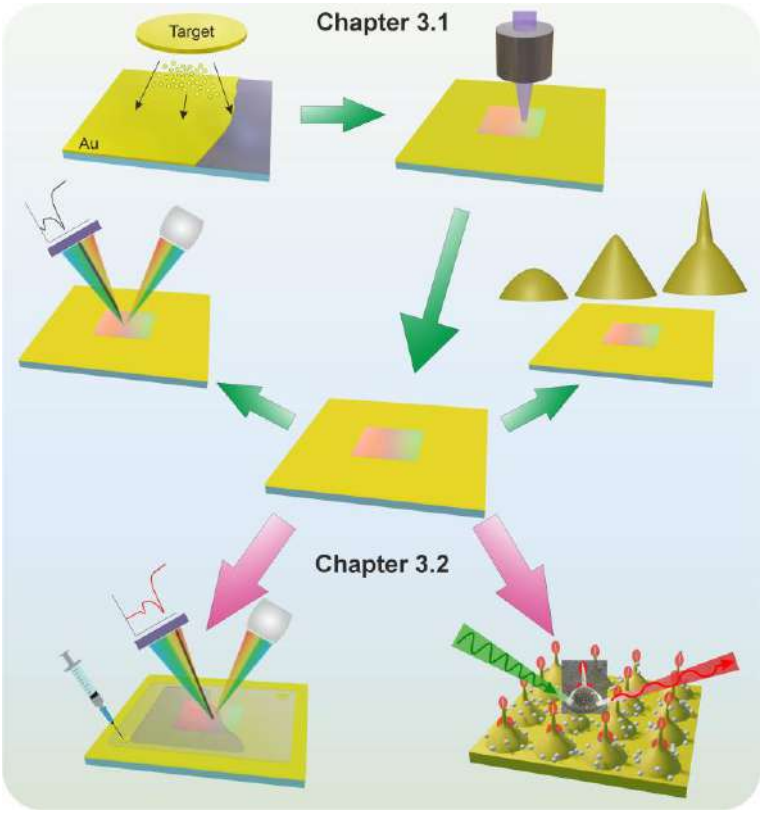

3.1. Laser-based formation and investigation of plasmonic nanostructure gratings

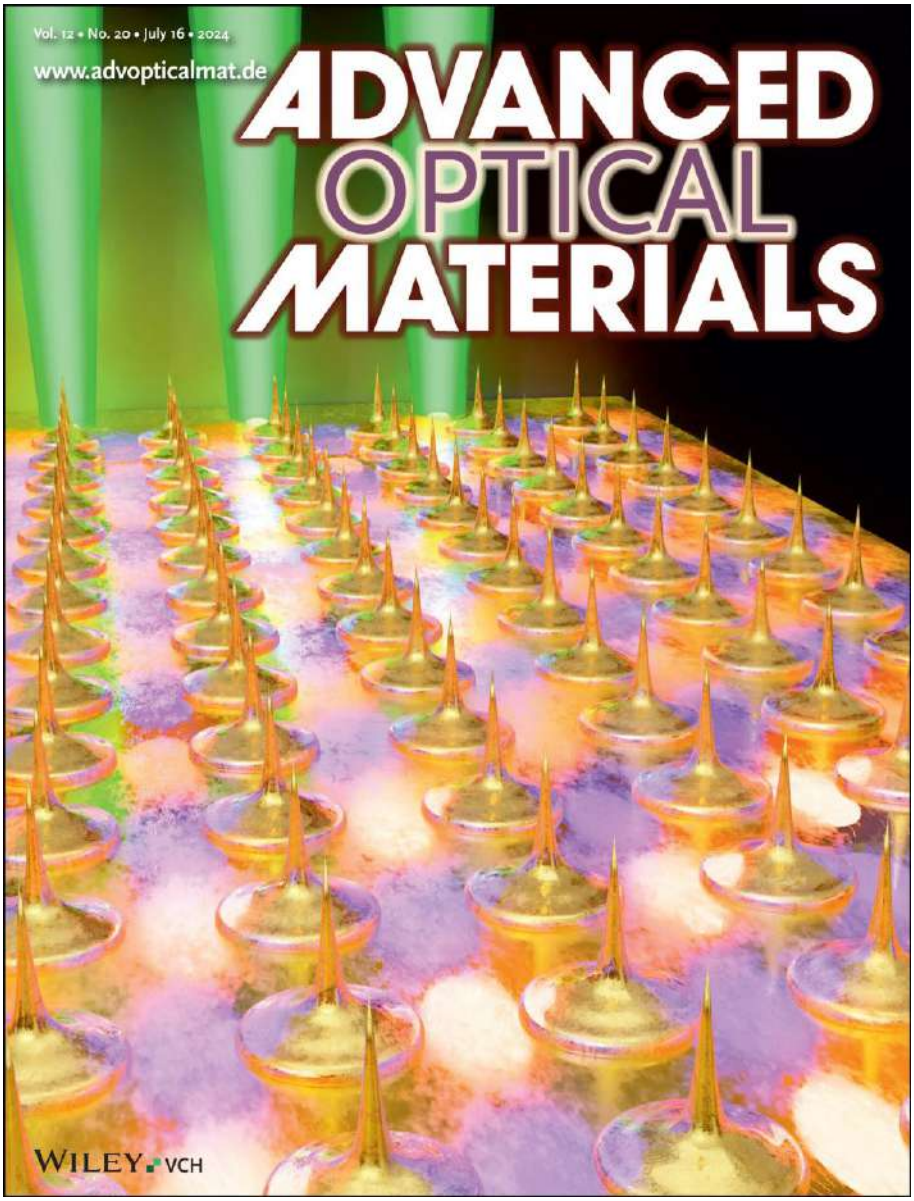

INSIDE FRONT COVER:
Kernius Vilkevičius, George D. Tsibidis, Algirdas Selskis, Emmanuel Stratakis, Evaldas Stankevičius, *Formation of Highly Tunable Periodic Plasmonic Structures on Gold Films Using Direct Laser Writing* (Advanced Optical Materials, Vol. 12 Issue 20, 2024)

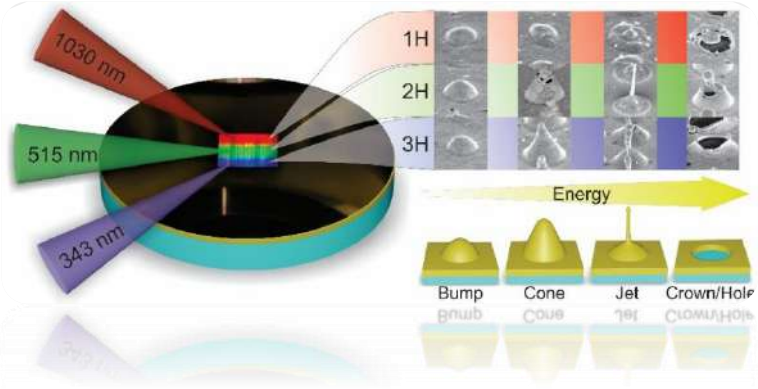

3.1.1. Wavelength-influenced plasmonic nanostructure fabrication

This subchapter is based on the paper [P1] published in *Applied Surface Science*, 617, 156629, 2023, by K. Vilkevičius, A. Selskis, and E. Stankevičius.

Laser-based techniques have emerged in the field of nanostructurization owing to fast, scalable, single-step, and chemical-free methodologies for material modification. In particular, direct laser writing with femtosecond-pulse irradiation enables precise and large-scale structuring of thin metallic films without the need for masks or multi-step processing. The process is governed by optical absorption, ultrafast energy deposition, heat diffusion, and thermally driven material redistribution. Therefore, physical system parameters, processing regimes, and their accurate control are essential for achieving precise, reproducible nanostructures suitable for application-oriented research.

Since metallic structures are fabricated using single fs pulses, the interaction strongly depends on the irradiation wavelength, which determines absorption efficiency, penetration depth, and the material's thermal response. This parameter is among the primary factors influencing the structures produced; therefore, understanding the wavelength-determined fabrication regimes and their impact on the resulting structures is the first step toward thorough control of plasmonic platforms and their optical response. To date, most research on nanostructurization using single fs pulses has been conducted at a single wavelength (800 nm [130-132], 515 nm [100], or 532 nm [133]), without a direct comparison of the effects of these parameters, necessitating further investigation.

In this study, thin gold films with a uniform thickness of 50 nm were irradiated with Pharos femtosecond laser pulses at wavelengths of 1030 nm,

515 nm, and 343 nm using a fixed-NA objective. The measured optical losses, consisting of absorption, scattering, and diffraction into non-zero orders, for the 1st harmonic (1H) were 3.56%, for the 2nd harmonic (2H) 33.06%, and for the 3rd harmonic (3H) 53.62% (Figure 3.1a). These were determined by measuring transmittance and zero-order reflectance, and then subtracting them from the total signal. Since the 1H response is dominated by reflectance, this graph might indicate that 3H is more absorbable, as the optical losses increase. An objective with NA = 0.5 was used, and the beams were focused to 2.2 µm, 1.1 µm, and 0.8 µm diameter spots at 1030 nm, 515 nm, and 343 nm, respectively. Nanostructure arrays with periods up to 2.2 µm were initially produced to avoid beam overlap, but the structures remained uninfluenced even at 1.2 µm distances, so only periods below 1.3 µm were studied in-depth.

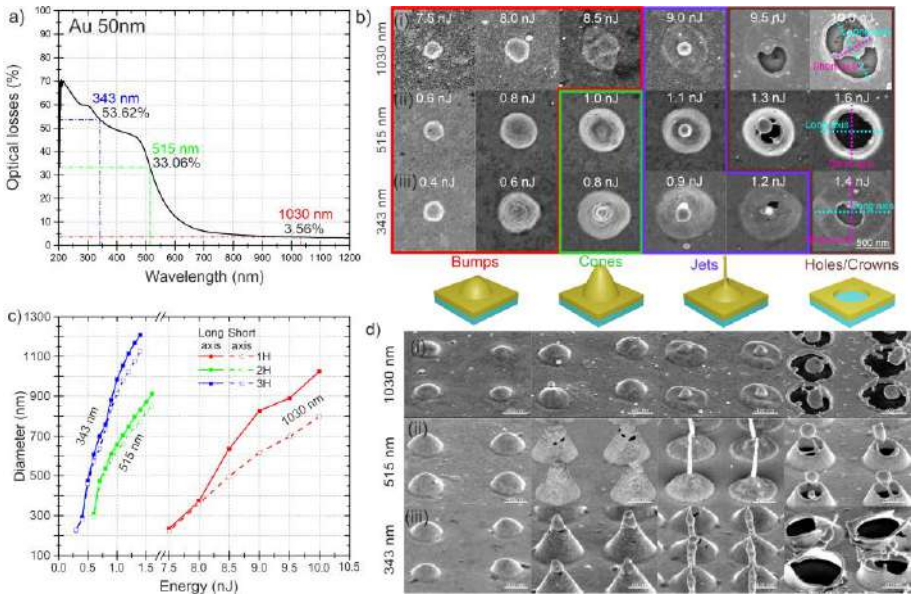

Figure 3.1. a) Optical loss spectra of a 50 nm thick gold film. b) SEM micrographs of gold nanostructures in 1.2 µm period gratings fabricated with (i) 1030 nm, (ii) 515 nm, and (iii) 343 nm. c) Dependence of the diameters of the long (solid line) and short (dashed line) axes on pulse energy. d) SEM images of nanostructures tilted at a 57° angle obtained using (i) 1H, (ii) 2H, and (iii) 3H.

By reducing the wavelengths to more absorbable ones, it was determined from experimental observations that the pulse energy and fluence required to initiate modification of the layer decreased – from 7.5 nJ (0.4 J/cm^2) at IR to 0.55 nJ (0.117 J/cm^2) at visible, and to 0.3 nJ (0.109 J/cm^2) at UV beam. At larger periods (1.2 µm), where beam overlap does not affect the structure, the effects of pure wavelength and pulse energy on structural dimensions were analyzed. An increase in energy results in larger structures, accompanied by changes in their morphology. Such a transition is observed at all investigated

wavelengths (Figure 3.1b). The shape transitioned from small hemispherical bumps to cones, jets, and ablated holes with crowns. At higher pulse energies, the structures exhibited ellipticity, attributed to the laser's linear polarization. Figure 3.1c depicts the growth in diameter of both long and short axes, as well as the difference between them, with increasing energy. Solid lines represent the long-axis data, and dashed lines represent the short-axis data. The polarization impact on the structure's ellipticity increases with energy and is most pronounced for the fundamental harmonic, with a diameter difference of over 200 nm. Additionally, using shorter-wavelength pulses yields steeper curves, indicating that a larger diameter range can be achieved within a narrower energy range, consistent with increased absorption of these pulses.

Wavelength influences not only lateral dimensions but also vertical dimensions (Figure 3.1d). The bumps produced by all three harmonics are similar in shape but are lower in height (150-180 nm) at the IR wavelength than at the visible and UV wavelengths (300-400 nm). As observed in SEM analysis, conical structures are not formed at 1H irradiation because of minimal absorption, and the structure height remains below the diameter, while other harmonics produce cones reaching heights of 700-750 nm. The most prominent morphological difference is obtained at the jet regime. 2H and 3H produce sharp, narrow spikes exceeding 1 μm in height, indicating strong material ejection and hydrodynamic flow. Under 1H irradiation, the resulting morphology is highly elliptical, with a non-protruding, round bump only 150 nm in height. This behavior is attributed to insufficient momentum transfer from poorly absorbed radiation, limiting vertical material displacement.

Furthermore, an additional period-related investigation was performed. The minimum periods achievable for each harmonic were determined at the modification-threshold energies corresponding to small-bump fabrication regimes. Arrays with a period of 0.8 μm are achievable using 1H, whereas for 2H the period can be reduced to 0.5 μm, and for 3H to 0.45 μm or 0.4 μm. The smallest achievable distance is limited by the size of the laser-modified region and the resulting protrusion-like structure. While IR radiation is focused into a relatively large spot, the interplay between the Gaussian beam intensity threshold and minimal absorption enables structure formation in the high-intensity central region, resulting in features smaller than the beam diameter. Nevertheless, the focal spot size remains the dominant factor governing the structural dimensions, rather than the interplay between absorption and Gaussian intensity, leading to UV radiation forming the smallest-period arrays. The nanostructure short-axis diameter dependence on pulse fluence and grating period is depicted in Figure 3.2a, where distinct

fluence ranges are observed. Layer modification with the fundamental harmonic is relatively high at 0.4 J/cm^2, with a narrow modification range of 0.15 J/cm^2. By increasing laser harmonics, the modification threshold is greatly reduced to 0.1 J/cm^2, and the modification range is expanded to 0.2 J/cm^2 at 515 nm and 0.4 J/cm^2 at 343 nm. An increased fluence range enables more precise control of the parameters and structural dimensions under UV radiation. The inter-structure distance also affects the diameter and formation energy, as observed in Figure 3.2a, where the left corners of the graphs indicate this effect. A shorter period requires a lower fluence to induce thin film ablation due to pulse overlap. Analysis of the lattice temperature history using the two-temperature model showed that the interval between pulses allows the lattice to cool down. This confirms that shape changes influenced by the period are not caused by heat accumulation but rather result from visible and invisible modifications throughout the irradiated area, as well as induced mechanical stresses and delamination. This phenomenon leads to an additional increase in structure size with a reduction in period, as the fabricated structures, with diameters equal to or slightly larger than the period, begin to touch and overlap, thereby limiting the minimum periodicity at that fluence. At a wavelength of 340 nm and a constant fluence of 0.33 J/cm^2, the diameter at the 1.3 μm period is approximately 850 nm, increasing to 950 nm at the 0.9 μm period, when the structures overlap.

SEM images of the structures were used to determine the precise energy ranges for each morphological state and their corresponding transitional fluences. Figure 3.2b shows the formation zones for each wavelength, with colored lines indicating the transitional fluences. These thresholds were determined solely from SEM images, while the additional squared dependence of lateral size on the natural logarithm of the pulse energy (Figure 3.2c) was used to calculate the theoretical thin-film modification threshold via a linear approximation of the data for each period. This parameter is in good agreement with the practically determined values. In the graphs, a clear reduction in transitional fluences is observed at periods below 1 μm due to beam overlap. By transitioning from 1H to 2H and 3H, bumps are produced at fluence ranges with widths of 0.067 J/cm^2, 0.083 J/cm^2, and 0.127 J/cm^2. Cones are produced only with 2H and 3H in fluence range widths of 0.021 J/cm^2 and 0.055 J/cm^2, respectively. The same tendency is maintained for jet formation. It is clear that reducing the wavelength increases the ranges over which specific morphological states are fabricated, as well as the overall nanostructurization range. Bumps and jets are obtained over a wider fluence range than cones, because the bumps continuously grow in height, quickly surpassing the nanocone phase.

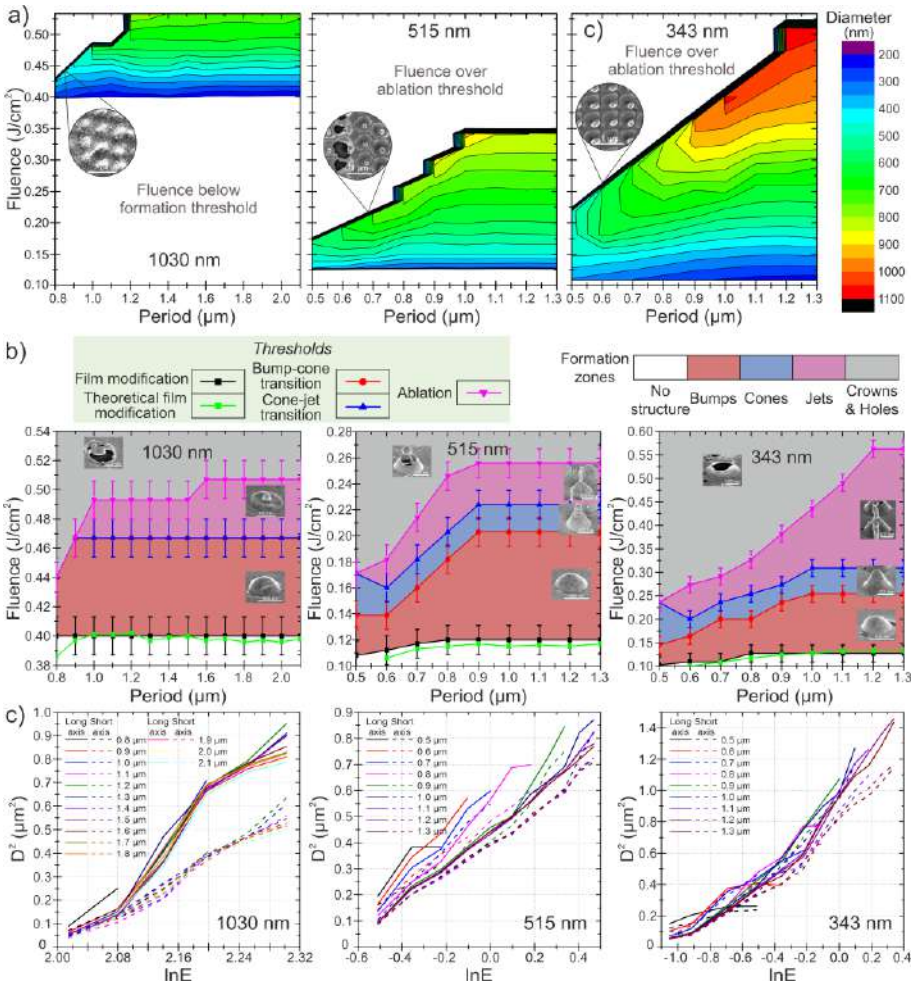

Figure 3.2. a) Short-axis diameter dependence on the grating period and laser beam fluence colormap. b) Morphological phase transitional fluence thresholds (lines) and each morphology formation range (colored areas) for different laser wavelengths. c) Squared lateral size dependence on the natural logarithm of laser pulse energy for different laser wavelengths. For all graphs, the first column shows results for 1030 nm, the second for 515 nm, and the third for 343 nm.

Ultimately, the plasmonic properties of a 1 μm-period bump array were evaluated using a spectrophotometer to assess their dependence on laser wavelength. SEM images of the produced gratings are presented in Figure 3.3a-c, while the reflectance responses for s- and p-polarizations are given in Figure 3.3d-e. The investigated hemispheres were of similar dimensions, with diameters of 400-500 nm and heights of 125-200 nm. The comparison shows that although the laser harmonic strongly affects the structure's shape and limitations, the plasmon resonances remain within a narrow range and are not strongly affected by this parameter. The differences observed in the p-

polarization resonant wavelengths arise from height variations among the bumps. The evaluated quality factors are relatively high, with QF approximately 40 for s-polarization and approximately 30 for p-polarization. When accounting for resonance depth, the MQF is largest for s-polarization (MQF = 8.82) in gratings produced using 3H, whereas for p-polarization, the results are comparable for both 2H and 3H (9.95 and 8.96, respectively). Since the structures produced with 1030 nm are more elliptical, non-spherical, and less uniform, such gratings provide lower-quality resonances than arrays obtained with other harmonics. As plasmonic performance improves with reduced lateral lattice spacing due to stronger coupling between the nanostructures, achieving smaller periods at 2H and 3H makes these wavelengths more desirable for practical applications.

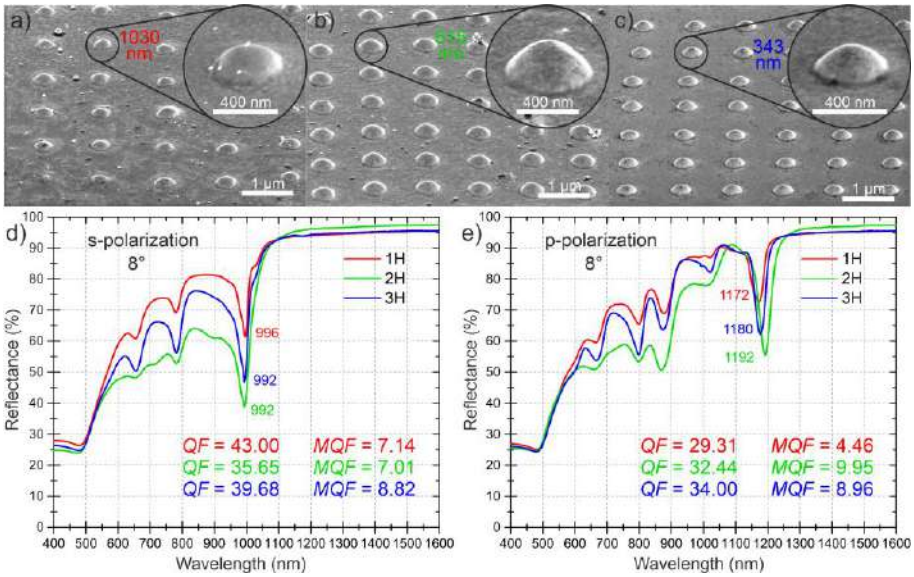

Figure 3.3. SEM images of 1 µm-period bump gratings produced using a) 1030 nm, b) 515 nm, and c) 343 nm. Reflectance spectra of d) s-polarization and e) p-polarization response of the gratings.

In summary, decreasing the femtosecond laser wavelength significantly enhances the precision and versatility of gold nanostructure fabrication by lowering modification thresholds and expanding the viable fluence range for diverse morphological states. Using higher-frequency laser pulses enables the fabrication of arrays with smaller periods, providing a more effective platform for plasmonic excitations.

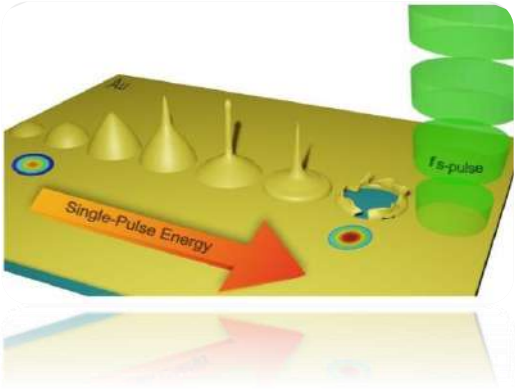

3.1.2. Combined effect of fluence and grating period for morphological tuning

This subchapter is based on part of the results published in [P2]: *Advanced Optical Materials*, 12 (20), 2400172, 2024, by K. Vilkevičius, G. D. Tsibidis, A. Selskis, E. Stratakis, and E. Stankevičius.

Building upon the foundational understanding of wavelength-dependent formation regimes explored in the previous section, the precise engineering of plasmonic nanostructures necessitates a deeper exploration of the sample's influence on these regimes and the interplay between laser fluence and grating period. In DLW, morphological evolution from hemispherical bumps to high-aspect-ratio jets is primarily driven by the single-pulse energy, while periodic arrays introduce a secondary, yet governing, factor: the grating period and spatial pulse overlap.

The morphology of laser-induced nanostructures plays a pivotal role in determining their optical, chemical, and plasmonic properties. Thus, the ability to accurately control structural dimensions is essential for tailoring functional properties. In addition to laser parameters, sample characteristics, such as film thickness or the metal itself, can be adjusted to influence layer modification dynamics and obtain differently shaped structures. Although several formation mechanisms for single-pulse-produced structures have been explained by thermoelastic stress and thin-film delamination [99], a comprehensive understanding of how pulse energy, film thickness, and grating period jointly determine morphological tunability remains incomplete. While most research focuses on isolated pulse interactions without considering collective spatial effects, multi-pulse-affected areas remain underexplored and hold high potential for increased control. This knowledge is essential for achieving precise spectral control in photonic devices, as insufficient control over the morphology of periodically arranged

nanostructures limits optical performance and the ability to hybridize plasmonic modes, thereby enhancing plasmonic activity.

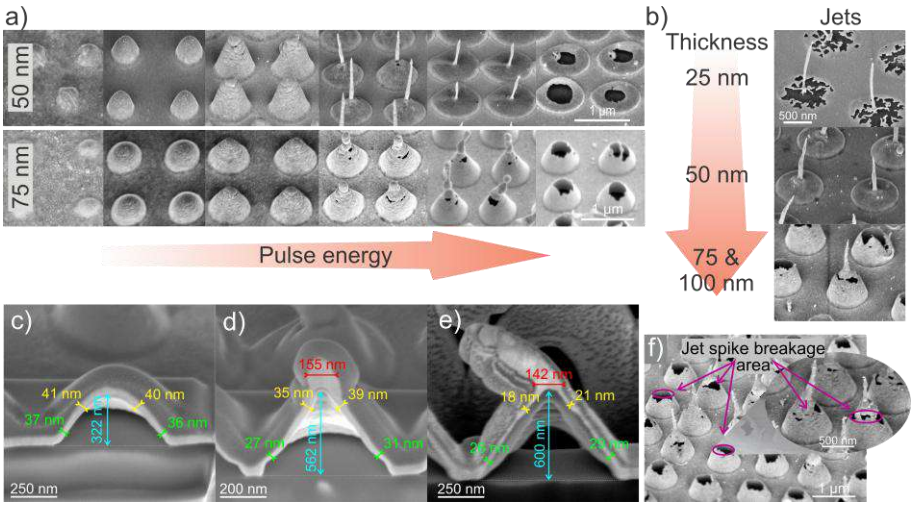

Figure 3.4. a) SEM images of different morphology nanostructures on 50 nm (upper row) and 75 nm (lower row) gold film. b) Jet shape change with gold film thickness. Cross-section of c) bump, d) cone, and e) jet fabricated on a 75 nm film. The Au layer is bright grey, while dark grey is Pt used for contrast enhancement. Blue measurements mark internal height, red – spike width, green – Au thickness in the structure's periphery, yellow – Au thickness near the structure's center. f) Broken jets on 100 nm gold film with marked jet breakage zone.

In this study, thin gold films with thicknesses of 25, 50, 75, and 100 nm were irradiated with single pulses of 2H (515 nm) to produce gratings with varying periods. The beam is focused into approximately a 1-1.1 µm spot, so a period-independent morphological investigation was performed at 1 µm arrays. As the laser pulse energy increases, various morphological structures are produced and classified into four categories: bumps, cones, jets, and crowns. Using just enough energy to modify the thin film, small bumpy protrusions are produced at the energies of 0.2 nJ, 0.4 nJ, 0.6 nJ, and 0.75 nJ for 25, 50, 75, and 100 nm Au films, respectively. The cones are obtained at 0.3 nJ, 0.75 nJ, 1 nJ, and 1.25 nJ for the same thicknesses, while the jets are obtained from the energies of 0.4 nJ (25 nm), 0.95 nJ (50 nm), 1.25 nJ (75 nm), and 1.4 nJ (100 nm). All morphological stages are depicted in the SEM images in Figure 3.4a for thicknesses of 50 nm and 75 nm. The lower-energy bumps are rather similar across all investigated thicknesses, since their formation is not based on melting but rather on delamination of the film. Meanwhile, the jets (Figure 3.4b) produced by molten-metal flow depend strongly on the layer. Thinner-film structures have sharp, narrow, and high spikes formed either on the surface of the glass (25 nm) with a diameter-to-

height ratio of 1:17, or on a disk-like platform (50 nm) with a diameter-to-height ratio of 1:13. During the material redistribution, the molten metal flows towards the spike, causing the surrounding layer to collapse. Meanwhile, in thicker layers (75 nm and 100 nm), broader, non-uniform spikes form atop the conical base, with diameter-to-height ratios of 1:9 for 75 nm and 1:7 for 100 nm. Here, a larger portion of the metal remains at the sides of the structure, maintaining the conical shape.

Detailed cross-sectional analysis of 75 nm-thick film hollow nanostructures (Figure 3.4c-e) revealed that in the bump regime, a consistent wall thickness is maintained, indicating that the driving force is primarily metal detachment from the substrate, while melt movement remains minimal. The transition to cones is accompanied by an increase in internal height of the structure (in this case, from 322 nm to 562 nm) and a reduction in peripheral wall thickness (from 37 nm to 27 nm), as molten material moves from the irradiated area periphery toward the center to form a small solid tip. This flow is driven by the temperature gradient and the induced velocity it generates. During jet formation, the increase in inner height is greatly reduced, and material redistributes within the structure. The gold layer around the tip is significantly thinned (from 39 nm to 21 nm), indicating that spike growth is primarily fueled by the impact of the material at the center. This thinning around the apex provides a physical explanation for the structural failure and spike breakage observed at higher energy levels (Figure 3.4f).

Theoretical thermal response analysis performed using the two-temperature model (TTM) during laser irradiation (Figure 3.5) indicated that both film thickness and pulse energy are critical parameters governing the transition between the morphologies. A decrease in thickness increases the lattice temperature due to electron diffusion, confining hot electrons to a smaller volume. At a constant pulse energy (0.8 nJ), a 25 nm film exceeds the critical ablation threshold, whereas thicker films remain within the melting regime when mass displacement occurs. Similarly, the lattice temperature increases with laser energy. This shows that the transition from bumps to ablated holes is governed by the peak lattice temperature relative to the material's melting and critical ablation values.

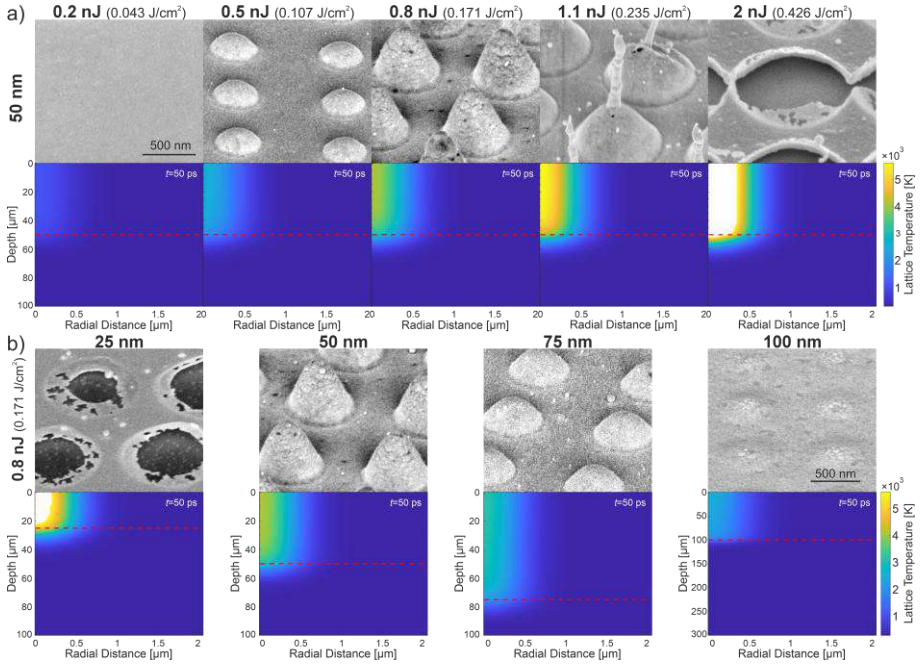

Figure 3.5. a) SEM images and corresponding lattice temperature profiles at 50 ps after the laser pulse for the structures in a 50 nm Au film using different pulse energies. b) SEM images and corresponding lattice temperature profiles at 50 ps after the laser pulse for the structures in different-thickness films using 0.8 nJ pulse energy.

Gaussian intensity distribution enables the formation of smaller diameters and array periods than the laser focal spot size, as the modification threshold can be exceeded only in the central part. While the morphological transition from hemispherical bumps at low energies to sharp jets at higher energies is primarily determined by pulse energy, the grating period serves as a critical secondary tuning parameter. When the period is reduced below the beam diameter at a constant energy (Figure 3.6a), the resulting structures transition towards morphologies typically acquired at higher energies. However, the period influence is lower than the pulse energy, leading to structural changes by only one morphological state – bumps to cones or cones to jets. The same shape control with interstructural distance tendency is observed across all investigated film thicknesses (Figure 3.6b). Conversely, when the period exceeds the beam diameter, the morphology and size of the structures remain constant and independent of the distance.

This phenomenon is governed by the laser beam overlapping effect, where, in sub-diameter gratings, fabrication thresholds are lowered due to subsequent pulse interactions with a previously modified zone. The physical mechanism behind this is attributed to induced mechanical stresses and non-visible delaminations, together with intrinsic modifications in the peripheral part of

the irradiated area, since the structure is produced only in the central part. The time interval between the successive pulses (143 μs at 7 kHz repetition rate) is relatively long, so this effect cannot be attributed to heat accumulation. In addition, only at higher fluences within the overlapping regime, structures exhibit non-centrality, with the apex shifted toward the previously modified zone relative to the base center (Figure 3.6c).

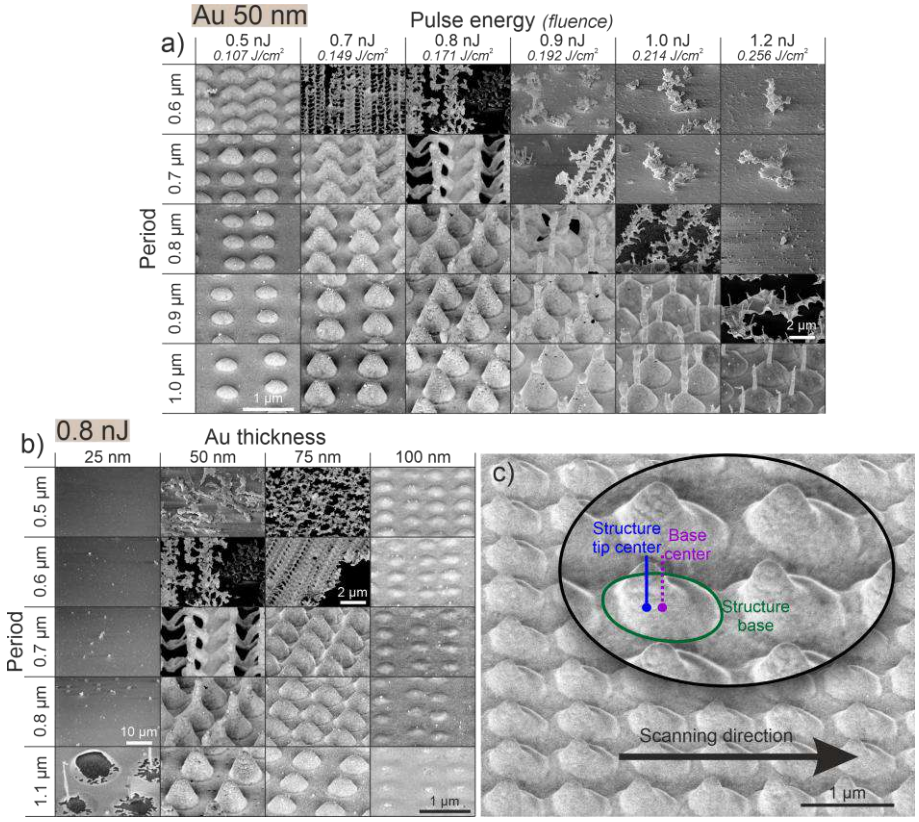

Figure 3.6. a) Morphology dependence on period and pulse fluence for a 50 nm thickness Au film. b) Morphology dependence on period and Au thickness for 0.8 nJ (0.171 J/cm^2) pulses. c) Shift of the structure's tip in the opposite direction to scanning.

To accurately determine the nanostructure formation parameters, the squared diameter of the visually modified areas is again plotted against the natural logarithm of the pulse energy (Figure 3.7a), revealing a nearly linear dependence across all thicknesses and grating periods. This methodology allowed us to calculate the practical layer-modification threshold (from the linear approximation of the line intersection with the energy axis) and the characteristic energy-deposition diameter (from the linear approximation of the line slope), which represent the effective area for energy absorption. The latter parameter, interestingly, showed that the effective beam diameter is

consistently smaller (0.79 µm at non-overlapping 1.1 µm periods and 0.9 µm at highly overlapping 0.7 µm periods) than the calculated focused Gaussian beam spot size of 1.1 µm. This suggests that the energy required for structure formation is effectively absorbed only in the central beam region and is increased by the pulse overlap.

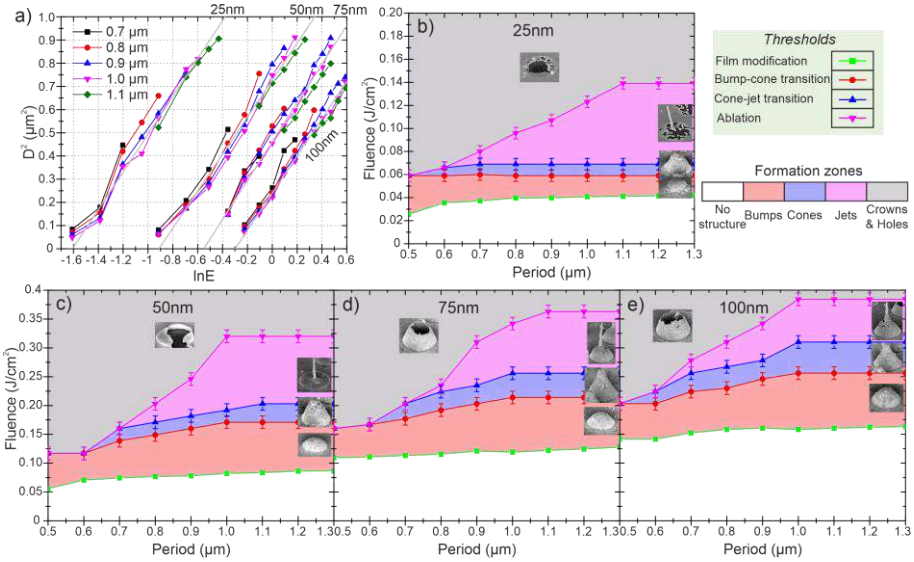

Figure 3.7. a) Squared lateral size dependence on the natural logarithm of laser pulse energy for different film thicknesses. Linearly approximated data is for a 1 µm period. Morphological phase-transition fluence thresholds (lines) and each morphology formation range (colored areas) for different film thicknesses of b) 25 nm, c) 50 nm, d) 75 nm, and e) 100 nm.

The modification threshold is highly sensitive to film thickness, with values determined from the approximation in Figure 3.7a being 0.2 nJ, 0.4 nJ, 0.58 nJ, and 0.74 nJ for thicknesses of 25, 50, 75, and 100 nm, respectively. The threshold increases with thickness, whereas the sensitivity to energy fluctuations is greater in thinner coatings. The calculated modificational and transitional fluences determined from SEM images, as well as the formation ranges for each shape, are summarized in Figure 3.7b-e, with a clear influence of period and film thickness. These thresholds are significantly modulated by the multi-pulse-affected areas at reduced distances, as the fluences for both ablation and shape changes decrease. While the fluence range for stable bump formation in relatively broad, higher-order structures are not produced at extremely small periods below 0.6 µm due to excessive overlapping that inhibits their formation. Therefore, selecting the exact laser, sample, and grating parameters is necessary to achieve the desired morphology.

In summary, the morphological evolution of laser-induced gold nanostructures is governed by a combined interplay among pulse energy, layer thickness, and grating periodicity. Pulse energy serves as the primary driving force for a shape transition, while thickness affects the final shape through the redistribution of material. The implementation of sub-diameter periods introduces an overlapping effect, providing an additional degree of freedom for structural control. By precisely leveraging these parameters, highly uniform arrays with easily tailored and well-defined geometries can be fabricated.

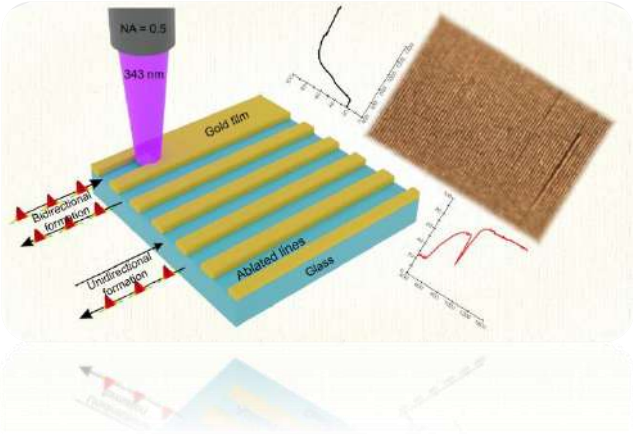

3.1.3. Morphologic and periodic alteration for spectrally distinguished plasmonic responses

This subchapter is based on the paper [P3] published in *Optics & Laser Technology*, 183, 112330, 2025, by K. Vilkevičius, K. Čepaitis, A. Selskis, and E. Stankevičius; and on part of the results published in [P2]: *Advanced Optical Materials*, 12 (20), 2400172, 2024, by K. Vilkevičius, G. D. Tsibidis, A. Selskis, E. Stratakis, and E. Stankevičius

The structural control of nanostructures in periodic gold film gratings establishes the foundation for tailoring their optical responses. However, the ultimate goal of morphological engineering is not the structural variation itself, but rather the intentional modulation of plasmonic resonances. In our periodically arranged metallic arrays, plasmonic behavior arises from the hybridization of LSPs, SPPs, and diffracted radiation at grazing angles, resulting in so-called HLPR (which will be referred to as grating-coupled resonance), with sharp absorption peaks in the visible and near-IR (Vis-NIR) range.

Since grating-induced plasmonic modes are highly sensitive to geometry and excitation conditions, accurate control of these provides a way towards spectrally distinguishable optical responses. Variations in structural dimensions, aspect ratio, and shape alter near-field confinement and localized excitation, while changes in lattice symmetry and periodicity modify the conditions for diffractive coupling. Therefore, both morphological tuning and dimensional arrangement fundamentally influence resonance position, linewidth, and quality factors. Although the role of geometry in plasmonics is well described, a thorough comparison of shape-driven spectral shifts together with dimensionality-induced coupling effects is lacking in laser-fabricated plasmonic platforms.

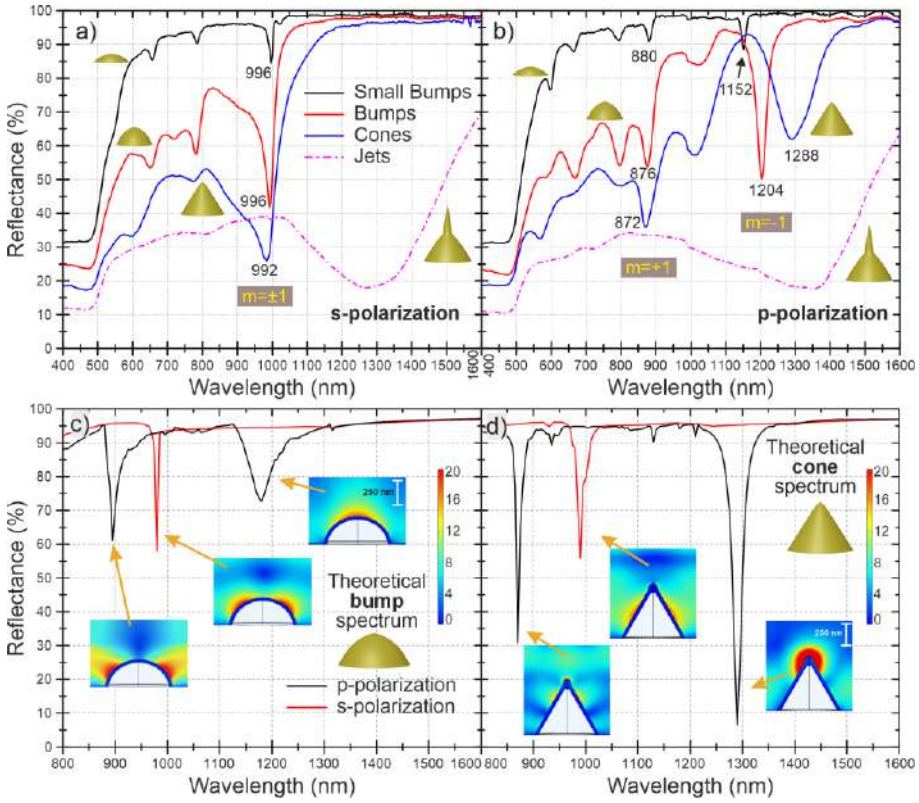

Figure 3.8. Measured reflectance spectra of different shape structure arrays of 1 μm period on a 100 nm thick Au for a) s-polarization and b) p-polarization. Numerically calculated reflectance spectra for c) bump and d) cone arrays of 1 μm period. The insets show the near-field profile of the investigated peaks.

In this study, large-scale (3×3 mm^2) arrays were fabricated and prepared for optical measurements using a spectrophotometer. For shape-influenced properties, 1 μm period arrays produced at 515 nm were used; for the period-induced spectral separation study, those produced at 343 nm were used. Due to the nonideal formation of arrays along perpendicular axes, the highest-quality results were obtained when the electric field was perpendicular to the scanning line: at $\varphi = 0°$ for s-polarization and at $\varphi = 90°$ for p-polarization. Resonant peaks are detected in the reflectance spectrum as intensity dips. The spectral behavior is strongly influenced by morphology, as shown in Figure 3.8a-b for four types of nanostructures – small bumps (height up to 100 nm), bumps, cones, and jets. The main 3 peaks were investigated: $m = \pm 1$ diffraction order in s-polarization (at 992-996 nm), $m = +1$ diffraction order in p-polarization (872-880 nm), and $m = -1$ diffraction order in p-polarization (1152-1288 nm). Specifically, the latter resonance exhibits a pronounced redshift as the structure height increases, whereas the $m = +1$ and $m = \pm 1$

resonances remain comparatively stable. Additionally, the change in morphology leads to peak broadening, possibly attributed to the structural nonuniformity. Meanwhile, the jet resonances become shallower and significantly wider, with a strong decrease in total reflection, rendering the induced resonances unobservable. Due to uncontrollable formation of jet spikes, each structure is slightly different and has a different inclination, leading to this extreme broadening of the resonance. Also, in this regime, part of the jet structures are broken, thus reducing the total intensity.

The spectral redshift with increasing structure height suggests that this feature is due to an out-of-plane electric component that arises when the vertical component of the incident beam excites a height-dependent plasmonic mode. Theoretical modeling (Figure 3.8c-d) and near-field profiles confirm that, while in-plane modes are localized at the sides of the structures and depend mainly on the grating parameters, the redshifting mode is out-of-plane in origin, with an enhancement at the apex and a strong dependence on the vertical dimension. These modes suffer from high Ohmic losses at large heights, which explains the jets' spectral broadening.

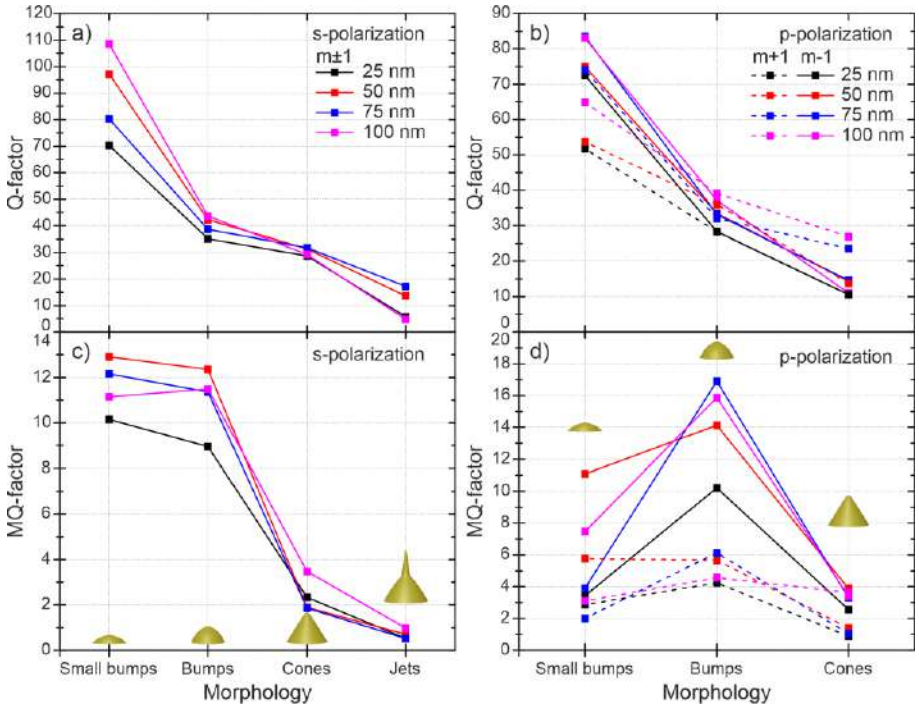

Figure 3.9. Measured resonant peak a,b) Q-factor and c,d) MQ-factor dependence on the morphology for a,c) s-polarization and b,d) p-polarization.

The qualities of the resonances are assessed using both the Q-factor and the MQ-factor, according to equations (8) and (9), to compare the influence

of the shape and gold film thickness on the resulting peaks. As mentioned previously, the MQ-factor includes the peak depth, indicating the coupling efficiency, but is only suitable for internal comparison of shape-influenced resonances described in this work. The values for the investigated peaks are shown in Figure 3.9. While small bumps yield the highest Q-factor (up to 100) due to their narrow linewidths, normal bump arrays are identified as the most practically applicable for resonance-related measurements. This is evidenced by their higher MQ-factors, indicating a superior balance between peak depth and width. This comparison further indicates that the gold film thickness slightly affects these factors: arrays in 25 nm thick films consistently yield the lowest-quality results due to the thinner structures, whereas in thicker 50-100 nm films, the QF and MQF are comparable.

An additional study revealed that reducing the grating period could also improve the peak qualities, as denser interacting elements lead to stronger interactions. This prompted further research into the period influence on the resonances. Three gratings with different periods were produced: a symmetric 2D array of bumps with a 0.8 μm period, an asymmetric 2D array of bumps with 0.5 μm in-line and 0.8 μm perpendicular periods, and a 1D array of ablated lines with a 1 μm period. While attempts were made to produce ablated arrays of lower periods, these resulted in a heavily damaged gold layer with no useful structures. Corresponding SEM images of the produced and investigated samples are given in Figure 3.10a-c. Here, reflectance measurements were performed at two perpendicular azimuthal angles, φ, and at three AOIs, θ. All resonant peaks follow the expected dependence on AOI and light polarization – increasing angle leads to a blueshift of s-polarization peaks ($m = \pm 1$) and a positive-order ($m = +1$) peak of p-polarization, while negative ($m = -1$) order peaks are redshifting. However, the quality and spectral purity of these resonances are strongly influenced by whether the arrays were produced via ablation or surface modification. Ablated 1D arrays yield shallow resonances (Figure 3.10d-e) of lower spectral quality due to structural disorder, characterized by rough-sided lines and splashed metallic debris that increase scattering losses, and reduced reflectance due to the removed gold layer. Conversely, modification-origin arrays yield profoundly deeper, spectrally distinguishable peaks.

A significant finding in the spectral behavior is the presence or absence of additional resonances arising from diagonal axes or azimuthal misalignment. An ablated array, while with low-intensity peaks, acts as a true 1D grating, with resonances excited only in the main azimuthal angle layout when grating lines are perpendicular to the incident electric field oscillations. In a uniform 2D array (Figure 3.10h-i), identical resonances are excited in both azimuthal

layouts, leading to increased spectral sensitivity to angular alignment and potential complexity from additional peak excitation and overlap, thereby degrading their quality. This spectral complexity is reduced in arrays fabricated by modifications that act as 1D gratings. A unique quasi-1D grating is obtained when a physical 2D geometry uses a short in-line period, thereby prohibiting diffraction-based coupling in one axis. This allows an array to exhibit the spectral simplicity of a 1D grating (Figure 3.10f-g) while maintaining spectral resolution – high-quality peaks only at the main azimuthal orientation (s-polarization response only at $\varphi = 0°$, p-polarization response only at $\varphi = 90°$). This control over the grating parameters enables elimination of undesirable diagonal resonances and provides single-peak plasmonic responses, thereby improving the platform's accuracy. It is worth noting that this design exhibits robustness to structural disorder, as minor lateral offsets do not degrade the quality or spectral position of the resonances, and it minimizes signal deterioration caused by structural defects, as the response is obtained from the large-scale grating.

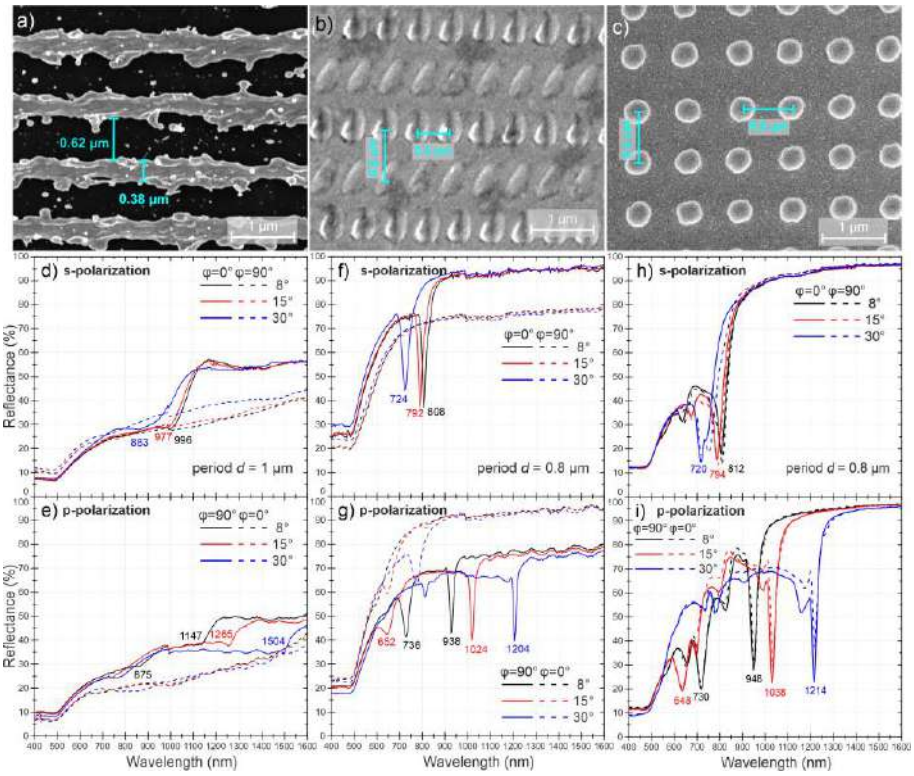

Figure 3.10. SEM images of a) 1D ablated, b) quasi-1D, and c) 2D arrays. S-polarized (d,f,h) and p-polarized (e,g,i) reflectance response of d,e) 1D ablated, g,f) quasi-1D, and h,i) 2D arrays. Different colors mark different AOIs.

Finally, the qualitative evaluation and comparison of the 2D and quasi-1D arrays were performed using the Q-factor and MQ-factor (Figure 3.11). For the symmetric 2D grating, resonances were evaluated at both azimuthal positions – the "main" angle (electric field perpendicular to scanning lines, denoted as solid lines in Figure 3.10h-i) and the "shifted" angle (field parallel to scanning lines, Figure 3.10h-i dashed lines). Comparison reveals that the quasi-1D array outperforms the uniform 2D array in resonance width (as indicated by the Q-factor) and s-polarization resonance depth (as evidenced by the MQ-factor). Angular shift causes a linear increase in the quality of the redshifting resonance and a stable or slight decrease in the quality of blueshifting peaks. This allows a quasi-1D array to achieve a QF of 93 and an MQ of 25, and illustrates the benefit of eliminating additional resonances, resulting in more intense, narrower peaks.

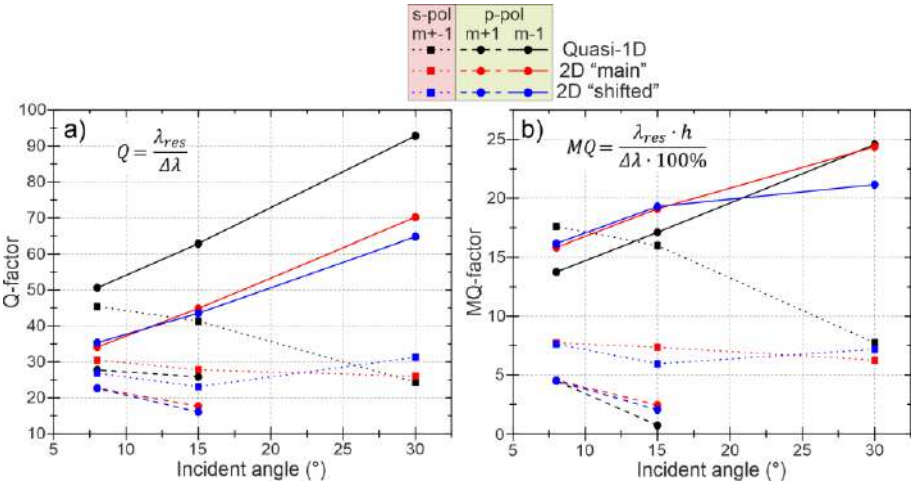

Figure 3.11. a) Q-factor and b) MQ-factor dependence on the light incidence angle. Different colors mark different gratings, while solid and dashed lines distinguish resonant peaks.

Summing up, the plasmonic performance of laser-produced Au nanostructure gratings is linked to both the individual nanostructure morphology and collective lattice geometry. Growth of the structure enables spectral redshifting of specific resonances by exciting the out-of-plane mode, while the hemispherical bumps exhibit the highest-quality resonant peaks. Additionally, implementing a quasi-1D configuration enables the acquisition of 2D-grating-quality resonances while maintaining 1D-like spectral simplicity, thus eliminating parasitic diagonal resonances. By effectively combining surface modification regimes with arrangement parameters, the platforms provide easily tunable, high-quality plasmonic resonances for practical applications.

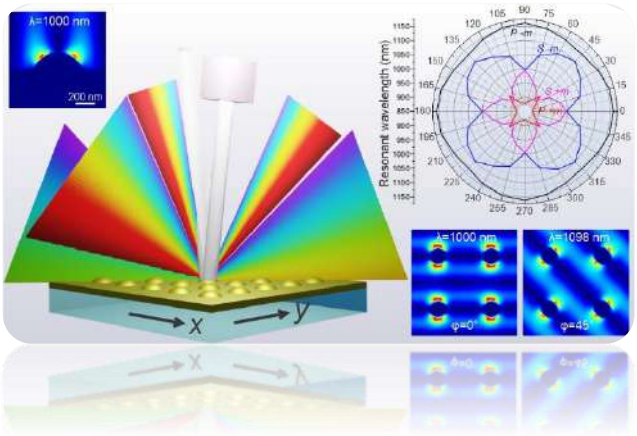

3.1.4. Angular control and theoretical modeling of grating-coupled resonances in symmetric arrays

This subchapter is based on the paper [P4] published in *ACS Applied Materials & Interfaces*, 18(23), 33007-33023, 2026, by K. Vilkevičius, L. A. Letelier, L. Grinevičiūtė, and E. Stankevičius.

While morphology and periodicity define the intrinsic plasmonic properties of the arrays, their optical response can further be governed by excitation geometry. In two-dimensional gratings, multiple coupling pathways coexist, including excitations along the principal lattice axes and diagonal directions. These several channels often result in spectrally overlapping or shifting resonances, complicating the interpretation of experimental results. Determining the physical origin of the observed peaks and modes, thus, requires more in-depth experimental and theoretical analysis.

Growing interest in grating-coupled plasmonic modes has spurred extensive research into the fabrication of such gratings, yet the full picture of the modes' origin, angular evolution, and controllability remains unclear. A primary challenge in current research is the reliance on simplified 1D array models for analytical convenience, which fail to capture the multi-directional plasmonic coupling and higher-order diffraction effects observed in 2D systems. While the production is well described, the interplay between the main-axis and diagonal diffraction orders remains underexplored. Therefore, a combined theoretical-experimental analysis is needed to identify the contributions of multiple lattices, resolve the dispersion behavior, and establish a framework for resonance engineering.

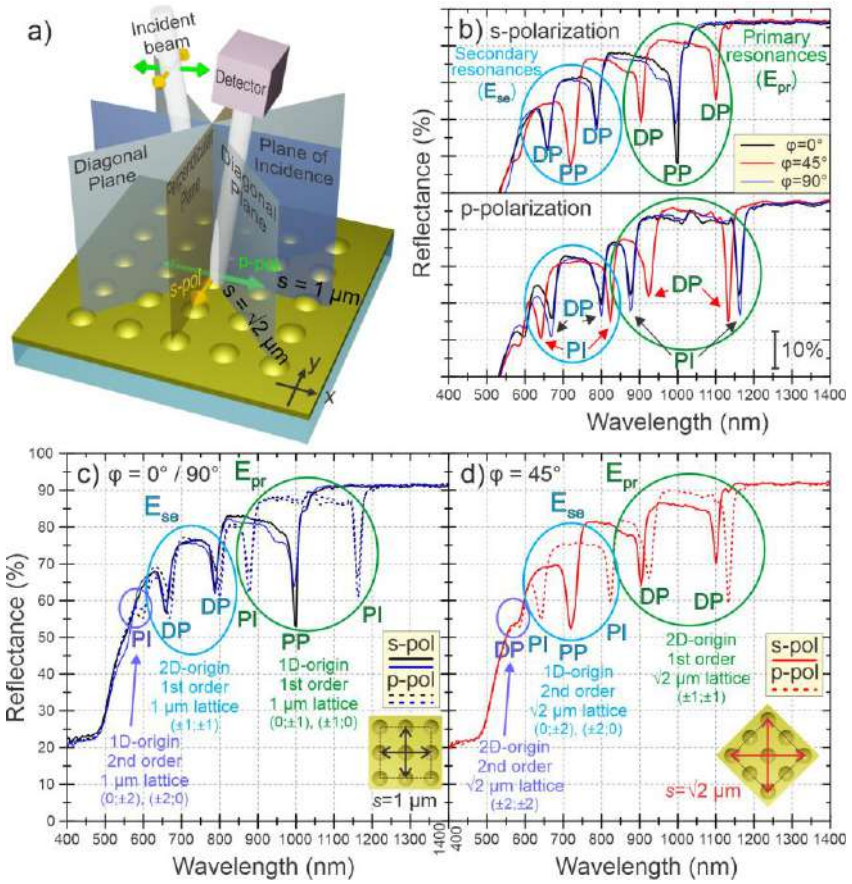

Figure 3.12. a) Main diffraction planes: plane of incidence (PI), perpendicular plane (PP), and diagonal planes (DP). b) Reflectance spectra of gold nanobumps with a 1 μm period for s- and p-polarization at $\varphi = 0°$ (black line), 45° (red), and 90° (blue) angles. Reflectance spectra of c) main-lattice (1 μm) resonances at $\varphi = 0° / 90°$ and d) diagonal-lattice (√2 μm) resonances at $\varphi = 45°$, with attributed origins of the peaks determined from the theoretical diffraction grating model.

For this investigation, 3×3 mm^2 symmetric 2D arrays of gold bumps on a 100 nm-thick film were fabricated using 343 nm pulses with 0.8 nJ of energy, with a grating period of 1 μm in both axes. The optical response of these symmetric 2D arrays is governed by conical diffraction, which involves four primary diffraction planes (Figure 3.12a): the plane of incidence (PI), the perpendicular plane (PP), and two diagonal planes (DP). At a near-normal incidence angle ($\theta = 8°$), the observed resonances (Figure 3.12b) can be classified into primary (E_{pr}) resonances, which appear at longer wavelengths (850-1200 nm), and secondary (E_{se}) resonances, appearing at shorter wavelengths (600-850 nm). Experimental analysis of the reflectance spectra demonstrates that these peaks are highly sensitive to the sample's azimuthal (φ) orientation. At high-symmetry angles ($\varphi = 0°$ or 90°), 1D-type diffraction

resonances dominate in the PI and PP, while at DP, the 2D-origin peaks are simultaneously excited. Meanwhile, as the sample is rotated to $\varphi = 45°$, the main excitation transitions from the principal lattice of 1 μm to a diagonal lattice with an effective period of √2 μm. This rotation leads to 1D-type resonances (one resonance at s-polarization splits into two), while secondary peaks of 2D-origin merge into one (for s-polarization) resonance of 1D-type as the PI is aligned with the symmetrical diagonal lattice. The validity and physical attribution of the observations are confirmed by the agreement between the experimental data and the theoretical 2D diffraction formula, given by equation (6), for 1 μm and √2 μm periods. Spectral dips were assigned to diffraction orders of (0;±1) and (±1;0) for 1D-type origin of s- and p-polarization response, as well as (±1;±1) for 2D-type origin. The exact attribution of each peak is summed up in Figure 3.12c-d. A change in azimuth angle leads to a change in coupling into a different lattice with its period.

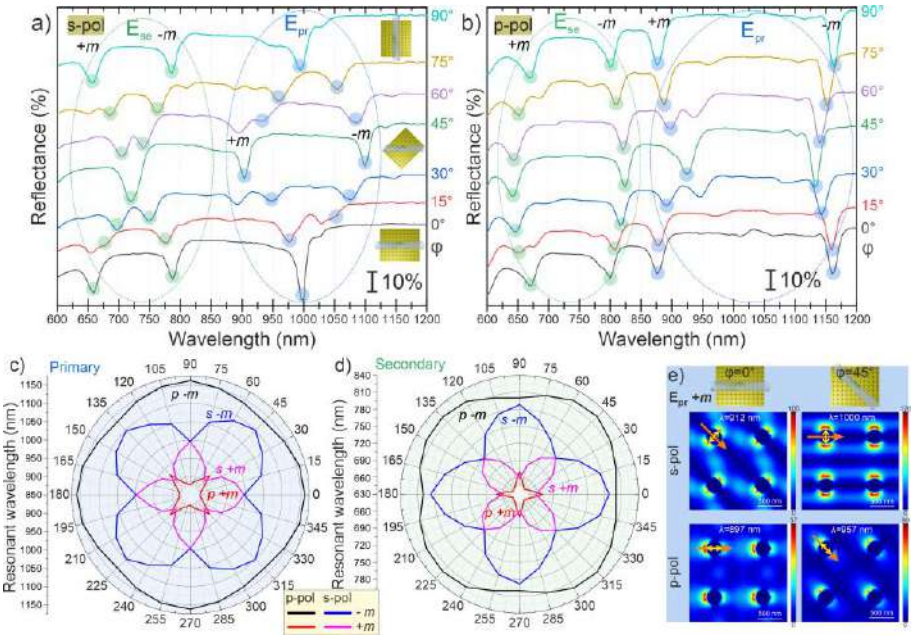

Figure 3.13. Reflectance spectra of a gold nanobump grating at azimuthal angles from $\varphi = 0°$ to 90° with a step of 15° for a) s- and b) p-polarization. Resonant wavelength change of c) primary and d) secondary resonances in the polar coordinate system. e) Simulated near-field enhancement of s- and p-polarization response at $\varphi = 0°$ and 45° azimuthal angles.

A more in-depth analysis of the influence of azimuthal rotation was performed by measuring reflectance over the range $\varphi = 0°$ to 90° in 15° steps (Figure 3.13a-b). The investigation reveals a dynamic spectral response characterized by the splitting and merging of the resonant peaks. As the

sample is rotated, the incident wavevector is projected differently onto different lattices, resulting in a smooth peak shift across the spectrum and a change in the type of excitation. At non-aligned intermediate angles, resonances appear as shallow dips with reduced coupling strength, as the wavevector is projected across both main and diagonal lattices and the diffraction condition is not strictly confined to a single in-plane mode. Such cross-coupling reduces efficiency, marking the need for accurate alignment with the symmetric lattices. The angular evolution of these primary and secondary resonances is visualized in polar plots (Figure 3.13c-d), revealing a four-lobed pattern aligned with either principal grating axis or along the diagonals, noting a consistent pattern across all azimuthal rotations. The modes exhibit minimal splitting and merge when excitation is 1D-type diffraction in PP. An intermediate distance between the opposite-sign ($+m$ and $-m$) peaks is observed with 2D-type diffraction at DP, and the largest splitting is attained at 1D-type excitation in PI.

To validate the origin of the resonances, near-field simulations were performed using the Lumerical FDTD solver. Analysis showed that all resonances excited with s-polarization are in-plane modes, while negative-order 1D-type resonances are of out-of-plane nature. The spatial distribution of these modes is highly sensitive to the azimuthal angle; at high-symmetry angles ($\varphi = 0°$ and 45°), the fields are distributed with lobes aligned along the main or diagonal lattice directions (Figure 3.13e). Also, p-polarization exhibits a pronounced asymmetry when more intense near-field hot spots appear on one side of the structure, corresponding to the positive or negative diffraction component.

Finally, the double-angular manipulation was investigated by simultaneously controlling the azimuthal and incidence angles, thereby providing additional tuning of the plasmonic excitations. An increase in incidence angle leads to greater spectral separation between resonances of opposite diffraction orders (Figure 3.14a-b), with a redshift of negative-order and blueshift of positive-order resonances in p-polarization responses. Meanwhile, in s-polarization, the tendency is also partially dependent on azimuthal angle, with a blueshift of both positive and negative resonances at angles close to 1D-type excitation ($\varphi = 0°$, 15°, 75°, and 90° for primary E_{pr} and $\varphi = 30°$, 45°, and 60° for secondary E_{se} resonances). This angular control affects the sensitivity of the peaks to changes in φ, as larger incidence angles yield steeper dispersion curves. Qualitative analysis of the MQ-factor (Figure 3.14c-d) revealed that the resonant efficiency is also highly influenced by the azimuthal shift. The highest-quality resonances are consistently reached when the excitation plane is aligned with the high-symmetry lattice directions ($\varphi =$

0°, 45°, and 90°). For example, under s-polarization, the highest MQF values occur at $\varphi = 0°$, followed by a sharp decrease at intermediate angles, indicating that these resonances are tightly confined to excitation along the grating's main symmetry direction. A moderate secondary maximum at $\varphi = 45°$ corresponds to coupling into the diagonal lattice, albeit with lower efficiency. Increasing the incidence angle enhances the angular selectivity of the peaks, maintaining similar quality along the main grating and reducing the quality of the diagonally coupled resonances.

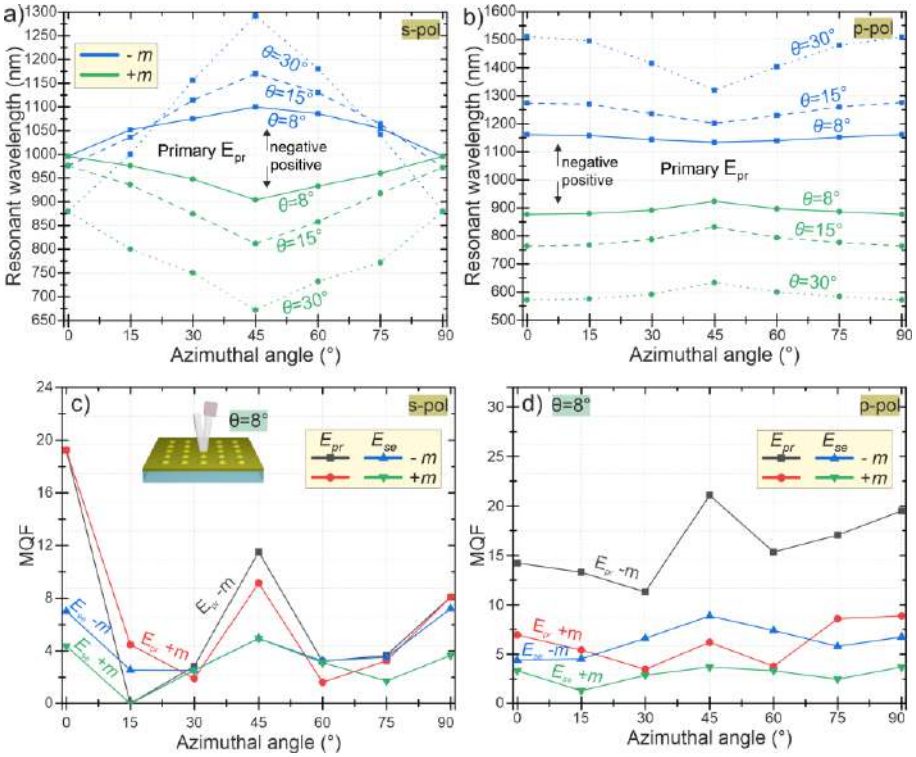

Figure 3.14. Experimental primary E_{pr} resonant wavelength dependence on azimuthal angle, with incident angle influence for a) s- and b) p-polarization. Modified quality factor dependence on azimuthal angle for c) s- and d) p-polarization at $\theta = 8°$ angle of incidence.

In summary, DLW-produced symmetric 2D gratings demonstrate complex, high-quality grating-coupled responses with spectral tunability across the entire Vis-NIR range, achieved through the dual-angular control of the azimuthal and incidence angles. Azimuthal shift changes the excitation planes from the principal to the diagonal lattice, causing splitting and merging of resonant peaks. Therefore, the accurate alignment of the grating lattices with the plane of excitation is essential for high-quality resonances, which is achieved through efficient coupling into high-symmetry lattices.

3.1.5. Main results and conclusions

This section described the implementation of direct laser writing as a high-throughput and single-step methodology for the fabrication of periodic gold nanostructures. By varying the laser and sample parameters (laser wavelength, pulse energy, film thickness, grating period, and pulse overlap), large-scale arrays supporting hybrid grating-coupled plasmonic resonances were produced, and the possibilities for controlling their shape and the tunability of plasmonic properties were investigated in depth. Also, detailed analysis and simulations of explored resonances were performed to describe plasmonic excitation in symmetric gratings and the origins of resonant modes. Such a detailed analysis provides a solid basis for further research into the practical applications of these metallic gratings.

Three statements to defend were formulated according to the accomplished results described in this chapter:

- Using a constant-NA objective, decreasing fs laser wavelength from 1030 nm to 343 nm expands the energy-dependent nanostructure formation fluence window by 3 times and reduces the achievable grating period down to 450 nm, while control of film thickness and an increase in spatial pulse overlap provide additional morphological tuning with a lower modification threshold.
- Plasmonic resonances in 2D arrays exhibit morphology-dependent spectral behavior, as increasing nanostructure height leads to a redshift of the out-of-plane resonance, while manufactured quasi-1D gratings enable spectral-mode isolation by suppressing diagonal resonances.
- Grating-coupled resonances in symmetric 2D arrays possess the highest quality when excited along the high-symmetry axes (0°, 45°, and 90°), while their spectral positions across the whole Vis-NIR (400-1600 nm) range can be tuned through double-angular control by changing azimuthal (0°-90°) and incidence (8°-30°) angles.

3.2. Functional performance of laser-fabricated plasmonic nanostructure gratings

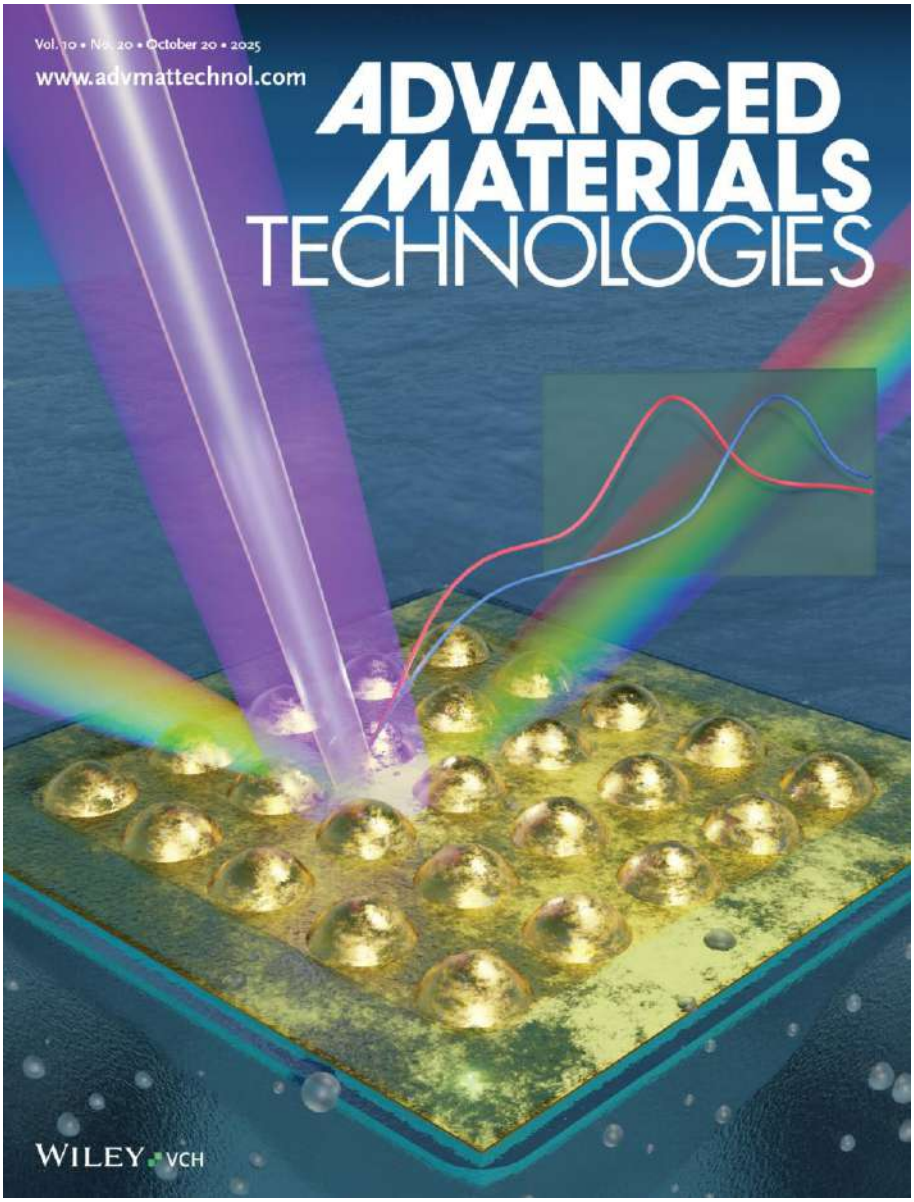

BACK COVER:
Kernius Vilkevičius, Tomas Rakickas, Evaldas Stankevičius, *High-Quality Plasmonic Ag-Au Nanobump Grating Sensor* (Advanced Materials Technologies, Vol. 10 Issue 20, 2025)

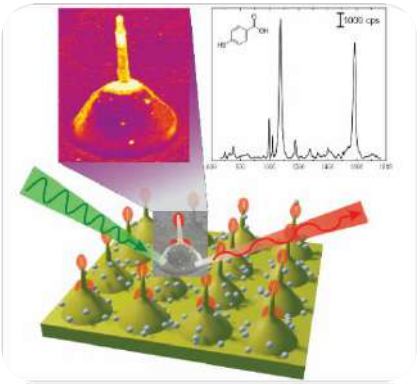

3.2.1. Morphologically tunable platform for SERS signal enhancement

This subchapter is based on the paper [P5] published in *Applied Surface Science*, 660, 160003, 2024, by K. Vilkevičius, I. Ignatjev, A. Selskis, G. Niaura, and E. Stankevičius.

Following the establishment of strategies for controllable nanostructure fabrication and accurate resonance engineering, the next step is the development of application-oriented plasmonic platforms. While the previous section demonstrated the ability to tune morphology, periodicity, and hybrid resonances, the practical relevance of this management is revealed in the context of functional performance, as described in the following sections. Among plasmon-enhanced techniques, surface-enhanced Raman spectroscopy is a sensitive method for evaluating plasmonic fields, as the Raman signal intensity strongly correlates with the local electromagnetic field enhancement at metal nanostructures. The overall signal is associated with the excitation of LSPs, which, at optimized features and hot-spot induction, enables ultrasensitive molecular fingerprint detection. Field localization is determined by the shape and relative arrangement of the nanostructure, therefore, a wide variety of parameters lead to improved signal.

Conventional SERS substrates, usually produced by chemical synthesis or lithographic techniques, are limited in shape and morphology control, complexity and multi-step processing, or high reproducibility and throughput. Therefore, a versatile, scalable tool for the formation of repetitive nanostructures is required, and the single-step DLW technique for morphology-controlled arrays is a promising route toward tunable, reproducible SERS substrates. For that, a systematic investigation of shape-

dependent Raman signal enhancement performance is conducted to establish a correlation between structural states and amplification values.

In this investigation, different-morphology nanostructures in symmetric arrays of 100×100 μm^2 were fabricated at a wavelength of 343 nm on Au substrates with varying thicknesses from 50 nm to 200 nm. Initially, a significant observation regarding the formation of the structure was made. As was already described in Section 3.1.2, thickening of the thin film mainly changes the required formation energies and affects the jet formation, resulting in widening of the spike and a decrease in the structure's total height. However, an additional increase in 175-200 nm thick layers alters the formation mechanism with film stratification and double fabrication of thinner jets, similar to the ones obtained at the thinnest 50 nm films (Figure 3.15a). In this regime, high-energy pulses produce jets in the upper layer that are removed, while secondary jets are then produced from the underlying stratified layer. Stratification is achieved due to excessive layer thickness, when the pulse effectively affects only part of it, leading to multilayer formation and repetitive fabrication of recurring thin spikes.

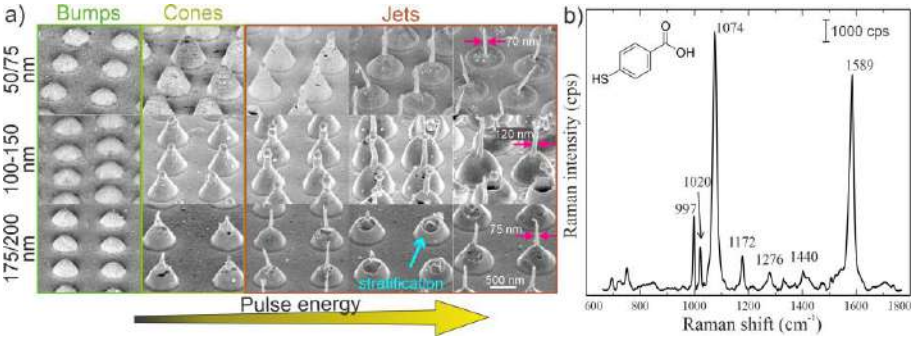

Figure 3.15. a) SEM images of various morphological structures on different-thickness gold films. b) Raman scattering spectrum obtained from a 100 nm-thick gold nanostructure grating with a 4-MBA monolayer.

For SERS evaluation, a 4-MBA self-assembled monolayer was deposited, serving as a Raman reporter with the two most prominent characteristic bands at 1074 cm^{-1} and 1589 cm^{-1} (Figure 3.15b). These are associated with the breathing vibration of the aromatic ring, coupled with the C-S stretching, and with the aromatic ring stretching mode, respectively. During the measurements, all shapes obtained from 100 nm-thick films were first compared to assess the influence of morphology on the signal, which was collected from a 1.2 μm spot with a mapping area of 5×5 μm^2. For each measurement, the signal was acquired from a single illuminated structure, with several measurements taken over time, and later normalized to 1 second. SERS activity is strongly influenced by the shape and roundness of the grating

structures; thus, eight distinct morphological states were measured, and the obtained Raman spectra are shown in Figure 3.16a, with the corresponding SEM images in Figure 3.16b. Rounded bumps exhibit the lowest signal enhancement, lacking sharp geometries and corners required for hot spot formation. Growing structures that result in cone and jet regimes lead to higher SERS intensities of the characteristic bands, as the apex introduces regions for high electromagnetic field enhancement. A subsequent rise in fabrication energy, which causes structures to fracture and form holes, results in a degraded signal, with no visible amplification at broken jets.

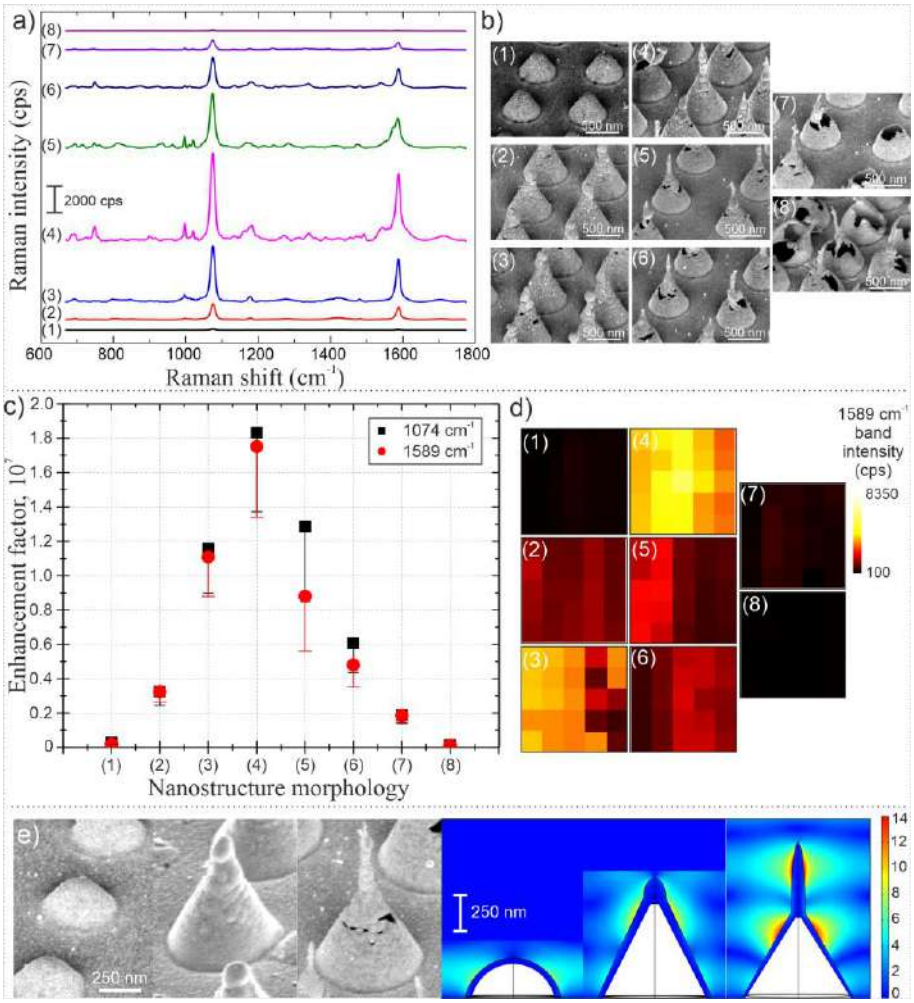

Figure 3.16. a) Raman intensity spectra and b) corresponding SEM images of different morphology structures on a 100 nm gold thick film. c) Enhancement factor dependence on the structure shape for two characteristic bands of 4-MBA. d) SERS intensity mapping of the 1589 cm^{-1} band. e) Near-field intensity simulations of different morphology structures with their corresponding SEM images.

By applying equation (10), the enhancement factor was calculated for two of the most prominent vibrational modes (Figure 3.16c). Here, the maximum values are marked as solid symbols, and the ranges of values obtained from mapping measurements are indicated next to them. This qualitative analysis confirmed that there is an optimal morphology for Raman signal amplification with the strongest field localization. It was determined to be solid jets, with the highest calculated EFs reaching 1.83×10^7 at 1074 cm^{-1} and 1.75×10^7 at 1589 cm^{-1}. Similar 10^7-order enhancements were also achieved in energetically close jets; for cones, it reduced to 10^6, while bumps and fractured jets exhibit an EF of only 10^5. Although the 1074 cm^{-1} mode is slightly higher in EF, the 1589 cm^{-1} mode is more inert to solvent and metal interactions, so the mapping of this latter mode was performed (Figure 3.16d). These demonstrate that the enhancement is recurring and can be obtained from repetitive individual structures.

Experimental observations are supported by numerical simulations of the near-field (Figure 3.16e), indicating that the electric field enhancement in jets is twice that of cones and 2.5 times that of bumps. While weak enhancement is observed along the sides of hemispherical structures, jets exhibit two hot spots, localized at the spike apex and at the junction of the spike and conical base. This highlights that sharp tips are the primary mechanism for achieving ultra-high plasmon-enhanced sensitivity.

Table 3. SERS signal intensity and EF of jets on different Au thicknesses.

No.	Au thickness	I_{SERS}, [cps]		EF	
		1074 cm^{-1}	**1589 cm^{-1}**	**1074 cm^{-1}**	**1589 cm^{-1}**
(3)	100 nm	6891	5265	1.83×10^7	1.75×10^7
(4)	125 nm	7363	7266	1.86×10^7	2.30×10^7
(5)	150 nm	11811	8531	2.73×10^7	2.46×10^7

Following the determination of the optimal shape, the effect of thin-film thickness was additionally investigated, since it strongly affects jet formation, as shown in Figure 3.15a. Varying the thickness of the solid jets again yields different Raman responses (Figure 3.17a), with distinct intensities in the two 4-MBA peaks. Experimental characterization demonstrates a clearly distinguishable maximum at 125 nm and 150 nm, where the Raman signal reaches 11811 cps. The observed performance trend is characterized by an increase with thickness growth up to 150 nm, followed by a decline toward 200 nm. This could be attributed to the thickening of the spikes and their

subsequent thinning due to stratification (Figure 3.17b). The EFs for both bands in different films were calculated (Figure 3.17c), with a clear distinction among three medium thicknesses, reaching an enhancement magnitude of 10^7. The exact intensity and maximum EF values for these samples are given in Table 3. Conversely, jet-like structures with thin spikes reach only the 10^6-order signal amplification. The mappings (Figure 3.17d) also display that the signal recurs periodically within these structures.

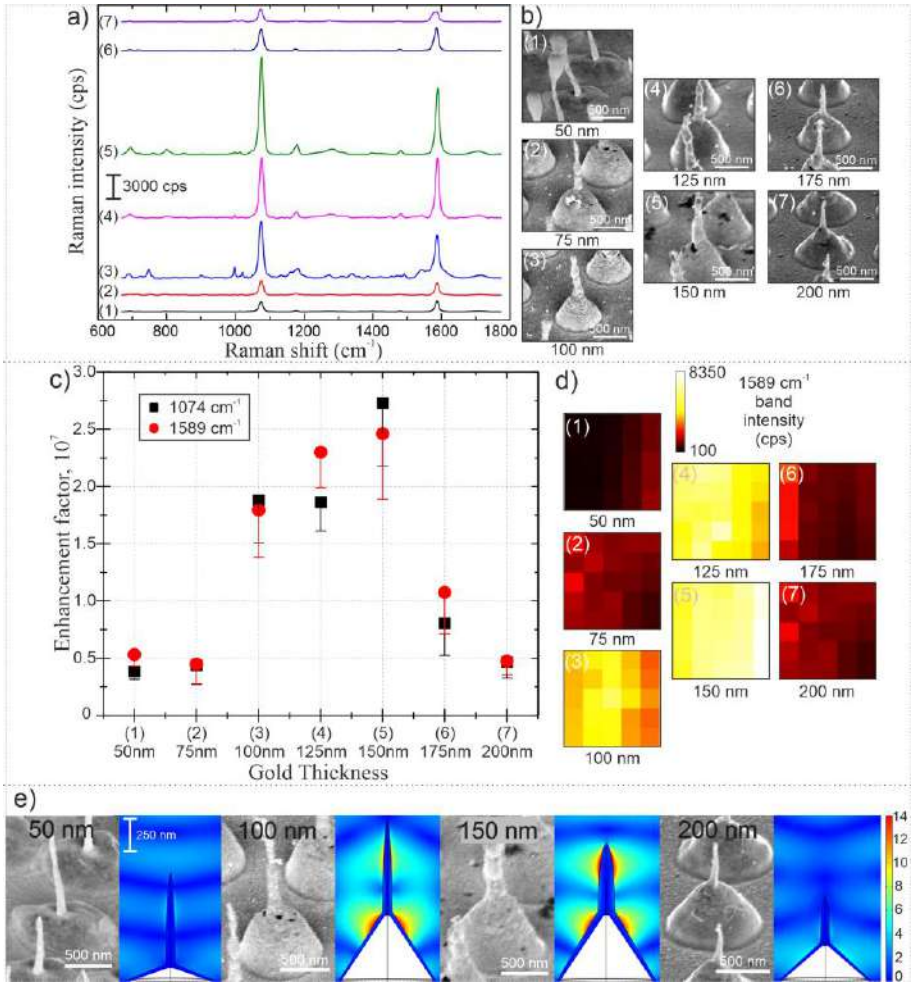

Figure 3.17. a) Raman intensity spectra and b) corresponding SEM images of different jet-like structures on various gold thick films. c) Enhancement factor dependence on the film thickness of the jet for two characteristic bands of 4-MBA. d) SERS intensity mapping of the 1589 cm^{-1} band. e) Near-field intensity simulations of different jets on various thickness films with their corresponding SEM images.

Different jets obtained at thicknesses of 50, 100, 150, and 200 nm were simulated for near-field analysis and interpretation of results (Figure 3.17e),

which evaluated changes in spike diameters, heights, and the conical base height. These suggest that the configuration, including a thick spike that interacts with a higher base, leads to double excitation of hot spots, with stronger interactions among them.

In summary, DLW-produced tunable nanostructures in periodic arrays can be implemented and effectively used as platforms for surface-enhanced Raman spectroscopy. Plasmonic efficiency and signal amplification are governed by morphology, with experimental results and numerical simulations indicating that the optimal shape for this application is a needle-like jet with sharp spikes, which generates multiple active hot spots. Additional optimization of gold film thickness led to an enhancement improvement, with a carefully tuned jet shape. Thick-spike structures achieve enhancement factors of 10^7. High reproducibility and structural uniformity mark this fabrication technique as a reliable approach for analytical detection platforms, offering high sensitivity and repeatability in results.

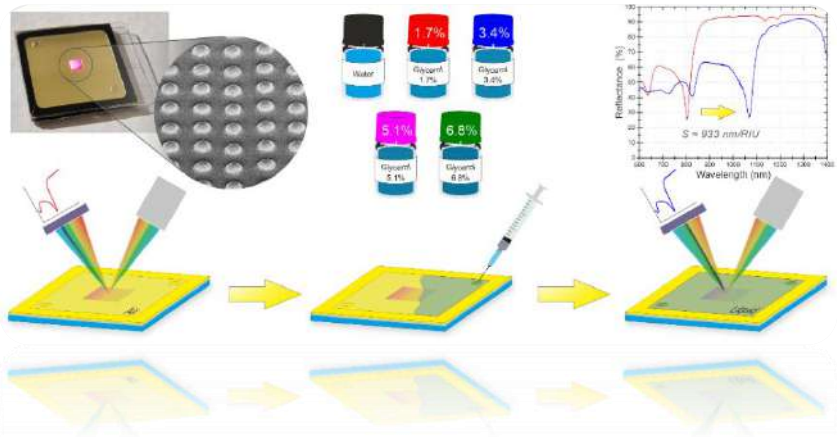

3.2.2. Bimetallic nanobump grating platforms for refractive index sensing

This subchapter is based on the paper [P6] published in *Advanced Materials Technologies*, 10(20), e01199, 2025, by K. Vilkevičius, T. Rakickas, and E. Stankevičius.

While SERS performance reflects the localized near-field enhancement, influenced by single structures, another metric of plasmonic platform functionality is the sensitivity of collective grating resonances to changes in the surrounding refractive index. Periodic arrays support grating-coupled modes with narrow peaks and dispersive features, making them suitable for RI sensing applications, where resonance shifts directly correspond to variations in the environment, enabling label-free detection of biomolecules, analytes, and other pathogens or chemical agents. Conventional SPR sensors typically employ prism-based configurations, which require bulky optical components. While providing high sensitivity, their overall size and device complexity limit their applicability to compact, on-chip, or portable solutions.

Therefore, the developed DLW fabrication methodology for thin metallic samples was applied to realize plasmonic sensors based on nanobump gratings. Building upon morphology- and dimension-controlled arrays, further performance improvements can be achieved through material combination. Bimetallic structures, specifically Ag-Au bilayers, offer a combined approach of both metals – the high plasmonic quality and low damping losses of silver paired with the chemical stability of gold. Here, a single-step fabrication process combined with material adjustments to enhance sensing capabilities is presented.

For this research, three different samples of nanobump gratings with a 0.8 μm period were fabricated on gold, silver, and a silver-gold bilayer of 50 nm using a 343 nm wavelength with pulse energies in the 0.46-0.55 nJ range. The size of the bump was kept at approximately 200 nm across all samples to enable comparative responses (Figure 3.18a-c). Three samples with 3×3 mm^2 arrays for each film were produced to ensure repeatability. To evaluate plasmonic performance, an adhesive chamber was attached, and reflectance spectra were measured for ultrapure water and glycerol solutions at concentrations of 1.7%, 3.4%, 5.1%, and 6.8%. Spectrophotometric measurements at a near-normal incidence angle (8°) revealed that the transition from air to a liquid environment induces a significant redshift of over 250 nm, indicating a high grating sensitivity to changes in the ambient refractive index for all three samples (Figure 3.18d-f). A 1.7% change in liquid concentration results in a redshift of the peaks by 2-3 nm.

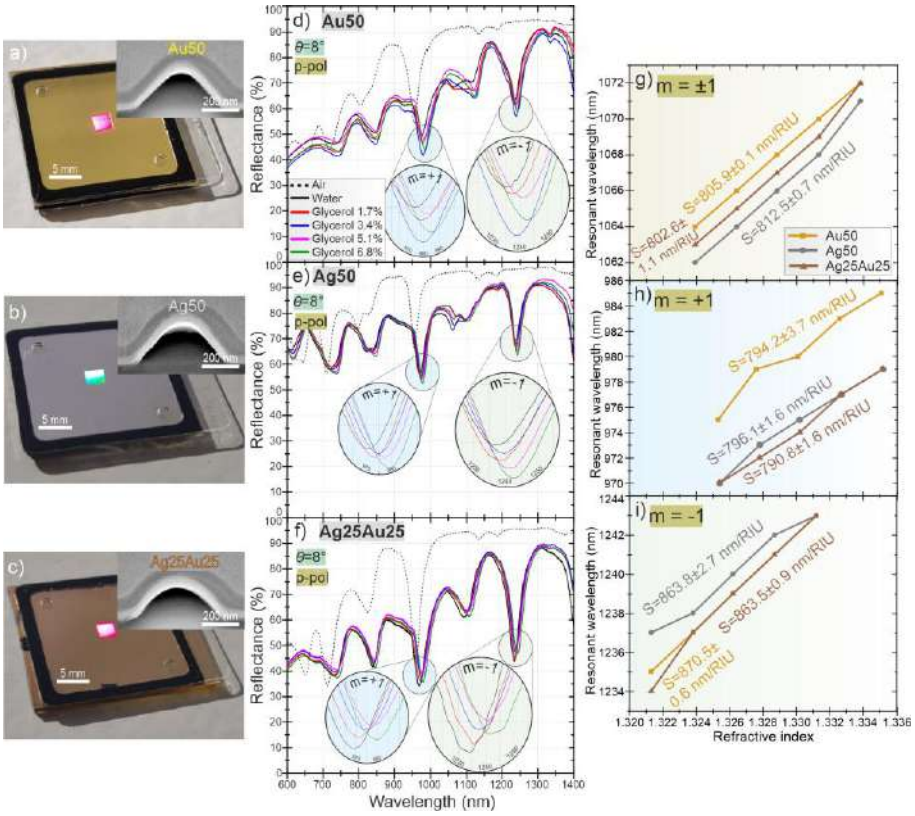

Figure 3.18. Photos with SEM insets of a) gold, b) silver, and c) silver-gold bilayer samples. Reflectance spectra of p-polarization in air (dashed line) and liquids (solid lines) for d) gold, e) silver, and f) silver-gold bilayer samples. Resonant wavelength dependence on RI with sensitivity of g) s-polarization ($m = \pm 1$), h) p-polarization ($m = +1$), and i) p-polarization ($m = -1$) resonant peaks.

Each of the three main resonant peaks ($m = \pm 1$ in s-polarization, $m = +1$, and $m = -1$ in p-polarization) exhibits slightly different dispersive properties; therefore, these were investigated separately for wavelength-RI dependence (Figure 3.18g-i) and compared across different samples. A nearly linear trend in resonant wavelength is observed as the liquid's RI gradually increases. Calculations of the performance parameters revealed that all platforms achieve sensitivities around 800 nm/RIU, with the $m = -1$ peak exhibiting the largest sensitivity (around 870 nm/RIU) and $m = +1$ being the least sensitive (790 nm/RIU). Despite that, no clear trend was observed in the material used, as all the samples yielded similar results. In addition, for the bilayer sample, the LoD was determined using lower-concentration solutions (0.2%, 0.41%, 0.84%, and 1.68%). Based on the measurements, the LoD concentration is approximately 0.84%, corresponding to an RI change of 0.0013. This is limited by the spectrophotometer's wavelength step size and by peak width.

While the metallic configuration has a low impact on sensitivity, it dictates the characteristics of the grating-coupled resonance peaks, thus influencing quality factors and the FOM parameter. In air, silver exhibits the strongest plasmonic properties due to its low damping losses, with the highest MQ-factor of 10.25 for the s-polarized peak. The gold bumps exhibit the lowest MQF (6.62), and the bilayer sample serves as a middle ground with an MQF of 8.18, using the upper gold layer as an oxidation protector. Interestingly, for the p-polarized $m = -1$ peak, associated with out-of-plane excitation, the bilayer sample outperforms pure silver (11.4) and gold (10), with the MQ-factor reaching 14. This affects the FOM presented in Table 4. The silver sample exhibits the largest FOM across all resonant peaks, as its resonant peaks are narrower than those of other samples. Meanwhile, the silver-gold bilayer sample shows intermediate FOM values, with only the out-of-plane resonance, influenced by the structures' height inhomogeneities, being identical to the least effective gold sample. Although silver demonstrates the strongest sensing properties, the most practical configuration is a bilayer sample, combining oxidation resistivity with moderate plasmonic response.

Table 4. Figure of merit (FOM) for the investigated samples and the main peaks.

Sample	**Figure of merit (FOM), [RIU^{-1}]**		
	$m = \pm 1$	$m = +1$	$m = -1$
Ag	42.1 ± 3.1	33.3 ± 0.3	31.8 ± 0.7
Au	30.1 ± 0.7	26.2 ± 0.6	24.4 ± 0.7
Ag-Au	38.4 ± 1.7	29.9 ± 0.5	24.2 ± 0.6

Since the resonant peaks are angle-dependent, the influence of the AOI on the performance of the silver-gold bilayer platform was investigated at 15°, 30°, 45°, and 60° for all liquids used. As discussed previously, s-polarization and p-polarization positive-order resonances blueshift, while the p-polarization negative-order peak undergoes a redshift with increasing angle (Figure 3.19a-b). This shift introduces additional practical constraints related to environmental absorption zones – the water absorption zone (at 1400-1500 nm) and the adhesive chamber absorption peaks (1650-1730 nm), which overlap with the $m = -1$ resonant peaks of p-polarization at 30° and 45° angles. This underscores the necessity of optimizing the AOI based on the liquid used to ensure high-quality spectral responses.

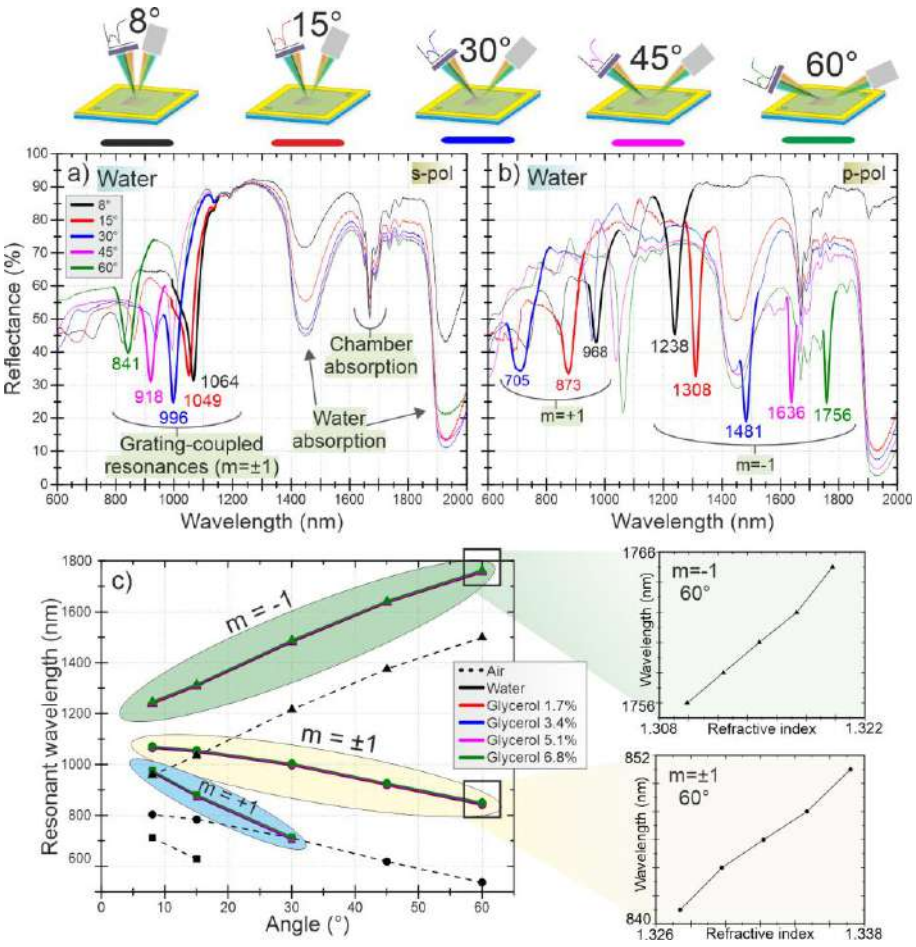

Figure 3.19. Reflectance dependence on AOI for a) s- and b) p-polarization in a water environment. c) Resonant wavelength change with angle in different liquids. Insets depict the dependence of the resonant wavelength on RI at a 60° angle for specific peaks.

Despite the angular shift, the platform maintains a linear response to RI changes, with a 2-4 nm resonant wavelength increment as glycerol concentration increases by 1.7% (Figure 3.19c). The optimal choices of AOI and resonant peak determine a critical compromise between sensitivity and FOM. As the AOI increases, both p-polarization resonances decrease in sensitivity and exhibit smaller wavelength shifts, whereas the s-polarization resonance exhibits enhanced sensitivity, reaching 933 nm/RIU. The opposite tendency is observed in the FOM, where this $m = \pm 1$ peak blueshift is accompanied by spectral broadening and a decreasing FOM trend. And since the $m = -1$ peak preserves its narrow width while redshifting, the FOM of this resonance is growing with increasing AOI, reaching 57 RIU^{-1}. Specific values of sensitivity and FOM for each peak and angle are given in Table 5. This proves that s-polarization resonances are preferable at lower angles due to higher initial quality, while p-polarization negative-order resonances become more advantageous at higher angles.

Table 5. Sensitivity and FOM for the Ag-Au sample at different AOIs.

Angle	Sensitivity, [nm/RIU]			FOM, [RIU^{-1}]		
	$m = \pm 1$	$m = +1$	$m = -1$	$m = \pm 1$	$m = +1$	$m = -1$
8°	802	790	863	38	29	24
15°	817	751	854	35	22	30
30°	877	-	839	33	-	38
45°	920	-	829	31	-	42
60°	933	-	826	24	-	57

The stability of the bimetallic sensing platform was evaluated by repetitive spectral measurements, which showed identical resonant peak positions and confirmed the robustness of the results. Repeatability was assessed by comparing three independently fabricated Ag-Au samples under identical conditions, revealing high consistency in their spectral responses. While with minor deviations in absolute resonant wavelengths, the fundamental sensing performance remained uniform across the samples, with sensitivity differences of only 3 nm/RIU. The platform's durability was investigated by taking repeated measurements after 6 months, with the attached chamber serving as a protective layer. Spectral measurements (Figure 3.20) confirmed that the resonant wavelengths remained unchanged, with minor fluctuations in peak intensities but maintained sensitivity values.

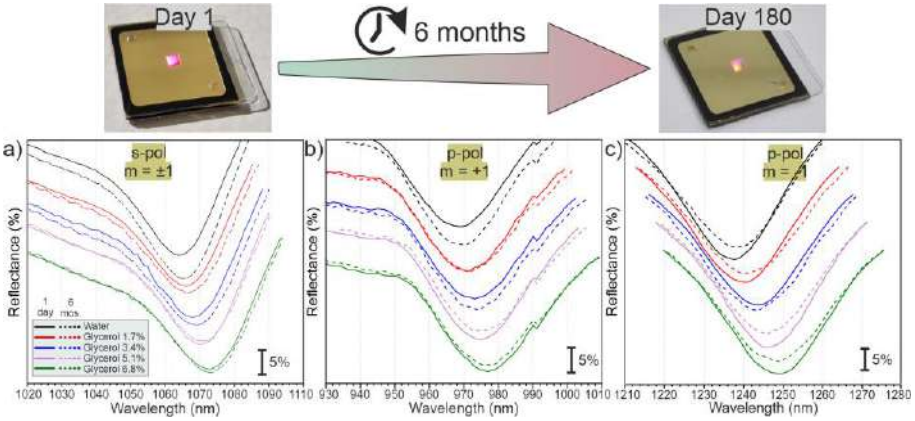

Figure 3.20. Durability measurements of a) $m = \pm 1$, b) $m = +1$, and c) $m = -1$ resonant peaks on the day of fabrication (solid lines) and after 6 months (dashed lines).

In summary, single-step DLW-based production of large-scale nanobump gratings can be effectively employed and designed for high-performance RI sensing platforms, with a clear resonant shift corresponding to environmental changes and a minimal RI change detection limit of 0.0013. Although the results were demonstrated only with glycerol, they indicate the potential to adapt the platform for affinity-based sensing through surface functionalization, which will be further explored in future experiments. Material substitution and the use of a silver-gold bilayer structure enable the benefits of both metals, achieving high plasmonic performance and long-term chemical stability. Additional tuning of the AOI enables more flexible management and enhancement of sensitivity or FOM parameters, achieving up to 933 nm/RIU and 57 RIU^{-1} values. Repeatability and durability, as evidenced by stable performance over long-term measurements, make this compact platform a reliable solution for label-free detection.

3.2.3. Main results and conclusions

This section described the practical utilization of DLW-produced gratings for plasmonic applications. By controlling laser-induced morphological transitions and material combinations, the platforms can be adjusted for specific applications – either SERS or RI-based sensing – and achieve high sensitivities and enhancement factors. Jet-like structure optimization enables SERS enhancement to reach 10^7 orders of magnitude. Meanwhile, hemispherical bumps show potential for environmental RI sensing, with sensitivity exceeding 850 nm/RIU. These results confirm that DLW-based periodic arrays provide a reliable and scalable alternative for compact and label-free detection platforms.

One statement to defend was formulated according to the accomplished results described in this chapter:

- Morphological engineering of laser-fabricated plasmonic nanostructures provides application-specific functionality of large-scale gratings: high-aspect-ratio nanojets maximize SERS enhancement factor up to 2.73×10^{7}, while Ag-Au bimetallic nanobump gratings offer stability and tunable sensitivities exceeding 850 nm/RIU, sufficient for RI sensing.

4. MAIN RESULTS AND CONCLUSIONS OF THE THESIS

The research presented in this thesis provides a broad analysis of femtosecond direct laser writing as a single-step, easily tunable methodology for the nanoengineering of noble metal films for large-scale plasmonic grating formation. By manipulating laser parameters, material configurations, and array geometries, this work demonstrates precise control over grating-coupled resonances, which can be effectively applied to advanced analytical applications.

The main results and conclusions supporting the statements to defend:

- The reduction of the laser wavelength from 1030 nm to 343 nm results in increased absorption in thin films, enabling a lower modification threshold (0.1 J/cm^2) and expanding morphological tuning over a broader fluence range (0.4 J/cm^2).
- The reduction of the laser wavelength from 1030 nm to 343 nm results in reduced beam size, allowing the production of arrays with the smallest submicron periods that are unattainable with IR wavelengths.
- Morphology of single fs laser pulse-induced nanostructures can be tuned from hemispherical nanobumps to sharp jets by increasing pulse energy, while increasing metal thickness results in thickening of the produced structures.
- Morphology manipulation can be achieved by reducing the grating period below the focused beam size, as an overlapping effect decreases the modificational thin-film fluence due to intrinsic layer modification.
- Resonant wavelength spectral position and its quality are highly influenced by the structure morphology, as the out-of-plane mode is excited, which depends on the height component.
- Arrays with a small-period tendency in one axis produce quasi-1D arrays, possessing 2D physical geometry but exhibiting 1D spectral characteristics, as diagonal excitation is eliminated.
- In symmetric 2D gratings, spectral positions and coupling efficiency are governed by the manipulation of azimuthal and incidence angles, corresponding to high-symmetry axes, enabling continuous tuning of the resonance across the entire Vis-NIR range.
- Among DLW-produced morphologies, needle-like jets provide the largest enhancement factor, as the sharp tip creates a hot spot that can be further

amplified by film thickness optimization (at 150 nm), thus exhibiting a 2.73×10^7 enhancement factor.

- A bimetallic Ag-Au configuration combines advantageous properties of both metals, providing a platform consisting of periodic bumps for a plasmonic RI sensor with high environmental resistivity and stability, and an intermediate metal sensitivity (over 850 nm/RIU), which can be improved by an additional angular control (up to 933 nm/RIU).

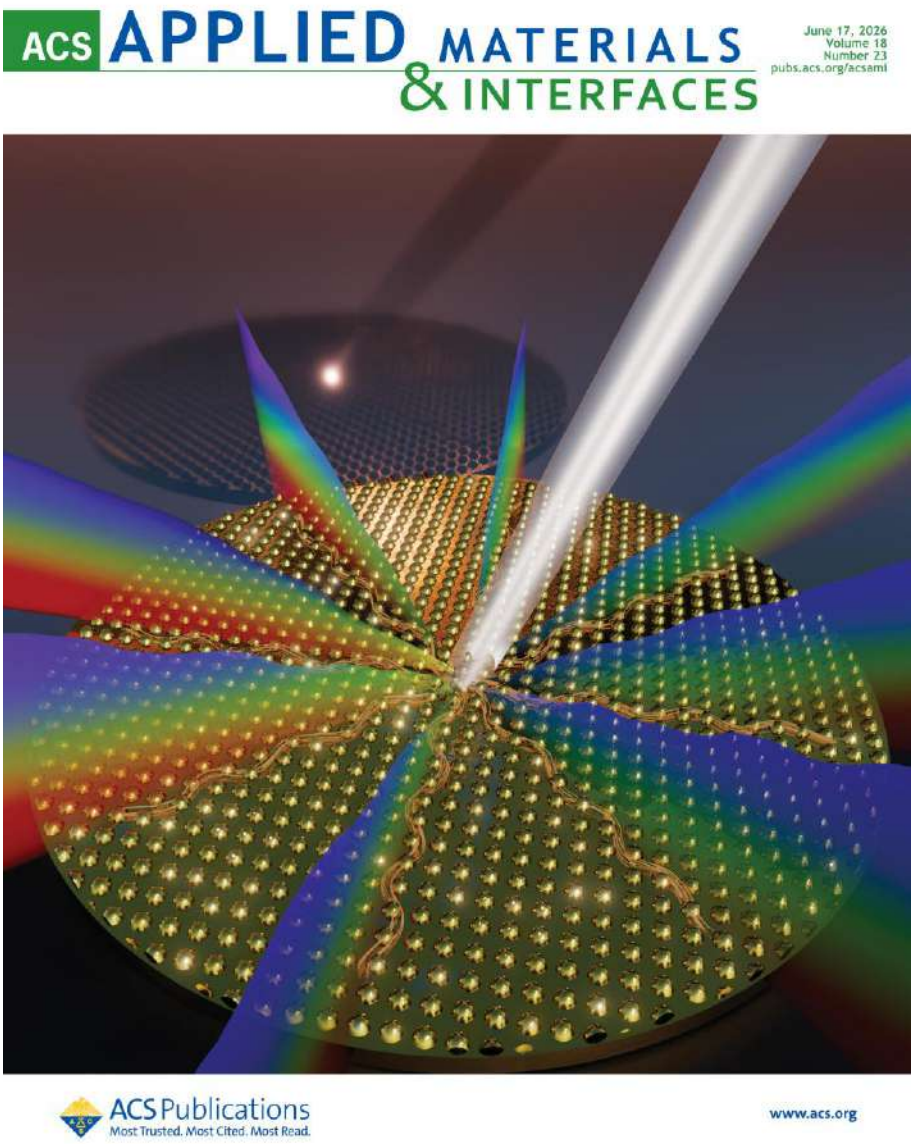

SUPPLEMENTARY COVER:

Kernius Vilkevičius, Lucciano A. Letelier, Lina Grinevičiūtė, Evaldas Stankevičius, *Grating-Coupled Plasmonic Resonances in Symmetric 2D Gold Nanobump Grating: Theory Meets Experiments* (ACS Applied Materials & Interfaces, Vol. 18 Issue 23, 2026)

5. SANTRAUKA

ĮVADAS

Plazmoniniai mikro- ir nanodariniai per pastaruosius dešimtmečius sulaukė didelio susidomėjimo dėl jų gebėjimo lokalizuoti šviesą ir sustiprinti elektromagnetinius (EM) laukus mažesniuose už bangos ilgį matmenyse, sužadinant paviršinius plazmonus (SP) [1-3]. Nors plazmonikos srityje dėl stipraus laisvųjų elektronų atsako pagrinde naudojami taurieji metalai, plazmonikos struktūroms gali būti taikomos ir kitos medžiagos – stipriai legiruoti puslaidininkių kristalai [4, 5], dvimatės (2D) medžiagos [6] bei laidieji polimerai [7]. Kiekviena medžiagų klasė remiasi skirtingais mechanizmais: puslaidininkiuose plazmoniniai reiškiniai susiję su laisvosiomis skylėmis, 2D medžiagose – su elektronų ir skylių sąveika, o polimeruose – su polaroniniais krūvininkais. Tačiau dėl sudėtingų gamybos iššūkių, susijusių su pastarosiomis medžiagomis, taurieji metalai, tokie kaip auksas (Au) ar sidabras (Ag), išlieka pagrindinėmis medžiagomis didelio efektyvumo plazmoniniams taikymams [8].

Tauriuosiuose metaluose šviesos ir medžiagos sąveiką lemia kolektyvūs laidumo elektronų virpesiai, kurie apibūdinami kaip lokalizuoti paviršiniai plazmonai (LSP) pavienėse nanodalelėse bei kaip sklindantys paviršiniai plazmonų poliaritonai (SPP) metalo-dielektriko sandūroje. Plazmoninio rezonanso (SPR) dažniu sužadinti laisvieji elektronai sustiprina krintančios spinduliuotės sugertį ir sklaidą bei lemia reikšmingą artimojo lauko sustiprėjimą [9]. Tokių metalinių darinių išdėstymas į periodines gardeles ant plonų metalinių dangų sukuria papildomą difrakcinio pobūdžio sąryšį, leidžiantį šioms modoms sąveikauti. Toks ryšys lemia LSP ir SPP hibridizaciją, dėl kurios sustiprėja jų sąveika, sumažėja nuostoliai ir pagerėja optinės savybės [10-12].

Šios unikalios savybės atveria plačias taikymo galimybes – nuo teršalų aptikimo [13], biologinių žymenų nereikalaujančios biomedicininės diagnostikos [3, 14] ir aplinkos stebėsenos [15] iki fotoninių įrenginių [16], energijos surinkimo sistemų [17] bei nanolazerių [18, 19]. Stipri EM lauko lokalizacija struktūrose leidžia kurti jautrias aptikimo platformas ir kompaktiškus fotoninius prietaisus. Nuolat augant pažangių analitinių ir diagnostinių technologijų poreikiui, plazmoninės platformos sulaukia vis didesnio dėmesio dėl didelio jautrumo, greito atsako, tikslumo ir suderinamumo su integruotomis sistemomis.

Tradicinė tokių metalinių plazmoninių struktūrų gamyba remiasi *iš viršaus į apačią* (angl. *top-down*) litografijos metodais, kurie dažnai derinami su

metalo nusodinimo ir *lift-off* technikomis [20, 21]. Nors šie metodai ir yra tikslūs, jų daugiapakopiai procesai ribojami mažu našumu, didelėmis gamybos sąnaudomis arba ribotu atkartojamumu bei struktūrų kontrole. Todėl tiesioginis lazerinis rašymas (DLW) iškilo kaip greita, vieno žingsnio ir ekonomiškai efektyvi alternatyva tokių darinių formavimui [22-25]. Ultrasparčiųjų femtosekundinių impulsų naudojimas medžiagos struktūrizavimui suteikia naujų galimybių padidinti gamybos spartą bei pagerinti suformuotų darinių ir jų savybių valdymą. Rezonanso padėtis, kokybės faktorius ar artimojo lauko sustiprinimo efektyvumas gali būti tiksliai reguliuojamas keičiant įvairius technologinius parametrus [26, 27]. Nepaisant DLW potencialo, ši metodika vis dar susiduria su tam tikrais iššūkiais. Siekiant užtikrinti stabilias ir atkartojamas darinių savybes, būtina tiksli struktūrų kontrolė, o tam reikalinga nuodugni pagrindinių lazerinės sistemos, bandinio bei gardelės parametrų analizė. Taip pat iki šiol nepakankamai ištirtas sudėtingas daugiakryptis sužadinimas 2D gardelėse bei jų gebėjimas pasižymėti vienmačių (1D) gardelių savybėmis. Tad šiame darbe nagrinėjama tauriųjų metalų nanoinžinerija femtosekundiniu lazeriu bei plazmoninių gardelių formavimas pažangiems plazmoniniams taikymams.

Pagrindinis šio disertacijos tyrimo tikslas – ištirti ir optimizuoti morfologiškai valdomų tauriųjų metalų nanodarinių didelio ploto gardelių vienažingsnę gamybą, naudojant femtosekundinę (fs) tiesioginio lazerinio rašymo technologiją, eksperimentiškai ir teoriškai charakterizuoti jų plazmonines savybes bei įvertinti pritaikomumą su plazmonika susijusiose srityse, įskaitant paviršiumi sustiprintą Ramano spektroskopiją (SERS) bei lūžio rodiklio (RI) jutiklius.

Darbo tikslui pasiekti buvo suformuluoti šie **uždaviniai**:

1. Sukurti greitą ir lengvai išplečiamą tiesioginio lazerinio rašymo metodą, skirtą formuoti didelių plotų 1D ir 2D gardeles, sudarytas iš morfologiškai valdomų metalinių nanodarinių.
2. Ištirti nanodarinių morfologijos valdymo galimybes ir optimizuoti formavimo parametrus, reikalingus skirtingos geometrijos struktūroms pagaminti.
3. Eksperimentiškai ir teoriškai charakterizuoti suformuotų gardelių plazmonines savybes bei nustatyti jų sąryšį su morfologija ir gardelės simetrija.
4. Ištirti periodinių nanodarinių taikymo galimybes SERS srityje.
5. Ištirti periodinių nanodarinių taikymo galimybes metalinių plazmoninių RI jutiklių srityje.

Darbo mokslinis naujumas ir aktualumas

Darbe pristatytas ir išsamiai ištirtas spartus tiesioginio lazerinio rašymo (DLW) metodas, skirtas plonų metalinių dangų struktūrizavimui ir laisvos formos ir didelio ploto gardelių gamybai su bangos ilgio eilės periodais. Šiame tyrime pirmą kartą atlikta detali DLW būdu suformuotų aukso nanodarinių analizė, ištiriant periodo lemiamus morfologinius pokyčius bei impulsų persidengimo efekto įtaką formavimosi parametrams. Taip pat pirmą kartą pristatytos DLW būdu suformuotos kvazi-1D gardelės, kurios turi dvimatę geometriją, tačiau pasižymi aukštos kokybės vienmatėms sistemoms būdingomis spektrinėmis charakteristikomis. Darbe pateikiama teorinė ir eksperimentinė simetrinėse 2D gardelėse sužadinamo plazmonų rezonansų dvigubo kampinio valdymo analizė, atskleidžianti pagrindinių ir įstrižainių difrakcinių gardelių tarpusavio sąveiką bei jų įtaką rezonansinėms savybėms. Galiausiai pademonstruotas metodo potencialas kurti didelio ploto plazmonines struktūras, kuių morgolofija pritaikoma konkrečioms taikymo sritims: sukurtos kompaktiškos bei didelio našumo analitinės platformos lūžio rodiklio matavimams bei SERS detekcijai.

Ginamieji teiginiai

1. Naudojant pastovios NA objektyvą, fs lazerio bangos ilgio mažinimas nuo 1030 nm iki 343 nm tris kartus išplečia nanodarinių formavimosi energijos įtėkio diapazoną ir sumažina pasiekiamą gardelės periodą iki 450 nm, o papildomas dangos storio valdymas bei impulsų persidengimo didinimas leidžia tiksliau valdyti nanodarinių morfologiją, sumažinant modifikacijos slenkstį.

2. 2D gardelėse plazmoninių rezonansų spektrinės savybės priklauso nuo nanodarinių morfologijos, kai darinio aukščio didėjimas lemia neplokštuminio rezonanso poslinkį į didesnius bangus ilgius, o suformuotos kvazi-1D gardelės slopina įstrižainės rezonansus ir leidžia spektriškai izoliuoti žadinamas modas.

3. Simetrinėse 2D gardelėse žadinami rezonansai pasižymi aukščiausia kokybe kai jie yra žadinami išilgai aukštos simetrijos ašių (0°, 45°, 90°), o jų spektrinė padėtis visame Vis-NIR (400-1600 nm) diapazone gali būti koreguojama dvigubu kampiniu valdymu, keičiant azimutinį (0°-90°) ir spinduliuotės kritimo (8°-30°) kampus.

4. Lazeriu suformuotų plazmoninių nanodarinių morfologinis valdymas leidžia koreguoti didelio ploto gardelių funkcionalumą, pritaikant jį konkrečioms sritims: aukštos antenos maksimaliai padidina SERS stiprinimo koeficientą iki $2{,}73\times10^{7}$, o Ag-Au bimetalinių gumbelių gardelės užtikrina stabilumą bei koreguojamą jautrumą virš 850 nm/RIU, tinkamą RI jutikliams.

Aprobacija

Disertacija paremta 6 moksliniais straipsniais [P1]-[P6], publikuotais tarptautiniuose mokslo leidiniuose, indeksuojamuose ir turinčiuose cituojamumo rodiklį *Clarivate Analytics Web of Science (CA WoS)* duomenų bazėje. Turimas 1 publikuotas su disertacija susijęs lietuviškas patentas [T1]. Taip pat 3 su disertacija tiesiogiai susiję rezultatai paskelbti konferencijų medžiagose [P7]-[P9]. Kiti, su disertacija nesusiję, rezultatai publikuoti 4 tarptautiniuose mokslo leidiniuose, indeksuojamuose ir turinčiuose cituojamumo rodiklį *CA WoS* duomenų bazėje [OP1]-[OP4] bei 2 konferencijų medžiagose [OP5]-[OP6].

Doktorantūros metu su disertacija susiję rezultatai pristatyti 26 konferencijose [C1]-[C26], iš kurių 13 tarptautinėse, 8 nacionalinėse konferencijose bei 5 vasaros mokyklose.

Autoriaus ir bendraautorių indėlis

Autorius savarankiškai atliko didžiąją dalį eksperimentinių tyrimų – nuo mėginių paruošimo ir metalų nusodinimo iki lazerinės sistemos derinimo bei nanodarinių formavimo DLW metodu. Autorius atliko visus kitiems bendraautoriams nepriskirtus darbus: darinių charakterizavimą, duomenų analizę, teorinius skaičiavimus bei rezultatų vizualizavimą. Autorius parengė visų [P1]-[P6] publikacijų rankraščius, atsižvelgiant į bendraautorių pastabas ir pasiūlymus. Taip pat autorius sukūrė tris viršelių dizainus, kurie buvo publikuoti žurnaluose kartu su [P2], [P4] bei [P6] darbais.

Dr. Evaldas Stankevičius pasiūlė tyrimo idėją ir vadovavo doktorantūros studijoms bei atliekamiems darbams. **Dr. Algirdas Selskis** atliko visus SEM matavimus. **Dr. George D. Tsibidis** atliko [P2] publikacijoje skelbiamus šiluminius modeliavimus, taikant dviejų temperatūrų modelį (TTM). **Dr. Emmanuel Stratakis** suteikė tyrimų įrangą, reikalingą [P2] publikacijai, bei konsultavo šiame darbe aprašytų formavimo bei modeliavimo rezultatų klausimais. **Kipras Čepaitis**, kuruojant autoriui, atliko [P3] publikacijoje aprašytų gardelių gamybą ir jų optinius matavimus. **Dr. Lina Grinevičiūtė** konsultavo [P4] publikacijos difrakcinių gardelių modeliavimo klausimais. **Doktorantas Lucciano A. Letelier** atliko spektrinius ir artimojo lauko FDTD modeliavimus, naudotus [P4] publikacijoje. **Dr. Ilja Ignatjev** atliko [P5] publikacijoje aprašytus SERS matavimus. **Dr. Gediminas Niaura** konsultavo [P5] publikacijoje pateiktų SERS eksperimentinių rezultatų klausimais. **Tomas Rakickas** paruošė [P6] publikacijoje naudotus skysčius lūžio rodiklio matavimams bei atliko jų elipsometrinį charakterizavimą.

LITERATŪROS APŽVALGA

Šiame disertacijos skyriuje pateikiama literatūros apžvalga, susijusi su disertacijos tyrimais bei metodais.

Poskyris 1.1. Nanofotonikos srities plėtra paskatino didelį susidomėjimą šviesos ir medžiagos sąveikos valdymu mažesniuose nei bangos ilgis masteliuose, o viena iš svarbiausių sričių yra plazmonika. Paviršiniai plazmonai (SP) yra kolektyviniai laidumo elektronų virpesiai metaluose, sužadinami elektromagnetine (EM) spinduliuote esant rezonansinėms sąlygoms [9]. Jų žadinimas lemia optinę ekstinkciją bei EM lauko stiprinimą, o tai sudaro pagrindą daugeliui plazmoninių taikymų. Plazmonų rezonansas (SPR) pasireiškia spinduliuotės sugertimi, kuri priklauso nuo aplinkos savybių, plazmoninių dalelių dydžio, formos, koncentracijos ar sudėties [28-30]. Dažniausiai plazmoninėms sistemoms naudojami auksas ir sidabras dėl rezonanso pasireiškimo matomosios ir artimosios infraraudonosios (NIR) spinduliuotės diapazonuose [32].

Poskyris 1.2. Metalinių nanodarinių optines savybes lemia sužadinamos plazmoninės modos. Pagrindinės yra lokalizuoti paviršiniai plazmonai (LSP) ir paviršiniai plazmonų poliaritonai (SPP), tačiau jų sąveika lemia hibridizaciją bei naujų modų susidarymą. LSP sužadinami pavienėse metalų nanodalelėse, kurios yra mažesnės už krintančios spinduliuotės bangos ilgį. Taip EM sužadina kolektyvius elektronų svyravimus visame dalelės tūryje, o LSP savybės stipriai priklauso nuo dalelės dydžio, formos, medžiagos bei aplinkos parametrų [11, 29]. Antroji SPP moda susidaro metalo-dielektriko sandūroje, tačiau dėl SPP ir šviesos bangos vektorių nesutapimo, ji negali būti sužadinta tiesiogiai. Sužadinimui naudojama prizmė, kai dėl visiško vidaus atspindžio suderinami banginiai vektoriai [33, 35]. Alternatyvus metodas, kuriam nereikia papildomo elemento, yra difrakcinis sužadinimas, naudojant periodinę gardelę metalo paviršiuje. Tokių rezonansų charakteristikos priklauso nuo gardelės periodo, formos bei spinduliuotės žadinimo sąlygų [38-40]. Lyginant su LSP, SPP pasižymi didesniu sklidimo atstumu ir jautrumu, tad pastaroji moda yra tinkamesnė praktiniams taikymams. Siekiant dar labiau išplėsti plazmoninių darinių funkcionalumą, naudojamos ne pavienės, bet tarpusavyje susietos – hibridinės – modos. Viena tokių yra paviršinis gardelės rezonansas (SLR), pasiekiamas periodinėse metalinių nanodarinių gardelėse dėl pasikartojančių LSP ir difragavusios spinduliuotės sąveikos [45-48]. Dėl kolektyvinio atsako sumažinami spinduliavimo nuostoliai, taip susiaurinant rezonanso plotį ir padidinant jo kokybę. Dar sudėtingesnės hibridinės modos susidaro, kai periodinės struktūros formuojamos ant metalinių dangų. Šiuo atveju SLR, SPP ir difrakcijos sąveika

lemia hibridinių gardelės plazmoninių rezonansų (HLPR) sužadinimą [22, 53]. Jie pasižymi didele kokybe ir lengvu savybių valdymu, tad yra perspektyvūs kuriant platformas nanofotonikos įrenginiams. Būtent šios hibridinės gardele žadinamos modos ir pasireiškia tiriamuose dariniuose.

Poskyris 1.3. Paviršiaus nanostruktūrizavimas reikšmingai keičia ne tik pavienių struktūrų, bet ir visos plazmoninės sistemos savybes. Darinių charakteristikos, tokios kaip dydis [28, 56], forma [57-60], medžiagos sudėtis [2, 62-65], koncentracija ir struktūrų kiekis [66-68] turi didelę įtaką tiek darinių gebėjimui sugerti spinduliuotę, tiek kitoms plazmoninėms savybėms.

Poskyris 1.4. Metaliniai nanodariniai ypač paklausūs plazmonikos ir nanofotonikos srityse dėl jų atkartojamumo, homogeniškumo ir galimybės išplėsti gamybos apimtis, tad jų formavimui sukurta nemažai skirtingų technologinių metodų. Vienas pagrindinių metodų yra elektronų pluošto litografija (EBL), leidžianti pasiekti itin didelė skiriamąją gebą bei formuoti itin mažų matmenų darinius, tačiau apribota mažo našumo bei nedidelių plotų apdirbamumu [72-74]. Fokusuoto jonų pluošto (FIB) litografija leidžia tiesiogiai šalinti medžiagą pasiekiant panašią skiriamąją gebą, tačiau pats metodas yra brangus, lėtas ir galintis užteršti bandinį jonais [55, 72]. Siekiant įveikti našumo ir sąnaudų apribojimui, minkštoji bei nanoįspaudo litografijos tapo efektyviomis alternatyvomis didelio ploto struktūrizavimui, naudojant štampavimą bei polimeriniais dariniais paremtą formavimą [71, 83]. Nors greiti, šie metodai apriboti darinių valdyme, kadangi kiekvienai naujai modifikacijai reikalinga nauja brangi štampo gamyba. Alternatyvi kryptis periodinių darinių gamyboje – lazerinis apdirbimas, apimantis įvairius procesus nuo lazeriu indukuoto tiesioginio medžiagos pernešimo (LIFT), lazeriu indukuotų periodinių paviršiaus struktūrų (LIPSS) bei tiesioginio lazerinio rašymo (DLW) [88-95]. Ultraspartūs femtosekundiniai impulsai leidžia itin tiksliai apdirbti medžiagas su minimalia šilumine įtaka, o energijos valdymas įgalina skirtingą apdirbimo būdą bei gaunamos struktūros formos keitimą [96-98]. DLW atveju, kai lazerio spindulys aštriai sufokusuojamas metalo dangos paviršiuje, dėl medžiagos šildymo ir termodinaminių bei mechaninių procesų susiformuoja sudėtingos morfologijos dariniai, sunkiai pasiekiami kitais aprašytais metodais.

Poskyris 1.5. Pažangios plazmoninių struktūrų formavimo technologijos leidžia tiksliai valdyti jų parametrus ir, atitinkamai, optines savybes, tad tokie dariniai gali būti plačiai pritaikomi įvairiose srityse. Viena svarbiausių plazmoninių struktūrų savybių – EM lauko stiprinimas artimajame lauke, kas sudaro pagrindą paviršiumi sustiprintai Ramano spektroskopijai (SERS). Naudojant tokias struktūras galima žymiai padidinti įprastai silpną Ramano sklaidos signalą ir taip aptikti net mažas molekulių koncentracijas bei tiksliai

nusakyti tiriamąsias medžiagas [102-104]. Dėl didelio jautrumo ir molekulinio specifiškumo, plazmoninių gardelių SERS tyrimai taikomi cheminėje analizėje, aplinkos stebėsenoje ir maisto saugos srityse aptikti dažų, maisto alergenų, teršalų, sprogmenų bei kitų pavojingų medžiagų pėdsakus [13, 107-109]. Metodas taip pat taikomas bioanalizėje aptikti DNR, baltymus, biomolekules, nustatyti infekcines ligas ar navikus [110, 111]. Kita svarbi taikymo sritis – lūžio rodiklio (RI) jutikliai, paremti SPR jautrumu aplinkos pokyčiams, kai įvykus paviršiniams pokyčiams ar reakcijoms stebimas rezonansinės smailės poslinkis spektre [38, 50]. Tokių jutiklių jautrumas priklauso nuo rezonanso pločio, tad siekiant užregistruoti itin mažus pokyčius, kuriamos periodinės gardelės ir hibridiniai masyvai, pasižymintys siaurais rezonansais. Šios RI jutiklių platformos sėkmingai naudojamos bežymeniam biologinių ir cheminių medžiagų aptikimui, įskaitant vėžinius darinius ir bakterijas, dujų bei skysčių analizei [14, 15, 114]. Be šių taikymų, plazmoninės struktūros taip pat naudojamos fotoliuminescencijos, sugerties ir netiesinių procesų stiprinimui, taip jas pritaikant sustiprintos fluorescencijos, kvantikos, spinduliuotės sugėriklių bei nanolazerių srityse [118-126].

EKSPERIMENTINĖ ĮRANGA IR METODOLOGIJA

Šio skyriaus pirmojoje dalyje aprašomas bandinio paruošimas bei darinių formavimas, o antrojoje – struktūrų ir jų savybių charakterizavimas.

Poskyris 2.1. Eksperimentinis darinių formavimas buvo atliekamas skirtingo storio plonose metalų dangose (aukso (Au) ar sidabro (Ag)), padengtose ant titano (Ti) pasluoksnio. Naudotos dangos pateiktos lentelėje Table 1. Plazmoniniai dariniai suformuoti naudojant DLW metodiką, aštriai sufokusavus lazerio spindulį metalo paviršiuje bei naudojant pavienį fs impulsą darinio formavimui. Periodinės gardelės pagamintos atliekant lazerinį skenavimą judinant bandinį transliaciniu staliuku. Formavimo parametrai pateikti lentelėje Table 2. Dėl lazerio pluošto Gausinio intensyvumo pasiskirstymo, kai didžioji impulso energijos dalis sutelkta centre, buvo galima suformuoti mažesnių nei pluoštas matmenų darinius bei išgauti impulsų persidengimą, taip pagaminant submikroninių periodų gardeles.

Poskyris 2.2. Po formavimo, struktūrine darinių analizė buvo atliekama naudojant optinį mikroskopą bei skenuojantį elektroninį mikroskopą (SEM). Morfologija nustatinėta pagal darinių aukščio ir skersmens santykį: pussferės formos struktūros, kurių aukštis mažesnis už diametrą, buvo pavadintos gumbeliais, struktūros su panašiais aukščio-diametro matmenimis – kūgiais, o dariniai su siaura ir aukšta smaile – antenomis. Spektrinė analizė ir atspindžio matavimai buvo atliekami spektrofotometru, naudojant skirtingas

poliarizacijas, spinduliuotės kritimo kampus bei bandinio pasukimo azimutinius kampus. Iš rezonansinių smailių pagal jų bangos ilgį, plotį bei gylį buvo apskaičiuojami kokybės faktoriai, aprašyti (8) ir (9) formulėse. Teoriniai EM laukų pasiskirstymo skaičiavimai bei atspindžio spektrai buvo sumodeliuoti naudojant tiek baigtinių elementų metodą (FEM), tiek baigtinių skirtumų laiko srities (FDTD) metodą. Siekianti įvertinti Ramano signalo stiprinimą, atlikti SERS matavimai, naudojant savaime susiformavusį 4-merkaptobenzoinės rūgšties (4-MBA) monosluoksnį ant aukso gardelių. Stiprinimas buvo lyginamas su kontroliniu Ramano matavimu, atliktu 4-MBA tirpalu izopropanolyje. Pagrindinis SERS parametras, stiprinimo faktorius (EF), apskaičiuotas pagal (10) formulę, įvertinant paviršiaus padengimą bei šiurkštumą skirtingos morfologijos dariniams. Siekiant ištirti lūžio rodiklio jutimo galimybes, ant suformuotų gardelių paviršiaus buvo pritvirtinta kamera, į kurią buvo įleidžiamas skystis – vanduo bei skirtingos koncentracijos glicerolio tirpalai. Lyginant atsaką ore ir skystyje bei stebint rezonansinės smailės poslinkį, buvo apskaičiuotas platformos jautrumas pagal (13) formulę bei efektyvumo rodiklis pagal (14) formulę. Galiausiai, siekiant nustatyti jutiklio atsparumą bei ilgaamžiškumą, bandiniai buvo laikyti 6 mėnesius, po kurių atlikti pakartotiniai matavimai.

REZULTATAI

Rezultatų skyrius išskaidytas į dvi dalis ir išdėstytas taip, kad atspindėtų tyrimo eigą: pradedant pagrindiniais formavimo parametrais ir baigiant taikymais. Pirmoji dalis aprašo nanodarinių gamybą DLW metodu įvairiomis sąlygomis bei jų įtaką plazmoninėms savybėms. Šie rezultatai paskelbti [P1]-[P4] publikacijose. Antroji dalis aprašo plazmoninių gardelių funkcines charakteristikas ir jų pritaikymus, kurie paskelbti [P5]-[P6] publikacijose.

Plazmoninių nanodarinių gardelių lazerinis formavimas ir jų ištyrimas.

Poskyris 3.1.1. *Bangos ilgio nulemtas plazmoninių nanodarinių formavimas*. Šis poskyris paremtas straipsniu [P1]. Tiesioginis lazerinis rašymas (DLW) fs impulsais leidžia tiksliai struktūrizuoti plonas metalines dangas, o sistemos ir apdirbimo parametrai turi itin didelę įtaką pagaminamų darinių formai bei kokybei. Vienas pirminių tokių parametrų – lazerio bangos ilgis, lemiantis sugerties efektyvumą ir medžiagos atsaką. Plonas aukso dangas paveikus 1030 nm, 515 nm bei 343 nm bangos ilgių impulsais, dėl besiskiriančios spinduliuotės sugerties (Figure 3.1a) bei fokusavimo dėmės dydžio, buvo suformuoti skirtingos morfologijos dariniai. Nesant pluošto persidengimui, bangos ilgio mažinimas ir, atitinkamai, sugerties didinimas, žemina sluoksnio modifikacijos slenkstį nuo 7,5 nJ (0,4 J/cm^2) ties IR iki

0,3 nJ (0,109 J/cm^2) ties UV impulsais. Naudojant pagrindinę lazerio harmoniką (1H, 1030 nm), ryškiausiai pasireiškia poliarizacijos nulemtas darinio elipsiškumas (Figure 3.1c). Skirtingos sugerties spinduliuotė lemia ir darinių aukštį – naudojant 1030 nm suformuojami daug žemesni gumbeliai (150-180 nm aukščio) nei su kitais bangos ilgiais (300-400 nm aukščio). Kūginės struktūros su 1H net nesiformuoja, o antenose gaunamas tik nedidelis 150 nm aukščio iškilimas, kai tuo tarpu ties 515 nm ir 343 nm suformuojama aukšta, 700-750 nm aukščio smailė. Ištyrus mažiausią pasiekiamą gardelių periodą nustatyta, jog naudojant 1H impulsus neišabliavus suformuojami tik 0,8 μm periodo masyvai, o su žemesniais bangos ilgiais gaunamos 0,5 μm ir 0,45 μm periodo gardelės. Taip pat aukštesnės harmonikos naudojimas lemia platesnį formavimo energijos įtėkio diapazoną, kuris nuo 0,15 J/cm^2 ties 1030 nm padidinamas iki 0,4 J/cm^2 ties 343 nm, o tai leidžia tiksliau valdyti darinių struktūrinius parametrus (Figure 3.2a-b). Skirtingais bangos ilgiais suformuotų gumbelių spektrinio atsako palyginimas (Figure 3.3) parodė, jog šis parametras didelės įtakos rezonansams neturi, tačiau trumpesni bangos ilgiai turi pranašumą dėl mažesnių periodų formavimo galimybių, kai sustiprinama plazmoninė sąveika. Apibendrinant, mažinant fs lazerio bangos ilgį žymiai padidėja aukso nanodarinių formavimo tikslumas ir universalumas, nes sumažėja modifikacijos slenkstis ir išplečiamas formacijos diapazonas bei sudaromos galimybės pagaminti mažesnio periodo masyvus, tinkamus efektyvesniam plazmoniniam žadinimui.

Poskyris 3.1.2. *Energijos ir periodo sąveika valdant nanodarinių morfologiją*. Šis poskyris paremtas straipsnio [P2] dalimi. Norint tiksliai valdyti plazmonines struktūras, būtina įvertinti ne tik lazerio, bet ir bandinio įtaką formavimo režimams. Nors DLW atveju morfologiją iš esmės lemia pavienio impulso energija, periodiniuose masyvuose svarbiais veiksniais tampa ir gardelės periodas bei impulsų persidengimas. Formuojant nanodarinius skirtingo storio (25-100 nm) aukso dangose, nustatyta, kad didėjant sluoksnio storiui, tai pačiai morfologijai pasiekti reikalinga vis didesnė impulso energija. Gumbelių ir kūgių formos visuose tirtuose storiuose išlieka panašios, tačiau antenų forma stipriai priklauso nuo dangos – plonuose sluoksniuose susidaro itin siauros ir aukštos antenos, o storėjant dangai formuojasi plačios antenos ant kūginio pagrindo (Figure 3.4a-b). Skerspjūvio analizė (Figure 3.4c-e) bei temperatūriniai modeliavimai (Figure 3.5) patvirtina, jog gumbelių formavimosi metu danga deformuojama išlaikant pastovų storį visame darinyje, o kūgiai ir antenos formuojasi dėl metalo išlydymo, kai vyksta lydalo persiskirstymas. Mažinant gardelės periodą žemiau lazerio pluošto diametro (<1 μm), pasireiškia persidengimo efektas, kuris sumažina atitinkamai morfologijai pasiekti reikalingą energiją (Figure

3.6) ir lemia struktūrinius pokyčius per vieną morfologinę būseną – iš gumbelių į kūgius arba iš kūgių į antenas. Šis efektas siejamas su ankstesnio impulso sukeltais mechaniniais įtempiais bei vizualiai nematomomis vidinėmis dangos modifikacijomis. Taip pat nustatyta, kad nors energijos įtėkio diapazonas darinių formavimui yra ganėtinai platus, sudėtingesnės morfologijos antenos nesusidaro itin mažuose perioduose (< 0,6 μm) dėl per didelio impulsų persidengimo (Figure 3.7). Apibendrinant, fs lazeriu suformuotų metalinių nanodarinių morfologinę raidą lemia impulso energijos, dangos storio bei gardelės periodo sąveika, tad tiksli šių parametrų kontrolė leidžia pasiekti atsikartojančios ir lengvai valdomos morfologijos darinius.

Poskyris 3.1.3. *Morfologijos ir gardelės periodo poveikis plazmoninio spektrinio atsako valdymui.* Šis poskyris paremtas straipsniu [P3] bei straipsnio [P2] dalimi. Tikslus nanodarinių struktūrinių parametrų valdymas sudaro pagrindą tikslingai optinių savybių bei plazmonų rezonansų kontrolei plačiame spektre. Visų tirtų morfologijų spektruose stebimi trys pagrindiniai rezonansai: vienas s-poliarizacijoje (m = ±1 difrakcinės eilės) ties bangos ilgiu, atitinkančiu periodą, bei du p-poliarizacijoje (m = −1 ir m = +1 difrakcinių eilių). Nustatyta, kad plazmoninių gardelių spektrinis atsakas yra stipriai priklausomas nuo nanodarinių formos (Figure 3.8) – pereinant nuo gumbelių prie kūgių ir antenų, stebimas m = −1 difrakcinio rezonanso poslinkis į ilgesnių bangų sritį, kuris siejamas su neplokštuminės (angl. *out-of-plane*) modos sužadinimu (Figure 3.8c-d), stipriai priklausančios nuo struktūros aukščio. Tuo pačiu, kintant formai, vyksta ir nuoseklus visų rezonansų platėjimas, kol antenų masyvuose stebimas itin išplitęs ir susilpnėjęs rezonansas, aiškinamas padidėjusiu struktūrų nevienodumu ir dideliu darinių aukščio pasiskirstymu. Didžiausiais kokybės faktoriais (Figure 3.9) pasižymi gumbeliai, žadinantys siaurus ir gilius rezonansus (Q-faktorius apie 40, MQ-faktorius apie 15). Kadangi gardelės periodas lemia plazmoninės sąveikos stiprumą, šio parametro keitimas viena ašimi leidžia suformuoti išabliuotas 1D bei efektyvias modifikuotas kvazi-1D gardeles. Pastarosios, nors turi 2D geometrinį išdėstymą, tačiau pasižymi 1D gardelės spektriniu atsaku – stebima tik viena aukštos kokybės rezonansinė smailė (Figure 3.10), susijusi su pagrindiniu gardelės periodu. Lyginant su 2D simetrine gardele, šiuo atveju eliminuojami pašaliniai rezonansai, atsirandantys nuo difrakcijos įstrižainėje, bei taip užtikrinamas tikslus ir aukštos kokybės (Q-faktorius iki 90, MQ-faktorius iki 25) rezonansas (Figure 3.11), visiškai eliminuojant kelių smailių persidengimo tikimybę. Apibendrinant, lazeriu suformuotų nanodarinių gardelių plazmoninės savybės yra susijusios tiek su atskirų struktūrų morfologija, tiek su bendra gardelės geometrija, o keičiant šiuos

parametrus valdoma rezonansų spektrinė padėtis, jų kokybė ir išskiriamos pavienės praktiniams taikymams tinkamos smailės.

Poskyris 3.1.4. *Simetrinėse gardelėse žadinamų rezonansų kampinis valdymas ir modeliavimas*. Šis poskyris paremtas straipsniu [P4]. Nors morfologija ir periodiškumas apibrėžia gardelių vidines plazmonines savybes, tačiau jų optinis atsakas gali būti nulemtas ir žadinimo geometrijos. Dvimatėse gardelėse optinį atsaką lemia kūginė difrakcija, todėl egzistuoja keletas žadinimo kanalų aukštos simetrijos kryptimis, apimančiomis pagrindines bei įstrižaines ašis. Simetrinėse gardelėse žadinimas vyksta kritimo plokštumoje (PI), jai statmenoje plokštumoje (PP) bei dviejose įstrižinėse plokštumose (DP), o priklausomai nuo to realizuojamas 1D-tipo difrakcinis (PI ir PP atveju) arba 2D-tipo difrakcinis (DP atveju) plazmoninis žadinimas (Figure 3.12). Azimutinis bandinio sukimas keičia gardelės simetriškumo ir žadinimo kryptis ir, tuo pačiu, lemia žadinimo pobūdžio pasikeitimą iš 1D į 2D, arba atvirkščiai. Tolygiai keičiant azimutinį kampą (Figure 3.13a-d), pasiekiamas dinaminis spektrinis valdymas, pasireiškiantis rezonansinių smailių skilimu ar susiliejimu, taip pasiekiant efektyviausią sąveiką pagrindinėse gardelės ašyse. Teorinė analizė patvirtina hibridinę rezonansų prigimtį, kai s-poliarizacijos spinduliuotė sukelia simetrišką plokštuminės modos žadinimą su tolygiu EM lauko stiprinimu darinio kraštuose, o p-poliarizacija sužadina tiek neplokštuminę modą su lauko stiprinimu viršūnėje, tiek plokštumines modas, pasižyminčias asimetriškais lauko stiprinimais darinio kraštuose (Figure 3.13e). Atliekant dvigubą kampinį valdymą ir vienu metu keičiant azimutinį bei spinduliuotės kritimo kampus, įvedamos papildomos plazmoninių rezonansų derinimo galimybės dar platesniame spektre (Figure 3.14) bei padidinamas jautrumas azimutiniam poslinkiui. Vis dėlto aukščiausia rezonansų kokybė pasiekiama kai žadinimo plokštuma sutampa su didelės simetrijos gardelės kryptimis (0°, 45°, 90°). Apibendrinant, DLW metodu pagamintos simetrinės gardelės pasižymi sudėtingu, tačiau plačiame Vis-NIR ruože valdomu spektriniu atsaku, kuris gali būti koreguojamas net keliais nepriklausomais parametrais, taip užtikrinant žadinimo efektyvumą.

Poskyris 3.1.5. *Pagrindiniai skyriaus rezultatai*. Šiame skyriuje aprašytas tiesioginio lazerinio rašymo kaip didelio našumo ir vienažingsnės metodikos taikymas periodinių aukso nanodarinių gamybai. Keičiant formavimo parametrus (lazerio bangos ilgį, impulso energiją, dangos storį, gardelės periodą ir impulsų persidengimą), buvo pagaminti masyvai, žadinantys hibridinius plazmoninius rezonansus, ir išsamiai ištirtos jų formos bei plazmoninių rezonansų kontrolės galimybės. Taip pat atlikta išsami analizė, pagrindžianti simetrinėse gardelėse žadinamų rezonansų kilmę. Tai suteikia tvirtą pagrindą tolesniems tyrimams, susijusiems su praktiniu gardelių

taikymu. Remiantis šiais rezultatais, buvo suformuluoti pirmieji trys ginamieji teiginiai.

Lazeriu pagamintų plazmoninių nanodarinių gardelių funkcinės savybės

Poskyris 3.2.1. *Morfologiškai valdomos platformos SERS signalo stiprinimui*. Šis poskyris paremtas straipsniu [P5]. Užtikrinus tikslią nanodarinių ir jų žadinamų plazmoninių savybių kontrolę, šiame skyriuje pereinama prie taikomųjų plazmoninių platformų kūrimo. Paviršiumi sustiprinta Ramano spektroskopija (SERS) yra viena pagrindinių plazmoninių struktūrų panaudojimo sričių molekulių detekcijai. Skirtingos morfologijos nanodariniai buvo suformuoti ant skirtingo storio (50-200 nm) aukso dangų. Kaip išnagrinėta 3.1.2 poskyryje, dangos storinimas iki 100 nm priveda prie storesnių antenų formavimosi, tačiau šiuo atveju ištirtas papildomas storio didinimas virš 175 nm sukelia dangos sluoksniavimąsi ir pakartotinį plonų antenų formavimąsi (Figure 3.15a). Matuojant SERS atsaką, iš 4-MBA monosluosknio stebimas dviejų pagrindinių charakteringų Ramano juostų ties 1074 cm^{-1} ir 1589 cm^{-1} stiprinimas. Signalo intensyvumas stipriai priklauso nuo darinių formos – pussferių gumbelių masyvuose stebimas mažiausias stiprinimas (stiprinimo faktorius EF yra 10^5 eilės), kūgiuose EF padidėja iki 10^6 eilės, o smailose antenose pasiekiamas net $1{,}83\times10^7$ stiprinimo faktorius (Figure 3.16a-d). Atliktas masyvo skenavimas (Figure 3.16e) parodė, jog šis stiprinimas yra atsikartojantis ir pasiekiamas nuo kiekvienos periodinės struktūros. Teorinis modeliavimas patvirtino, jog lokalaus EM lauko stiprinimas antenose yra bent 2 kartus didesnis nei kūgiuose dėl kelių karštųjų taškų susidarymo smaigalio viršūnėje bei jų tarpusavio sąveikos. Skirtingo storio dangose formuojamos antenos taip pat pasižymi optimalia forma efektyviausiam žadinimui – maksimalus stiprinimas stebimas 125 nm ir 150 nm storio dangose, kur EF siekia $2{,}73\times10^7$ (Figure 3.17a-d). Artimojo lauko analizė (Figure 3.17e) parodė, jog storesnis antenos smaigalys leidžia efektyviau sužadinti kelis karštuosius taškus, o tai plonose antenose (50 nm bei 200 nm storiuose) nepasiekiama. Apibendrinant, DLW būdu pagamintos nanodarinių gardelės gali būti sėkmingai naudojamos kaip SERS platformos, kurių efektyvumą lemia darinių morfologija, o didžiausias stiprinimas šiam taikymui pasiekiamas naudojant aštrias antenas su storesniais smaigaliais.

Poskyris 3.2.2. *Bimetalinės nanogumbelių gardelės lūžio rodiklio jutikliams*. Šis poskyris paremtas straipsniu [P6]. Praeitame poskyryje nagrinėtos SERS charakteristikos atspindi pavienių nanodarinių atsaką, tuo tarpu periodiniai masyvai, pasižymintys dispersinėmis savybėmis bei siaurais spektriniais rezonansais, tinkami ir lūžio rodiklio jutimo tyrimams. Siekiant pagerinti jutiklių savybes bei atsparumą aplinkos poveikiui, buvo pritaikyta

dvisluoksnė medžiagų kombinacija ir atlikti gryno aukso (Au), gryno sidabro (Ag) bei bimetalinės Ag-Au dangos gardelių tyrimai matuojant įvairios koncentracijos glicerolio tirpalus. Nustatyta, kad visi bandiniai jautrūs aplinkos lūžio rodiklio pokyčiams (Figure 3.18), kai didinant skysčio koncentraciją stebimas rezonansų poslinkis į raudonąją spektro sritį (2-3 nm poslinkis padidėjus glicerolio koncentracijai per 1,7%). Skirtingos prigimties difrakciniai rezonansai pasižymi besiskiriančiomis dispersinėmis savybėmis, tačiau išlaiko tiesinę bangos ilgio priklausomybę nuo lūžio rodiklio, o didžiausiu 870 nm/RIU jautrumu pasižymi $m = -1$ smailė. Visų metalo konfigūracijų bandiniai pasiekia didesnį nei 800 nm/RIU jautrumą, o bimetalinė gardelė pasižymi tarpinėmis rezonansų kokybės vertėmis (prastesnėmis nei Ag, bet geresnėmis nei Au) ir yra praktiškiausia dėl apjungto stipraus plazmoninio atsako bei atsparumo oksidacijai. Ag-Au gardelėms nustatyta aptikimo riba siekia 0,0013 RIU, kas atitinka išskiriamą 1 nm poslinkį spektre. Kadangi difrakcinės kilmės rezonansai priklauso nuo spinduliuotės kritimo kampo (Figure 3.19), papildomai ištyrus šio parametro įtaką nustatyta, jog skirtingos prigimties smailėms galima padidinti jautrumą iki 933 nm/RIU, o efektyvumo rodiklį (FOM) iki 57 RIU^{-1}. Vis dėlto, skirtingoms matavimo sąlygoms reikalingas tinkamas smailių pasirinkimas: s-poliarizacijos rezonansai yra priimtinesni mažuose kampuose dėl didesnio efektyvumo rodiklio, o p-poliarizacijos neigiamos difrakcinės eilės rezonansai tampa pranašesniais ties didesniais kritimo kampais. Jutiklio rezultatų patikimumas, atkartojamumas bei platformos patvarumas buvo patvirtintas atliekant pakartotinius matavimus po pusės metų, kai jautrumo vertės ir charakteristikos išliko nepakitusios. Apibendrinant, DLW būdu suformuotos gumbelių gardelės gali būti taikomos kaip stabilūs ir jautrūs lūžio rodiklio jutikliai, demonstruojantys aukštas jautrumo vertes.

Poskyris 3.2.3. *Pagrindiniai skyriaus rezultatai.* Šiame skyriuje aprašytas DLW technologija pagamintų gardelių praktinis taikymas. Tiksliai valdant suformuotų darinių morfologiją bei medžiagų kompoziciją, pagamintas platformas galima panaudoti konkretiems taikymams – tiek SERS analizei, tiek lūžio rodiklio jutikliams, ir pasiekti aukštas jautrumo, efektyvumo bei stiprinimo faktoriaus vertes. Antenų morfologijos optimizavimas leidžia SERS stiprinimą padidinti iki 10^7 eilės, suteikiant potencialo vienmolekulinei detekcijai, o gumbelių masyvai demonstruoja patikimumą RI analizei su jautrumu, viršijančiu 850 nm/RIU. Tai parodo, jog DLW būdu pagamintos gardelės yra patikima ir lengvai pritaikoma alternatyva kompaktiškoms ir bežymenėms detekcijos platformoms. Remiantis šiais rezultatais, buvo suformuluotas paskutinis ginamasis teiginys

PAGRINDINIAI DISERTACIJOS REZULTATAI IR IŠVADOS

Šiame darbe pateikta išsami femtosekundinio tiesioginio lazerinio rašymo analizė, atskleidžianti metodo galimybes vienažingsniam ir lengvai keičiamos metodikos procesui, skirto tauriųjų metalų dangų nanoinžinerijai, siekiant suformuoti didelių plotų plazmonines gardeles. Keičiant lazerio parametrus, medžiagų konfigūracijas ir gardelių geometriją, pademonstruota tiksli hibridinių plazmonų rezonansų kontrolė, kuri gali būti efektyviai taikoma pažangiose analitinėse sistemose.

Pagrindiniai rezultatai ir išvados, pagrindžiantys ginamuosius teiginius:

- Sumažinus lazerio bangos ilgį nuo 1030 nm iki 343 nm, padidėja plonų aukso dangų sugertis, todėl sumažėja modifikacijos slenkstis (iki 0,1 J/cm^2) ir išplečiamas morfologinio valdymo energijos įtėkio diapazonas (iki 0,4 J/cm^2).
- Sumažinus lazerio bangos ilgį nuo 1030 nm iki 343 nm, sumažėja sufokusuoto pluošto skersmuo, o tai leidžia pagaminti submikroninių periodų (0,45 μm) gardeles, kurių neįmanoma pasiekti su IR spinduliuote.
- Impulso energijos didinimas keičia pavieniais fs lazerio impulsais suformuotų nanodarinių morfologiją – nuo pussferių gumbelių iki smailių antenų, o metalo dangos storinimas lemia didesnių struktūrų formavimąsi.
- Nanodarinių morfologiją galima valdyti mažinant gardelės periodą žemiau lazerio pluošto dydžio, kai pasireiškiantis persidengimo efektas sumažina sluoksnio modifikacines ribas dėl sukeltų vidinių dangos modifikacijų.
- Rezonanso padėtis spektre ir jo kokybė stipriai priklauso nuo darinių morfologijos, nes sužadinama neplokštuminė (angl. *out-of-plane*) plazmoninė moda, priklausanti nuo struktūrų aukščio.
- Gardelės, kurių periodas vienoje ašyje yra žymiai mažesnis nei kitoje, sudaro kvazi-1D masyvus, turinčius 2D geometriją, tačiau pasižyminčius 1D spektrinėmis savybėmis dėl eliminuojamo įstrižinio sužadinimo.
- Simetrinėse 2D gardelėse rezonansų spektrinė padėtis bei sąveikos efektyvumas priklauso nuo azimutinio ir kritimo kampų reguliavimo didelės simetrijos ašyse, o tai leidžia tolygiai valdyti rezonansą visame Vis-NIR diapazone.
- Iš visų DLW pagaminamų struktūrų, didžiausiu stiprinimo faktoriumi pasižymi antenos, sukuriančios karštuosius taškus viršūnėse, kurie gali būti dar sustiprinami optimizuojant metalo dangos storį (150 nm), taip pasiekiant $2{,}73\times10^7$ stiprinimo faktorių.
- Bimetalinė Ag-Au konfigūracija sujungia abiejų metalų privalumus ir sudaro platformą periodinių gumbelių pagrindu veikiantiems

plazmoniniams RI jutikliams, pasižyminčią atsparumu aplinkos poveikiui, stabilumu bei aukštu jautrumu (virš 850 nm/RIU), kuris papildomai gali būti padidintas taikant kampinį valdymą (iki 933 nm/RIU).

REFERENCES

[1] W.L. Barnes, A. Dereux, T.W. Ebbesen, Surface plasmon subwavelength optics, *Nature* 424(6950), 824-830 (2003). doi:10.1038/nature01937

[2] V. Amendola, R. Pilot, M. Frasconi, O.M. Maragò, M.A. Iatì, Surface plasmon resonance in gold nanoparticles: a review, *J. Phys.: Condens. Matter* 29(20), 203002 (2017). doi:10.1088/1361-648X/aa60f3

[3] D. Capelli, V. Scognamiglio, R. Montanari, Surface plasmon resonance technology: Recent advances, applications and experimental cases, *TrAC: Trends Anal. Chem.* 163, 117079 (2023). doi:10.1016/j.trac.2023.117079

[4] A. Agrawal, S.H. Cho, O. Zandi, S. Ghosh, R.W. Johns, D.J. Milliron, Localized Surface Plasmon Resonance in Semiconductor Nanocrystals, *Chem. Rev.* 118(6), 3121-3207 (2018). doi:10.1021/acs.chemrev.7b00613

[5] Y. Guo, Z. Xu, A.G. Curto, Y.-J. Zeng, D. Van Thourhout, Plasmonic semiconductors: materials, tunability and applications, *Prog. Mater. Sci.* 138, 101158 (2023). doi:10.1016/j.pmatsci.2023.101158

[6] Y. Li, Z. Li, C. Chi, H. Shan, L. Zheng, Z. Fang, Plasmonics of 2D Nanomaterials: Properties and Applications, *Adv. Sci.* 4(8), 1600430 (2017). doi:10.1002/advs.201600430

[7] D. Lin, Y. Duan, P. Bandaru, P. Li, M.S. Ansari, A.Y. Polyakov, J. Wilhelmsen, M.P. Jonsson, Switchable narrow nonlocal conducting polymer plasmonics, *Nat. Commun.* 16(1), 4484 (2025). doi:10.1038/s41467-025-59764-5

[8] L. Wang, M. Hasanzadeh Kafshgari, M. Meunier, Optical Properties and Applications of Plasmonic-Metal Nanoparticles, *Adv. Funct. Mater.* 30(51), 2005400 (2020). doi:10.1002/adfm.202005400

[9] P.G. Kik, M.L. Brongersma, Surface Plasmon Nanophotonics, in: M.L. Brongersma, P.G. Kik (Eds.) Surface Plasmon Nanophotonics, Springer Netherlands, Dordrecht, 2007, pp. 1-9.

[10] R.M. Kim, S.M. Lee, J.H. Han, S.H. Cho, J. Lv, S.W. Im, I.H. Ha, Y.H. Lee, D. Lim, H. Kim, N.H. Cho, H.-E. Lee, S.D. Namgung, K.T. Nam, Helicoid Grating-Coupled Surface Plasmon Resonance Sensor, *Nano Lett.* 24(49), 15668-15675 (2024). doi:10.1021/acs.nanolett.4c04212

[11] K. Yang, X. Yao, B. Liu, B. Ren, Metallic Plasmonic Array Structures: Principles, Fabrications, Properties, and Applications, *Adv. Mater.* 33(50), 2007988 (2021). doi:10.1002/adma.202007988

[12] M.S. Bin-Alam, O. Reshef, Y. Mamchur, M.Z. Alam, G. Carlow, J. Upham, B.T. Sullivan, J.-M. Ménard, M.J. Huttunen, R.W. Boyd, K. Dolgaleva, Ultra-high-Q resonances in plasmonic metasurfaces, *Nat. Commun.* 12(1), 974 (2021). doi:10.1038/s41467-021-21196-2

[13] Y. Wang, H. Ni, H. Li, J. Chen, D. Zhang, L. Fu, Plasmonic microneedle arrays for rapid extraction, SERS detection, and inactivation of bacteria, *Chem. Eng. J.* 442, 136140 (2022). doi:10.1016/j.cej.2022.136140

[14] J. Zhu, Z. Wang, S. Lin, S. Jiang, X. Liu, S. Guo, Low-cost flexible plasmonic nanobump metasurfaces for label-free sensing of serum tumor

marker, *Biosens. Bioelectron.* 150, 111905 (2020). doi:10.1016/j.bios.2019.111905
[15] X. Lv, F. Wu, Y. Tian, P. Zuo, F. Li, G. Xu, W. Niu, Engineering the Intrinsic Chirality of Plasmonic Au@Pd Metamaterials for Highly Sensitive Chiroplasmonic Hydrogen Sensing, *Adv. Mater.* 35(51), 2305429 (2023). doi:10.1002/adma.202305429
[16] D. Ge, S. Marguet, A. Issa, S. Jradi, T.H. Nguyen, M. Nahra, J. Béal, R. Deturche, H. Chen, S. Blaize, J. Plain, C. Fiorini, L. Douillard, O. Soppera, X.Q. Dinh, C. Dang, X. Yang, T. Xu, B. Wei, X.W. Sun, C. Couteau, R. Bachelot, Hybrid plasmonic nano-emitters with controlled single quantum emitter positioning on the local excitation field, *Nat. Commun.* 11(1), 3414 (2020). doi:10.1038/s41467-020-17248-8
[17] D.S. Lee, W. Kim, B.G. Cha, J. Kwon, S.J. Kim, M. Kim, J. Kim, D.H. Wang, J.H. Park, Self-Position of Au NPs in Perovskite Solar Cells: Optical and Electrical Contribution, *ACS Appl. Mater. Interfaces* 8(1), 449-454 (2016). doi:10.1021/acsami.5b09365
[18] Y. Lin, D. Wang, J. Hu, J. Liu, W. Wang, J. Guan, R.D. Schaller, T.W. Odom, Engineering Symmetry-Breaking Nanocrescent Arrays for Nanolasing, *Adv. Funct. Mater.* 29(42), 1904157 (2019). doi:10.1002/adfm.201904157
[19] M. Juodėnas, N. Khinevich, G. Klyvis, J. Henzie, T. Tamulevičius, S. Tamulevičius, Lasing in an assembled array of silver nanocubes, *Nanoscale Horiz.* 10(1), 142-149 (2025). doi:10.1039/D4NH00263F
[20] T. Wu, Y.-W. Lin, Surface-enhanced Raman scattering active gold nanoparticle/nanohole arrays fabricated through electron beam lithography, *Appl. Surf. Sci.* 435, 1143-1149 (2018). doi:10.1016/j.apsusc.2017.11.213
[21] V. Suresh, L. Ding, A.B. Chew, F.L. Yap, Fabrication of Large-Area Flexible SERS Substrates by Nanoimprint Lithography, *ACS Appl. Nano Mater.* 1(2), 886-893 (2018). doi:10.1021/acsanm.7b00295
[22] E. Stankevičius, K. Vilkevičius, M. Gedvilas, E. Bužavaitė-Vertelienė, A. Selskis, Z. Balevičius, Direct Laser Writing for the Formation of Large-Scale Gold Microbumps Arrays Generating Hybrid Lattice Plasmon Polaritons in Vis–NIR Range, *Adv. Opt. Mater.* 9(12), 2100027 (2021). doi:10.1002/adom.202100027
[23] T. Pinheiro, M. Morais, S. Silvestre, E. Carlos, J. Coelho, H.V. Almeida, P. Barquinha, E. Fortunato, R. Martins, Direct Laser Writing: From Materials Synthesis and Conversion to Electronic Device Processing, *Adv. Mater.* 36(26), 2402014 (2024). doi:10.1002/adma.202402014
[24] Y. Zhang, D. Wu, Y. Zhang, Y. Bian, C. Wang, J. Li, J. Chu, Y. Hu, Femtosecond laser direct writing of functional stimulus-responsive structures and applications, *Int. J. Extreme Manuf.* 5(4), 042012 (2023). doi:10.1088/2631-7990/acf798
[25] H. Zhu, B. Wu, M. Gao, F. Ren, W. Qin, S. Juodkazis, F. Chen, Femtosecond Laser Direct-Write Plasmonic Nanolithography in Dielectrics, *Small Sci.* 2(9), 2200038 (2022). doi:10.1002/smsc.202200038

[26] D. Pavlov, A. Zhizhchenko, L. Pan, A.A. Kuchmizhak, Tuning Collective Plasmon Resonances of Femtosecond Laser-Printed Metasurface, *Materials* 15(5), 1834 (2022). doi:10.3390/ma15051834
[27] S. Mu, H. Chen, C. Shi, J. Zhang, B. Yang, Au nanoring arrays with tunable morphological features and plasmonic resonances, *Nano Res.* 14(12), 4674-4679 (2021). doi:10.1007/s12274-021-3402-3
[28] M.A. Garcia, Surface plasmons in metallic nanoparticles: fundamentals and applications, *J. Phys. D: Appl. Phys.* 44(28), 283001 (2011). doi:10.1088/0022-3727/44/28/283001
[29] S. Maier, Plasmonics: Fundamentals and Applications, 2007.
[30] L.T.M. Huynh, S. Kim, S. Yoon, Effect of Material and Shape of Nanoparticles on Hot Carrier Generation, *ACS Photonics* 9(10), 3260-3267 (2022). doi:10.1021/acsphotonics.2c00530
[31] S.V. Boriskina, T.A. Cooper, L. Zeng, G. Ni, J.K. Tong, Y. Tsurimaki, Y. Huang, L. Meroueh, G. Mahan, G. Chen, Losses in plasmonics: from mitigating energy dissipation to embracing loss-enabled functionalities, *Adv. Opt. Photon.* 9(4), 775-827 (2017). doi:10.1364/AOP.9.000775
[32] P.R. West, S. Ishii, G.V. Naik, N.K. Emani, V.M. Shalaev, A. Boltasseva, Searching for better plasmonic materials, *Laser Photonics Rev.* 4(6), 795-808 (2010). doi:10.1002/lpor.200900055
[33] W.A. Murray, W.L. Barnes, Plasmonic Materials, *Adv. Mater.* 19(22), 3771-3782 (2007). doi:10.1002/adma.200700678
[34] R. Ameling, H. Giessen, Microcavity plasmonics: strong coupling of photonic cavities and plasmons, *Laser Photonics Rev.* 7(2), 141-169 (2013). doi:10.1002/lpor.201100041
[35] A.P. Vinogradov, A.V. Dorofeenko, A.A. Pukhov, A.A. Lisyansky, Exciting surface plasmon polaritons in the Kretschmann configuration by a light beam, *Phys. Rev. B* 97(23), 235407 (2018). doi:10.1103/PhysRevB.97.235407
[36] V.Z. Anatoly, I.S. Igor, Near-field photonics: surface plasmon polaritons and localized surface plasmons, *J. Opt. A-Pure Appl. Opt.* 5(4), S16 (2003). doi:10.1088/1464-4258/5/4/353
[37] S. Maegawa, J. Yamaguchi, F. Itoigawa, T. Nakamura, Discussion on Surface Plasmon Resonance Technique in the Otto Configuration for Measurement of Lubricant Film Thickness, *Tribol. Lett.* 62(2), 14 (2016). doi:10.1007/s11249-016-0659-x
[38] D. Murugan, M. Tintelott, M.S. Narayanan, X.-T. Vu, T. Kurkina, C. Rodriguez-Emmenegger, U. Schwaneberg, J. Dostalek, S. Ingebrandt, V. Pachauri, Recent Advances in Grating Coupled Surface Plasmon Resonance Technology, *Adv. Opt. Mater.* 12(34), 2401862 (2024). doi:10.1002/adom.202401862
[39] W. Liu, G. Wang, K. Wen, X. Hu, Y. Qin, Efficient unidirectional SPP launcher: coupling the SPP to a smooth surface for propagation, *Opt. Lett.* 47(3), 621-624 (2022). doi:10.1364/OL.447489

[40] H. Raether, Surface plasmons on gratings, in: H. Raether (Ed.) Surface Plasmons on Smooth and Rough Surfaces and on Gratings, Springer Berlin Heidelberg, Berlin, Heidelberg, 1988, pp. 91-116.
[41] M. Seo, J. Lee, M. Lee, Grating-coupled surface plasmon resonance on bulk stainless steel, *Opt. Express* 25(22), 26939-26949 (2017). doi:10.1364/OE.25.026939
[42] H. Kano, S. Mizuguchi, S. Kawata, Excitation of surface-plasmon polaritons by a focused laser beam, *J. Opt. Soc. Am. B* 15(4), 1381-1386 (1998). doi:10.1364/JOSAB.15.001381
[43] F. Walla, M.M. Wiecha, N. Mecklenbeck, S. Beldi, F. Keilmann, M.D. Thomson, H.G. Roskos, Anisotropic excitation of surface plasmon polaritons on a metal film by a scattering-type scanning near-field microscope with a non-rotationally-symmetric probe tip, *Nanophotonics* 7(1), 269-276 (2018). doi:10.1515/nanoph-2017-0042
[44] N.J. Halas, S. Lal, W.-S. Chang, S. Link, P. Nordlander, Plasmons in Strongly Coupled Metallic Nanostructures, *Chem. Rev.* 111(6), 3913-3961 (2011). doi:10.1021/cr200061k
[45] V.G. Kravets, A.V. Kabashin, W.L. Barnes, A.N. Grigorenko, Plasmonic Surface Lattice Resonances: A Review of Properties and Applications, *Chem. Rev.* 118(12), 5912-5951 (2018). doi:10.1021/acs.chemrev.8b00243
[46] B. Auguié, W.L. Barnes, Collective Resonances in Gold Nanoparticle Arrays, *Phys. Rev. Lett.* 101(14), 143902 (2008). doi:10.1103/PhysRevLett.101.143902
[47] C. Cherqui, M.R. Bourgeois, D. Wang, G.C. Schatz, Plasmonic Surface Lattice Resonances: Theory and Computation, *Acc. Chem. Res.* 52(9), 2548-2558 (2019). doi:10.1021/acs.accounts.9b00312
[48] A.D. Utyushev, V.I. Zakomirnyi, I.L. Rasskazov, Collective lattice resonances: Plasmonics and beyond, *Rev. Phys.* 6, 100051 (2021). doi:10.1016/j.revip.2021.100051
[49] F. Liu, X. Guo, Y. Chen, H. Jia, R. Ren, X. Zhang, M. Huang, Excitation of high-Q out-of-plane lattice resonance at normal incidence and applications in sensor, *Opt. Express* 33(20), 43015-43025 (2025). doi:10.1364/OE.574524
[50] A. Danilov, G. Tselikov, F. Wu, V.G. Kravets, I. Ozerov, F. Bedu, A.N. Grigorenko, A.V. Kabashin, Ultra-narrow surface lattice resonances in plasmonic metamaterial arrays for biosensing applications, *Biosens. Bioelectron.* 104, 102-112 (2018). doi:10.1016/j.bios.2017.12.001
[51] G. Li, X. Du, L. Xiong, X. Yang, Plasmonic Metasurfaces with Quality Factors Up to 790 in the Visible Regime, *Adv. Opt. Mater.* 11(20), 2301205 (2023). doi:10.1002/adom.202301205
[52] M. Sarkar, M. Besbes, J. Moreau, J.-F. Bryche, A. Olivéro, G. Barbillon, A.-L. Coutrot, B. Bartenlian, M. Canva, Hybrid Plasmonic Mode by Resonant Coupling of Localized Plasmons to Propagating Plasmons in a Kretschmann Configuration, *ACS Photonics* 2(2), 237-245 (2015). doi:10.1021/ph500351b
[53] R. Liudvinavičius, K. Vilkevičius, E. Stankevičius, High-quality grating-coupled surface plasmon resonances in silver and gold bumps arrays

fabricated in thin metallic films using the third harmonic of femtosecond laser, *Appl. Surf. Sci.* 711, 164127 (2025). doi:10.1016/j.apsusc.2025.164127
[54] M. Seo, M. Lee, Surface plasmon resonance and coloration in stainless steel with a 2D periodic texture, *Appl. Phys. A* 125(9), 624 (2019). doi:10.1007/s00339-019-2926-9
[55] S. Kasani, K. Curtin, N. Wu, A review of 2D and 3D plasmonic nanostructure array patterns: fabrication, light management and sensing applications, *Nanophotonics* 8(12), 2065-2089 (2019). doi:10.1515/nanoph-2019-0158
[56] R. Borah, S.W. Verbruggen, Effect of size distribution, skewness and roughness on the optical properties of colloidal plasmonic nanoparticles, *Colloid Surf. A: Physicochem. Eng. Asp.* 640, 128521 (2022). doi:10.1016/j.colsurfa.2022.128521
[57] D. Peckus, A. Tamulevičienė, K. Mougin, A. Spangenberg, L. Vidal, Q. Bauerlin, M. Keller, J. Henzie, L. Puodžiukynas, T. Tamulevičius, S. Tamulevičius, Shape influence on the ultrafast plasmonic properties of gold nanoparticles, *Opt. Express* 30(15), 27730-27745 (2022). doi:10.1364/OE.463961
[58] J. Zheng, X. Cheng, H. Zhang, X. Bai, R. Ai, L. Shao, J. Wang, Gold Nanorods: The Most Versatile Plasmonic Nanoparticles, *Chem. Rev.* 121(21), 13342-13453 (2021). doi:10.1021/acs.chemrev.1c00422
[59] S. Stangherlin, N. Cathcart, F. Sato, V. Kitaev, Gold Nanoprisms: Synthetic Approaches for Mastering Plasmonic Properties and Implications for Biomedical Applications, *ACS Appl. Nano Mater.* 3(8), 8304-8318 (2020). doi:10.1021/acsanm.0c01741
[60] J. Barrio, R. Manzorro, A. Sánchez-Iglesias, D. Rodríguez-San-Miguel, M. Coronado-Puchau, C. Moreno, J. Langer, A.I. Fernández-Domínguez, S. Trasobares, L.M. Liz-Marzán, F. Zamora, B.H. Juárez, Influence of the Gap Distance and Morphology on the Plasmon Modes of Gold Nanocube Dimers, *Adv. Opt. Mater.* 13(15), 2500042 (2025). doi:10.1002/adom.202500042
[61] H. Wei, H. Xu, Plasmonics in composite nanostructures, *Mater. Today* 17(8), 372-380 (2014). doi:10.1016/j.mattod.2014.05.012
[62] M.G. Blaber, M.D. Arnold, M.J. Ford, A review of the optical properties of alloys and intermetallics for plasmonics, *J. Phys.: Condens. Matter* 22(14), 143201 (2010). doi:10.1088/0953-8984/22/14/143201
[63] S. Kadkhodazadeh, F.A.A. Nugroho, C. Langhammer, M. Beleggia, J.B. Wagner, Optical Property–Composition Correlation in Noble Metal Alloy Nanoparticles Studied with EELS, *ACS Photonics* 6(3), 779-786 (2019). doi:10.1021/acsphotonics.8b01791
[64] M.B. Cortie, A.M. McDonagh, Synthesis and Optical Properties of Hybrid and Alloy Plasmonic Nanoparticles, *Chem. Rev.* 111(6), 3713-3735 (2011). doi:10.1021/cr1002529
[65] L. Mikoliunaite, E. Stankevičius, S. Adomavičiūtė-Grabusovė, V. Petrikaitė, R. Trusovas, M. Talaikis, M. Skapas, A. Zdaniauskienė, A. Selskis, V. Šablinskas, G. Niaura, Magneto-Plasmonic Nanoparticles Generated by

Laser Ablation of Layered Fe/Au and Fe/Au/Fe Composite Films for SERS Application, *Coatings* 13(9), 1523 (2023). doi:10.3390/coatings13091523
[66] B.D. Dana, J. Boyu, J. Lin, L. Li, A.N. Koya, W. Li, Hybrid Plasmonic Modes for Enhanced Refractive Index Sensing, *Adv. Sens. Res.* 2(12), 2300066 (2023). doi:10.1002/adsr.202300066
[67] J.J. Alvarez-Serrano, J.R. Deop-Ruano, V. Aglieri, A. Toma, A. Manjavacas, Normal Incidence Excitation of Out-of-Plane Lattice Resonances in Bipartite Arrays of Metallic Nanostructures, *ACS Photonics* 11(1), 301-309 (2024). doi:10.1021/acsphotonics.3c01535
[68] S. Yan, H. Ma, Y.-F. Bao, M. Cao, C. Liu, K. Zhang, X. Wu, J. He, X. Wang, B. Ren, Optical responses of metallic plasmonic arrays under the localized excitation, *Nano Res.* 17(3), 1571-1577 (2024). doi:10.1007/s12274-023-5927-0
[69] D. Wang, A. Yang, A.J. Hryn, G.C. Schatz, T.W. Odom, Superlattice Plasmons in Hierarchical Au Nanoparticle Arrays, *ACS Photonics* 2(12), 1789-1794 (2015). doi:10.1021/acsphotonics.5b00546
[70] M.E. Stewart, C.R. Anderton, L.B. Thompson, J. Maria, S.K. Gray, J.A. Rogers, R.G. Nuzzo, Nanostructured Plasmonic Sensors, *Chem. Rev.* 108(2), 494-521 (2008). doi:10.1021/cr068126n
[71] S. Fruncillo, X. Su, H. Liu, L.S. Wong, Lithographic Processes for the Scalable Fabrication of Micro- and Nanostructures for Biochips and Biosensors, *ACS Sens.* 6(6), 2002-2024 (2021). doi:10.1021/acssensors.0c02704
[72] D. Baek, S.H. Lee, B.H. Jun, S.H. Lee, Lithography Technology for Micro- and Nanofabrication, *Adv. Exp. Med. Biol.* 1309, 217-233 (2021). doi:10.1007/978-981-33-6158-4_9
[73] H. Duan, H. Hu, K. Kumar, Z. Shen, J.K.W. Yang, Direct and Reliable Patterning of Plasmonic Nanostructures with Sub-10-nm Gaps, *ACS Nano* 5(9), 7593-7600 (2011). doi:10.1021/nn2025868
[74] V.R. Manfrinato, L. Zhang, D. Su, H. Duan, R.G. Hobbs, E.A. Stach, K.K. Berggren, Resolution Limits of Electron-Beam Lithography toward the Atomic Scale, *Nano Lett.* 13(4), 1555-1558 (2013). doi:10.1021/nl304715p
[75] S. Zhu, H.-H. Cheng, I. Blakey, N. Stokes, K. Ostrikov, M. Cortie, Plasmonic ‘top-hat’ nano-star arrays by electron beam lithography, *Microelectron. Eng.* 139, 13-18 (2015). doi:10.1016/j.mee.2015.04.084
[76] L. Petti, R. Capasso, M. Rippa, M. Pannico, P. La Manna, G. Peluso, A. Calarco, E. Bobeico, P. Musto, A plasmonic nanostructure fabricated by electron beam lithography as a sensitive and highly homogeneous SERS substrate for bio-sensing applications, *Vib. Spectrosc.* 82, 22-30 (2016). doi:10.1016/j.vibspec.2015.11.007
[77] Y. Zhou, Z. Guo, X. Zhao, F. Wang, Z. Yu, Y. Chen, Z. Liu, S. Zhang, S. Sun, X. Wu, Dual-Quasi Bound States in the Continuum Enabled Plasmonic Metasurfaces, *Adv. Opt. Mater.* 10(19), 2200965 (2022). doi:10.1002/adom.202200965

[78] G. Yoon, I. Kim, S. So, J. Mun, M. Kim, J. Rho, Fabrication of three-dimensional suspended, interlayered and hierarchical nanostructures by accuracy-improved electron beam lithography overlay, *Sci. Rep.* 7(1), 6668 (2017). doi:10.1038/s41598-017-06833-5
[79] C. Hahn, A. Hajebifard, P. Berini, Helium focused ion beam direct milling of plasmonic heptamer-arranged nanohole arrays, *Nanophotonics* 9(2), 393-399 (2020). doi:10.1515/nanoph-2019-0385
[80] M.L. Tseng, Z.-H. Lin, H.Y. Kuo, T.-T. Huang, Y.-T. Huang, T.L. Chung, C.H. Chu, J.-S. Huang, D.P. Tsai, Stress-Induced 3D Chiral Fractal Metasurface for Enhanced and Stabilized Broadband Near-Field Optical Chirality, *Adv. Opt. Mater.* 7(15), 1900617 (2019). doi:10.1002/adom.201900617
[81] Y. Chen, K. Bi, Q. Wang, M. Zheng, Q. Liu, Y. Han, J. Yang, S. Chang, G. Zhang, H. Duan, Rapid Focused Ion Beam Milling Based Fabrication of Plasmonic Nanoparticles and Assemblies via "Sketch and Peel" Strategy, *ACS Nano* 10(12), 11228-11236 (2016). doi:10.1021/acsnano.6b06290
[82] Q. Liu, Y. Song, P. Zeng, C. Zhang, Y. Chen, H. Wang, Y. Luo, H. Duan, High-fidelity fabrication of plasmonic nanoholes array via ion-beam planarization for extraordinary transmission applications, *Appl. Surf. Sci.* 526, 146690 (2020). doi:10.1016/j.apsusc.2020.146690
[83] B.D. Gates, Q. Xu, M. Stewart, D. Ryan, C.G. Willson, G.M. Whitesides, New Approaches to Nanofabrication: Molding, Printing, and Other Techniques, *Chem. Rev.* 105(4), 1171-1196 (2005). doi:10.1021/cr030076o
[84] W. Che, J. Wu, M. Cheng, L. Xu, J. Fang, Polymer-nanoimprinting route for the construction of large-area Au@Ag plasmonic arrays using as highly-uniform SERS platforms, *Opt. Mater.* 121, 111532 (2021). doi:10.1016/j.optmat.2021.111532
[85] D.K. Oh, T. Lee, B. Ko, T. Badloe, J.G. Ok, J. Rho, Nanoimprint lithography for high-throughput fabrication of metasurfaces, *Front. Optoelectron.* 14(2), 229-251 (2021). doi:10.1007/s12200-021-1121-8
[86] M. Juodėnas, T. Tamulevičius, J. Henzie, D. Erts, S. Tamulevičius, Surface Lattice Resonances in Self-Assembled Arrays of Monodisperse Ag Cuboctahedra, *ACS Nano* 13(8), 9038-9047 (2019). doi:10.1021/acsnano.9b03191
[87] M. Juodėnas, D. Peckus, T. Tamulevičius, Y. Yamauchi, S. Tamulevičius, J. Henzie, Effect of Ag Nanocube Optomechanical Modes on Plasmonic Surface Lattice Resonances, *ACS Photonics* 7(11), 3130-3140 (2020). doi:10.1021/acsphotonics.0c01187
[88] Z. Lin, L.V. Zhigilei, V. Celli, Electron-phonon coupling and electron heat capacity of metals under conditions of strong electron-phonon nonequilibrium, *Phys. Rev. B* 77(7), 075133 (2008). doi:10.1103/PhysRevB.77.075133
[89] Z. Ur Rehman, F. Yang, M. Wang, T. Zhu, Fundamentals and Advances in Laser-Induced Transfer, *Opt. Laser Technol.* 160, 109065 (2023). doi:10.1016/j.optlastec.2022.109065

[90] P. Serra, A. Piqué, Laser-Induced Forward Transfer: Fundamentals and Applications, *Adv. Mater. Technol.* 4(1), 1800099 (2019). doi:10.1002/admt.201800099
[91] Y. Zhou, G. Luo, Y. Hu, D. Wu, C. Hu, M. Qu, Femtosecond laser printing patterned nanoparticles on flexible substrate by tuning plasmon resonances via polarization modulation, *Int. J. Mach. Tools Manuf.* 189, 104040 (2023). doi:10.1016/j.ijmachtools.2023.104040
[92] P. Gregorčič, M. Sedlaček, B. Podgornik, J. Reif, Formation of laser-induced periodic surface structures (LIPSS) on tool steel by multiple picosecond laser pulses of different polarizations, *Appl. Surf. Sci.* 387, 698-706 (2016). doi:10.1016/j.apsusc.2016.06.174
[93] H. Sun, J. Li, M. Liu, D. Yang, F. Li, A Review of Effects of Femtosecond Laser Parameters on Metal Surface Properties, *Coatings* 12(10), 1596 (2022). doi:10.3390/coatings12101596
[94] E. Skliutas, M. Lebedevaite, E. Kabouraki, T. Baldacchini, J. Ostrauskaite, M. Vamvakaki, M. Farsari, S. Juodkazis, M. Malinauskas, Polymerization mechanisms initiated by spatio-temporally confined light, *Nanophotonics* 10(4), 1211-1242 (2021). doi:10.1515/nanoph-2020-0551
[95] E. Sedghamiz, M. Liu, W. Wenzel, Challenges and limits of mechanical stability in 3D direct laser writing, *Nat. Commun.* 13(1), 2115 (2022). doi:10.1038/s41467-022-29749-9
[96] Y. Nakata, T. Okada, M. Maeda, Nano-Sized Hollow Bump Array Generated by Single Femtosecond Laser Pulse, *Jpn. J. Appl. Phys.* 42(Part 2, No. 12A), L1452-L1454 (2003). doi:10.1143/jjap.42.l1452
[97] Y. Nakata, N. Miyanaga, T. Okada, Effect of pulse width and fluence of femtosecond laser on the size of nanobump array, *Appl. Surf. Sci.* 253(15), 6555-6557 (2007). doi:10.1016/j.apsusc.2007.01.080
[98] F. Korte, J. Koch, B.N. Chichkov, Formation of microbumps and nanojets on gold targets by femtosecond laser pulses, *Appl. Phys. A* 79(4), 879-881 (2004). doi:10.1007/s00339-004-2590-5
[99] Y.P. Meshcheryakov, N.M. Bulgakova, Thermoelastic modeling of microbump and nanojet formation on nanosize gold films under femtosecond laser irradiation, *Appl. Phys. A* 82(2), 363-368 (2006). doi:10.1007/s00339-005-3319-9
[100] D. Pavlov, S. Syubaev, A. Kuchmizhak, S. Gurbatov, O. Vitrik, E. Modin, S. Kudryashov, X. Wang, S. Juodkazis, M. Lapine, Direct laser printing of tunable IR resonant nanoantenna arrays, *Appl. Surf. Sci.* 469, 514-520 (2019). doi:10.1016/j.apsusc.2018.11.069
[101] A.I. Kuznetsov, C. Unger, J. Koch, B.N. Chichkov, Laser-induced jet formation and droplet ejection from thin metal films, *Appl. Phys. A* 106(3), 479-487 (2012). doi:10.1007/s00339-011-6747-8
[102] A.I. Pérez-Jiménez, D. Lyu, Z. Lu, G. Liu, B. Ren, Surface-enhanced Raman spectroscopy: benefits, trade-offs and future developments, *Chem. Sci.* 11(18), 4563-4577 (2020). doi:10.1039/D0SC00809E

[103] J.-M. Nam, J.-W. Oh, H. Lee, Y.D. Suh, Plasmonic Nanogap-Enhanced Raman Scattering with Nanoparticles, *Acc. Chem. Res.* 49(12), 2746-2755 (2016). doi:10.1021/acs.accounts.6b00409
[104] N. Khinevich, M. Juodėnas, A. Tamulevičienė, T. Tamulevičius, M. Talaikis, G. Niaura, S. Tamulevičius, Wavelength-tailored enhancement of Raman scattering on a resonant plasmonic lattice, *Sens. Actuators, B* 394, 134418 (2023). doi:10.1016/j.snb.2023.134418
[105] L. Long, W. Ju, H.-Y. Yang, Z. Li, Dimensional Design for Surface-Enhanced Raman Spectroscopy, *ACS Mater. Au* 2(5), 552-575 (2022). doi:10.1021/acsmaterialsau.2c00005
[106] S. Seçkin, P. Singh, A. Jaiswal, T.A.F. König, Super-Radiant SERS Enhancement by Plasmonic Particle Gratings, *ACS Appl. Mater. Interfaces* 15(36), 43124-43134 (2023). doi:10.1021/acsami.3c07532
[107] Q. Zhao, H. Hilal, J. Kim, W. Park, M. Haddadnezhad, J. Lee, W. Park, J.-W. Lee, S. Lee, I. Jung, S. Park, All-Hot-Spot Bulk Surface-Enhanced Raman Scattering (SERS) Substrates: Attomolar Detection of Adsorbates with Designer Plasmonic Nanoparticles, *J. Am. Chem. Soc.* 144(29), 13285-13293 (2022). doi:10.1021/jacs.2c04514
[108] M.S.S. Bharati, V.R. Soma, Flexible SERS substrates for hazardous materials detection: recent advances, *Opto-Electronic Advances* 4(11), 210048 (2021). doi:10.29026/oea.2021.210048
[109] J. Choi, J.-H. Kim, J.-W. Oh, J.-M. Nam, Surface-enhanced Raman scattering-based detection of hazardous chemicals in various phases and matrices with plasmonic nanostructures, *Nanoscale* 11(43), 20379-20391 (2019). doi:10.1039/C9NR07439B
[110] X. Zhao, X. Liu, D. Chen, G. Shi, G. Li, X. Tang, X. Zhu, M. Li, L. Yao, Y. Wei, W. Song, Z. Sun, X. Fan, Z. Zhou, T. Qiu, Q. Hao, Plasmonic trimers designed as SERS-active chemical traps for subtyping of lung tumors, *Nat. Commun.* 15(1), 5855 (2024). doi:10.1038/s41467-024-50321-0
[111] W.H. Kim, J.U. Lee, S. Song, S. Kim, Y.J. Choi, S.J. Sim, A label-free, ultra-highly sensitive and multiplexed SERS nanoplasmonic biosensor for miRNA detection using a head-flocked gold nanopillar, *Analyst* 144(5), 1768-1776 (2019). doi:10.1039/C8AN01745J
[112] B. Liu, S. Chen, J. Zhang, X. Yao, J. Zhong, H. Lin, T. Huang, Z. Yang, J. Zhu, S. Liu, C. Lienau, L. Wang, B. Ren, A Plasmonic Sensor Array with Ultrahigh Figures of Merit and Resonance Linewidths down to 3 nm, *Adv. Mater.* 30(12), 1706031 (2018). doi:10.1002/adma.201706031
[113] X. Wen, S. Deng, Plasmonic Nanostructure Lattices for High-Performance Sensing, *Adv. Opt. Mater.* 11(16), 2300401 (2023). doi:10.1002/adom.202300401
[114] M. Soler, A. Belushkin, A. Cavallini, C. Kebbi-Beghdadi, G. Greub, H. Altug, Multiplexed nanoplasmonic biosensor for one-step simultaneous detection of Chlamydia trachomatis and Neisseria gonorrhoeae in urine, *Biosens. Bioelectron.* 94, 560-567 (2017). doi:10.1016/j.bios.2017.03.047

[115] G. Borile, S. Rossi, A. Filippi, E. Gazzola, P. Capaldo, C. Tregnago, M. Pigazzi, F. Romanato, Label-free, real-time on-chip sensing of living cells via grating-coupled surface plasmon resonance, *Biophysical Chemistry* 254, 106262 (2019). doi:10.1016/j.bpc.2019.106262
[116] X.-Y. Wang, Y.-L. Wang, S. Wang, B. Li, X.-W. Zhang, L. Dai, R.-M. Ma, Lasing Enhanced Surface Plasmon Resonance Sensing, *Nanophotonics* 6(2), 472-478 (2017). doi:10.1515/nanoph-2016-0006
[117] Z. Zhang, L. Nest, S. Wang, S.-Y. Wang, R.-M. Ma, Lasing-enhanced surface plasmon resonance spectroscopy and sensing, *Photonics Research* 9(9), 1699-1714 (2021). doi:10.1364/PRJ.431612
[118] C. Gautam, S. Yadav, A. Kumar, M. Pal, A.K. Ghosh, A. Giri, Plasmonic Grating on Monolayer MoS2 for Strong Photoluminescence Enhancement and Ultrasensitive Surface-Enhanced Raman Scattering (SERS) Detection, *Nano Lett.* 25(49), 17152-17159 (2025). doi:10.1021/acs.nanolett.5c04726
[119] B.-Y. Wen, J.-Y. Wang, T.-L. Shen, Z.-W. Zhu, P.-C. Guan, J.-S. Lin, W. Peng, W.-W. Cai, H. Jin, Q.-C. Xu, Z.-L. Yang, Z.-Q. Tian, J.-F. Li, Manipulating the light-matter interactions in plasmonic nanocavities at 1 nm spatial resolution, *Light Sci. Appl.* 11(1), 235 (2022). doi:10.1038/s41377-022-00918-1
[120] L. Liu, L.Y.M. Tobing, X. Yu, J. Tong, B. Qiang, A.I. Fernández-Domínguez, F.J. Garcia-Vidal, D.H. Zhang, Q.J. Wang, Y. Luo, Strong Plasmon–Exciton Interactions on Nanoantenna Array–Monolayer WS2 Hybrid System, *Adv. Opt. Mater.* 8(5), 1901002 (2020). doi:10.1002/adom.201901002
[121] A.A. Sergeev, D.V. Pavlov, A.A. Kuchmizhak, M.V. Lapine, W.K. Yiu, Y. Dong, N. Ke, S. Juodkazis, N. Zhao, S.V. Kershaw, A.L. Rogach, Tailoring spontaneous infrared emission of HgTe quantum dots with laser-printed plasmonic arrays, *Light Sci. Appl.* 9(1), 16 (2020). doi:10.1038/s41377-020-0247-6
[122] J. Shi, W.-Y. Liang, S.S. Raja, Y. Sang, X.-Q. Zhang, C.-A. Chen, Y. Wang, X. Yang, Y.-H. Lee, H. Ahn, S. Gwo, Plasmonic Enhancement and Manipulation of Optical Nonlinearity in Monolayer Tungsten Disulfide, *Laser Photonics Rev.* 12(10), 1800188 (2018). doi:10.1002/lpor.201800188
[123] S. Beer, J. Gour, A. Alberucci, C. David, S. Nolte, U.D. Zeitner, Second harmonic generation under doubly resonant lattice plasmon excitation, *Opt. Express* 30(22), 40884-40896 (2022). doi:10.1364/OE.470578
[124] Y. Nishijima, A. Balčytis, S. Naganuma, G. Seniutinas, S. Juodkazis, Tailoring Metal and Insulator Contributions in Plasmonic Perfect Absorber Metasurfaces, *ACS Appl. Nano Mater.* 1(7), 3557-3564 (2018). doi:10.1021/acsanm.8b00710
[125] Y. Qu, Q. Li, H. Gong, K. Du, S. Bai, D. Zhao, H. Ye, M. Qiu, Spatially and Spectrally Resolved Narrowband Optical Absorber Based on 2D Grating Nanostructures on Metallic Films, *Adv. Opt. Mater.* 4(3), 480-486 (2016). doi:10.1002/adom.201500651

[126] A. Nagarajan, K. Vivek, M. Shah, V.G. Achanta, G. Gerini, A Broadband Plasmonic Metasurface Superabsorber at Optical Frequencies: Analytical Design Framework and Demonstration, *Adv. Opt. Mater.* 6(16), 1800253 (2018). doi:10.1002/adom.201800253
[127] P.B. Johnson, R.W. Christy, Optical Constants of the Noble Metals, *Phys. Rev. B* 6(12), 4370-4379 (1972). doi:10.1103/PhysRevB.6.4370
[128] S. Kedenburg, M. Vieweg, T. Gissibl, H. Giessen, Linear refractive index and absorption measurements of nonlinear optical liquids in the visible and near-infrared spectral region, *Opt. Mater. Express* 2(11), 1588-1611 (2012). doi:10.1364/OME.2.001588
[129] D. Jakubczyk, G. Derkachov, K. Nyandey, S. Alikhanzadeh-Arani, A. Derkachova, Chromatic dispersion and thermal coefficients of hygroscopic liquids: 5 glycols and glycerol, *Sci. Data* 10(1), 894 (2023). doi:10.1038/s41597-023-02819-3
[130] D. Wortmann, J. Koch, M. Reininghaus, C. Unger, C. Hulverscheidt, D. Ivanov, B.N. Chichkov, Experimental and theoretical investigation on fs-laser-induced nanostructure formation on thin gold films, *J. Laser Appl.* 24(4), 042017 (2012). doi:10.2351/1.4734048
[131] M. Reininghaus, D. Wortmann, Z. Cao, J.M. Hoffmann, T. Taubner, Fabrication and spectral tuning of standing gold infrared antennas using single fs-laser pulses, *Opt. Express* 21(26), 32176-32183 (2013). doi:10.1364/OE.21.032176
[132] Y. Yuan, W. Wang, D. Li, T. Zhao, W. Han, Controllable Large-Area Fabrication of Illumination Angle-Sensitive Metasurfaces Using Femtosecond Laser, *Plasmonics* 20(9), 7001-7010 (2025). doi:10.1007/s11468-024-02636-3
[133] A.A. Kuchmizhak, D.V. Pavlov, O.B. Vitrik, Y.N. Kulchin, Laser ablative fabrication of nanocrowns and nanojets on the Cu supported film surface using femtosecond laser pulses, *Appl. Surf. Sci.* 357, 2378-2384 (2015). doi:10.1016/j.apsusc.2015.09.255

Declaration on the use of generative AI and AI-assisted technologies in the writing process

During the preparation of this thesis, the author used AI tools (Grammarly Pro, DeepL, ChatGPT (OpenAI)) to assist with language editing and improve the clarity and readability of the text. After using the tools, the author revised and edited the content as needed and takes full responsibility for the published information.

PADĖKA

Nuoširdžiai dėkoju savo darbo vadovui dr. Evaldui Stankevičiui, kuris man dar būnant bakalauru priėmė į laboratoriją, supažindino su plazmonikos sritimi bei užkabino tęsti tyrimus magistrantūros ir doktorantūros metu. Esu dėkingas už skirtą laiką, patarimus ir pagalbą, pasitikėjimą bei suteiktą laisvę augti kaip tyrėjui.

Dėkoju laboratorijos kolegoms Vitai, Rodrigui, Justinai, Dariui, Ernestai, ir Zigmui už pagalbą tyrimuose bei darbuose, plazmonines diskusijas, patarimus aiškinantis studijų vingrybes, gerą kompaniją ir smagią kasdienybę laboratorijoje. Taip pat padėka keliauja kolegoms Andriui ir Mindaugui už efektyvų arimą Kretoje bei gerą nuotaiką „belangėje kamūrkėje“. Ačiū visiems lazerinių technologijų skyriaus darbuotojams: Miglei, Laimiui, Modestui, Arnui, Julianijai, Šarūnui, Juozui, Valdemarui, Edgarui, Simui, Romualdui, Karoliui, Pauliui ir Gediminui už fainą darbo aplinką bei pokalbius virtuvėlėje, taip atidėliojant disertacijos rašymą. Paminėjimo verta padėka keliauja Deimantei, Dovilei bei Guodai už doktorantūros pasiekimų, pasigyrimų ir nuoskaudų išsiliejimo chat‘ą bei vienas kito palaikymą savuose doktorantūros sunkumuose.

Dėkoju kolegoms iš kitų skyrių – dr. Algirdui Selskiui, dr. Aušrai Selskienei, dr. Ilja Ignatjev, dr. Gediminui Niaurai, dr. Linai Grinevičiūtei, Tomui Rakickui ir Lucciano A. Letelier – už pagalbą atliekant tyrimus, bendradarbiavimą bei suteiktus rezultatus, kurie tapo svarbia šio darbo bei išspausdintų publikacijų dalimi.

I am grateful to colleagues from FORTH in Crete, Greece, for accepting us into their laboratory and for their willingness to collaborate and achieve great results: Dr. Emmanuel Stratakis, Dr. George D. Tsibidis, Dr. Stella Maragkaki, Dr. Sotiris Psilodimitrakopoulos, Dr. Ioannis Paradisanos, Matina Vlachou, and Danae Katrisioti – Ευχαριστώ πολύ.

Ačiū tėvams, giminėms bei draugams už stiprų palaikymą ir tikėjimą manimi visos doktorantūros metu bei nesibaigiančius klausinėjimus „tai ką tu ten darai su tais lazeriais?“ – nors iki galo suprantamai atsakyti į šį klausimą, ko gero, taip ir nepavyko. Esu dėkingas seneliui, kurio pavyzdys ir paskatino siekti „dr.“ laipsnio bei eiti mokslo keliu.

Galiausiai dėkoju visiems, kurie vienaip ar kitaip prisidėjo prie smagių ir įsimintinų doktorantūros metų. O paskutinė ir didžiausia pagarba tiems, kurie perskaitė šį netrumpą darbą iki galo ir netgi kažką suprato.

Doktorantūros kelias

Savo ketverių metų doktorantūros kelią pabandžiau sutalpinti į grafikus, kurie vaizduoja, kaip ši įkalnė augo nuo pirmųjų mėnesių iki paskutinio disertacijos puslapio. Ankstesnė tyrimų patirtis leido greitai įsivažiuoti studijų pradžioje: iškart sudalyvauta lietuviškose konferencijose, spėta išleisti po vieną autorinį ir bendraautorinį straipsnį. Dar nepasibaigus pirmiesiems metams, buvo pasinaudota galimybe išvykti į stažuotę, o jos „vaisiai“ subrendo antraisiais studijų metais, kai pasirodė net du autoriniai straipsniai. Nuo tada nusistovėjo stabilus darbo ritmas ir kas 8-9 mėnesius „gimdavo“ po naują autorinį straipsnį. Antrieji metai taip pat buvo kupini pažinčių, gausiai keliaujant po konferencijas tiek Lietuvoje, tiek ir užsienyje. Tretieji metai pasižymėjo stažuotėmis, kai už Lietuvos ribų buvo praleisti beveik 2 mėnesiai. Na, o paskutiniais metais, šalia disertacijos rašymo, dar spėta pasimėgauti paskutinėmis studentiškomis konferencijomis. Noriu pasidžiaugti, jog ši disertacija ir jos rezultatai buvo pasiekti ne užsidarius vienoje vietoje, o tarp skirtingų laboratorijų, tyrėjų, konferencijų salių ir klaidžių oro uostų.

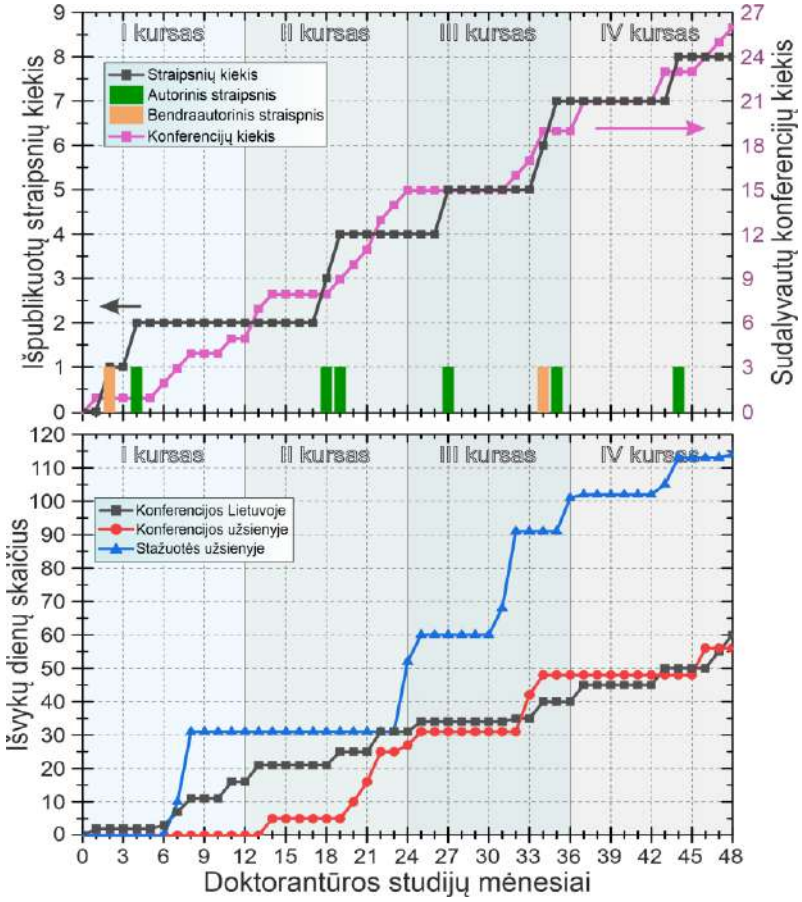

CURRICULUM VITAE

Name: Kernius
Surname: Vilkevičius

Education:

2022 – 2026	**Center for Physical Sciences and Technology (FTMC)** *PhD studies in Materials Engineering*
2020 – 2022	**Vilnius University (VU)** *Master's degree in Materials Technology* *Magna Cum Laude*
2016 – 2020	**Kaunas University of Technology (KTU)** *Double bachelor's degree in Materials Technology and Applied Mathematics* *Diploma with distinction*
2012 – 2016	**Kaunas Vytautas Magnus University „Rasa" gymnasium** *High school education* *Diploma with distinction*

Work experience:

2019 – present	**Center for Physical Sciences and Technology**
2023 – present	*Junior researcher*
2021 – 2023	*Engineer*
2020 – 2021	*Technician*
2019 – 2020	*Intern*
2024	**Vilnius University** *Junior laboratory assistant*
2016 – 2021	**KTU Students' Scientific Society** *Member, Member of the Board, Alumni*

Research internships:

2026 09 28 – 2026 10 13	Foundation for Research and Technology - Hellas (FORTH), Institute of Electronic Structure and Laser (IESL) in Heraklion, Crete, Greece. NFFA-Europe Internship ID1058.
2026 04 28 – 2026 05 08	National Cheng Kung University (NCKU), Department of Photonics in Tainan, Taiwan.
2025 09 21 – 2025 10 01	Technische Universität Wien (TU Wien), Institute of Materials Science and Technology in Vienna, Austria.

2025 04 23 – 2025 05 23	Foundation for Research and Technology - Hellas (FORTH), Institute of Electronic Structure and Laser (IESL) in Heraklion, Crete, Greece. NFFA-Europe Internship ID778.
2024 09 09 – 2024 10 08	Foundation for Research and Technology - Hellas (FORTH), Institute of Electronic Structure and Laser (IESL) in Heraklion, Crete, Greece. NFFA-Europe Internship ID626.
2023 04 20 – 2023 05 21	Foundation for Research and Technology - Hellas (FORTH), Institute of Electronic Structure and Laser (IESL) in Heraklion, Crete, Greece. NFFA-Europe Internship ID369.

Scientific awards and scholarships:

2026	**Novian and VITP eponymous scholarship winner**, Conference of Young Scientists "Interdisciplinary Research in the Physical and Technological Sciences 2026".
2026	**Research Excellence Award**, International Conference "Open Readings 2026".
2026	**Young Scientist of the Year 2025 award**, Center for Physical Sciences and Technology.
2026	**Award Winner** of the LMA 2025 Young Scientists' and Doctoral Students' Research Competition, Lithuanian Academy of Sciences.
2023-2026	**Grant for Academic Visit**, Research Council of Lithuania (4 times).
2023, 2025, 2026	**Scholarship for Academic Results**, Research Council of Lithuania (3 times).
2024	**Best Oral Presentation Award**, Conference "FizTeCh 2024".
2023	**Best Poster Presentation Award**, International Conference-School "Advanced Materials and Technologies 2023".
2023	**Best Oral Presentation Award**, International Conference "Open Readings 2023".
2021-2022	**Incentive Scholarship**¸Vilnius University (3 times).
2021	**Best Poster Presentation Award**, International Conference-School "Advanced Materials and Technologies 2021".
2017-2020	**KTU Talent Scholarship**, Kaunas University of Technology (7 times).

GYVENIMO APRAŠYMAS

Vardas: Kernius
Pavardė: Vilkevičius

Išsilavinimas:

2022 – 2026	**Fizinių ir technologijos mokslų centras (FTMC)** *Technologijų mokslų doktorantūros studijos*
2020 – 2022	**Vilniaus universitetas (VU)** *Technologijų mokslų magistro laispnis* *Magna Cum Laude diplomas*
2016 – 2020	**Kauno technologijos universitetas (KTU)** *Technologijų mokslų ir Matematikos mokslų bakalauro laipsniai* *Diplomas su pagyrimu*
2012 – 2016	**Kauno Vytauto Didžiojo universiteto „Rasos“ gimnazija** *Vidurinis išsilavinimas* *Diplomas su pagyrimu*

Darbo patirtis:

2019 – dabar	**Fizinių ir technologijos mokslų centras**
2023 – dabar	*Jaunesnysis mokslo darbuotojas*
2021 – 2023	*Inžinierius*
2020 – 2021	*Technikas*
2019 – 2020	*Praktikantas*
2024	**Vilniaus universitetas** *Jaunesnysis laboratorijos asistentas*
2016 – 2021	**KTU Studentų mokslinė draugija** *Narys, Valdybos narys, Alumni*

Mokslinės stažuotės:

2026 09 28 – 2026 10 13	Foundation for Research and Technology - Hellas (FORTH), Institute of Electronic Structure and Laser (IESL) – Heraklionas, Kreta, Graikija. NFFA-Europe ID1058.
2026 04 28 – 2026 05 08	National Cheng Kung University (NCKU), Department of Photonics – Tainanas, Taivanas.
2025 09 21 – 2025 10 01	Technische Universität Wien (TU Wien), Institute of Materials Science and Technology – Viena, Austrija.

2025 04 23 – 2025 05 23	Foundation for Research and Technology - Hellas (FORTH), Institute of Electronic Structure and Laser (IESL) – Heraklionas, Kreta, Graikija. NFFA-Europe ID778.
2024 09 09 – 2024 10 08	Foundation for Research and Technology - Hellas (FORTH), Institute of Electronic Structure and Laser (IESL) – Heraklionas, Kreta, Graikija. NFFA-Europe ID626.
2023 04 20 – 2023 05 21	Foundation for Research and Technology - Hellas (FORTH), Institute of Electronic Structure and Laser (IESL) – Heraklionas, Kreta, Graikija. NFFA-Europe ID369.

Moksliniai apdovanojimai ir stipendijos:

2026	**Novian ir VITP vardinės stipendijos laureatas**, Jaunųjų mokslininkų konferencija „Fizinių ir technologijos mokslų tarpdalykiniai tyrimai 2026“.
2026	**Research Excellence Award**, tarptautinė konferencija „Open Readings 2026“.
2026	**Geriausias 2025 metų jaunasis mokslininkas**, Fizinių ir technologijos mokslų centras.
2026	**LMA Jaunųjų mokslininkų ir doktorantų mokslinių darbų konkurso premijos laureatas**, Lietuvos mokslų akademija.
2023-2026	**Stipendija doktorantų akademinėms išvykoms**, Lietuvos mokslo taryba (4 kartai).
2023, 2025, 2026	**Stipendija už studijų rezultatus**, Lietuvos mokslo taryba (3 kartai).
2024	**Geriausio žodinio pranešimo apdovanojimas**, konferencija „FizTeCh 2024“.
2023	**Geriausio stendinio pranešimo apdovanojimas**, tarptautinė konferencija-mokykla „Advanced Materials and Technologies 2023“.
2023	**Geriausio žodinio pranešimo apdovanojimas**, tarptautinė konferencija „Open Readings 2023“.
2021-2022	**Skatinamoji stipendija**, Vilniaus universitetas (3 kartai).
2021	**Geriausio stendinio pranešimo apdovanojimas**, tarptautinė konferencija-mokykla „Advanced Materials and Technologies 2021“.
2017-2020	**Universiteto talento stipendija**, Kauno technologijos universitetas (7 kartai).

COPIES OF PUBLICATIONS

1st publication / 1 publikacija
K. Vilkevičius, A. Selskis, E. Stankevičius,
Femtosecond laser wavelength-dependent formation of plasmonic gold nanostructures,
Applied Surface Science, 617, 156629 (2023).

https://doi.org/10.1016/j.apsusc.2023.156629

Applied Surface Science 617 (2023) 156629

Contents lists available at ScienceDirect

Applied Surface Science

journal homepage: www.elsevier.com/locate/apsusc

Full Length Article

Femtosecond laser Wavelength-Dependent formation of plasmonic gold nanostructures

Kernius Vilkevičius [a,*], Algirdas Selskis [b], Evaldas Stankevičius [a]

[a] Department of Laser Technologies, Center for Physical Sciences and Technology, Savanoriu av. 231, LT-02300 Vilnius, Lithuania
[b] Department of Characterization of Materials Structure, Center for Physical Sciences and Technology, Saulėtekio av. 3, LT-10257 Vilnius, Lithuania

ARTICLE INFO

Keywords:
Surface lattice resonance
Direct laser writing
Plasmonic nanostructure arrays
Laser harmonics
Femtosecond laser pulses

ABSTRACT

Complex gold nanostructures fabricated on the surface of metal have a high potential for being used as plasmonic nanostructures. The precise shape and dimensions management of the structures enables accurate control of plasmonic properties. In this work, the formation of gold nanobumps, nanocones, and nanojets by laser direct writing technique was investigated using different laser wavelengths by changing harmonics. The used wavelength of laser irradiation impacts the size and shape of the formed structures. Additionally, the achievable minimal grating period, the layer modification fluence, and the formation fluence range change with the used laser harmonic. Experiments indicate that the reduction of the wavelength provides a more precise fabrication process and management of properties. The gratings of the wavelength-dependent nanostructures excite surface lattice resonances with high quality and have significant potential for practical uses.

1. Introduction

Noble metal nanostructures have been widely studied due to their exclusive interaction with light and the emergence of plasmonic properties. Depending on the structures, several plasmonic modes can be obtained, two of which are considered fundamental [1]. In the presence of spatially confined nanostructures smaller than the incident light wavelength, the collective free-electron excitations, also known as localized surface plasmons, are induced and the localized surface plasmon resonance (LSPR) phenomena occur featuring fixed and relatively broad resonance peaks [2–4]. Meanwhile, the use of a smooth metallic layer excites the propagating along the metal-dielectric interface surface plasmon polaritons (SPPs) having dispersion-relation [1,4,5]. Due to a mismatch of SPPs and light wavevectors, the SPPs cannot be directly excited by incident light [4]. Therefore, a prism [6] or diffraction grating [2,7] is used to excite it. As the compactness is appreciated for practical uses, the excitation using grating is more desirable. Additionally, such gratings scatter incident light and diffract rays that lead to the enhancement of plasmonic properties. By arranging nanoparticles in a lattice with a period close to the irradiating light wavelength, the diffracted ray traveling parallel to the lattice surface interacts with the LSPR-inducing nanostructures, resulting in stronger interactions between adjacent structures, higher enhancement of the electromagnetic field, and neglection in the radiative losses. Theoretically, the nanoparticles are observed as dipoles and the dipole sum in the grating case offsets the damping effect of a single nanoparticle, leading to the field enhancement [2]. This phenomenon is called surface lattice resonance (SLR) featuring high-quality resonances [1,2,8–12], and having a very narrow and tunable resonance peak in the Vis-NIR zone [13]. Refractive index-sensitive properties of SLR can be implemented in highly accurate and sensitive label-free biosensors [5,10,14,15], used for molecule concentration detection [15], nanolasers [1,10], nonlinear optics [16], Raman spectroscopy [5,17,18], photocatalysis and photovoltaics [2], etc. For instance, such SLR-inducing gratings were used for boosting the spontaneous emission of HgTe quantum dots [19], applied as security labels [20], and used to control the propagation length of strongly coupled Tamm plasmon polaritons and SPPs [21].

The resonant properties highly depend on the used material [10] and its thickness [22,23], nanostructure shape and dimensions [10,22,24–26], grating periodicity [17,27–29] and arrangement [10,30,31], dielectric environment [14,28,32], light angle of incidence and polarization [10,33], thus for practical applications geometrical and periodical uniformity [2,17] and formation accuracy of the structures is required. Silver has the strongest plasmonic properties [34,35], but the material is susceptible to oxidation, thus non-reactive gold with slightly poorer plasmonic properties is usually used [1]. Mostly plasmonic

* Corresponding author.
E-mail address: kernius.vilkevicius@ftmc.lt (K. Vilkevičius).

https://doi.org/10.1016/j.apsusc.2023.156629
Received 14 November 2022; Received in revised form 20 January 2023; Accepted 29 January 2023
Available online 2 February 2023

nanostructures are fabricated using electron-beam (EBL) [15,36] and focused ion-beam lithography (FIB) [37] or colloidal [1,25] and interference lithography (IL) [17,18,38] techniques, as the shape of the nanoparticles varies from spheres [39] and lines [15] to rods [36], mushrooms [38] and even nanorings [25]. EBL combined with the lift-off process easily allows controlling the pattern and the shape of the nanostructures. However, EBL and FIB have limitations, they are quite expensive and time-consuming, especially when producing large arrays of nanostructures [4]. Colloidal and interference lithography methods have higher throughput, but the resolution of IL is limited and the uniform formation conditions are not achieved in the whole exposed area, while the control of the assembly process is complicated and the uniformity of particles is hardly achieved in the colloidal method [1]. The alternative suggested way to fabricate uniform, cost- and time-effective sub-wavelength structures on the surface of the thin metal film is to implement laser direct writing (LDW) of ultrashort femtosecond (fs) laser and to use the temporal and lateral energy confinement to reduce the formation-zone size [11,13,18,40]. By irradiating the metal surface with one laser pulse, the fastly-heated and molten metal forms complex energy-dependent nanostructures – from small bumpy protrusions to high and sharp nanojets [12,16,39,41]. Wide studies have been made on investigating the formation of the structures that, with an accurate control of the fs-pulse energy, the four different morphological states can be obtained – metallic hollow bumps, cones, jets, and crowns with voids [13,42]. At small pulse energies, the small half-spherical protrusions are formed that grow in diameter and height and form pointier cones with increasing pulse energy. At certain energies, the solid structure collapses, and a sharp jet-like antenna appears in the middle of it. Further increase in energy leads to a change in the jet's height and the film's ablation with the formation of the crowns takes place [43,44]. The height and diameter are controlled only by the energy, but the additional use of an adjustable aperture to change the effective NA of the objective provides even more control of the shape and size of the nanostructures [24].

The formation is based on relatively slow electron–phonon energy transfer, resulting in an elongated molten phase and structure formation without the ablation of the thin film [45]. Several proposals and discussions about the formation mechanisms of specific structures are presently based on laser-induced dynamics. The effect of such formation is conditioned by the elastic metal characteristics and yield stress. Meshcheryakov et al. [46] described the formation using two-temperature and elasto-plastic flow models and stated that the bumps are formed using lower than the melting fluence when the film gains momentum normal to the surface leading to the uprise, which is extinguished by the plastic deformations. Meanwhile, when the fluence is above a melting threshold, the central part of the irradiated area is melted, and induced thermal stresses [42] lead to an acceleration of the molten material in the upward direction until it is stopped by the surface tension and stresses induced by the cooling of the melt. Other explanations of the bump formation are based on the inducing melting of the layer. The irradiated layer melts and detaches from the substrate due to compressive stress relaxation caused by the thermal expansion and plastic deformation of the metal film [12,47,48]. Nakata et al. [49] explain that melting initiates the evaporation of the metal at the bottom part of the layer, leading to the pressure-induced molten gold perpendicular detachment from the substrate and the formation of a hollow bump. Furthermore, Kuznetsov et al. [48] offer an explanation that with higher energy molten material exhibits movement of molt towards the apex of protrusion, and two jets in opposite directions are formed, inside and outside the bump. Korte et al. [50] suggest that when the gold film is molten, the waves that are produced on the surface collide at the center of the molten area, and the jet is formed. The formation of crowns in copper and gold using higher energies than required for the jets is explained by the development of hydrodynamic instabilities (Marangoni effect, Rayleigh-Plateau) in the sides of the molten area after the bump destruction [43,44].

The formation of bumps and cones is more controllable compared to the formation of jets as the tips can be tilted in different directions due to the splashing of molten metal upwards. Also, the surface non-uniformities and defects have an impact on the development of the structures, and both required fluence and formation mechanism changes [45]. Despite that, the fabrication wavelength, which determines the absorption of radiation, might also affect the formation and impact the parameters. The majority of research in nanostructurization with a single fs-laser pulse was applied using either 800 nm wavelength [22,41,42] or a second laser harmonic (515 nm / 532 nm) [12,13,27,44]. Also, a few works have been carried out using a picosecond laser with 1030 nm [51] and a nanosecond laser with 532 nm [52] wavelength, but the obtained structures were a bit different, so the influence of the laser wavelength on the formation is not fully clarified and need deeper investigation.

In this work, we investigate the influence of the laser wavelength (1030 nm, 515 nm, 343 nm) on the fabrication of periodic gold nanostructures – their formation energy threshold, minimal achievable period and diameter, morphology, and plasmonic properties. The influence of the wavelength is obvious and the correct choice of it is crucial for the required achievable lateral distance, size, and shape of protrusions. The research gives a better understanding of the formation of structures using different laser wavelengths and their plasmonic properties.

2. Material and methods

2.1. Metal film preparation

A thin gold film with a thickness of 50 nm was coated onto a fused silica glass substrate using a magnetron sputter coater (Quorum Q150T). The film thickness was chosen on the basis of previous studies as the optimum thickness for resonance condition and the lowest reflectivity [53,54]. The pressure inside the chamber was 9×10^{-3} mbar, and the deposition rate was ~ 0.26 nm/s. The film thickness was controlled by changing the sputtering time, which was set to 190 s.

2.2. Laser system

The 100×100 μm^2 and 3×3 mm^2 arrays of the nanostructures were fabricated using LDW with 1030 nm first- (1H), 515 nm second- (2H), and 343 nm third-harmonic (3H) 300 fs single laser pulses generated by Yb:KGW based fs-laser (Pharos, Light Conversion ltd.). The laser beam was tightly focused onto the metal surface using high-NA (0.5) objectives. A periodic array was fabricated by scanning lines and using an integrated pulse picker for the pulse-on-demand regime. Scanning speeds in the range of 3.5–14.7 mm/s were used. The sample was mounted on a 2D positioning platform, allowing to move the sample in the x- and y-axis, while the beam focus position was changed by moving the objective in the z-axis. Additionally, a CCD was used for imaging the fabrication through the same high-NA objective.

The shape of the structure highly depends on the formation pulse energy, thus arrays with different periods and formation energies were fabricated with each harmonic. The range of fabricated periods was 0.6–2.1 μm, 0.5–1.3 μm, and 0.5–1.3 μm for 1H, 2H, and 3H, respectively. The energy range was 7.5–10 nJ with a step of 0.5 nJ for 1030 nm pulses, 0.6–1.6 nJ with a step of 0.1 nJ for 515 nm pulses, and 0.3–1.4 nJ with a step of 0.1 nJ for 343 nm pulses. The lowest and highest formation energy limit was chosen by visually checking the formation process through an optical microscope.

2.3. Structure characterization and plasmonic properties measurement

The shapes of the fabricated structures in 100×100 μm^2 gratings were visualized and inspected using a scanning electron microscope (SEM, Helios NanoLab650). The diameters were measured from

obtained images when a sample is not tilted, while the shape and the height were determined from images when a sample was tilted at a 57° angle. The shape of the structures has been distinguished according to their physical properties: structures with a diameter greater than the height were classified as bumps, those with a height similar to the diameter were called cones, and the jets were structures with an additional narrow protrusion in the center.

The plasmonic properties of $3 \times 3\,mm^2$ arrays were measured using a spectrophotometer (Photon RT, Essentoptics). The reflectance spectra for *s*- and *p*-polarized light were recorded in the wavelength range of 0.4–1.5 μm using 8° and 15° angles of incidence.

3. Results and discussion

3.1. Fabrication of wavelength-dependent gold nanostructures

Different wavelengths interact differently with the thin gold film due to the changes in absorption. The extinction spectra of the 50 nm gold film, calculated from the data of measured transmission and reflection at 8° spectra, can be seen in Fig. 1a, where the extinction for 1H is 3.56 %, for 2H it is 33.06 % and for 3H – 53.62 %. The extinction results correspond to the absorption of the layer. As the wavelength increases, the diameter of the Gaussian beam at the focal position enlarges. The diameters of the irradiated area, obtained by tightly focusing laser pulses with used high-NA objectives, are estimated to be ~ 2.2 μm, ~1.1 μm, and ~ 0.8 μm for 1H, 2H, and 3H, respectively, as depicted in Fig. 1b. The energy required to modify the thin film and to form small bumpy protrusions decreases with decreasing fabrication wavelength. Using a 1030 nm wavelength with very low absorption, the bumps are formed at an energy of approximately 7.5 nJ, which is equivalent to a fluence of 0.4 J/cm^2. When the wavelength is reduced to the more absorbable 515 nm, the required energy decreases rapidly and the layer is modified at 0.55 nJ (fluence 0.117 J/cm^2). Using the even more absorbable 343 nm wavelength, the structures were fabricated using the lower energy of a single pulse (0.3 nJ, corresponding to a fluence of 0.109 J/cm^2).

The minimum periods achievable for each harmonic were determined using the modification threshold energies. The grating of the 0.8 μm period is achievable using 1030 nm wavelength, with the diameter of the structures being 552 ± 36 nm, while with 515 nm the 0.5 μm period array of structures with 440 ± 26 nm diameter was fabricated. Using 343 nm wavelength, the minimal-period grating of 351 ± 25 nm diameter structures was also fabricated with 0.5 μm, but the distance between the structures is sufficient enough to reduce it to 0.45 μm or even 0.4 μm. The smallest achievable period is limited by the size of the modified layer and the size of the protrusion-like structure. Longer wavelengths have been calculated to be focused into a larger diameter spot [55]. In contrast, the intensity distribution of the Gaussian beam and the lower absorption of such irradiation allows achieving structures of smaller diameter and period than the focused beam size. However, the size of the focus spot seems to have a greater impact than the absorption on the diameter and period of the structures, leading to the use of UV irradiation for the arrays with the smallest periods.

The diameter of the structures in the arrays fabricated with different parameters was measured to determine the quantitative dependency on energy and period. An increase in the energy produces larger structures in size and leads to the different morphological states in all investigated wavelengths, as shown in Fig. 2a-c. The base of the structures was observed to be elliptical due to the linear polarization of the used laser beam [56,57], as can be seen in hole images of Fig. 2a-c, and the diameters of both long (cyan line) and short (magenta line) axes were therefore measured. The increase in diameter with energy, as well as the difference in the length of these axes, can be seen in Fig. 2d, where the graph of diameter dependence on pulse energy for constant 1.2 μm period gratings is plotted. The solid lines represent the data of the long axis and the dashed lines – the data of the short axis, while the different colors of the lines correspond to the used wavelengths. The polarization impact on structure ellipticity grows with energy uprising and is the highest using fundamental harmonic (Fig. 2d). The structural shape varies and size increases by increasing single pulse energy. The maximum obtained diameters of the structures, more precisely holes, produced at the highest energies, increase with the use of higher-order harmonics, and the values in the short axis are 798 ± 28 nm, 860 ± 19 nm, and 1125 ± 31 nm for 1H, 2H, and 3H, consecutively. In addition, as can be seen from Fig. 2d, the use of shorter wavelength results in a steeper curve and a larger diameter can be achieved over a smaller energy range.

The measured data of diameter dependence on formation pulse fluence and grating period is depicted as the contour graph in Fig. 3 for the shorter axis. The data for the longer axis is in Fig. S1. The range of the fluence was set the same for all wavelengths. The fluence range of complex-shaped nanostructures formation with fundamental harmonic (1030 nm) is narrow, only 0.13 J/cm^2 and a quite high fluence is required to initiate the layer modification (0.4 J/cm^2) due to the very low absorption of gold film at such wavelength. The fabrication range is increased to 0.21 J/cm^2 by using frequency-doubled laser radiation and the fluence required to modify the film is greatly reduced to 0.13 J/cm^2. Frequency-tripled pulses greatly expand and double the structure formation range to larger fluences, the range being 0.4 J/cm^2, with the modification threshold being even lower than for 515 nm wavelength – 0.1 J/cm^2. Higher absorption of the radiation in shorter wavelengths leads to a decrease in the minimal layer modification fluence and an increase in the structurization range. This wider fluence range at shorter wavelengths allows for more precise control of the parameters of the structures.

The used wavelength has an impact not only on fluence range but

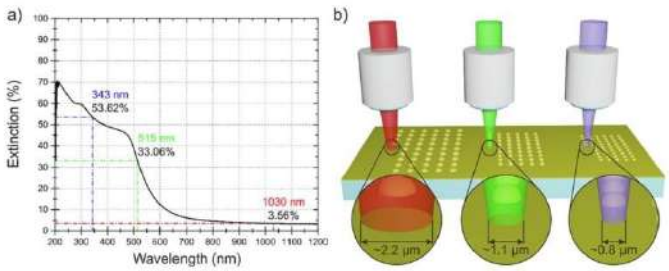

Fig. 1. A) extinction spectra of 50 nm thick gold layer deposited on silica glass. b) Diameters of focused beams for first-, second-, and third-harmonic.

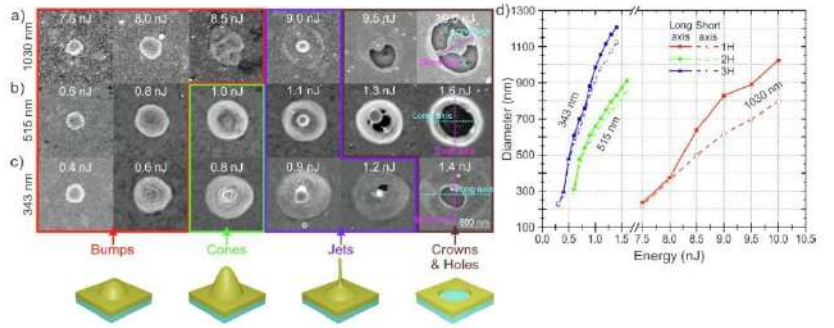

Fig. 2. SEM micrographs of gold nanostructures in 1.2 μm period gratings with increasing diameter fabricated using a) 1030 nm, b) 515 nm, and c) 343 nm wavelengths. d) Diameter of long (solid line) and short (dashed line) axis dependence on pulse energy for 1.2 μm period gratings fabricated with 1H (red line), 2H (green line), and 3H (blue line). (For interpretation of the references to colour in this figure legend, the reader is referred to the web version of this article.)

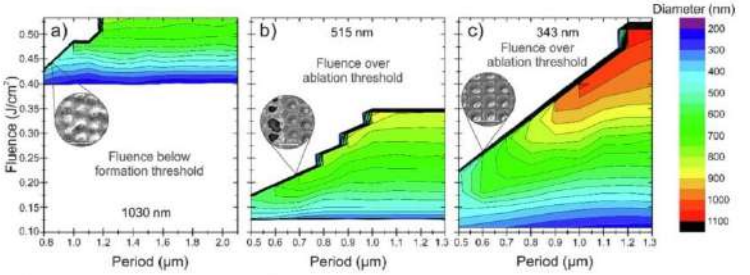

Fig. 3. Short axis diameter of the structures' dependence on grating period and formation beam fluence colormap for a) 1H, b) 2H, and c) 3H. The range of fluence is set the same for all harmonics, while the range of period is similar only for the data of the same wavelength. SEM micrographs show the overlapping of the structures in small periods.

also on the diameter. The smallest width nanostructures (<200 nm) are obtained with 1030 nm at large periods with no beam overlapping (>1.4 μm) because of very low absorption and formation only in the central part of the Gaussian beam, however, the period is quite high and the smallest period–diameter ratio is achieved using 343 nm wavelength (351 nm width structures at 0.5 μm period). Most of the structures can be of 500–700 nm in diameter for all wavelengths, while the highest lateral sizes are also achieved with 3H. Diameters of specific morphological nanostructures change rapidly with pulse wavelength. At large periods the maximum width of bumps at the short axis is 550 nm for 1H, 600 nm for 2H, and 640 nm for 3H. The cones in 1H are not obtained, while in 2H and 3H they have diameters of 640 nm and 790 nm, respectively. Meanwhile, the jets are of 675 nm for 1H, 780 nm for 2H, and around 1100 nm in diameter for 3H. The crowns and ablated holes are available in even higher sizes, which were not investigated. The diameters gradually increase with decreasing wavelength, meaning the higher absorbance of the wavelength leads to larger structures in diameter.

Another observable effect is period influence on the formation energy and structure diameter. There is a clear change in the ablation threshold of the thin gold film (left upper boundary of the Fig. 3 contour graphs) as the period decreases so that less fluence is required to ablate the film. This phenomenon is caused by the overlapping of the focused beam and the fabricated structures at periods smaller than the beam diameter. To investigate the thermal effects of the thin film, the temperature right after the pulse impinged to the metal and after 100 μs when the adjacent partially-overlapping pulse was released were calculated. A two-temperature model [58,59] was used for the lattice impact-temperature calculations at the moment when it reaches equilibrium with electron temperature. During the formation of the bumps, the maximum reached temperature of the lattice is around 450 K, 1700 K, and 3650 K for 1H, 2H, and 3H. Meanwhile, for the calculation of the heat accumulation and the remaining temperature after 100 μs, the temperature history was calculated [60]. The surface of the affected area after 100 μs is close to the initial temperature (300 K) for all three investigated wavelengths, as the calculated temperature history is close to zero. The marginal remaining temperature proves that the reduction in the fluence is not due to the thermal effects and heat accumulation. The origin of the decrease in the ablation and morphological shape formation fluence might be due to the modifications in the peripherical part of the irradiated zone. The part of absorbed energy is turned into potential energy that is coupled into mechanical stresses [61]. At the central part of the affected zone, these stresses are high enough to fabricate a protrusion (e.g. bump). The stresses in the peripherical parts that are affected with lower intensity are weaker. Thus, the non-significant delamination [62] or the intrinsic modifications that reduce the critical energy needed to modify the material are generated.

This phenomenon is similar to material fatigue due to the use of several fs-pulses impinging onto the same spot [63]. The analysis of diameter change in Fig. 3 shows not only the obvious diameter growth with increasing fluence but also the increase in size with the reduction of the period. This tendency, caused by the overlap between the focused beams, is observed in all harmonics but is most pronounced at 343 nm wavelength, where for the same fluence the diameter slowly increases with decreasing inter-structural distance. Under such conditions, the fabricated structures of diameters equal or slightly larger than the period begin to touch and overlap, thus limiting minimal periodicity at that used fluence. For example, in 3H at a constant 0.33 J/cm^2 fluence the diameter at the largest 1.3 μm period is around 850 nm and increases to 920 nm at 1.0 μm and 950 nm at 0.9 μm period. At this latter period, the structures already overlap and a further reduction in distance and diameter growth leads to the ablation of the array. Such overlapping structures on the edge of the ablation threshold at small periods are represented in the insets of Fig. 3.

3.2. Shape dependency on wavelength

As the shape of the nanostructure is energy-dependent, the differently shaped structures were also fabricated in different energy regions. Using SEM images, the transitional energies and fluences from one morphological state to another, as well as formation zones, were determined and represented in Fig. 4. The colored lines represent the fluences at which: the thin film is modified and the bumps begin to form (black line), bumps turn into cones (red line), cones turn into jets (blue line) and crowns are formed with the ablation of the center of the structure (magenta line). Additionally, the squared lateral size dependence on the natural energy logarithm was calculated for all fabricated grating periods and the graphs can be found in Fig. S2. The linear approximation of Fig. S2 data allows to obtain the theoretical layer modification threshold energy [24], and these theoretical fluences for each period are marked in green lines in Fig. 4 and are in good agreement with fluences calculated from SEM images. The obvious reduction of transitional fluences at smaller than 1.0 μm periods is observable due to the previously mentioned overlapping of the formation beam. A thin 50 nm gold layer is modified and the nanobumps are formed at 0.4 J/cm^2, 0.12 J/cm^2, and 0.105 J/cm^2 using 1H, 2H, and 3H, respectively. The formation range at periods with no beam overlapping for 1H, 2H, and 3H is: 0.067 J/cm^2, 0.083 J/cm^2, and 0.127 J/cm^2, accordingly. In gratings formed at 1030 nm, the cones were either not visible due to the very small forming range, less than a step change in the energy (0.5 nJ) during fabrication, or the cones are not fabricated at all, and the bumps directly become jets. As with 2H or 3H, the cones are formed in narrow ranges of ≈ 0.021 J/cm^2 (0.1 nJ pulse energy) and ≈0.055 J/cm^2 (0.15 nJ), respectively. The fluence ranges for the formation of the nanojets are wider than for cones – 0.04 J/cm^2, 0.076 J/cm^2, and 0.254 J/cm^2. It is clear that by reducing the wavelength, the ranges at which specific morphological states are fabricated, as well as the whole nanostructurization range, increase. Nanobumps and nanojets are obtained at a wider fluence range than the intermediate morphology (nanocones) because the bumps are constantly growing in height and the cones are defined only with similar height-diameter values, thus the bumps with smaller apex are more likely to be obtained, especially at low energies. Meanwhile, during the jet formation, the rising pulse energy increases the diameter of the molten film, resulting in a thicker tip. Also, due to the high overlapping of the pulses at small distances, there are some ranges where not all morphological states are achieved. At a period of 0.5 μm for 515 nm and 343 nm, the jets are not obtained and the ablation directly of cones happens, while at periods of 0.8–0.9 μm for 1030 nm both the cones and jets are not formed and the bumps are ablated without other morphological transition.

The distinctions in the morphology of the fabricated structure with different wavelengths are also apparent and can be seen in Fig. 5. The bumps in all three harmonics are of quite similar shapes, only with the difference in maximum achievable height. The bumps in 1 μm period gratings formed with 1030 nm due to much lower absorption are only up to 150–180 nm in height, while the ones fabricated with 515 nm and 343 nm can be achieved up to 300–400 nm. The transition from bumps to cones is continuous and the boundary between these morphological states is hardly distinguishable, since they are separated only by the height-diameter ratio and the presence small taper at the apex, so this maximum height is not accurate and may be higher. Meanwhile, there is an obvious distinction between cones and jets, and the height can be defined more accurately. As mentioned previously, the cones with 1H are not obtained, as the height of the structure is always smaller than its diameter, however, such bumps fabricated at higher energies of 1030 nm are not perfectly semi-spherical and the height profile varies along the perpendicular axes. The cross-section profile of the structure is parabolic in the short axis (green line in Fig. 5a), as in both short and long axes for other bumps, while the height in the long axis of 1H structures does not change gradually and the sides are shorter with the central part being more prominent (red line in Fig. 5a). Using other harmonics, the cones are obtained and their height is 720 nm and 780 nm in 2H and 3H gratings, respectively. Cones fabricated using 3H are a

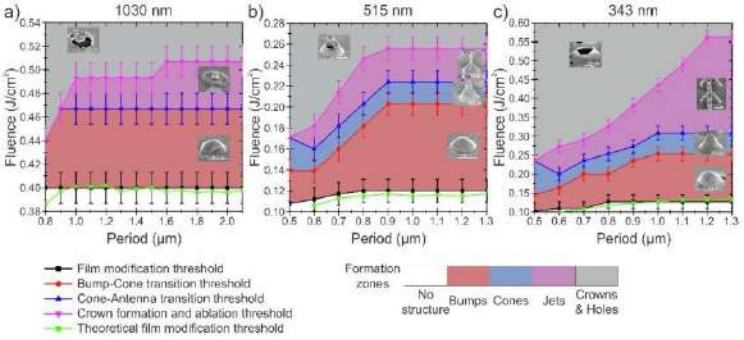

Fig. 4. Morphological state transitional fluence thresholds (for a) 1H, b) 2H, and c) 3H of bump (black), cone (red), jet (blue), and crown formation/ablation (magenta) with theoretically calculated layer modification/bump formation threshold (green) on long axis colormap. (For interpretation of the references to colour in this figure legend, the reader is referred to the web version of this article.)

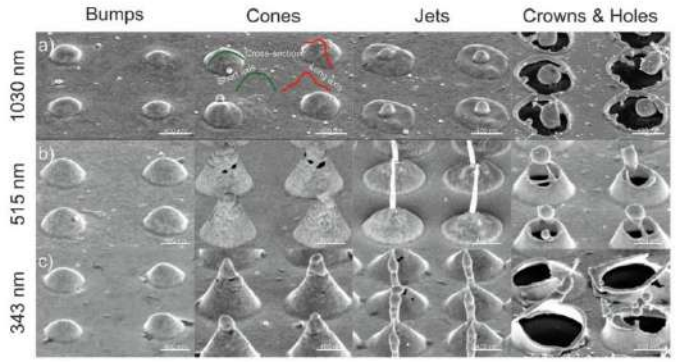

Fig. 5. SEM images of nanostructures tilted at 57° angle fabricated with a) 1030 nm, b) 515 nm, c) 343 nm wavelengths in 1 μm period gratings.

bit pointier compared to 2H cones. The most obvious is the difference between the jets, as can be seen in the third row of Fig. 4. Despite the high ellipticity, jets formed with 1H also have a much smaller, non-protruding, rounded, and unsharpened spike in the middle of the flat bump with a height of only 150 nm. In contrast, the 2H- and 3H-formed jets are tall and pointed, reaching as high as 1 μm. No significant difference was observed between the 515 nm and 343 nm jets. The small unshaped jets obtained at 1030 nm may be due to insufficient momentum provided by the poorly absorbed radiation to the molten metal and required for the melt to shoot upwards and form a jet. Finally, the ablated holes with the crowns on the sides are different in all harmonics. The use of fundamental harmonic produced ablated holes with a nanosphere in the center of it. The conical structures with the ablated center were observed in gratings fabricated with the second harmonic, while the crowns on the sides with ablated central part were formed with the third harmonic. The formation of such nanostructures is very unstable, as each structure can be obtained with different morphology due to the uncontrolled movement of melt, thus the clear influence of the wavelength on the crown formation is not stated.

3.3. Wavelength-dependent plasmon resonance

The plasmonic properties of the nanostructure periodic gratings are shape-dependent [13], thus the plasmonic properties of only the highest-quality resonance-attributing nanobumps were analyzed. The 1 μm period gratings of bumps were fabricated on a 50 nm thick gold layer using all three harmonics. The structures shown in Fig. 6a-c were measured and the diameters were found to be 397 ± 21 nm, 518 ± 15 nm, and 476 ± 11 nm, and the heights were 123 ± 13 nm, 211 ± 16 nm, and 163 ± 9 nm for 1H, 2H, and 3H, respectively. The reflectance

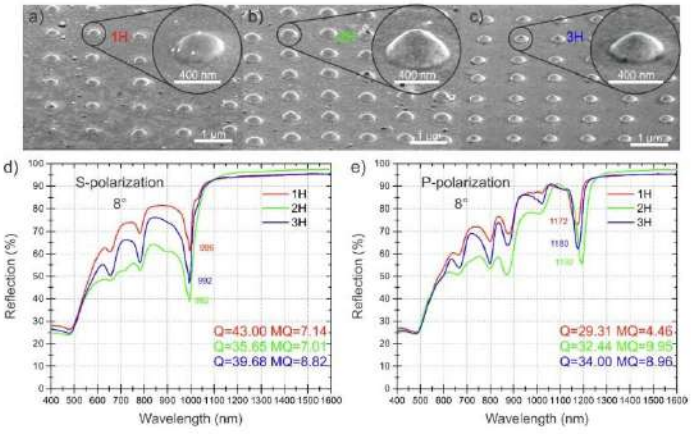

Fig. 6. SEM micrographs of bump gratings tilted at 57° angle fabricated with a) 1H, b) 2H, and c) 3H. d) *S*- and e) *p*-polarization 8° angle reflection spectra of 1 μm period gold bump gratings fabricated with 1H (red), 2H (green), and 3H (blue). (For interpretation of the references to colour in this figure legend, the reader is referred to the web version of this article.)

spectra of the *s*- and *p*-polarizations were measured to determine the plasmonic properties of the gratings rotated at an 8° angle. The azimuthal angle change was applied during the measurements so that the electric field oscillations were perpendicular to the laser scanning lines [11]. Here the results and SEM images of the gratings are represented in Fig. 6d-e, where the black line corresponds to 1030 nm grating, the red line – 515 nm, and the blue line – 343 nm. The analysis of the SLR peaks in Fig. 6d-e shows that the wavelength of fabrication has minimal influence on the resonance when the structures are bumps. The resonant wavelengths are within close limits and the difference is due to the unequal size of the structures, as it is extremely hard to produce structures of identical physical parameters at different harmonics due to energetical fluctuations and erratic formation dynamics. As the structure grows upwards, the resonance shifts to longer wavelengths [24]. The lowest bumps are in the 1H array and the highest structures are in the 2H array, which explains the wavelength shift in the latter grating.

The quality of the resonances is expressed in terms of the Q-factor, taking into account only the resonant wavelength λ_{res} and the width of the peak at half height $\Delta\lambda$ [4]:

$$Q = \lambda_{res}/\Delta\lambda \quad (1)$$

In such calculations, the peak height h is not included, although it is important for resonance properties and indicates the strength of the interaction and the resonance between structures. We have introduced a modified quality (MQ) factor, which includes the peak depth:

$$MQ = \frac{\lambda_{res} \bullet \lambda}{\Delta\lambda \bullet 100\%} \quad (2)$$

The Q-factor has been calculated for comparison with other Q-factors found in the literature, while MQ-factor was used for the wavelength comparison. The resonances in all investigated wavelengths are with relatively high Q-factor (around 40 for *s*-polarization, and 30 for *p*-polarization), as the similar gratings exhibit a Q-factor of 17 [24] and gratings supporting SLR typically achieve a Q-factor of 40–60 [2], thus such gratings reach adequate quality for practical uses. A comparison of the MQ-factor does not indicate a strong wavelength influence on plasmon resonance. The highest MQ-factor using *s*-polarized light is achieved in grating fabricated with 343 nm (MQ = 8.82), while with *p*-polarization the strongest resonance is observed in the 2H array (MQ = 9.95), although the MQ-factor of the 3H array is close to that as well (MQ = 8.96). The difference in the MQ may be due to the same reason for non-uniformity, as larger nanostructures interact more strongly with each other. The structures in the array fabricated with 1030 nm are more elliptical and non-spherical, as the shape of the structures is not uniform, and are therefore of lower quality than those fabricated with 2H or 3H. Despite the shift in the resonant wavelength, changing the angle of incidence by up to 15° does not have any additional impact on the peaks, and the difference is minimal. The spectra of the 15° angle of incidence can be found in Fig. S3. Since the resonant properties and quality increase with reducing lattice lateral distance and enhancing the coupling between the nanostructures, it is clear that the ability to achieve smaller periods at 2H and 3H makes these wavelengths more desirable and usable in practical applications.

4. Conclusions

The morphology of femtosecond laser-induced structures can be easily manipulated by changing laser pulse energy and grating period, while the laser wavelength has an impact on the fabrication parameters as well. The increase of laser wavelength reduces the formation fluence range of the nanostructures and the achievable minimal period of the gratings due to the higher overlapping of a larger focal spot beam. The reduction of the wavelength also decreases the thin film modification fluence as the absorption increase. The nanostructures of different morphologies in 3H and 2H are quite similar, while 1H-generated jets are of much smaller tips and the cones are not obtainable at all. Within three morphological states, the achievable height, as well as the diameter, not influenced by the polarization-induced ellipticity, gradually increases with a change to more absorbable lower wavelengths. Moreover, the plasmonic properties were measured of the bump gratings, showing no significant wavelength influence and reaching Q-factor up to 40, which is sufficient enough for practical applications. The results of this work give a better understanding of the wavelength influence on the formation of plasmonic structures and can help to select the parameters and have more precise control over the modification and variation of the morphology.

Declaration of Competing Interest

The authors declare that they have no known competing financial interests or personal relationships that could have appeared to influence the work reported in this paper.

Data availability

No data was used for the research described in the article.

Acknowledgement

None.

Appendix A. Supplementary material

Supplementary data to this article can be found online at https://doi.org/10.1016/j.apsusc.2023.156629.

References

[1] K. Yang, X. Yao, B. Liu, B. Ren, Metallic plasmonic array structures: principles, fabrications, properties, and applications, Adv. Mater. 33 (2021) 2007988, https://doi.org/10.1002/adma.202007988.
[2] V.G. Kravets, A.V. Kabashin, W.L. Barnes, A.N. Grigorenko, Plasmonic surface lattice resonances: a review of properties and applications, Chem. Rev. 118 (2018) 5912–5951, https://doi.org/10.1021/acs.chemrev.8b00243.
[3] E. Stankevičius, I. Ignatjev, V. Petrikaite, A. Selskis, G. Niaura, Gold nanoparticles generated using the nanosecond laser treatment of multilayer films and their use for SERS Applications, ACS Omega 6 (2021) 33889–33898, https://doi.org/10.1021/acsomega.1c05165.
[4] S. Kasani, K. Curtin, N. Wu, A review of 2D and 3D plasmonic nanostructure array patterns: fabrication, light management and sensing applications, Nanophotonics 8 (2019) 2065–2089, https://doi.org/10.1515/nanoph-2019-0158.
[5] J. Jiang, X. Wang, S. Li, F. Ding, N. Li, S. Meng, R. Li, J. Qi, Q. Liu, G.L. Liu, Plasmonic nano-arrays for ultrasensitive bio-sensing, Nanophotonics 7 (2018) 1517–1531, https://doi.org/10.1515/nanoph-2018-0023.
[6] Z. Balevicius, A. Baskys, Optical dispersions of bloch surface waves and surface plasmon polaritons: towards advanced biosensors, Materials 12 (2019) 3147, https://doi.org/10.3390/ma12193147.
[7] L. Avalos, A.K. González-Alcalde, E.I. Chaikina, E.E. García-Guerrero, A. A. Maradudin, E.R. Méndez, Excitation of plasmonic and photonic modes in metallic lamellar gratings, Opt. Commun. 500 (2021), 127324, https://doi.org/10.1016/j.optcom.2021.127324.
[8] M. Juodėnas, T. Tamulevičius, J. Henzie, D. Erts, S. Tamulevičius, Surface lattice resonances in self-assembled arrays of monodisperse Ag Cuboctahedra, ACS Nano 13 (2019) 9038–9047, https://doi.org/10.1021/acsnano.9b03191.
[9] S. Hamdad, A.T. Diallo, M. Chakaroun, A. Boudrioua, The role of Rayleigh anomalies in the coupling process of plasmonic gratings and the control of the emission properties of organic molecules, Sci. Rep. 12 (2022) 3218, https://doi.org/10.1038/s41598-022-07216-1.
[10] A.D. Utyushev, V.I. Zakomirnyi, I.L. Rasskazov, Collective lattice resonances: plasmonics and beyond, Rev. Phys. 6 (2021), 100051, https://doi.org/10.1016/j.revip.2021.100051.
[11] E. Stankevičius, K. Vilkevičius, M. Gedvilas, E. Bužavaitė-Vertelienė, A. Selskis, Z. Balevičius, Direct laser writing for the formation of large-scale gold microbumps arrays generating hybrid lattice plasmon polaritons in Vis–NIR Range, Adv. Opt. Mater. 9 (2021) 2100027, https://doi.org/10.1002/adom.202100027.
[12] Y. Guo, K. Zhang, M. Zhang, Y. Chai, Y. Du, G. Hu, Plasmonic gold nanojets fabricated by a femtosecond laser irradiation, Opt. Express 29 (2021) 20063–20076, https://doi.org/10.1364/OE.428676.
[13] D. Pavlov, S. Syubaev, A. Kuchmizhak, S. Gurbatov, O. Vitrik, E. Modin, S. Kudryashov, X. Wang, S. Juodkazis, M. Lapine, Direct laser printing of tunable IR resonant nanoantenna arrays, Appl. Surf. Sci. 469 (2019) 514–520, https://doi.org/10.1016/j.apsusc.2018.11.069.

[14] J. Zhu, Z. Wang, S. Liu, S. Jiang, X. Liu, S. Guo, Low-cost flexible plasmonic nanobump metasurfaces for label-free sensing of serum tumor marker, Biosens. Bioelectron. 150 (2020), 111905, https://doi.org/10.1016/j.bios.2019.111905.
[15] H. Cai, M. Wang, J. Liu, X. Wang, Theoretical and experimental study of a highly sensitive SPR biosensor based on Au grating and Au film coupling structure, Opt. Express 30 (2022) 25136–26148, https://doi.org/10.1364/OE.461768.
[16] A.B. Cherepakhin, D.V. Pavlov, L.I. Shishkin, P.M. Voroshilov, S. Juodkazis, S. V. Makarov, A.A. Kuchmizhak, Laser-printed hollow nanostructures for nonlinear plasmonics, Appl. Phys. Lett. 117 (2020), 041108, https://doi.org/10.1063/5.0016173.
[17] N. Gisbert Quilis, M. Lequeux, P. Venugopalan, I. Khan, W. Knoll, S. Boujday, M. Lamy de la Chapelle, J. Dostalek, Tunable laser interference lithography preparation of plasmonic nanoparticle arrays tailored for SERS, Nanoscale 10 (2018) 10268–10276, https://doi.org/10.1039/C7NR08905H.
[18] L. Yang, J. Wei, Z. Ma, P. Song, J. Ma, Y. Zhao, Z. Huang, M. Zhang, F. Yang, X. Wang, The Fabrication of Micro/Nano Structures by Laser Machining, Nanomaterials (Basel) 9 (2019) 1789, https://doi.org/10.3390/nano9121789.
[19] A.A. Sergeev, D.V. Pavlov, A.A. Kuchmizhak, M.V. Lapine, W.K. Yiu, Y. Dong, N. Ke, S. Juodkazis, N. Zhao, S.V. Kershaw, A.L. Rogach, Tailoring spontaneous infrared emission of HgTe quantum dots with laser-printed plasmonic arrays, Light Sci. Appl. 9 (2020) 16, https://doi.org/10.1038/s41377-020-0247-5.
[20] V. Lapidas, A. Zhizhchenko, E. Pustovalov, D. Storozhenko, A. Kuchmizhak, Direct laser printing of high-resolution physically uncloinable function anti-counterfeit labels, Appl. Phys. Lett. 120 (2022), 251104, https://doi.org/10.1063/5.0091213.
[21] J. Amulyte, E. Buzavaitė-Verteliene, V. Vertelis, E. Stankevicius, K. Vilkevicius, Z. Balevicius, Influence of a gold nano-bumps surface lattice array on the propagation length of strongly coupled Tamm and surface plasmon polaritons, J. Mater. Chem. C 10 (2022) 13234–13241, https://doi.org/10.1039/d2tc02174a.
[22] M. Reininghaus, D. Wortmann, Z. Cao, J.M. Hoffmann, T. Taubner, Fabrication and spectral tuning of standing gold infrared antennas using single fs-laser pulses, Opt. Express 21 (2013) 32176–32183, https://doi.org/10.1364/OE.21.032176.
[23] E. Stankevičius, M. Garliauskas, L. Laurinavičius, R. Trusovas, N. Tarasenko, R. Pauliukaitė, Engineering electrochemical sensors using nanosecond laser treatment of thin gold film on ITO glass, Electrochim. Acta 297 (2019) 511–522, https://doi.org/10.1016/j.electacta.2018.11.197.
[24] D. Pavlov, A. Zhizhchenko, L. Fan, A.A. Kuchmizhak, Tuning collective plasmon resonances of femtosecond laser-printed metasurface, Materials 15 (2022) 1834, https://doi.org/10.3390/ma15051834.
[25] S. Mu, H. Chen, C. Shi, J. Zhang, B. Yang, Au nanoring arrays with tunable morphological features and plasmonic resonances, Nano Res. 14 (2021) 4674–4679, https://doi.org/10.1007/s12274-021-3402-3.
[26] D. Peckus, A. Tamulevičienė, K. Mougin, A. Spangenberg, L. Vidal, Q. Bauerlin, M. Keller, J. Henzie, L. Puodžiukynas, T. Tamulevičius, S. Tamulevičius, Shape influence on the ultrafast plasmonic properties of gold nanoparticles, Opt. Express 30 (2022) 27730–27745, https://doi.org/10.1364/OE.463961.
[27] D.V. Pavlov, A.Y. Zhizhchenko, M. Honda, M. Yamanaka, O.B. Vitrik, S.A. Kulinich, S. Juodkazis, S.I. Kudryashov, A.A. Kuchmizhak, Multi-Purpose nanovoid array plasmonic sensor produced by direct laser patterning, Nanomaterials (Basel) 9 (2019) 1348, https://doi.org/10.3390/nano9101348.
[28] E. Ponomareva, K. Volk, P. Mulvaney, M. Karg, Surface lattice resonances in self-assembled gold nanoparticle arrays: impact of lattice period, structural disorder, and refractive index on resonance quality, Langmuir 36 (2020) 13601–13612, https://doi.org/10.1021/acs.langmuir.0c02430.
[29] E. Stankevičius, E. Daugnoraitė, I. Ignatjev, Z. Kuodis, G. Niaura, G. Račiukaitis, Concentric microring structures containing gold nanoparticles for SERS-based applications, Appl. Surf. Sci. 497 (2019), 143752, https://doi.org/10.1016/j.apsusc.2019.143752.
[30] D. Wang, A. Yang, A.J. Hryn, G.C. Schatz, T.W. Odom, Superlattice Plasmons in Hierarchical Au Nanoparticle Arrays, ACS Photonics 2 (2015) 1789–1794, https://doi.org/10.1021/acsphotonics.5b00546.
[31] E. Stankevicius, M. Garliauskas, M. Gedvilas, N. Tarasenko, G. Račiukaitis, Structuring of surfaces with gold nanoparticles by using bessel-like beams, Ann. Phys. 529 (2017) 1700174, https://doi.org/10.1002/andp.201700174.
[32] X. Yang, G. Xiao, Y. Lu, G. Li, Narrow plasmonic surface lattice resonances with preference to asymmetric dielectric environment, Opt. Express 27 (2019) 25384–25394, https://doi.org/10.1364/OE.27.025384.
[33] J. Guo, Z. Li, H. Guo, Near perfect light trapping in a 2D gold nanotrench grating at oblique angles of incidence and its application for sensing, Opt. Express 24 (2016) 17259–17271, https://doi.org/10.1364/OE.24.017259.
[34] P.I. West, S. Ishii, G.V. Naik, N.K. Emani, V.M. Shalaev, A. Boltasseva, Searching for better plasmonic materials, Laser Photonics Rev. 4 (2010) 795–808, https://doi.org/10.1002/lpor.200900055.
[35] V. Amendola, O. Bakr, F. Stellacci, A study of the surface plasmon resonance of silver nanoparticles by the discrete dipole approximation method: effect of shape, size, structure, and assembly, Plasmonics 5 (2010) 85–97, https://doi.org/10.1007/s11468-009-9120-4.
[36] A.B. Taylor, P. Michaux, A.S.M. Mohsin, J.W.M. Chon, Electron-beam lithography of plasmonic nanorod arrays for multilayered optical storage, Opt. Express 22 (2014) 13234–13243, https://doi.org/10.1364/OE.22.013234.
[37] Y. Chen, K. Bi, Q. Wang, M. Zheng, Q. Liu, Y. Han, J. Yang, S. Chang, G. Zhang, H. Duan, Rapid focused ion beam milling based fabrication of plasmonic nanoparticles and assemblies via "Sketch and Peel" Strategy, ACS Nano 10 (2016) 11228–11236, https://doi.org/10.1021/acsnano.6b06290.
[38] Y. Shen, J. Zhou, T. Liu, Y. Tao, R. Jiang, M. Liu, G. Xiao, J. Zhu, Z.-K. Zhou, X. Wang, C. Jin, J. Wang, Plasmonic gold mushroom arrays with refractive index sensing figures of merit approaching the theoretical limit, Nat. Commun. 4 (2013) 2381, https://doi.org/10.1038/ncomms3381.
[39] A. Barchanski, A.B. Evlyukhin, A. Koroleva, C. Reinhardt, C.L. Sajti, U. Zywietz, B. N. Chichkov, Laser Generation and Printing of Nanoparticles, in: V.P. Veiko, V. I. Konov (Eds.), Fundamentals of Laser-Assisted Micro- and Nanotechnologies, Springer, Cham, 2014, pp. 103–123.
[40] F. Mao, G.L. Ngo, C.T. Nguyen, I. Ledoux-Rak, N.D. Lai, Direct fabrication and characterization of gold nanohole arrays, Opt. Express 29 (2021) 29841–29856, https://doi.org/10.1364/OE.437510.
[41] Y. Nakata, T. Okada, M. Maeda, Nano-sized hollow bump array generated by single femtosecond laser pulse, Jpn. J. Appl. Phys. 42 (2003) L1452–L1454, https://doi.org/10.1143/jjap.42.l1452.
[42] D. Wortmann, J. Koch, M. Reininghaus, C. Unger, C. Hulverscheidt, D. Ivanov, B. N. Chichkov, Experimental and theoretical investigation on fs-laser-induced nanostructure formation on thin gold films, J. Laser Appl. 24 (2012), 042017, https://doi.org/10.2351/1.4734048.
[43] D.V. Pavlov, S.G. Gurbatov, S.I. Kudryashov, E.L. Gurevich, A.A. Kuchmizhak, Laser-induced surface relief nanocrowns as a manifestation of nanoscale Rayleigh-Plateau hydrodynamic instability, Appl. Surf. Sci. 511 (2020), 145463, https://doi.org/10.1016/j.apsusc.2020.145463.
[44] A.A. Kuchmizhak, D.V. Pavlov, O.B. Vitrik, Y.N. Kulchin, Laser ablative fabrication of nanocrowns and nanojets on the Cu supported film surface using femtosecond laser pulses, Appl. Surf. Sci. 357 (2015) 2378–2384, https://doi.org/10.1016/j.apsusc.2015.09.255.
[45] F. Ruffino, M.G. Grimaldi, Nanostructuration of thin metal films by pulsed laser irradiations: a review, Nanomaterials 9 (2019) 1133, https://doi.org/10.3390/nano9081133.
[46] Y.P. Meshcheryakov, N.M. Bulgakova, Thermoelastic modeling of microbump and nanojet formation on nanosize gold films under femtosecond laser irradiation, Appl. Phys. A 82 (2006) 363–368, https://doi.org/10.1007/s00339-005-3319-9.
[47] D.S. Ivanov, B. Rethfeld, G.M. O'Connor, T.J. Glynn, A.N. Volkov, L.V. Zhigilei, The mechanism of nanobump formation in femtosecond pulse laser nanostructuring of thin metal films, Appl. Phys. A 92 (2008) 791–796, https://doi.org/10.1007/s00339-008-4712-y.
[48] A.I. Kuznetsov, C. Unger, J. Koch, B.N. Chichkov, Laser-induced jet formation and droplet ejection from thin metal films, Appl. Phys. A 106 (2012) 479–487, https://doi.org/10.1007/s00339-011-6747-8.
[49] Y. Nakata, N. Miyanaga, T. Okada, Effect of pulse width and fluence of femtosecond laser on the size of nanobump array, Appl. Surf. Sci. 253 (2007) 6555–6557, https://doi.org/10.1016/j.apsusc.2007.01.089.
[50] F. Korte, J. Koch, B.N. Chichkov, Formation of microbumps and nanojets on gold targets by femtosecond laser pulses, Appl. Phys. A 79 (2004) 879–881, https://doi.org/10.1007/s00339-004-2590-5.
[51] S. Zhou, H. Shen, Experimental and numerical studies on micro-bumps without melting of gold films with different thicknesses induced by ultrafast laser, Opt. Commun. 514 (2022), 128178, https://doi.org/10.1016/j.optcom.2022.128178.
[52] A. Kuchmizhak, S. Gurbatov, O. Vitrik, Y. Kulchin, V. Milichko, S. Makarov, S. Kudryashov, Ion-beam assisted laser fabrication of sensing plasmonic nanostructures, Sci. Rep. 6 (2016) 19410, https://doi.org/10.1038/srep19410.
[53] J.S. Yuk, E.F. Guignon, M.A. Lynes, Sensitivity enhancement of a grating-based surface plasmon-coupled emission (SPCE) biosensor chip using gold thickness, Chem. Phys. Lett. 591 (2014) 5–9, https://doi.org/10.1016/j.cplett.2013.10.081.
[54] Y. Song, M. Sun, H. Wu, W. Zhao, Q. Wang, Temperature sensor based on surface plasmon resonance with TiO2-Au-TiO2 triple structure, Materials 15 (2022) 7766, https://doi.org/10.3390/ma15217766.
[55] E. Skliutas, M. Lebedevaite, E. Kabouraki, T. Baldacchini, J. Ostrauskaite, M. Vamvakaki, M. Farsari, S. Juodkazis, M. Malinauskas, Polymerization mechanisms initiated by spatio-temporally confined light, Nanophotonics 10 (2021) 1211–1242, https://doi.org/10.1515/nanoph-2020-0551.
[56] S. Reklaryte, T. Jonsevičius, D. Gailevičius, M. Malinauskas, V. Mizeikis, E. G. Gamaly, S. Juodkazis, Nanoscale precision of 3D polymerization via polarization control, Adv. Opt. Mater. 4 (2016) 1209–1214, https://doi.org/10.1002/adom.201600155.
[57] X. Xie, L. Li, S. Wang, Z. Wang, J. Zhou, Three-dimensional measurement of a tightly focused laser beam, AIP Adv. 3 (2013), 022110, https://doi.org/10.1063/1.4791764.
[58] G.D. Tsibidis, D. Mansour, E. Stratakis, Damage threshold evaluation of thin metallic films exposed to femtosecond laser pulses: the role of material thickness, Opt. Laser Technol. 156 (2022), 108484, https://doi.org/10.1016/j.optlastec.2022.108484.
[59] S.A. Uzunov, A.V. Bulgakov, E.E.B. Campbell, N.M. Bulgakova, Melting of gold by ultrashort laser pulses: advanced two-temperature modeling and comparison with surface damage experiments, Appl. Phys. A 128 (2022) 602, https://doi.org/10.1007/s00339-022-05733-4.
[60] J. Martan, L. Prokešová, D. Moskal, B.C. Ferreira de Faria, M. Honner, V. Lang, Heat accumulation temperature measurement in ultrashort pulse laser micromachining, Int. J. Heat Mass Transfer 168 (2021), 120866, https://doi.org/10.1016/j.ijheatmasstransfer.2020.120866.

[61] R. Geremia, D. Karnakis, D.P. Hand, The role of laser pulse overlap in ultrafast thin film structuring applications, Appl. Phys. A 124 (2018) 641, https://doi.org/10.1007/s00339-018-2045-z.
[62] A. Sharif, N. Farid, M. Wang, K.-L. Choy, G.M. O'Connor, The role of fluence in determining the response of thin molybdenum films to ultrashort laser irradiation; from laser-induced crystallization to ablation via photomechanical ablation and nanostructure formation, Appl. Surf. Sci. 592 (2022), 153315, https://doi.org/10.1016/j.apsusc.2022.153315.
[63] Z. Sun, M. Lenzner, W. Rudolph, Generic incubation law for laser damage and ablation thresholds, J. Appl. Phys. 117 (2015), 073102, https://doi.org/10.1063/1.4913282.

Supplementary Information

Femtosecond Laser Wavelength-Dependent Formation of Plasmonic Gold Nanostructures

Kernius Vilkevičius, Algirdas Selskis, Evaldas Stankevičius*

Author information

Corresponding Author
Kernius Vilkevičius - Department of Laser Technologies, Center for Physical Sciences and Technology (FTMC), Savanoriu Ave. 231, LT-02300, Vilnius, Lithuania;
orcid.org/0000-0001-8109-7286; Email: kernius.vilkevicius@ftmc.lt

Authors

Algirdas Selskis - Department of Characterisation of Materials Structure, Center for Physical Sciences and Technology (FTMC), Sauletekio Ave. 3, LT-10257, Vilnius, Lithuania;
Email: algirdas.selskis@ftmc.lt

Evaldas Stankevičius - Department of Laser Technologies, Center for Physical Sciences and Technology (FTMC), Savanoriu Ave. 231, LT-02300, Vilnius, Lithuania;
Email: evaldas.stankevicius@ftmc.lt

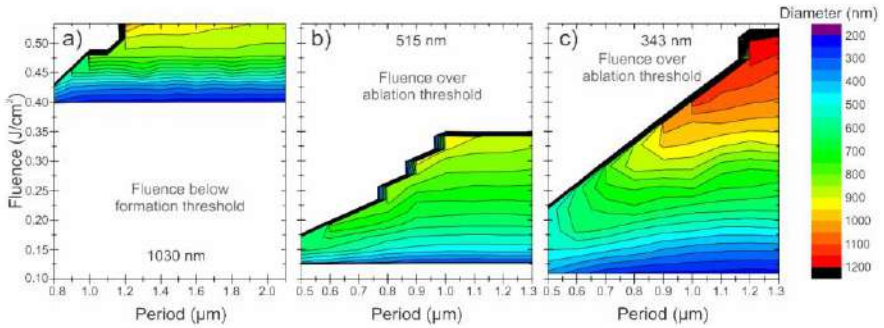

Figure S1. Long axis diameter of the structures' dependence on grating period and formation beam fluence colormap for a) 1H, b) 2H, and c) 3H. The range of fluence is set the same for all harmonics, while the range of period is similar only for the data of the same wavelength.

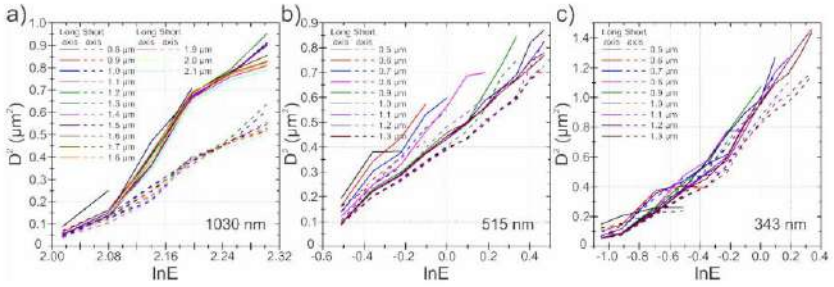

Figure S2. Squared lateral size dependence on the natural logarithm of energy for a) 1H, b) 2H, and c) 3H long and short axis and gratings with different periods.

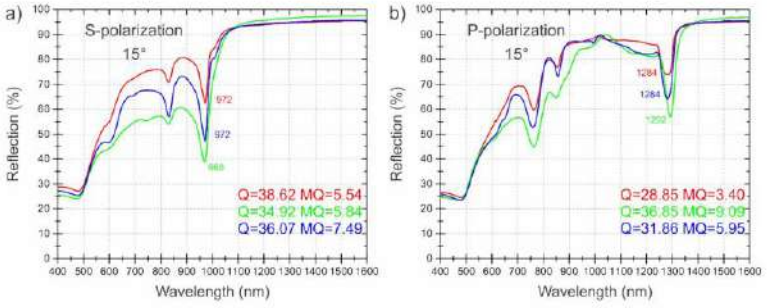

Figure S3. a) *S*- and b) *p*-polarization 15° angle reflection spectra of 1 μm period gold bump gratings fabricated with 1H (red), 2H (green), and 3H (blue).

2nd publication / 2 publikacija

K. Vilkevičius, G. D. Tsibidis, A. Selskis, E. Stratakis, E. Stankevičius, Formation of Highly Tunable Periodic Plasmonic Structures on Gold Films Using Direct Laser Writing,

Advanced Optical Materials, 12(20), 2400172 (2024).

https://doi.org/10.1002/adom.202400172

ADVANCED OPTICAL MATERIALS
www.advopticalmat.de

Formation of Highly Tunable Periodic Plasmonic Structures on Gold Films Using Direct Laser Writing

Kernius Vilkevičius, George D. Tsibidis, Algirdas Selskis, Emmanuel Stratakis, and Evaldas Stankevičius*

Direct laser writing method is a promising technique for the large-scale and cost-effective fabrication of periodic nanostructure arrays exciting hybrid lattice plasmons. This type of electromagnetic mode manifests a narrow and deep resonance peak with a high dispersion whose precise controllability is crucial for practical applications in photonic devices. Here, the formation of differently shaped gold nanostructures using the direct laser writing method on Au layers of different thicknesses is presented. The resonance peak is demonstrated to be highly dependent on the shape of the structures in the array, thus its position in the spectra, as well as the quality, can be additionally modulated by changing the morphology. The shape of the structure and the resonance itself pertain not only on the laser pulse energy but also on the grating period. This overlapping effect occurring at distances smaller than the diameter of the focused laser beam is studied in detail. By taking advantage of the highly controllable plasmonic resonance, the fabricated gratings open up new opportunities for applications in sensing.

1. Introduction

Plasmonic materials have gained significant attention due to their resonant properties and applicability in optical components and sensors,[1] Raman spectroscopy,[2] emitter-based devices,[3] and solar cells.[4] The driving force of such properties is the excitation of surface plasmon polaritons (SPP) and localized surface plasmons (LSP) in the noble metal. LSPs are excited in metallic particles with sizes smaller than the wavelength, while SPPs are excited on the plain metal surface by indirect coupling of photons with SPPs.[5] Although the most widely used method for such coupling is the Kretschmann configuration, which utilizes a glass prism,[6] a simpler and more efficient coupling technique is based on diffraction by fabricating periodic structures on the metal surface[7] when an additional element such as a prism is not required.

The fast fabrication and easy tuning of the absorption peak of such structures are crucial for extensive research and diverse applications. While ion or electron lithography methods are suitable for producing precise nanostructures, they prove to be expensive and time-consuming because these are multi-step fabrication techniques requiring a high vacuum.[8] Structures fabricated through chemical synthesis are more uniform and easier to produce on a large scale.[9] However, this method is also multi-step and requires additional chemicals, which increases manufacturing complexity and cost. Therefore, the use of ultrafast lasers is a promising cost- and time-efficient single-step alternative for nanostructuring. Femtosecond lasers enable fast and smooth processing with minimal thermal impact, leading to the fabrication of wavelength-sized structures on the surface of the material[10] or within its volume.[11] The large-scale arrays of uniformly shaped structures can be fabricated by direct laser writing (DLW)[12] or laser interference lithography (LIL).[13] LIL is a faster structuring process than the DLW method due to the single exposure formation. However, LIL is limited by the size of the array, and the structures in the entire treated area may be non-uniform due to the distribution of the Gaussian beam in the interfered area. In addition, in the case of LIL, beam alignment can be complicated and time-consuming. DLW involves modifying or removing a material with a directly focused laser beam. This method is attractive because of its high accuracy, flexibility, and simplicity compared to other structuring methods.

The morphology of the nanostructures plays a pivotal role in determining the optical[14] or chemical[15] properties of the material. Therefore, the ability to control the size and shape of the particles is crucial. Laser parameters, such as energy,[12a,16] or laser wavelength,[17] can be adjusted to obtain differently shaped and sized structures. When thin films are irradiated with single

K. Vilkevičius, E. Stankevičius
Department of Laser Technologies
Center for Physical Sciences and Technology
Savanoriu Ave. 231, Vilnius 02300, Lithuania
E-mail: kernius.vilkevicius@ftmc.lt
G. D. Tsibidis, E. Stratakis
Institute of Electronic Structure and Laser (IESL)
Foundation for Research and Technology (FORTH)
Vassilika Vouton, Heraklion, Crete 70013, Greece
A. Selskis
Department of Characterization of Materials
Center for Physical Sciences and Technology
Sauletekio Ave. 3, Vilnius 10257, Lithuania
E. Stratakis
Department of Physics
University of Crete
Heraklion, Crete 70013, Greece
The ORCID identification number(s) for the author(s) of this article can be found under https://doi.org/10.1002/adom.202400172

DOI: 10.1002/adom.202400172

pulses of a femtosecond laser, the fast phase transition is initiated and complex nanostructures with energy-dependent morphology at the metal surface are produced.[18] The formation of such hollow nanostructures has been recently widely discussed, and several formation mechanisms have been described. The formation of such single-pulse structures is determined by the thermoelastic stress and induced counterpressure of the substrate leading to the delamination of the film. The surface tension (if a film is not melted) and capillary forces (if a film is melted) decelerate the growth of the structure with the radial flow of the mass along the film with the direction to its axis.[19] Bumps having the shape of a hemisphere are the least pulse energy-requiring structures that form due to induced thermal stresses when the metal layer is heated, causing it to slightly lift upwards. When higher energies are applied and the layer is melted, cones and jets might be obtained as the molten metal gains momentum normal to the surface. During the formation of these shapes, the melt gains velocities towards the structure center, leading to the decrease of the film thickness at the structure sides. Additionally, the counter-motion melt colliding at the center gives rise to jets, both oriented upward and downward (counterjet), the latter being inside the structure.[20] The jets are produced due to the hydrodynamic movement of the molten metal and its height is limited by the surface tension caused by the Rayleigh-Plateau instability, causing the break of the jet and ejection of the spherical nanoparticles at even higher energies.[21]

Periodic arrangement of ordered structures has reached great interest compared to single or randomly distributed structures as the high-quality plasmonic resonances of hybrid modes are excited.[22] Arrays of gold bumps, fabricated by a single direct laser pulse on a thin Au layer, with a period comparable to the light wavelength, excite a hybrid plasmonic mode called hybrid lattice plasmon (HLP). This mode is achieved due to the hybridization of SPPs excited on the metal surface, LSPs excited on individual structures, and the scattered light from the grating, while the properties of such gratings are determined by the excitation of Bragg modes.[23] Gold bumps have demonstrated great results having both narrow and deep HLP resonance with a high dispersion relation in the Vis–NIR range.[24] As the morphologies of such structures have already been extensively described, the impact and formation of these in varying thickness metal layers, as well as the period-induced shape change, have not yet been investigated.

Here, the fabrication of different morphology periodical gold nanostructures on varying Au thicknesses is presented. The thin films from 25 nm up to 100 nm thick were observed to be optimal and sustain the highest-quality plasmon resonances having the largest figure of merits (FOMs),[25] thus this range was chosen for deeper investigation in this research. The resulting arrays excite HLP, with its spectral characteristics (quality and position in the spectra) being highly dependent on the shape. In this paper, to the best of our knowledge, for the first time, we extensively examine the nanostructure morphology change induced by the period reduction below the overlapping threshold. The change in the period and metal thickness provides an additional degree of freedom to easily tune the morphology of the nanostructures, with precise control of the plasmonic properties.

2. Results and Discussion

2.1. Formation of Periodic Nanostructures on Au Films of Different Thickness

The periodic nanostructure arrays were produced on a thin Au film that was deposited onto a clear silica glass using a magnetron sputter coater. The layer thickness was chosen to be 25, 50, 75, and 100 nm and the deposition was done at a constant 0.27 nm s^{-1} coating rate. The films were prepared without an additional adhesion layer, which not only improves the adhesion properties of the coating but also affects the formation parameters of the structures.[26] Subsequently, the structures were fabricated using a Yb:KGW based femtosecond laser (Pharos, Light Conversion Ltd.) and its second harmonic (515 nm), as the formation was achieved with a single laser pulse (**Figure 1a**). The DLW technique was employed to produce large-scale arrays (3×3 mm^2). The fabrication time of such a size array with a period of 1 μm was 30 min, while the production of an array with a period of 700 nm took 45 min. A tightly focused laser beam with a 1.1 μm spot and an objective featuring a numerical aperture of 0.5 were used. The Gaussian intensity distribution of the laser beam allowed us to achieve smaller diameters of the structures and periods of the arrays than the beam size. However, in this chapter, where we compare different shapes on various thicknesses of Au films, to ensure that the outcome is not affected by the beam overlapping, we investigate arrays with an equal 1 μm period.

As the laser pulse energy is increased, various morphological structures are produced. Based on their structural dimensions and characteristic shapes, the main four morphological states were distinguished: bumps, featuring a diameter greater than the apex height; cones, having similar lateral and height dimensions; jets, which have tips taller than their diameter; and crowns, featuring ablated holes in their centers. The bumps, cones, and jets are shown in Figure 1b. Using just enough energy to modify the Au layer, small roundly-shaped protrusions known as bumps are formed. The formation of these requires varying amounts of energy: 0.2, 0.4, 0.6, and 0.75 nJ for 25, 50, 75, and 100 nm Au films, respectively. At higher pulse energies (0.3 nJ (25 nm), 0.75 nJ (50 nm), 1 nJ (75 nm), and 1.25 nJ (100 nm)), the protrusion height increases, and more pronounced cones are produced. At 0.4 nJ (25 nm), 0.95 nJ (50 nm), 1.25 nJ (75 nm), and 1.4 nJ (100 nm), we were able to produce jets with sharp, high, and narrow needle-like tips. Finally, when the energy levels exceed the point of jet splashing, the crowns and holes are fabricated.

Figure 2a illustrates the energy-dependent morphological change with corresponding SEM images of the fabricated structures on 50 and 75 nm Au layers. The bumps and cones observed across all four different thicknesses of metal are quite similar. However, the formation of jets varies depending on film thickness (Figure 2b). For the thinner layers, the produced jets have sharp spikes that are narrow and high, standing either on the surface of the glass (25 nm) or on a cone or a disk-like platform that is made of a collapsed cone (50 nm). By contrast, for the thicker layers (75 and 100 nm), broader jets are formed at the top and in the center of the cone. Jets formed on the 25 nm Au layer manifestly have the thinnest spikes with a diameter-to-height ratio being 1:17, while on 50, 75, and 100 nm Au films the ratios are

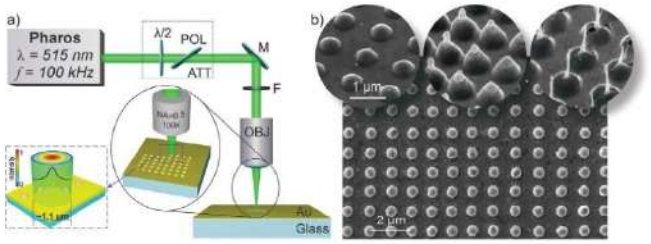

Figure 1. a) Nanostructure formation scheme: fs-laser Pharos, attenuator (ATT) used for the energy control, mirror (M), filter (F) used for an additional energy reduction, and focusing objective (OBJ). The beam is tightly focused onto the metal surface using a high-NA objective. Due to the Gaussian beam distribution, the structures are fabricated only in the central part of the beam. b) SEM images of the top-view periodic array and different morphological states (bumps, cones, jets) at a 53° angle.

1:13, 1:9, and 1:7, respectively. Differences in morphology may be attributed to the varying quantity of the metal in the spike. On the other hand, for the 25 and 50 nm Au layers, hydrothermal phenomena allow the molten part of the metal to flow towards the spike causing the collapse of the surrounding thin layer of the cone. When a thicker metal is used, there is more gold in the regions around the antenna and therefore the pedestal remains conical.

2.2. Thermal Effects Induced in Different Au Thicknesses

An analysis of the thermal effects following irradiation of the Au/SiO_2 two-layered complex at $E = 0.8$ nJ for four values of distinctly different thicknesses ($d = 25$, 50, 75, 100 nm) has been conducted. The results of the induced spatial distribution lattice temperature are illustrated in **Figure 3**, along with the SEM images of the structures obtained at the same conditions. To evaluate the magnitude of the thermal effects, T_i is illustrated in Figure 3 at three different time points (first column: at $6\tau_p$ when laser is switched off (τ_p = 300 fs), second column: when maximum temperature is attained, third column: at $t = 50$ ps).

Theoretical predictions show that a decrease in the material thickness leads to higher lattice temperatures (T_i). This originates predominantly from the fact that smaller thicknesses result in a smaller depth in which the electrons can diffuse.[27] It is known that the electron system loses energy via two competing effects, diffusion and electron-phonon scattering. As the electron diffusion is inhibited for smaller d, hot electrons remain confined in a small volume and, thus, they lose energy, in principle, through electron-phonon scattering. Therefore, the electron temperature decrease is not as rapid as in the case of thicker materials. Thus, as the thickness decreases, the phonon subsystem will interact with an electron system, which is highly energetic and attains large temperatures. Interestingly, at $d = 25$ nm, the maximum T_i attained exceeds a critical temperature T_i^c above which it is assumed that material is ablated (i.e., removed) (shown as a white region in the second and third column in Figure 3a). A thermal criterion was used to select T_i^c. More specifically, $T_i^c = 0.9T_{cr}$ where $T_{cr} = 6250$ K is the critical point for Au[28] and is

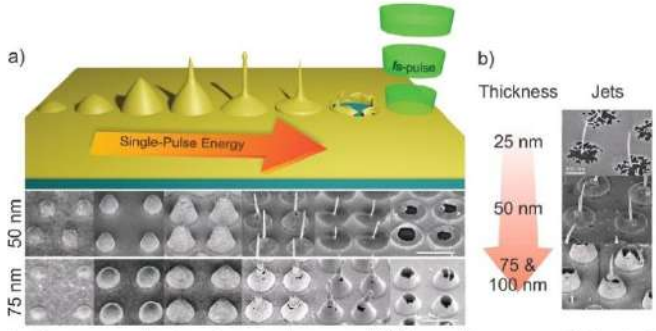

Figure 2. a) Illustration of nanostructure shape dependence on pulse energy and SEM images of nanostructures fabricated on 50 nm (upper row of SEM images) and 75 nm (lower row) thickness Au layer. b) SEM micrographs of jet shape dependence on Au thickness.

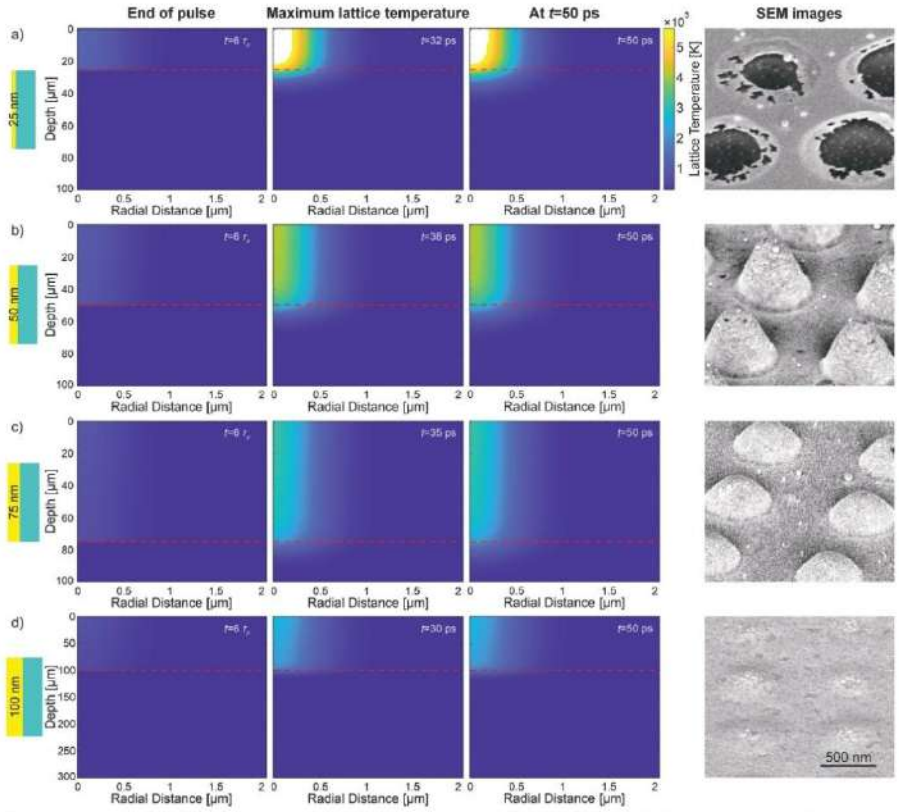

Figure 3. Lattice temperature (T_L) profile in the propagation plane at three-time points: just after the end of the pulse ($6\tau_p$), when T_L reaches the maximum value, and at $t = 50$ ps. The first, second, and third column corresponds to these, respectively. The fourth column represents the SEM images of the practically obtained structures. The first, second, third, and fourth rows refer to the analysis of the T_L for a) $d = 25$ nm, b) 50 nm, c) 75 nm and d) 100 nm. The red dashed line stands for the interface between Au and SiO_2. White region in the first row (second and third column) indicates the ablated part of Au. All simulations were performed at $\lambda_L = 515$ nm, $\tau_p = 300$ fs, and $E = 0.8$ nJ. The same colormap (min–max values) is used in all figures.

taken as the critical value of temperature above which ablation starts to occur. By contrast, for all thicknesses, a phase transition (i.e., melting) occurs in some parts of the material as the lattice temperature exceeds the melting point of Au (i.e., $T_{melt} = 1337$ K). In that case, surface modification is via a mass displacement and not due to mass removal.

The simulated results correspond to the actual structures obtained using the exact parameters. SEM images of those are depicted in the fourth column of Figure 3. Ablated holes are obtained in the thinnest layer, while as the thickness increases, smaller protrusions are achieved due to phase transition occurring in a smaller part of the irradiated zone.

2.3. Tunable Morphology of Energy-Dependent Structures

To analyze the formation of the nanostructures, we utilized a focused Ga ion beam to create the cross-sections of the ones obtained in 75 nm thick Au. Corresponding SEM images can be observed in **Figure 4**. Three distinct morphological structures are all hollow inside, whereas the growing antenna appears to be solid. Comparing the internal height of these structures (cyan arrows in Figure 4), we observe an increase with growing bumps (in this case 322 nm) until the cones are reached (562 nm), when the growth rate for jets slows down (600 nm). At this point, the growth of the spike is rapidly increasing. To analyze the

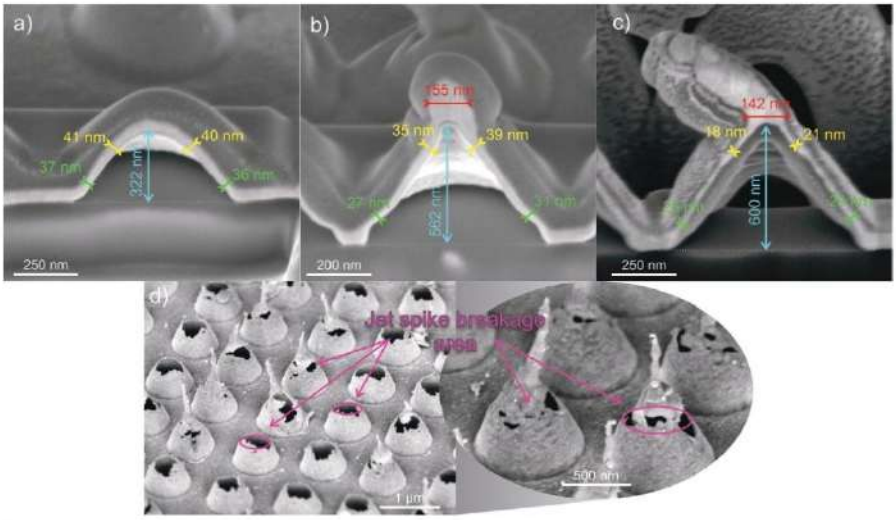

Figure 4. Gold a) bump, b) cone, and c) jet cross-section with internal height and Au thickness measurements fabricated on 75 nm Au. The Au layer is in bright grey, while dark gray is platinum used for better contrast. Blue measurement shows the inside height of the structure, red—spike width, green—Au thickness in the periphery of the structure, yellow—thickness closer to the center of the structure. d) SEM images of broken jets on 100 nm Au with marked jet spike breakage area at the top of the structure, where the layer is the thinnest.

movement of melted material and the formation of specific structures, we measured the thickness of the film in both the lower periphery (green measurements) and upper parts closer to the center of the structure (yellow measurements). The bumps (Figure 4a) have a consistent thickness of approximately 40 nm over the entire cross-section. This suggests that the metal only detaches from the substrate and the movement of the melt has not yet begun. The wall thickness of the cones (Figure 4b) has decreased to 29 nm at the bottom (periphery) of the structure, while it has only slightly reduced at the top (37 nm). Additionally, a small antenna starts to grow at the top of the cone. This demonstrates that molten metal moves from the irradiated periphery to the center, resulting in the formation of a growing small solid tip at the top of the structure. As previously mentioned, such flow towards the center appears due to the temperature gradient and resultant induced velocity.[20a] Here, the collision of the melt at the center has not yet fully started, thus the growing spike is minimal. In the jets (Figure 4c), the wall thickness is consistent at the bottom relative to the cones (27 nm), while the top layer becomes significantly thinner (20 nm), indicating that the impact of melt and further growth of the jet spike is mainly influenced by the movement of material from the areas surrounding the center. This significant thinning of the coating around the peak can explain the jet spike breakage at higher energies in thick coatings, as there is a lower film thickness in that area (Figure 4d).

2.4. Thermal Effects of Different Energy Pulses

An analysis of the thermal effects following irradiation of the Au/SiO_2 two-layered complex for a 50 nm-thick Au layer placed on a SiO_2 substrate has also been conducted for five values of the laser energy (E = 0.2, 0.5, 0.8, 1.1, 2 nJ) and results of the induced spatial distribution lattice temperature are illustrated in **Figure 5**. To evaluate the magnitude of the thermal effects, T_l is illustrated in Figure 5 at three different time points (first column: at $6\tau_p$ when laser is switched off, second column: when maximum temperature is attained, third column: at t = 50 ps).

Theoretical predictions show an anticipated increase of the lattice temperature of Au at increasing the laser energy. In particular, ablation occurs at E = 2 nJ while only melting takes place at lower energies (at E = 0.5 nJ). By contrast, for the lowest value of the energy (E = 0.2 nJ), a phase transition and therefore a surface modification is not predicted. The simulation results are in agreement with the experimental observations illustrated in the SEM images assuming similar laser parameters.

2.5. Grating Period-Induced Tunability of Structure Shape

As previously mentioned, the Gaussian intensity distribution of the laser beam allowed us to achieve smaller diameters of the structures and array periods than the focused beam diameter. To

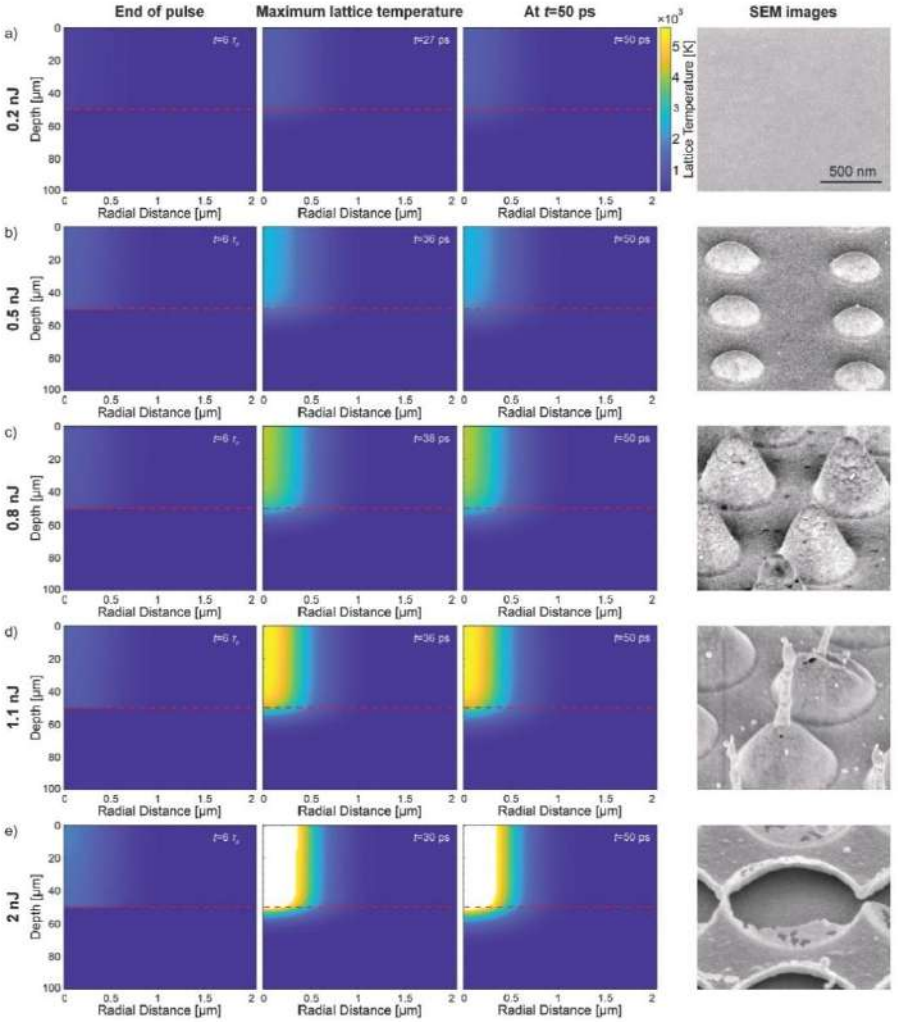

Figure 5. Lattice temperature (T_L) profile in the propagation plane at three-time points: just after the end of the pulse ($6\tau_p$), when T_L reaches the maximum value, at $t = 50$ ps. The first, second, and third column corresponds to these, respectively. The fourth column represents the SEM images of the practically obtained structures. The first, second, third, fourth, and fifth rows refer to the analysis of the T_L for a) $E = 0.2$ nJ, b) 0.5 nJ, c) 0.8 nJ, d) 1.1 nJ, e) 2 nJ. The red dashed line stands for the interface between Au and SiO_2 (assuming a 50 nm Au thick film). White region in the last row (second and third column) indicates the ablated part of Au. All simulations were performed at $\lambda_L = 515$ nm and $\tau_p = 300$ fs. The same colormap (min-max values) is used in all figures.

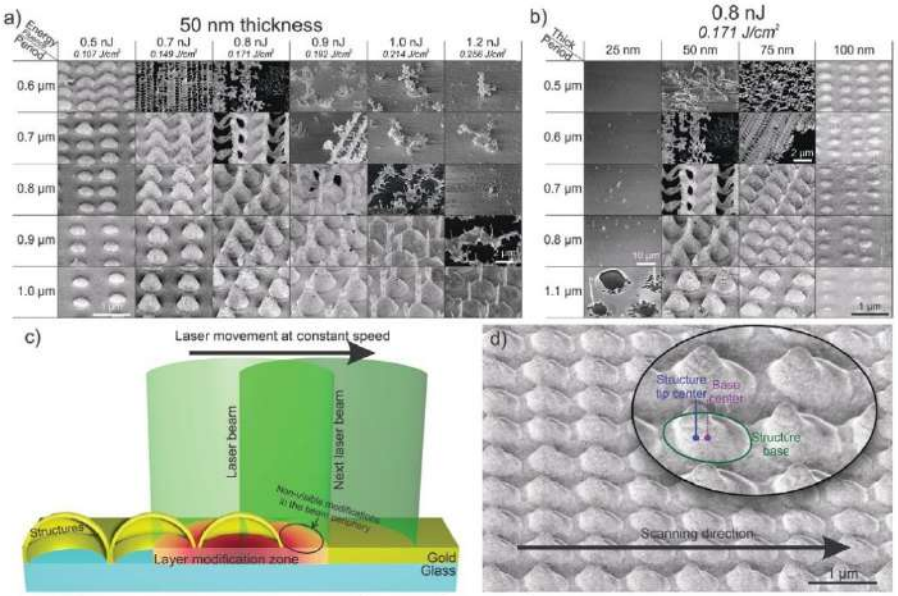

Figure 6. a) Morphology dependence on period and energy/fluence map for 50 nm thickness Au. The period is in rows, while energy is in columns. b) Morphology dependence on period and Au thickness map for constant energy 0.8 nJ (0.171 J cm^{-2}) pulses. c) Illustration of the overlapping effect of the laser beam and the layer modification zone in arrays with periods smaller than the focused laser beam diameter. d) The shift of the structure's tip to the previously modified area in the opposite direction of scanning.

fully understand and gain insight into the effect of the period on the formation energy and morphology, arrays with periods ranging from 0.5 to 1.3 µm were fabricated on all four different thicknesses.

After examining SEM images of each array, a map of the morphology dependence on energy and period was created and represented in **Figure 6a**. First, we observe an energy-dependent change in morphology in the graph, with bumps at lower energies and jets at higher ones. Furthermore, the impact of the period is also demonstrated. For periods smaller than the focused beam diameter (1 µm, a decrease in distance at a constant energy results in the fabrication of the higher-energy requiring structures. Cones are formed by decreasing the bump array period, whereas by reducing the cones' grating inter-structural distance, jets can be produced. The impact of the period on shape is lower than that of pulse energy, thus changing only the distance with constant energy will not lead to the fabrication of all morphological states. Additionally, Figure 6b illustrates the comparison of different period gratings fabricated on various thicknesses of Au using the same pulse energy. The alterations of both distance and thickness lead to an evident change in the structure shape. The full energy-period morphology change maps for 25, 50, 75, and 100 nm can be found in Figures S1,S2, S3, and S4 (Supporting Information), respectively.

Our results demonstrate that by utilizing a sub-diameter period the energy required to fabricate specific shape structures can be lowered. This reduction occurs because a smaller period causes higher overlapping of the irradiated area, leading to fabrication within a previously modified zone. As the laser beam hits the metal surface, the affected layer gains mechanical stresses throughout the whole irradiated region. This effect cannot be attributed to the heat accumulation,[29] as the time between adjacent pulses is quite long (i.e., 7 mm s^{-1} scanning speed with 10 kHz pulse repetition rate, leading to 100 µs between successive pulses). Induced stresses in the peripherical parts of the irradiated area are not high enough to visibly lift the film. Thus, the surface modification in the central area leads to the formation of protrusions, while in the periphery the non-visible slight delamination or intrinsic modifications in the metal are obtained. These only affect the fabrication of the next structure formed with the subsequent overlapping beam pulse, leading to the reduction of the required fluence by reducing the period. Beam overlapping effect is represented in Figure 6c. Meanwhile, if the grating period exceeds the diameter of the focused beam, the shape and

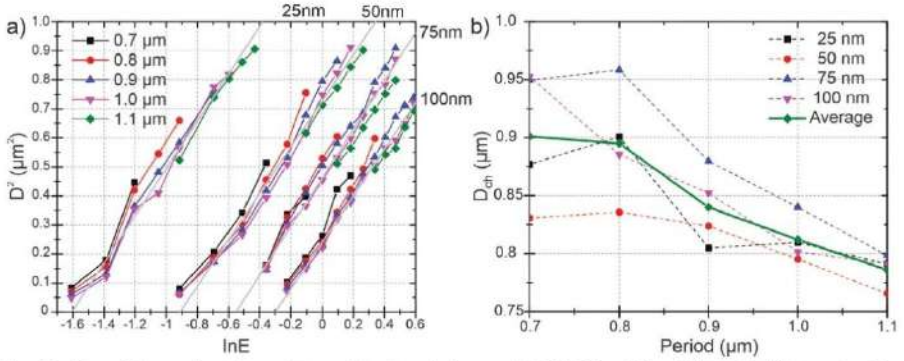

Figure 7. a) Squared diameter dependence on the natural logarithm of pulse energy for 25, 50, 75, and 100 nm Au layers. The different colors depict different grating periods. The linearly approximated 1 μm period array data is represented by a gray line. b) Energy deposition diameter dependence on the grating period. The colored dashed lines depict different layer thicknesses. Solid line represents the averaged values of all different thicknesses for each period.

size of the structures remain constant and are not affected by the distance (can be observed in Figures S1–S4 (Supporting Information) at periods larger than 1.1 μm). In addition, due to the higher overlapping, the shape appears inhomogeneous and nonuniform in the scanning axis. The tip of the structure is formed with a shift towards the previously modified area (already formed structure) relative to its base center (Figure 6d). Such noncentrality is only observable at higher fluences when part of the affected layer is melted.

2.6. Structure Formation Thresholds

In order to determine the formation parameters more accurately, the diameters of all the structures were measured and the dependence of squared diameter on the natural logarithm of formation energy for four distinct Au layer thicknesses was plotted in **Figure 7a**. The differently colored lines illustrate this dependence for different grating periods. By linear approximation of the graph data, the practical layer modification threshold energy and the characteristic energy deposition diameter (area in which laser energy is effectively absorbed for the formation of single-pulse induced nanostructures) can be calculated. The latter diameter is obtained from the slope of the approximated line, while its intersection with the energy axis indicates the minimum energy required for layer modification.

The data dependence for all thicknesses and periods is nearly linear. Comparing the diameters of the structures formed with the same energies but different periods, a tendency of a slight increase in size by reducing the period can be observed, which is attributed to the overlapping effect described above. The characteristic energy deposition diameter dependence on the grating period for each thickness is represented in Figure 7b as dashed lines, with the averaged value for each period as well (green solid line). Here, the general trend of the energy deposition diameter reduction with period increase is observed—from averaged (green solid line in Figure 7b) $D_{ch} = 0.9$ μm at highly overlapping 0.7 and 0.8 μm arrays to $D_{ch} = 0.79$ μm at nonoverlapping 1.1 μm arrays. This change confirms the overlapping effect, indicating that a larger modified zone (structure with a larger diameter) at smaller periods corresponds to a greater-diameter zone at which energy is effectively absorbed for the structure formation. Also, it is worth mentioning that this characteristic energy deposition diameter ($D_{ch} = 0.79$ μm) is smaller than the theoretically calculated Gaussian beam spot size ($D_{spt} = \frac{4 \cdot M^2 \cdot \lambda \cdot f}{\pi \cdot d}$), which in this case is 1.1 μm. Such a discrepancy could be attributed to the idea that the effective energy absorption for structure formation occurs in a region of a smaller radius than the Gaussian beam size (in its center) where the threshold is crossed.

Table 1. Different thickness thin Au layer modification threshold.

Thickness [nm]	25	50	75	100
ln*E*	−1.61	−0.91	−0.545	−0.295
E_{th}, nJ	0.2	0.4	0.58	0.74
F_{th}, J cm^{-2}	0.043	0.085	0.124	0.158

To determine the modification energy while excluding the overlapping effect, the data from the arrays with a period of 1.1 μm was linearly approximated. This approximation is marked in Figure 7a as a gray line. The computed layer modification energy and fluence for each thickness are represented in **Table 1**.

In the thinnest 25 nm coating, the line intersects the abscissa axis at ln$E$ = -1.61, corresponding to energy $E_{th} = 0.2$ nJ. The modification threshold for thicker 50, 75, and 100 nm coatings stands at 0.4, 0.58, and 0.74 nJ, respectively. By comparing the threshold energies at 50 and 25 nm, the change of it is two times, while in thicker 100 and 75 nm this change is only 1.28 times. These results show that in thinner coatings, the modification energy

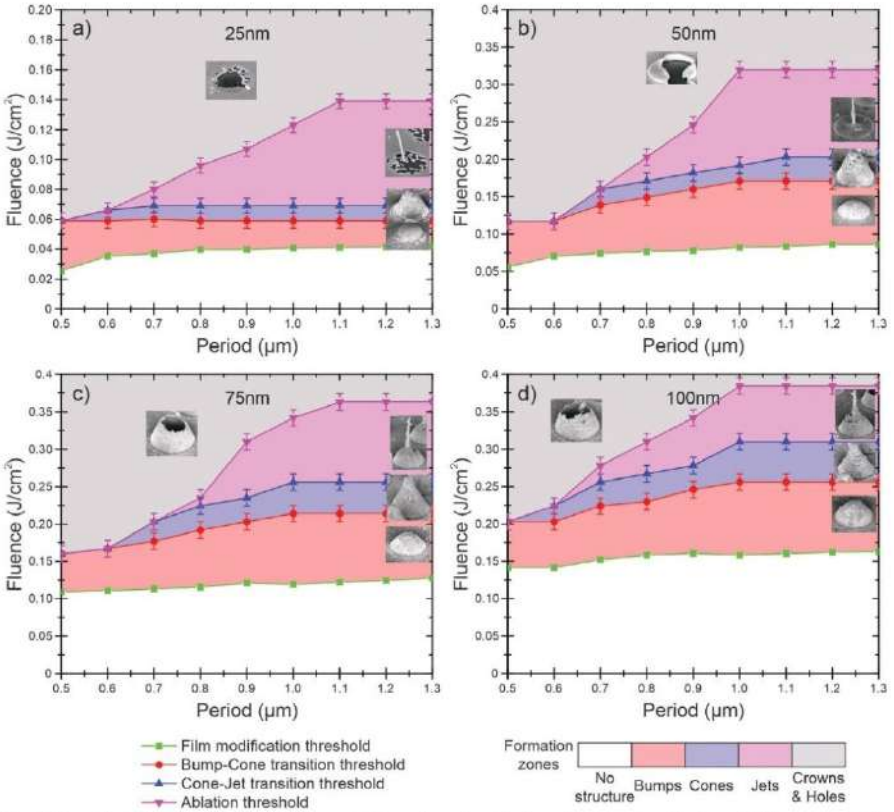

Figure 8. Morphological state transition fluences: layer modification and bump formation (green line), bump transition to cone (red line), cone transition to the jet (blue line), and layer ablation (pink line) fluences in a) 25 nm, b) 50 nm, c) 75 nm, and d) 100 nm layer.

changes more rapidly based on the thickness and the coatings are more sensitive to energy fluctuations.

The fluences for morphological state transitions were determined depending on the period by utilizing the data and maps from Figures S1–S4 (Supporting Information). The transitional fluences are graphically represented in **Figure 8**. The green line indicates the threshold for the bump formation and layer modification, which was obtained from the linear approximation in Figure 7a. The red line represents the fluence at which the morphological phase transition occurs from bumps to cones. The blue line shows the fluence at which cones transition to jets. The pink line indicates the critical fluence at which the destruction of the structures occurs, along with the formation of crowns.

Additionally, the graphs demonstrate a period-influenced overlapping effect, manifested by changes in ablation and shape transition fluences in arrays with a period smaller than the beam size. At higher periods, the fluences remain constant; however, as the period decreases, these decrease as well. The range of fluences where the bumps are fabricated (red zone) is quite broad and can be achieved in all gratings. On the other hand, cones and jets are not produced at extremely small periods (0.5–0.6 μm) and only appear in arrays with a pitch larger than 0.6 μm due to excessive overlapping. In addition, the formation energy range of the cones is the narrowest compared to that of the bump-like and jet-like structures. This is because only structures with similar heights and diameters are considered as the latter morphological state.

2.7. Dependence of Plasmonic Properties on Morphology and Layer Thickness

The fabricated 3×3 mm² periodic gratings generate hybrid lattice plasmon resonance (HLPR), which can be observed as a drop in the reflectance intensity. The reflectance spectra of the arrays were measured using Essentoptics Photon RT UV–Vis–NIR spectrophotometer in the range of 400–1600 nm wavelength with the step of 4 nm. A circular-shaped, 2 mm diameter incident beam was used, and the spectra were measured for both s- and p-polarized light, with a constant 8° angle of incidence. Due to the non-uniform formation of arrays in perpendicular axes, the highest-quality results were achieved when the electric field was perpendicular to the scanning line. Therefore, for different polarizations, the sample was rotated along an azimuthal axis. **Figure 9a,b** displays the reflection spectra of four types of nanostructures—small bumps (height of up to 100 nm), normal bumps, cones, and jets, on a 100 nm thick Au layer with a 1 µm period. Here, mainly the 3 resonant peaks are investigated that correspond to the perpendicular grating of 1 µm: in p-polarization, two peaks corresponding to $m = +1$ (875 nm) and $m = -1$ (1147 nm) diffraction order, and in s-polarization one peak corresponding to $m = \pm 1$ (1000 nm) diffraction order. Other observed peaks are either for higher diffraction order or diagonal grating plane, but these are not investigated. The spectra of the matrix of small bumps are barely distinguishable from an ordinary reflection of plain Au in both s- and p-polarization and only shallow and narrow HLPR dips are visible. For higher bumps, the narrow dip corresponding to $m = -1$ diffraction order becomes intense, with a slight shift to higher wavelengths (1204 nm) for p-polarized light in comparison with smaller structures, while the wavelength remains almost the same for $m = +1$ diffraction order (876 nm) and s-polarization. The resonant wavelength for this type of grating can be calculated theoretically using the diffractive grating formula.[24] For higher cones, this model is not applicable as the $m = -1$ resonant wavelength shifts toward longer wavelengths at p-polarization (1288 nm) and is itself wider and shallower. Arrays of sharp jets have a much wider HLPR with either a significant redshift or a strong decrease in the total reflection in the whole measured range, making induced resonance unobservable. This same tendency is observed across all four different thicknesses.

The main aspect is that the resonance shift is only observed for one peak—at longer wavelengths in p-polarization. Such shift of the resonant wavelength with increasing height of the structure was previously explained by the increased effective period,[30] which covers not only the distance between the structures but also the surface length of the protrusion (Figure 9c). Bumps feature a smoother and shorter top surface, whereas cones and jets possess longer surface distances. Consequently, the larger effective period contributes to the resonance shift. However, the shift with changing height might suggest that this spectral feature can be associated with the out-of-plane (z-axis) electric component of the incident light. Since the p-polarized light incident at an oblique angle covers the vertical component of the electric field, it excites height-dependent out-of-plane plasmonic modes.[31] The out-of-plane mode is determined to suffer from high Ohmic losses at large heights of the structures, which might explain the results of the jet spectrum. The perpendicular component excites in-plane modes that mainly depend on the array period and structure diameter.

The broadening of the peak can be attributed to the nonuniformity of the nanostructures in the array. As previously discussed, the change in height leads to a redshift. The bump structures are quite uniform and the collective resonance occurs at a similar wavelength. With the application of higher fluence and the fabrication of cones, the resulting structure height is more susceptible to fluctuations in pulse energy. A larger distribution of heights results in a distribution of resonant wavelengths and a broadening of the total resonant peak. In jet arrays, each structure is slightly different (jet length, inclination), thus wide variation in height can lead to an extreme broadening of the resonance. Additionally, as it was observed in SEM images (Figure 4d), some structures in jet arrays were broken, which might reduce the total intensity of the reflection.

For theoretical estimation, we used COMSOL Multiphysics modeling to calculate the reflection spectra and near-field profiles of the structures at the main three investigated dips (880, 996 nm, and redshifting 1150–1300 nm). The sizes of the structures for simulations were determined from SEM images. Figure 9d,e shows the calculated reflection spectra for the bump and cone arrays. Meanwhile, the reflection spectrum of the jets is not included because the theoretical calculations do not match the practical results; in fabricated arrays, each structure varies slightly in terms of jet length or inclination, and some structures may even be broken. Therefore, the real spectrum is completely different from the theoretical one, and it is difficult to model such an array. The calculated results are in quite good agreement with the practical ones and the redshift of the longer-wavelength resonance is also observable. The increase in structure height (either bump or cone) leads to a further change in the wavelength. Near-field profiles in the insets of Figure 9d,e additionally give an insight into the nature of these plasmonic modes. Redshifting resonance at longer wavelengths tends to enhance the local field at the top of the structure suggesting the out-of-plane nature of this peak. Other investigated peaks exhibit enhancement at the sides of the structure coinciding with the in-plane excitations.

The main quality parameters of the resonance—width and depth were calculated for matrices of various thicknesses. The depth was measured from the upper-left corner of the most prominent peak and its full width at half minimum (FWHM) was determined. Quality measurements included the calculation of quality (Q)-factor ($Q = \lambda_{res}/\Delta\lambda$), where λ_{res} is resonant wavelength and $\Delta\lambda$ is FWHM. Also, the modified quality (MQ)-factor ($MQ = \frac{\lambda_{res} \cdot h}{\Delta\lambda \cdot 100\%}$), which includes the depth h of the resonant peak. The results of the 1 µm gratings with various structure shapes and Au thicknesses for both s- and p-polarizations at 8° incident light angles are represented in **Figure 10**. The factors of s-polarization results were measured for small bumps, bumps, cones, and jets, while for p-polarized light the jet resonances were not determined due to high redshift. By increasing the formation energy and changing the morphology, the Q-factor from $Q = 100$ at small bump gratings decreases by tenfold in cone and jet arrays. Nonetheless, the MQ-factor for s-polarization is quite similar in small bump and normal bump arrays, whereas for p-polarization the normal bumps exhibit higher quality. The misfit between factors shows that although the Q-factor is higher in

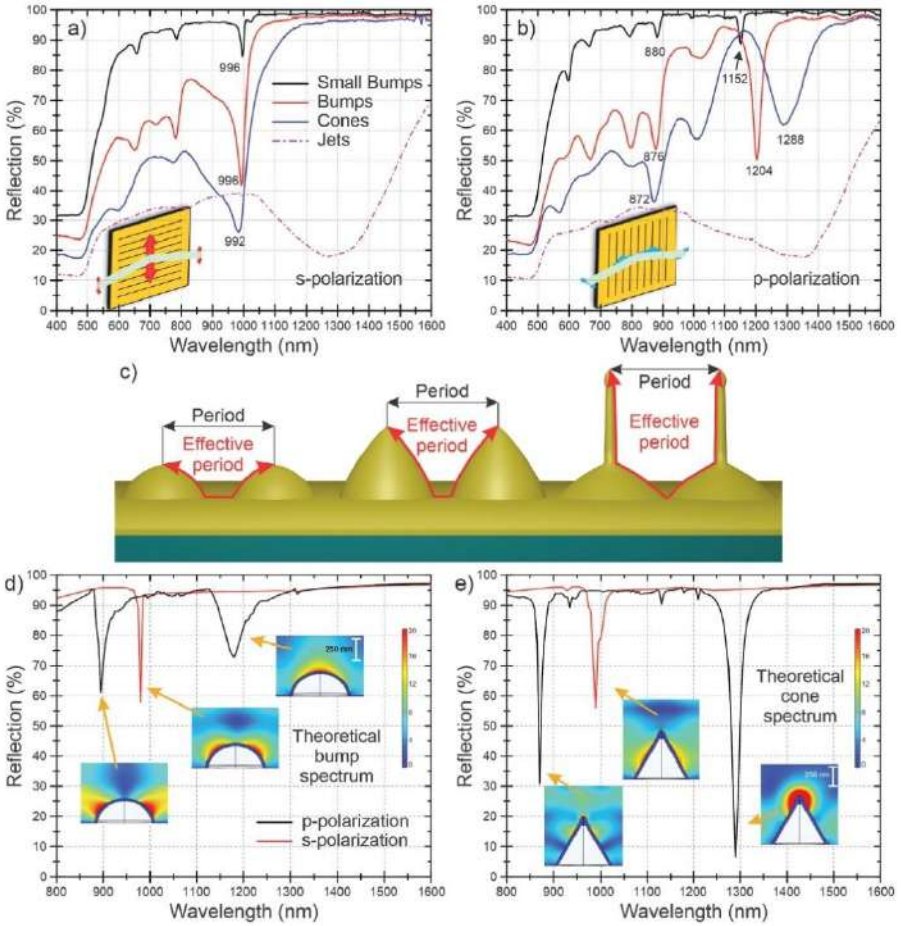

Figure 9. The measured reflectance spectra of different morphological structures: small bumps (black line), bumps (red line), cones (blue line), and jets (purple line) arrays of 1 μm period on 100 nm thickness Au for a) s- and b) p-polarization at 8° light incidence angle. The insets show the azimuthal rotation of the sample. c) Grating period and effective period comparison for different shape structures. Numerically calculated reflection spectra for 1 μm period d) bump and e) cone arrays on 100 nm gold. The insets show the near-field profile at the main 3 investigated resonant peaks.

smaller structures due to the narrow FWHM, the more practical HLPR is observed in higher bumps arrays. This is due to the higher intensity resonance and larger intensity-width ratio. In addition, while there is no significant difference in distinct thicknesses, the 25 nm Au film yields the lowest quality factors, as the structures are small and thin, and the layer itself possesses the lowest reflectivity.

Furthermore, we investigated the impact of reducing the period below the beam diameter on the quality of the resonance. **Figure 11** displays the reflectance spectra of 0.7 μm and 1 μm bump gratings on 50 nm Au film. As the period was reduced, the resonance peak's depth and quality increased despite the observed resonant wavelength shift. The Q-factor increased from $Q = 33.5$ at 1 μm grating to $Q = 43.3$ at 0.7 μm grating in the

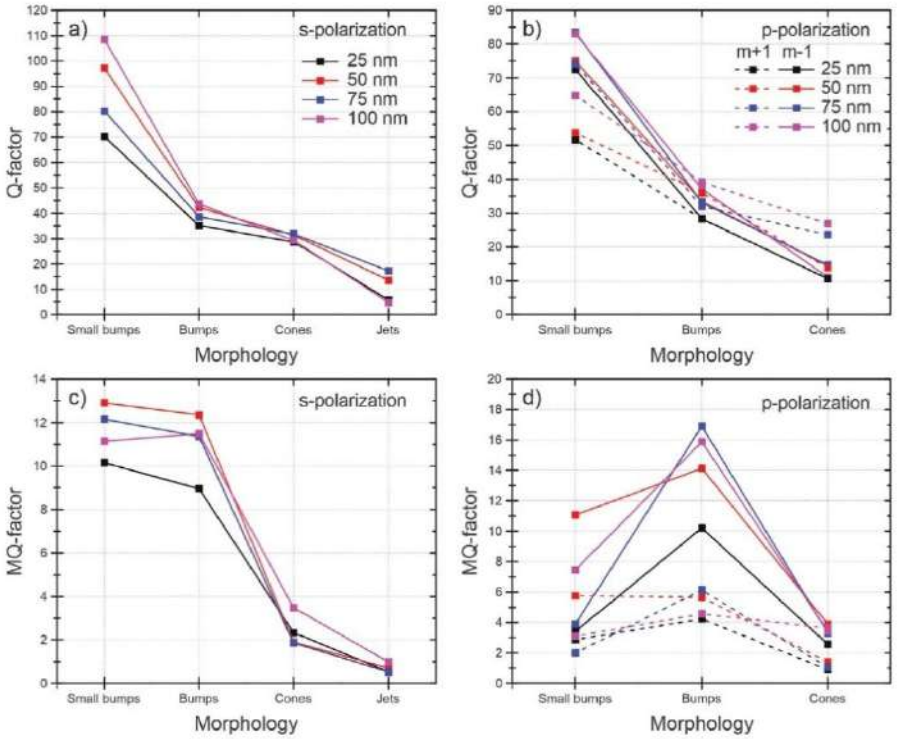

Figure 10. The 1 μm period grating resonant peak a,b) Q-factor and c,d) MQ-factor dependence on the shape of the structure and Au thickness for a,c) s- and b,d) p-polarization at an 8° light incidence angle.

p-polarization measurement, while the MQ-factor changed from MQ = 14.1 to MQ = 23. Meanwhile, in the case of s-polarization, the MQ-factor increased slightly and the Q-factor decreased due to a reduction in the resonant wavelength and a consequent under-reduction of FWHM. When the period is reduced, the interaction among nanostructures intensifies and the HLPR becomes stronger. This is because there are more interacting structures in the same irradiated area.

3. Conclusions

It is shown that the morphology of single ultrashort laser pulses-induced nanostructures can be controlled via an appropriate selection of the pulse energy, thin metal film thickness, and array period. Thin films provide the formation of sharp and narrow jet-like structures, while the thickening of the material changes the formation principle, and shorter but wider structures are obtained. The melt flow during the formation of different morphology structures was also investigated and it was shown that at small energies the molten material moves from the sides of the structures to the central part, while at higher the movement from the central part to the tip occurs. The simulations prove that during all morphological stages, the formation of the material undergoes a phase transformation, and only reaches the ablation threshold when the crowns are formed. Further manipulation in shape can be achieved by reducing the grating period below the size of the beam diameter, as an overlapping effect takes place, which has been studied in detail. Finally, the morphology change offers new opportunities to control plasmon resonance, as the resonant wavelength and its quality change with structure shape, film thickness, and grating distance, thus providing an additional degree of freedom for the tunability of the plasmonic properties.

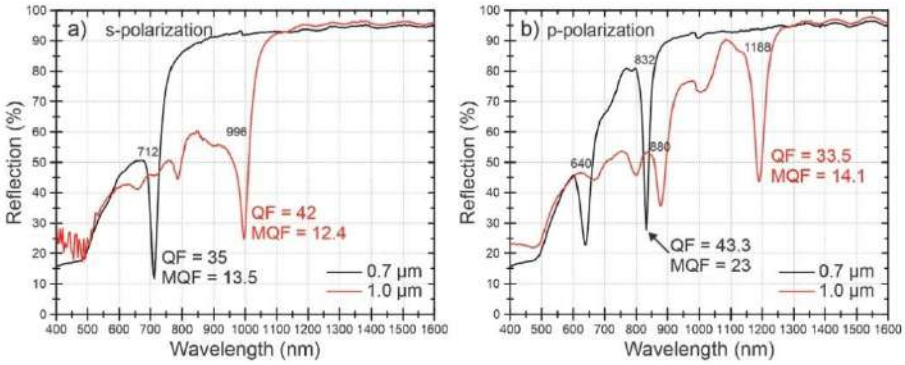

Figure 11. The 0.7 μm (black line) and 1 μm (red line) period bump grating reflection spectra for a) s- and b) p-polarization at 8° light incidence angle on 50 nm Au film.

4. Experimental Section

Sample Preparation: A magnetron sputter coater (Quorum Q150T) was used for the deposition of the thin Au films (25, 50, 75, 100 nm) on soda lime glass. The film thickness was controlled by changing the deposition time from 94 s to 376 s with a constant sputtering rate of ≈0.27 nm s^{-1}.

Laser Processing: The periodic structures were fabricated using single pulses generated by Yb:KGW based femtosecond laser (Pharos, Light Conversion Ltd.). The second harmonic (515 nm) of the laser was used and the DLW technique was employed, tightly focusing the laser beam into a 1.1 μm spot using an objective featuring a numerical aperture of 0.5. The size of the fabricated arrays for SEM imaging was 100 × 100 μm^2 and for reflectance measurements was 3 × 3 mm^2. The range of investigated periods was 0.5–1.3 μm.

Characterization: The structures in the gratings were characterized using a scanning electron microscope (Helios NanoLab650). The diameters were measured from the images tilted at a 57° angle, using the image processing tool ImageJ. The morphology was distinguished according to the height-diameter ratio: structures with diameters larger than the height were considered bumps, the ones having similar dimensions (ratio close to 1) were cones, while those with high and narrow spikes were jets. The cross-sectional cuts of the structures were performed using a focused Ga ions beam, followed by a Pt layer deposition on the top using FIB-SEM Helios NanoLab650. The plasmonic properties of the gratings were characterized using a spectrophotometer (Photon RT, Essentoptics). The reflectance spectra for linearly polarized light were measured in the wavelength range of 400–1600 nm using 8° angle of incidence.

Theoretical Model: To describe the effects on the Au/SiO_2 two-layered complex following irradiation with fs pulses, a theoretical framework is employed to explore the excitation and thermal response of the structure. The simulation algorithm is based on the use of a Two Temperature Model (TTM) that represents the standard approach to evaluate the dynamics of electron excitation and relaxation processes in solids.[32] In this work, the response of the structure with laser pulses of wavelength λ_L = 515 nm and pulse duration equal to τ_p = 300 fs is simulated assuming a Gaussian beam of radius (r_0 = 0.68 μm). The intensity profile of the laser beam is provided by the following expression:

$$S = \frac{(1-R-T)\sqrt{4\log(2)F}}{\sqrt{\pi}\tau_p(\alpha^{-1}+L_b)} \frac{1}{(1-\exp(-d/(\alpha^{-1}+L_b))} \exp\left(-4\log(2)\left(\frac{t-3t_p}{t_p}\right)^2\right)\exp\left(-2\left(\frac{r}{r_0}\right)^2\right) \quad (1)$$

where R and T stand for the reflectivity and transmissivity, respectively, L_b corresponds to the ballistic length for Au (≈100 nm[33]), α is the absorption coefficient for Au, and F is the peak fluence of the laser beam ($F = \frac{2E}{\pi r_0^2}$) where E stands for the laser energy. On the other hand, t is the time, assuming the laser beam is switched on at $t = 0$ and it is switched off at $t = 6\tau_p$ and r is the radial distance from the spot center. Due to the small thickness of the superstrate (Au), the optical parameters of the complex (Au/SiO_2) are expected to be influenced by the optical characteristics of both Au and SiO_2. Thus, a multireflection theory is employed to calculate these parameters which determine the excitation level in Au. Thermal effects occur in both materials; however, the transmitted energy is not sufficient to produce excitation to the substrate. A more detailed investigation of the excitation and thermal effects in the Au/SiO_2 is presented in ref.[27]

Numerical Simulation: The reflection spectra and near-field profile of the plasmonic nanostructures were calculated using the finite element method implemented in COMSOL Multiphysics solver. The wavelength ranging from 800 to 1600 nm (the zone of interest for the main 3 investigated peaks) with a step of 5 nm was used to irradiate the structures at an 8° angle of incidence. The structure was described in a rectangular domain with periodic boundary conditions (Floquet periodicity) in both axes (1 μm period). To avoid boundary reflections, two perfectly matched layers were applied to the top and bottom of the domain. The structures were described as hollow ellipsoids or truncated cones with very short (for cones) or long (for jets) solid elliptical tips on a 100 nm gold layer. The dimensions of the structures were taken from SEM images. Johnson and Christy's data[34] were used for the dielectric function of gold. The thin film and structure were located on a soda-lime glass substrate with a

determined thickness of 1 µm. Air domain was used above the structure with its thickness being double the used wavelength.

Supporting Information

Supporting Information is available from the Wiley Online Library or from the author.

Acknowledgements

Ev.S. and K.V. have received funding from the Research Council of Lithuania (LMT, Lithuania) under the project No. S-MIP-23-32. This work was also supported by the EU-Horizon 2020 Nanoscience Foundries and Fine Analysis (NEP) Project (Grant agreement ID 101007417) having benefited from the access provided by the Foundation for Research and Technology Hellas (FORTH) (Access project ID 369).

Conflict of Interest

The authors declare no conflict of interest.

Data Availability Statement

The data that support the findings of this study are available from the corresponding author upon reasonable request.

Keywords

direct laser writing, gold nanobumps, gold nanocones, gold nanojets, periodic plasmonic structures, thermal effects simulations

Received: January 19, 2024
Revised: March 15, 2024
Published online: April 11, 2024

[1] a) X. Wen, S. Deng, *Adv. Opt. Mater.* **2023**, *11*, 2300401; b) X. Lv, F. Wu, Y. Tian, P. Zuo, F. Li, G. Xu, W. Niu, *Adv. Mater.* **2023**, *35*, 2305429; c) M. Vala, C. T. Ertsgaard, N. J. Wittenberg, S.-H. Oh, *ACS Sens.* **2019**, *4*, 3265.

[2] a) X. Wang, S.-C. Huang, S. Hu, S. Yan, B. Ren, *Nat. Rev. Phys.* **2020**, *2*, 253; b) V. Petrikaitė, I. Ignatjev, A. Selskis, G. Niaura, E. Stankevičius, *Opt. Laser Technol.* **2024**, *168*, 109956.

[3] a) K. A. Sergeeva, D. V. Pavlov, A. A. Seredin, E. V. Mitsai, A. A. Sergeev, E. B. Modin, A. V. Sokolova, T. C. Lau, K. V. Baryshnikova, M. I. Petrov, S. V. Kershaw, A. A. Kuchmizhak, K. S. Wong, A. L. Rogach, *Adv. Funct. Mater.* **2023**, *33*, 2307660; b) D. Ge, S. Marguet, A. Issa, S. Jradi, T. H. Nguyen, M. Nahra, J. Béal, R. Deturche, H. Chen, S. Blaize, J. Plain, C. Fiorini, L. Douillard, O. Soppera, X. Q. Dinh, C. Dang, X. Yang, T. Xu, B. Wei, X. W. Sun, C. Couteau, R. Bachelot, *Nat. Commun.* **2020**, *11*, 3414.

[4] E. Stratakis, E. Kymakis, *Mater. Today* **2013**, *16*, 133.

[5] B. Wang, P. Yu, W. Wang, X. Zhang, H.-C. Kuo, H. Xu, Z. M. Wang, *Adv. Opt. Mater.* **2021**, *9*, 2001520.

[6] a) N. Shukla, P. Chetri, R. Boruah, A. Gogoi, G. A. Ahmed, in *Recent Advances in Plasmonic Probes: Theory and Practice* (Eds: R. Biswas, N. Mazumder), Springer International Publishing, Cham, Switzerland **2022**; pp. 191–222. b) P. Arora, E. Talker, N. Mazurski, U. Levy, *Sci. Rep.* **2018**, *8*, 9060.

[7] a) A. Danilov, G. Tselikov, F. Wu, V. G. Kravets, I. Ozerov, F. Bedu, A. N. Grigorenko, A. V. Kabashin, *Biosens. Bioelectron.* **2018**, *104*, 102; b) Y. Bai, H. Zheng, Q. Zhang, Y. Yu, S.-d. Liu, *Opt. Express* **2022**, *30*, 45400.

[8] a) H. Duan, H. Hu, K. Kumar, Z. Shen, J. K. W. Yang, *ACS Nano* **2011**, *5*, 7593; b) Q. Liu, Y. Song, P. Zeng, C. Zhang, Y. Chen, H. Wang, Y. Luo, H. Duan, *Appl. Surf. Sci.* **2020**, *526*, 146690; c) M. Hentschel, J. Karst, H. Giessen, *Adv. Opt. Mater.* **2020**, *8*, 2000879.

[9] a) X. Xu, Q. Yang, N. Wattanatorn, C. Zhao, N. Chiang, S. J. Jonas, P. S. Weiss, *ACS Nano* **2017**, *11*, 10384; b) S. D. Golze, R. A. Hughes, S. Rouvimov, R. D. Neal, T. B. Demille, S. Neretina, *Nano Lett.* **2019**, *19*, 5653.

[10] a) V. V. Belloni, M. Hassan, L. Furfaro, R. Giust, A.-M. Seydoux-Guillaume, S. Sao-Joao, F. Courvoisier, *Laser Photonics Rev.* **2024**, *8*, 2300687; b) E. H. Waller, S. Duran, G. v. Freymann, *Nanophotonics* **2023**, *12*, 1549.

[11] a) Y. Zhang, D. Wu, Y. Zhang, Y. Bian, C. Wang, J. Li, J. Chu, Y. Hu, *Int. J. Extreme Manuf.* **2023**, *5*, 042012; b) E. Stankevičius, M. Garliauskas, M. Gedvilas, G. Račiukaitis, *Opt. Express* **2015**, *23*, 28557; c) E. Stankevičius, M. Garliauskas, G. Raciukaitis, *J. Laser Micro/Nanoeng.* **2016**, *11*, 352.

[12] a) W. Han, L. Jiang, X. Li, Q. Wang, S. Wang, J. Hu, Y. Lu, *Sci. Rep.* **2017**, *7*, 17333; b) C. Ruiz de Galarreta, N. Casquero, E. Humphreys, J. Bertolotti, J. Solis, C. D. Wright, J. Siegel, *ACS Appl. Mater. Interfaces* **2022**, *14*, 3446; c) D. Pavlov, A. Porfirev, S. Khonina, L. Pan, S. I. Kudryashov, A. A. Kuchmizhak, *Appl. Surf. Sci.* **2021**, *541*, 148602.

[13] a) Y. Nakata, K. Murakawa, N. Miyanaga, A. Narazaki, T. Shoji, Y. Tsuboi, *Nanomaterials* **2018**, *8*, 477; b) E. Stankevicius, M. Gedvilas, G. Raciukaitis, *Appl. Phys. B* **2015**, *119*, 525.

[14] a) Z. Guo, G. Yu, Z. Zhang, Y. Han, G. Guan, W. Yang, M.-Y. Han, *Adv. Mater.* **2023**, *35*, 2206700; b) A. Gentile, F. Ruffino, M. G. Grimaldi, *Nanomaterials* **2016**, *6*, 110.

[15] a) L. Yuan, M. Lou, B. D. Clark, M. Lou, L. Zhou, S. Tian, C. R. Jacobson, P. Nordlander, N. J. Halas, *ACS Nano* **2020**, *14*, 12054; b) L. Yang, Z. Zhou, J. Song, X. Chen, *Chem. Soc. Rev.* **2019**, *48*, 5140.

[16] V. Piotto, L. Litti, M. Meneghetti, *J. Phys. Chem. C* **2020**, *124*, 4820.

[17] a) K. Vilkevičius, A. Selskis, E. Stankevičius, *Appl. Surf. Sci.* **2023**, *617*, 156629; b) E. Solati, L. Dejam, D. Dorranian, *Opt. Laser Technol.* **2014**, *58*, 26.

[18] a) D. Pavlov, S. Syubaev, A. Kuchmizhak, S. Gurbatov, O. Vitrik, E. Modin, S. Kudryashov, X. Wang, S. Juodkazis, M. Lapine, *Appl. Surf. Sci.* **2019**, *469*, 514; b) C. Unger, J. Koch, L. Overmeyer, B. N. Chichkov, *Opt. Express* **2012**, *20*, 24864.

[19] a) Y. P. Meshcheryakov, N. M. Bulgakova, *Appl. Phys. A* **2006**, *82*, 363; b) N. A. Inogamov, V. V. Zhakhovsky, V. A. Khokhlov, Y. V. Petrov, K. P. Migdal, *Nanoscale Res. Lett.* **2016**, *11*, 177.

[20] a) N. A. Inogamov, V. V. Zhakhovskii, V. A. Khokhlov, *J. Exp. Theor. Phys.* **2015**, *120*, 15; b) X. Wang, Y. Zhang, L. Wang, J. Xian, M. Jin, M. Kang, *Appl. Phys. A* **2016**, *123*, 51; c) Y. Guo, K. Zhang, M. Zhang, Y. Chai, Y. Du, G. Hu, *Opt. Express* **2021**, *29*, 20063.

[21] a) J. Bonse, J. Krüger, *Appl. Phys. A* **2022**, *129*, 14; b) A. Kuchmizhak, S. Gurbatov, O. Vitrik, Y. Kulchin, V. Milichko, S. Makarov, S. Kudryashov, *Sci. Rep.* **2016**, *6*, 19410; c) V. I. Emel'yanov, D. A. Zayarniy, A. A. Ionin, I. V. Kiseleva, S. I. Kudryashov, S. V. Makarov, T. H. T. Nguyen, A. A. Rudenko, *JETP Lett.* **2014**, *99*, 518.

[22] a) X. Qi, L. A. Pérez, M. I. Alonso, A. Mihi, *ACS Appl. Mater. Interfaces* **2024**, *16*, 1259; b) M. S. Bin-Alam, O. Reshef, Y. Mamchur, M. Z. Alam, G. Carlow, J. Upham, B. T. Sullivan, J.-M. Ménard, M. J. Huttunen, R. W. Boyd, K. Dolgaleva, *Nat. Commun.* **2021**, *12*, 974; c) M. Braïk, T. Geronimi-Jourdain, S. Lau-Truong, A. Belkhir, S. Gam-Derouich, A. Chevillot-Biraud, C. Mangeney, N. Félidj, *Nanophotonics* **2023**, *12*, 2179.

[23] a) M. Sarkar, J.-F. Bryche, J. Moreau, M. Besbes, G. Barbillon, B. Bartenlian, M. Canva, *Opt. Express* **2015**, *23*, 27376; b) M. Sarkar, M.

Besbes, J. Moreau, J.-F. Bryche, A. Olivéro, G. Barbillon, A.-L. Coutrot, B. Bartenlian, M. Canva, *ACS Photonics* **2015**, *2*, 237.
[24] E. Stankevičius, K. Vilkevičius, M. Gedvilas, E. Bužavaitė-Vertelienė, A. Selskis, Z. Balevičius, *Adv. Opt. Mater.* **2021**, *9*, 2100027.
[25] a) J. S. Yuk, E. F. Guignon, M. A. Lynes, *Chem. Phys. Lett.* **2014**, *591*, 5; b) R. Zhang, S. Pu, X. Li, *Sensors* **2019**, *19*, 4345; c) R. Ghayoor, S. Zangenehzadeh, A. Keshavarz, *Plasmonics* **2022**, *17*, 1831.
[26] R. Liudvinavičius, A. Selskis, E. Stankevičius, *Opt. Laser Technol.* **2024**, *175*, 110807.
[27] G. D. Tsibidis, D. Mansour, E. Stratakis, *Opt. Laser Technol.* **2022**, *156*, 108484.
[28] a) N. Bulgakova, I. Burakov, Y. Meshcheryakov, R. Stoian, A. Rosenfeld, I. Hertel, *J. Laser Micro/Nanoeng.* **2007**, *2*, 76; b) G. D. Tsibidis, E. Stratakis, *Sci. Rep.* **2020**, *10*, 8675.
[29] a) D. S. Ivanov, P. Shakhov, G. Tikhonowsky, A. A. Popov, A. N. Mayorov, I. N. Zavestovskaya, S. M. Klimentov, A. V. Kabashin, *Appl. Surf. Sci.* **2024**, *643*, 158662; b) A. S. Nikolov, I. I. Balchev, N. N. Nedyalkov, I. K. Kostadinov, D. B. Karashanova, G. B. Atanasova, *Appl. Phys. A* **2017**, *123*, 719.
[30] D. Pavlov, A. Zhizhchenko, L. Pan, A. A. Kuchmizhak, *Micromachines* **2022**, *15*, 1834.
[31] a) W. Zhou, T. W. Odom, *Nat. Nanotechnol.* **2011**, *6*, 423; b) G. H. Y. Li, G. Li, *J. Opt. Soc. Am. B* **2019**, *36*, 805; c) W. Zhou, Y. Hua, M. D. Huntington, T. W. Odom, *J. Phys. Chem. Lett.* **2012**, *3*, 1381.
[32] S. Anisimov, B. Kapeliovich, T. Perelman, *Zh. Eksp. Teor. Fiz.* **1974**, *66*, 375.
[33] J. Hohlfeld, S. S. Wellershoff, J. Güdde, U. Conrad, V. Jähnke, E. Matthias, *Chem. Phys.* **2000**, *251*, 237.
[34] P. B. Johnson, R. W. Christy, *Phys. Rev. B* **1972**, *6*, 4370.

ADVANCED OPTICAL MATERIALS

Supporting Information

for *Adv. Optical Mater.*, DOI 10.1002/adom.202400172

Formation of Highly Tunable Periodic Plasmonic Structures on Gold Films Using Direct Laser Writing

Kernius Vilkevičius, George D. Tsibidis, Algirdas Selskis, Emmanuel Stratakis and Evaldas Stankevičius*

Supporting Information

Plasmonic structures formation in different thicknesses of gold film using direct laser writing

Kernius Vilkevičius, George D. Tsibidis, Algirdas Selskis, Emmanuel Stratakis, and Evaldas Stankevičius*

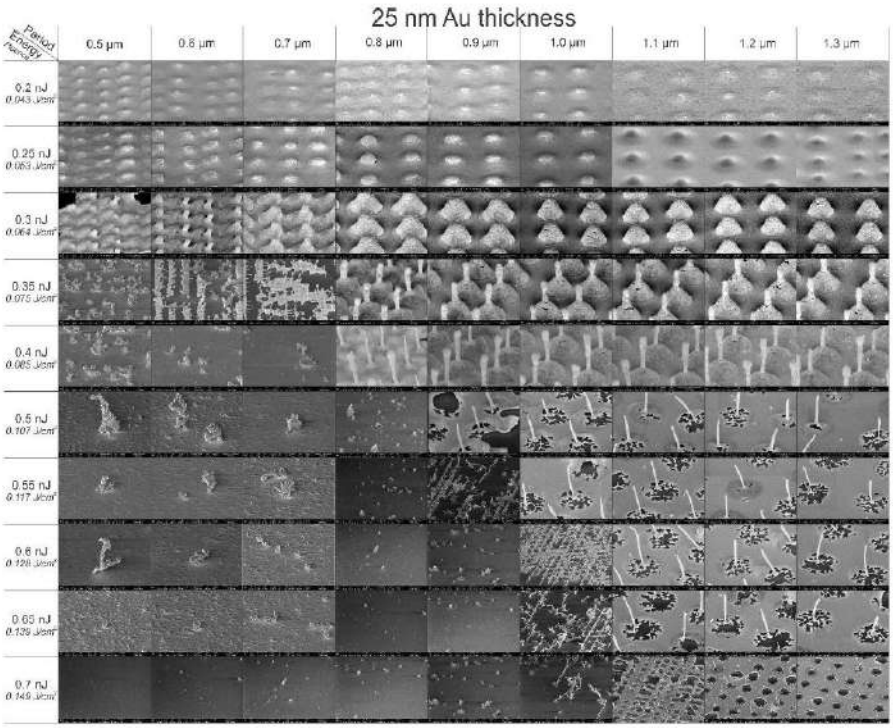

S1. Morphology dependence on period and energy/fluence map for 25 nm thickness Au.

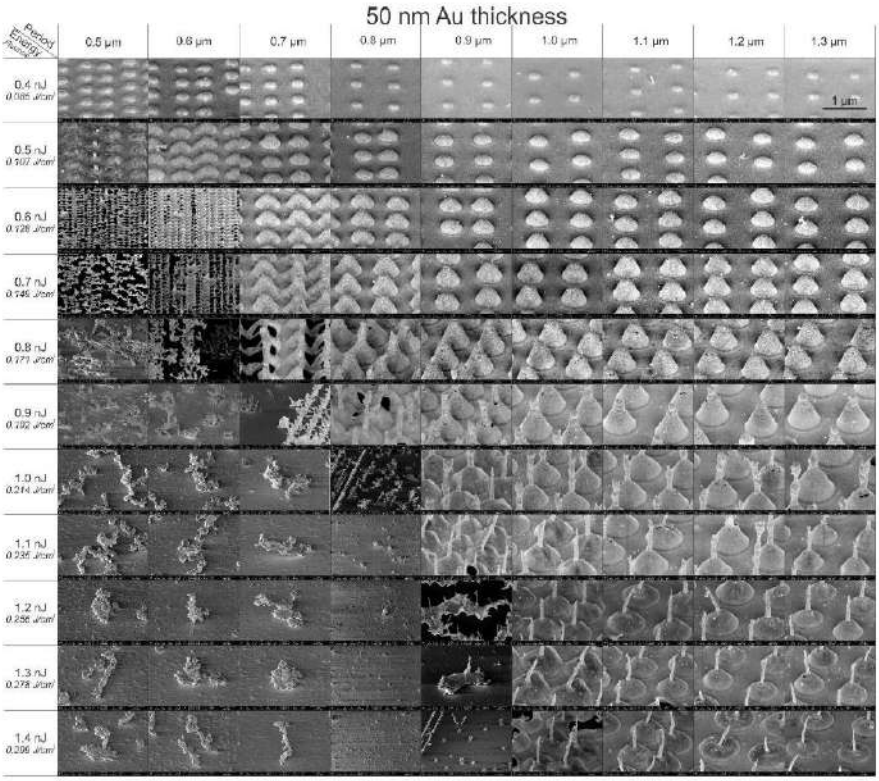

S2. Morphology dependence on period and energy/fluence map for 50 nm thickness Au.

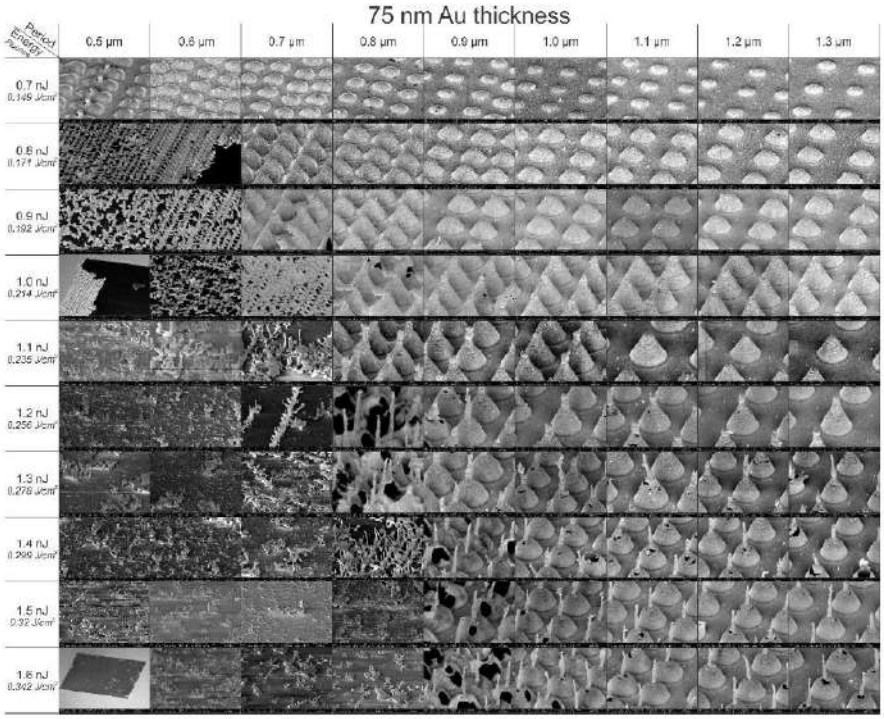

S3. Morphology dependence on period and energy/fluence map for 75 nm thickness Au.

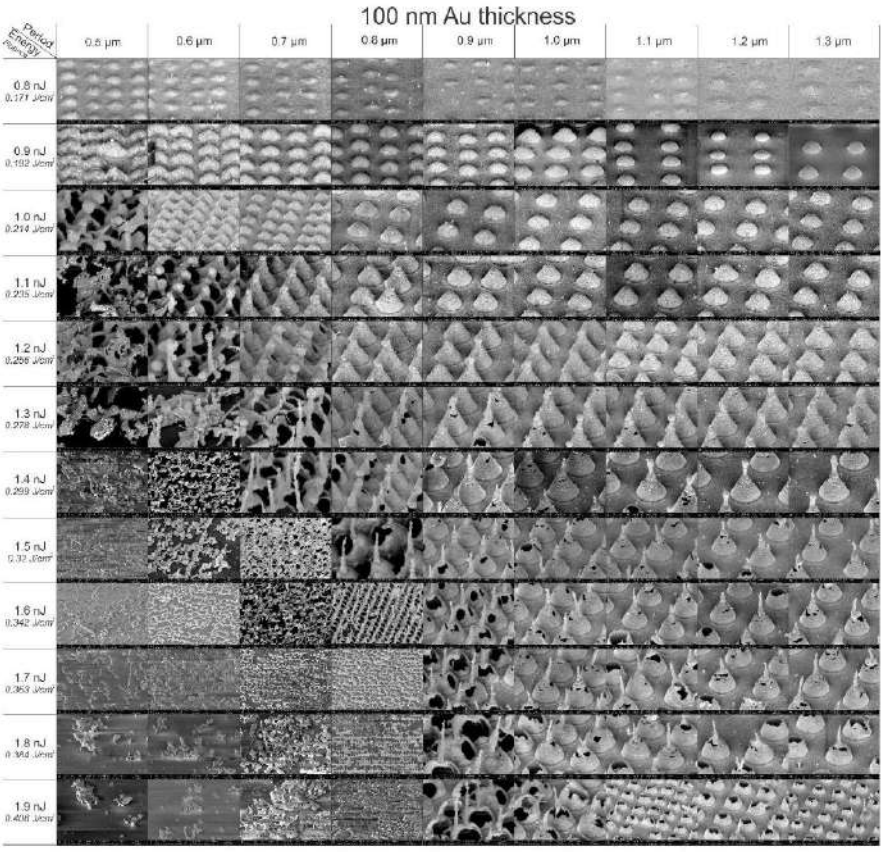

S4. Morphology dependence on period and energy/fluence map for 100 nm thickness Au.

3rd publication / 3 publikacija

K. Vilkevičius, K. Čepaitis, A. Selskis, E. Stankevičius,

Ultrafast Laser Ablation and Modification of Thin Metal Film for Quasi-1D Array Formation,

Optics & Laser Technology, 183, 112330 (2025).

https://doi.org/10.1016/j.optlastec.2024.112330

Optics & Laser Technology 183 (2025) 112330

Contents lists available at ScienceDirect

Optics and Laser Technology

journal homepage: www.elsevier.com/locate/optlastec

Full length article

Ultrafast laser ablation and modification of thin metal film for quasi-1D array formation

Kernius Vilkevičius [a,*], Kipras Čepaitis [a], Algirdas Selskis [b], Evaldas Stankevičius [a]

[a] Department of Laser Technologies, Center for Physical Sciences and Technology, Savanoriu av. 231, LT-02300 Vilnius, Lithuania
[b] Department of Characterization of Materials Structure, Center for Physical Sciences and Technology, Sauletekio av. 3, LT-10257 Vilnius, Lithuania

ARTICLE INFO

Keywords:
Direct laser writing
Laser modification
Laser ablation
Plasmonic grating
Gold nanostructuring

ABSTRACT

One-dimensional and two-dimensional periodic gratings on thin gold film surfaces are fabricated with direct laser writing, employing both ablation and layer modification mechanisms. The variation in the pulse energy and pulse overlapping results in the formation of arrays with distinct plasmonic properties. Ablation is employed for the formation of 1D lattices, whereas metal surface modification is used for the fabrication of quasi-1D and 2D gratings. Laser-scanning fabrication allows for the individual control of grating and in-line periods, leading to the production of a quasi-1D array with 2D geometry and 1D plasmonic properties. The formation of such an array allows for the acquisition of 2D-grating quality hybrid lattice plasmonic resonances with the spectral characteristics of a 1D-grating while eradicating the occurrence of additional resonances that are typical of 2D arrays. The resulting quasi-1D arrays thus combine the advantages of both 1D and 2D designs, offering a unique platform for tuning plasmonic resonances for various optical applications.

1. Introduction

Various 1D and 2D gratings and arrays are constantly being examined for their potential applications in the micro- and nanotechnology areas. Often these structures are fabricated using plasmonic metals (gold, silver, aluminum), which enable strong light-matter interactions and coupling of incident light with collective electron oscillations at the metal surface. These properties allow for the application of such surface modifications in various fields, such as surface-enhanced Raman spectroscopy (SERS) [1–5], superhydrophobic and antibacterial surfaces [6–8], photovoltaics [9,10] and various sensors [11–14]. Some of the applications are based more on localized surface plasmons (LSPs) [15–17], which are the collective oscillations of electrons confined to a nanoparticle, or surface plasmon polaritons (SPPs) [18,19], which occur when incident light excites surface plasmons and couples with them, resulting in a wave that propagates along a metal-dielectric surface. While LSPs are easily excited by incident light, SPPs require a method to address the momentum mismatch between incident light and the SPP to couple efficiently. The momentum mismatch can be resolved using prisms in Otto or Kretschmann configurations [20] or through the use of a diffraction grating [21]. The utilization of the aforementioned configuration facilitates the excitation of the SPPs directly at the sample surface, obviating the necessity for an additional element. Some of the fabrication methods of such gratings include focused ion beam milling [22,23], laser interference [24], electron-beam [25,26], or nanosphere lithography [27].

Another promising method of fabricating such gratings is by implementing direct laser writing (DLW). The DLW technique allows for direct modification or ablation of various surfaces by ultrafast laser pulses. While often used in polymers to produce structures within the material [28,29], DLW is being explored as a fabrication method for periodic nanostructures on thin layers, including both polymers [30] and metals [31,32]. The localized nature of the light-matter interactions of ultrashort laser pulses is of great benefit. Femtosecond laser pulses with high-quality spatial characteristics can result in sub-diffraction modifications in target materials. This occurs because of the Gaussian intensity distribution – the material in the middle of the spot is illuminated with a fluence large enough to modify or ablate the material, while the fluence surrounding the center does not exceed the threshold [33]. Different morphologies are obtained using a single laser pulse, depending on the fluence used [34,35]. The formation of the modifications can be modeled using thermoelastic models [36]. The bumps, cones, and jets generally form due to the resulting stress from temperature gradients caused by the laser pulse. With lower laser fluence, hollow bumps form,

* Corresponding author.
E-mail address: kernius.vilkevicius@ftmc.lt (K. Vilkevičius).

https://doi.org/10.1016/j.optlastec.2024.112330
Received 6 September 2024; Received in revised form 25 November 2024; Accepted 13 December 2024

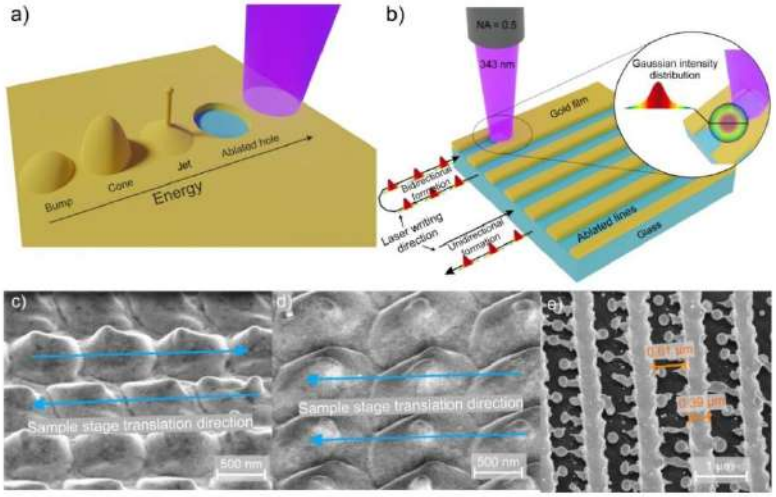

Fig. 1. a) Morphologies of the laser-induced surface modifications. b) Ablation of gold film, using unidirectional and bidirectional formation. Red pulses mark the firing direction. c) SEM image of a bidirectional formation of surface modifications. d) SEM image of a unidirectional formation of surface modifications. e) SEM image of 1 µm period ablated array.

while at a certain fluence corresponding to the absolute loss of film strength the center of the bump melts and expands upwards. This results in a nanojet structure. At even higher fluences, the material is ejected and the nanojet is destroyed due to the excess momentum imparted to the melt, which cannot be counterbalanced by the combined effects of plastic deformation and surface tension. Kuchmizhak et al. reason that the resulting formation of nanocrowns is explained by hydrodynamic instability (Marangoni, Plateau-Rayleigh) [37,38].

If the aforementioned nanostructures are arranged in a periodic lattice, the grating serves a dual purpose – it matches the momentum of incident light and excites SPP. Furthermore, if the period of the array is similar to the wavelength of the incident light, the in-plane Bragg reflections of one nanostructure can be in phase with LSPs in neighboring structures, thereby enhancing the plasmonic response. The excitation of both LSPs and propagating SPPs results in the hybridization and emergence of hybrid lattice plasmon resonance (HLPR). The main consequence of this is the reduction of dampening of resonances [39], resulting in very sharp hybrid lattice resonances that can be tuned by modifying the period of the lattice [35]. The so-called surface lattice resonances (SLRs) observed in periodic metallic nanostructures separated by insulator gaps yield comparable results. However, in the case of HLPR, the presence of a metallic layer between the structures gives rise to SPP, which induces additional losses compared to SLR. Although the electric field amplification of SPPs is reduced, the nature of this mode results in a more uniform distribution of the electric field along the metal film, which has a beneficial impact on practical applications, such as the enhanced convergence of the SERS [40] or photoluminescence [41] signal.

DLW naturally lends itself to the formation of large-scale arrays of plasmonic nanostructures on metals [35], because of its lower cost and complexity in comparison to the usual lithographic techniques [42], while still being capable of producing structures that exhibit narrow resonances in the Vis-NIR range. However, this method was only used for the fabrication of 2D arrays [35,43]. In contrast, 1D arrays have both been modeled [1,10] and fabricated by other techniques such as lift-off [12,44] or laser interference lithography [24].

In this work, both ultrafast direct laser modification and ablation methods were examined and characterized for forming periodic structures on thin gold films. The resulting gratings excite HLPR exhibiting tunable optical properties. The change in the pulse overlap and laser scanning speed produces not only ordinary 1D and 2D gratings but also 1D-like grating with 2D geometry but 1D optical properties. Such geometrical arrangement provides new opportunities for shape-dependent and high-quality resonances excluding the impact of the diagonal grating excitation and acting as 1D-resonances.

2. Results and discussion

2.1. Formation of arrays

The 3x3 mm^2 arrays of modifications/ablation were fabricated using 300 fs pulses of the third harmonic (343 nm) produced by Yb:KGW based fs-laser (Pharos, Light Conversion Ltd.). The laser pulses were focused through an objective having a numerical aperture of 0.5 to a spot of about 0.8 µm. The arrays were formed on a gold layer of 50 nm deposited using a magnetron sputter coater (Quorum Q150T). As shown in other works [45,46], a layer of titanium (3 nm) was sputtered on the glass to act as an adhesive between the glass and gold layer, as the gold film was susceptible to being ripped off when using higher energies. The thickness of the layers was controlled by the sputtering time at a constant sputtering rate. By scanning thin metal film and changing pulse energy, repetition rate, and transition speed, large-scale arrays of different nanostructures were formed. During the formation, the energy that the material has gained is dissipated through plastic deformation [36]. As a result, different hollow structures are produced according to the pulse energy (Fig. 1a) [47]. Bumps are formed when the lowest

Table 1
Fabricated periodic gold gratings.

	1D grating	Quasi-1D grating	2D grating
Formation mechanism	Ablation	Modification	Modification
Pulse energy	≈ 1.0 nJ	≈ 0.4 nJ	≈ 0.6 nJ
Grating period	1.0 μm	0.8 μm	0.8 μm
In-line period	0.25 μm	0.5 μm	0.8 μm
Repetition rate	7 kHz	20 kHz	7 kHz
Scanning speed	1.75 mm/s	10 mm/s	5.6 mm/s
Pulse overlap	69 %	38 %	0 %

modification-threshold energies are used, while larger-diameter cones and jets are obtained at higher fluences. When the ablation threshold is exceeded, the film is ablated and crowns may be produced. During the production of surface modifications, it was observed that the structures formed more consistently when the laser writing was unidirectional (firing laser pulses when translating in one direction and returning with a closed shutter) than when performing scanning in both directions (Fig. 1b). During the bidirectional formation with pulse overlapping, the tips of the structures were shifted to opposite sides with respect to the structures in adjacent lines (Fig. 1c), while implementing unidirectional scanning the slight offset of the tips is repetitive and identical in each row (Fig. 1d). This is the result of the pulse overlap [48], as the tip is shifted to the previously modified zone (opposite to the direction of scanning). The use of bidirectional scanning was implemented for the formation of the investigated arrays. Although this introduces alterations in the formation, such scanning speeds up the process, and the shift of the tip does not highly affect the required plasmonic properties of the hybridized plasmonic response. Nevertheless, this directional discrepancy would be more pronounced in the context of structure tip-influenced applications, such as SERS [3].

To produce both 1D and 2D gratings, the laser scanning speed and pulse repetition rate (and hence the pulse overlap) were changed. Two-dimensional arrays of 0.8 μm period (between the scanning lines) were formed by modifying the surface with lower energies than the ablation threshold and different scanning speeds. These arrays for spectra and HLPR investigation were $5 \times 5\ mm^2$ in size. One of the arrays was produced using a pulse repetition rate in the scanning direction of 20 kHz and a transition speed of 10 mm/s, leading to a pulse overlapping of 38 %. Such grating had different periods in scanning (in-line period of 0.5 μm) and perpendicular (grating period of 0.8 μm) axes. This type of array was referred to as a quasi-1D grating. For a two-dimensional array of metal modifications with 0 % overlapping, the 7 kHz repetition rate and 5.6 mm/s were used. In this way, the in-line and grating periods were both equal to 0.8 μm and the array was referred to as a uniform 2D grating. Also, a one-dimensional array with a period of 1 μm was fabricated using an ablation method (Fig. 1e) at energies above the ablation threshold. The pulse repetition rate was 7 kHz and the scanning speed was 1.75 mm/s, leading to a large pulse overlapping of 69 %. Due to the high overlapping, the irradiated areas were completely ablated, thus such an array was referred to as 1D grating. While ablated gratings of smaller periods were attempted to be produced, these resulted in the gold surface being too damaged overall with no periodic structures of use obtained. One of the limiting factors in fabricating smaller period ablated gratings using DLW is that the Gaussian intensity distribution of the beam is no longer beneficial at higher energies (Fig. 1b). At lower energies, the diameter of the produced structures is smaller than the focused beam width, as a larger part of the energy is transferred to the center of the focused spot [49]. On the other hand, higher-energy pulses affect the periphery of the beam, resulting in a larger zone of surface modification over the entire beam spot area. Thus, limiting ablation to only the center of the focused spot is challenging for large-scale plasmonic arrays. In general, this makes the period of arrays fabricated using ablation more limited by the numerical aperture of the system. This results in surface modification rather than ablation being more suitable for smaller lattice periods. The formation parameters of all 3 produced and investigated gratings are summarized in Table 1.

Additionally, to investigate the scanning speed and in-line period influence on the produced grating type and quality, several $50 \times 50\ \mu m^2$ size 1 μm period gratings were produced. A constant 7 kHz repetition rate was used with 0.6 nJ and 0.8 nJ pulse energies. The scanning speed was varied from 0.7 mm/s to 3.5 mm/s with a step of 0.7 mm/s so that the in-line period would change from 0.1 μm to 0.5 μm with a step of 0.1 μm. Obtained SEM images are depicted in Fig. 2, where the blue measurement is the size of an ablated line, yellow – is the size of the remaining unmodified gold, and green – is the size of the modified structure. As observed in Fig. 1e, the quality of the 1D grating ablated lines is not ideal, exhibiting some residual splashed metal. Therefore, by reducing the scanning speed and increasing the pulse overlap, the sides of the 1D grating metallic lines become smoother, while maintaining the width of ablated lines (0.5 μm for 0.6 nJ pulses and 0.65 μm for 0.8 nJ pulses). In contrast, by increasing the scanning speed and in-line period, the transition from ablated 1D to modified quasi-1D grating can be observed and the threshold can be determined. For pulses with an energy of 0.6 nJ, the threshold scanning speed is 2.1 mm/s (0.3 μm in-line period) above which the modified structures are produced and the film is not ablated anymore. At higher pulse energies (0.8 nJ), the threshold scanning speed is approximately 3.5 mm/s (0.5 μm in-line periods) because some modified structures are already preserved using these parameters. Furthermore at even higher speeds, when the in-line period is large enough, the modified 2D arrays are produced. Although a lower scanning speed improves the quality of the ablated lines, this also greatly prolongs the overall formation time. Consequently, a trade-off between the quality and the formation speed must be chosen.

2.2. Characterization of the fabricated structures

To investigate how incident light couples with the fabricated arrays,

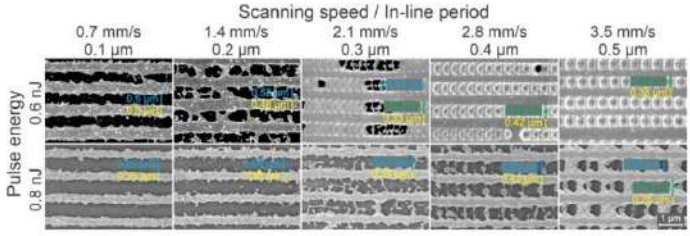

Fig. 2. SEM images of 1 μm periodic ablated and modified arrays produced at 0.6 nJ and 0.8 nJ with different scanning speeds and in-line periods. Blue measurement is the size of the ablated zone, yellow – is the size of the remaining unmodified gold, and green – is the size of the modified structure.

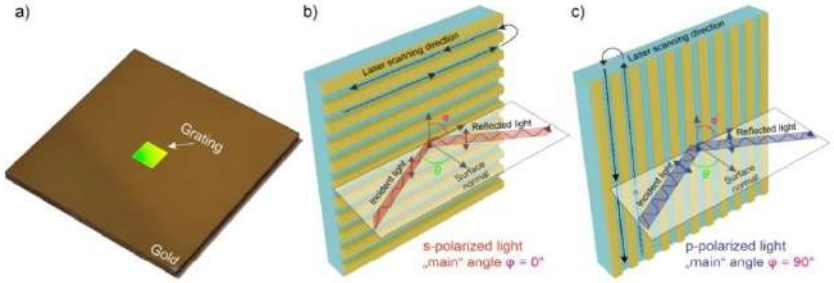

Fig. 3. a) The produced 3 × 3 mm^2 gold grating, b) s-polarized and c) p-polarized light spectra measurement from the diffraction gratings at "main" azimuthal angle. θ is the angle of incidence, and φ is the azimuthal angle (referring to the orientation between the grating or scanning lines and the plane of incidence).

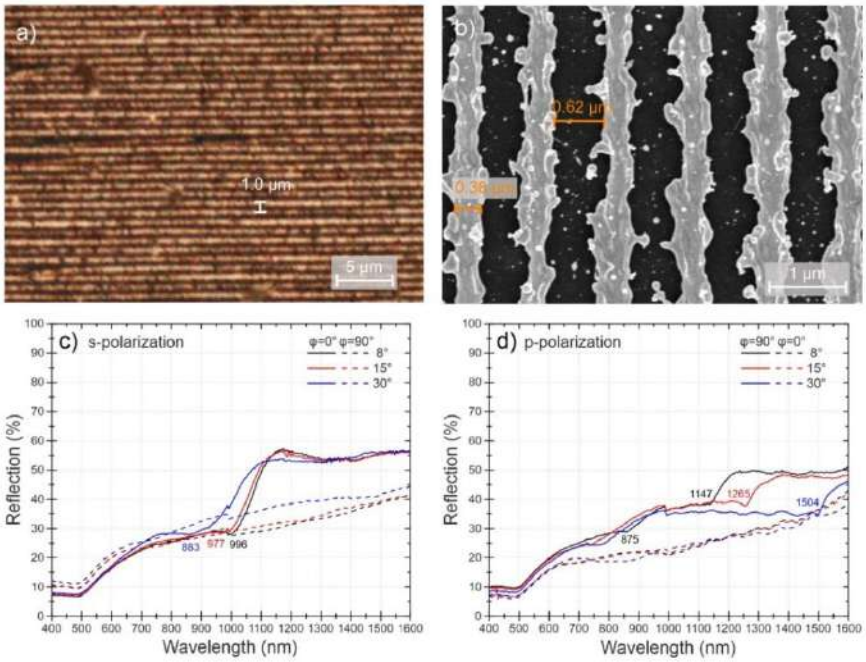

Fig. 4. a) The optical microscope and b) SEM photos of the 1D ablated gold array of 1 µm period. c) s-polarized and d) p-polarized light reflection spectra of the grating. The "main" azimuthal angle φ is shown with solid lines ($\varphi = 0°$ for s-polarization and $\varphi = 90°$ for p-polarization), while the "shifted" azimuthal angle is shown with dashed lines. Angles of incidence of 8°, 15°, and 30° are shown.

reflectance spectra were measured using a spectrophotometer (Photon RT, Essentoptics) from 400 to 1600 nm using both s- and p-polarized light. Since the transmission spectra for the investigated gratings were only a few percent in intensity and with no evident resonance absorption peaks, only the reflection spectra were examined. Angles of incidence θ of 8°, 15°, and 30° were used. The gratings were also rotated at an azimuthal angle by 90° to examine the effects of different light polarization. The scheme of the measurements is shown below in Fig. 3. For 1D

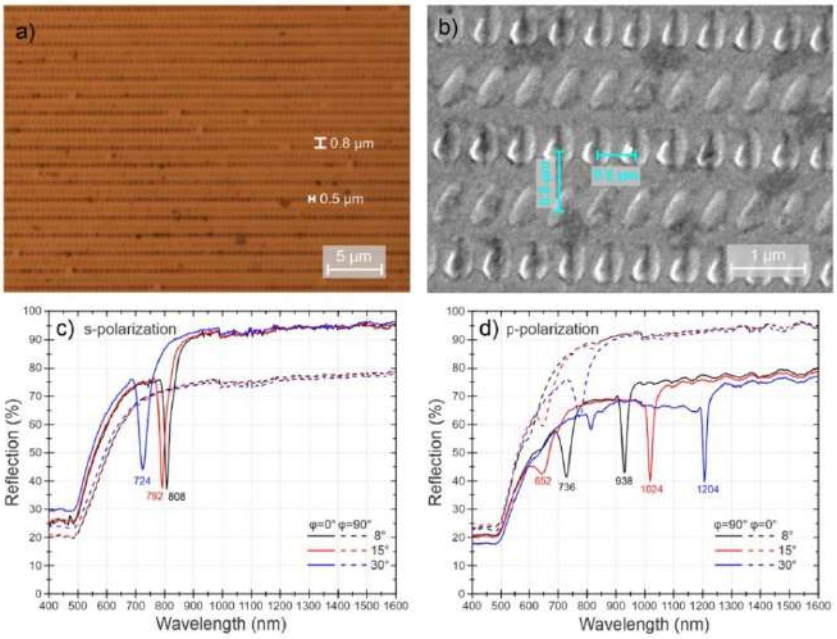

Fig. 5. a) The optical microscope and b) SEM photos of the quasi-1D gold nanostructure array. c) s-polarized and d) p-polarized light reflection spectra of the grating. The "main" azimuthal angle φ is shown with solid lines, while the "shifted" azimuthal angle is shown with dashed lines. Angles of incidence of 8°, 15°, and 30° are shown.

grating, the hybrid lattice plasmons are excited with the light which electric field oscillates perpendicularly to the grating (laser scanning) lines. For 2D grating, the plasmons are excited at both azimuthal angles, however, as it was previously investigated [35], a stronger response is also obtained with the electric field oscillating perpendicularly to the laser scanning lines. Thus, in further experiments the main plasmonic response was measured with s-polarization at $\varphi = 0°$, and with p-polarization at $\varphi = 90°$. This azimuthal measurement is referred to as the "main" azimuthal angle. In 2D gratings, where the resonance is also observable at perpendicular angles, this latter measurement is referred to as the "shifted" azimuthal angle (s-polarization at $\varphi = 90°$ and p-polarization at $\varphi = 0°$).

2.2.1. Ablated 1D grating

Firstly, the ablation-produced array of 1 µm period was investigated for plasmonic properties. The structures consisted of 0.62 µm width gap and 0.38 µm rough-sided gold (Fig. 4a,b). High pulse overlapping and high pulse energy lead to the total ablation of the scanned area with debris on the sides. The resulting HLPRs of the ablated array (Fig. 4c,d) were quite shallow but still visible. In general, the intensity of the gold reflectance spectra was quite reduced because of the ablated layer and increased transmission. In both light polarizations, the resonances are observable only in a layout with grating lines perpendicular to the electric field oscillations – at the "main" azimuthal angle ($\varphi = 0°$ for s-polarization and $\varphi = 90°$ for p-polarization). In contrast, other azimuthal angles do not elicit a diffractively-coupled plasmonic response. This indicates that the array is spectrally acting as a one-dimensional grating, which aligns with its intrinsic geometry. In the *s*-polarized light response, one resonance is visible per angle of incidence, which shifts to lower wavelengths when increasing θ. In the *p*-polarized light response, two absorption resonances should be visible – one at a wavelength larger than the grating period (corresponding to $m = -1$ diffraction order), and the other at a wavelength lower than the grating period (corresponding to $m = +1$ diffraction order). In both cases, the expected relationship is observed – resonances that correspond to $m = -1$ shift to higher wavelengths with higher θ, while those that correspond to $m = +1$ decrease [35]. Due to the largely disturbed reflection spectra, mostly only $m = -1$ order resonances are visible. In general, the observed resonances are of much lower quality than in similar arrays shown in the work by Hua et al. [44], most probably because the formed arrays are quite unorderly. SEM image (Fig. 4b) indicates that the formation of the 1D gratings using direct laser ablation is not optimal for high-quality plasmonic structures, as the remaining film exhibits non-uniform and high-roughness sides, in addition to the debris of the splashed metal.

2.2.2. Modified quasi-1D grating

A quasi-1D array of gold film modifications was formed using lower pulse energy and larger scanning speed so that the pulse overlapping would be smaller. The array with 38 % overlap had a period between the scanning lines of 0.8 µm, while the in-line period turned out to be 0.5 µm. This results in a different structure separation along both axes. The optical microscope and SEM photos of the formed arrays are shown in

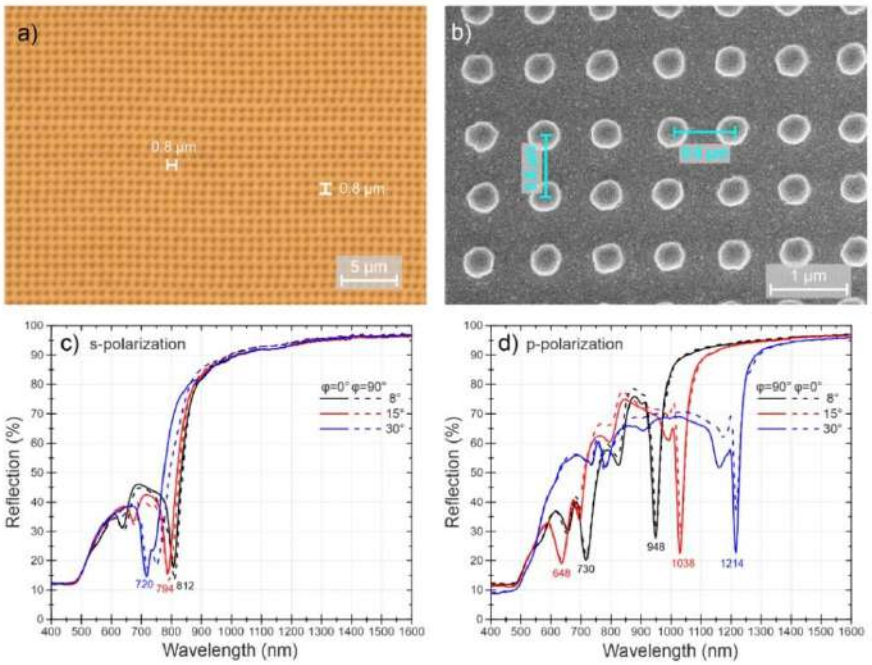

Fig. 6. a) The optical microscope and b) SEM photos of the 2D modified gold array of 0.8 μm period. c) s-polarized and d) p-polarized light reflection spectra of the grating. The "main" azimuthal angle φ is shown with solid lines, while the "shifted" azimuthal angle is shown with dashed lines. Angles of incidence of 8°, 15°, and 30° are shown.

Fig. 5**a,b**. An alternation of the formed structures can be seen in both the regular and SEM images, which seems to be caused by the bidirectional scanning (Fig. 1c). However, as compared to the other samples, this alternation of the structures did not seem to have a strong effect on the optical or plasmonic properties of the material.

This time, the resulting spectra are of larger reflection intensity, the HLPRs are a lot deeper, and the resonance dependence on polarization and angle of incidence of the incoming light is easier to distinguish (Fig. 5c,d). Same as in the ablated array, in the s-polarized light response, one absorption resonance is visible per angle of incidence, which shifts to lower wavelengths with increasing angle. With p-polarized light, the resonances spread further from the wavelength of the grating period with increasing angle of incidence. While the array is two-dimensional, in practice it acts as a one-dimensional array. The resonances are observable only in one azimuthal angle for each polarization – in *s*-polarization, the clear peaks are observed only at φ = 0° angle, while using *p*-polarization the sharp peaks are obtained at φ = 90° angle. The resulting HLPR is associated with the main periodicity of 0.8 μm, while the resonance of the in-line periodicity of 0.5 μm is almost not visible in the spectra, as it occurs in the gold absorption zone. However, the non-1D nature of the grating is observed at larger incident angles (15°, 30°), where some resonances can be visible at the φ = 0° angle of the *p*-polarization reflection spectrum (648 nm at 15° and 776 nm at 30°). These correspond to the m = -1 diffraction order from the in-line grating when the resonant peak shifts to longer wavelengths and comes out of the gold absorption zone. So even though the grating is two-dimensional with two periods, it can be considered one-dimensional at small angles. This approach eliminates the azimuthal angle misalignment and diagonal resonances in the spectra, thereby providing only a high-quality 1D grating response.

2.2.3. *Modified uniform 2D grating*

Finally, a uniform 2D grating of gold modifications was produced using similar pulse energies and defined scanning speed so that the pulses would not overlap. In this way, both the scanning line and in-line period of 0.8 μm were achieved with uniform distribution of the nanostructures in both axes. The optical microscope and SEM photos of the array are shown in Fig. 6**a,b**. The array was also produced in bidirectional scanning, however, as there is no overlap of the pulses, the scanning direction did not affect the shape of the structures and all of the produced bumps have a circular shape. The resulting reflection spectra are depicted in Fig. 6c,d with a solid line marking the response from the "main" azimuthal angle providing higher intensity (φ = 0° for s-polarization and φ = 90° for p-polarization). Meanwhile, the dashed line marks the response from a "shifted" azimuthal angle differing from the "main" by 90°.

The results at both azimuthal angles are quite similar with identical resonant wavelengths. However, in addition to the main resonances

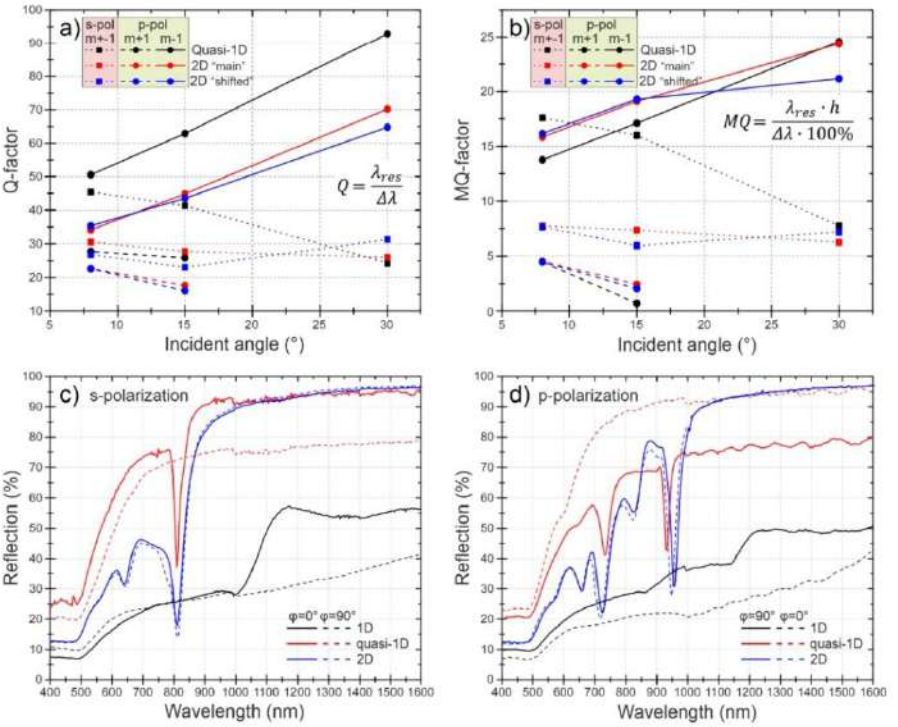

Fig. 7. a) The Q-factor and b) the MQ-factor of the HLPR dependence on the light incidence angle. Black lines mark the results of quasi-1D grating, red line – 2D grating "main" azimuthal angle, and blue line – 2D grating "shifted" azimuthal angle. Solid lines show the results of m = −1 resonance (p-polarization), dashed lines – m = +1 resonance (p-polarization), and dotted lines – m = ±1 resonance (s-polarization). c) s-polarized and d) p-polarized light reflection spectra of the 1D (black line), quasi-1D (red line), and 2D (blue line) gratings at 8° angle of incidence. The "main" azimuthal angle φ is shown with solid lines, while the "shifted" azimuthal angle is shown with dashed lines.

from the 0.8 μm period diffraction grating, other peaks are visible in the spectra corresponding to either diffractive resonances from diagonal grating or to resonances from another axis due to the misalignment of the azimuthal angle. These additional peaks can overlap with the main resonances and thus broaden them, degrading the quality of the resonances.

2.2.4. Resonant properties of the produced gratings

The quality and modified quality factors [42] of the produced quasi-1D and 2D arrays were calculated and depicted in Fig. 7**a**,**b** for the measured light incidence angles (8°, 15°, and 30°) for the final comparison of the plasmonic properties. The black line denotes the quasi-1D results, red – 2D grating results at the "main" angle, and blue – 2D grating results at the "shifted" angle (solid lines correspond to m = −1 resonance at p-polarization, dashed lines – m = +1 resonance at p-polarization, and dotted lines – m = ±1 resonance at s-polarization). It is not feasible to utilize the resonances of the 1D array for the calculation of these parameters. Also, the corresponding spectra of all 3 gratings at θ = 8° for both "main" and "shifted" azimuthal angles are compared in Fig. 7c,d. Here, the black line corresponds to 1D, the red line – quasi-1D, and the blue line – 2D grating (solid lines – "main" azimuthal angle, dashed lines – "shifted" angle). The quality factor (Q-factor) in Fig. 7a is measured as the ratio of the resonance wavelength to the resonance width. The modified factor (MQ-factor) in Fig. 7b additionally includes the depth of the resonance peak.

The tendency of the quality factors with increasing angle of incident is evident. HLPR excited by s-polarization (dotted line in Fig. 7a,b) in a 2D grating demonstrates a consistent quality as the angles change, with a Q-factor of about 30 and an MQ-factor of 7, while the one excited in a quasi-1D grating results in a loss of quality as the angle increases. The latter decrease can be attributed to the resonance shift closer to the absorption zone. At higher angles, the resonances of the in-line period grating can potentially exit the absorption zone and overlap with the resonances already observed in the spectrum, thus broadening them. HLPR of m = +1 order excited by p-polarization (dashed line in Fig. 7a, b) shows a steady decline in quality in both quasi-1D and 2D gratings due to the convergence of the resonant peak and gold absorption zone edge. Finally, the HLPR of m = −1 order excited by p-polarization (solid

line in Fig. 7a,b) represents almost a linear incline in quality with an angle increase, as the resonant peak maintains its width while shifting to longer wavelengths. Here, the Q-factor reaches up to 93 in the quasi-1D array, with the MQ-factor being approximately 25.

All in all, quasi-1D grating provides larger Q-factor results in comparison to uniform 2D grating, as the resonance peaks are more narrow due to the elimination of overlapping resonances. The Q-factor of the s-polarization response is increased by 8, while that of p-polarization (m = -1) is enhanced by a value of 20. In addition, the MQ-factors of both quasi-1D and 2D gratings are found to be quite similar for p-polarization, suggesting that both methods can be employed to produce high-quality samples for practical applications. Nevertheless, the results of the s-polarization response are greater in quasi-1D gratings at small angles, which illustrates the benefit of eliminating additional resonances, resulting in more intense and narrow HLPR peaks.

3. Conclusions

The fabrication of ablated and modified large-scale arrays exhibiting hybrid lattice plasmon resonances is demonstrated. Both the ablated and modified arrays follow the resonance wavelength dependencies on the angle of incidence and polarization of incoming light. However, material modification proves to be a more advantageous approach for manufacturing such HLPR arrays. It offers several key benefits, including the ability to produce more precise, sub-diffraction limit structures without the sample surface contamination of splashed metal associated with the ablation technique. The change in the scanning speed and in-line period determines the threshold between the ablated 1D grating and quasi-1D grating consisting of modification-induced nanostructures. Surface modification rather than ablation produces gratings exhibiting more narrow and practically applicable diffraction-coupled resonances. Finally, the research demonstrates the novel promising technique of quasi-1D grating fabrications. A 1D-like spectral response can be achieved at a single azimuthal angle with sharp resonances through the utilization of large-scale ($3 \times 3\ mm^2$) 2D arrays of surface modifications, employing small in-line periods. Such quasi-1D gratings provide the ability to eradicate undesirable resonances arising from a diagonal grating or non-optimal azimuthal alignment. Only a single resonant peak response in the spectra increases the accuracy of the results without the overlap of several peaks and signal deterioration. The promising results presented here underscore the potential of the DLW technique to create tunable and large-scale HLPR-exhibiting arrays for optical applications.

CRediT authorship contribution statement

Kernius Vilkevičius: Writing – review & editing, Writing – original draft, Visualization, Validation, Methodology, Formal analysis, Data curation, Conceptualization. **Kipras Cepaitis:** Writing – review & editing, Writing – original draft, Visualization, Validation, Investigation, Formal analysis. **Algirdas Selskis:** Methodology, Investigation, Formal analysis. **Evaldas Stankevičius:** Writing – review & editing, Supervision, Project administration, Funding acquisition, Conceptualization.

Declaration of competing interest

The authors declare that they have no known competing financial interests or personal relationships that could have appeared to influence the work reported in this paper.

Acknowledgment

This project has received funding from the Research Council of Lithuania (LMTLT), agreement No. S-MIP-23-32.

Data availability

Data will be made available on request.

References

[1] T. Iqbal, Z. Ashfaq, S. Afsheen, M. Ijaz, M.Y. Khan, M. Rafique, G. Nabi, Surface-enhanced raman scattering (SERS) on 1D nano-gratings, Plasmonics 15 (2020) 1053–1059, https://doi.org/10.1007/s11468-019-01114-5.

[2] O. Guselnikova, B. Dvornakova, K. Kakisheva, Y. Kalachyova, P. Postnikov, V. Svorcik, O. Lyutakov, Rapid SERS-based recognition of cell secretome on the folic acid-functionalized gold gratings, Anal. Bioanal.chem. 411 (2019) 3309–3319, https://doi.org/10.1007/s00216-019-01801-6.

[3] K. Vilkevičius, I. Ignatjev, A. Selskis, G. Niaura, E. Stankevičius, Tuning SERS performance through the laser-induced morphology changes of gold nanostructures, Appl. Surf. Sci. 660 (2024) 160003, https://doi.org/10.1016/j.apsusc.2024.160003.

[4] E. Stankevičius, E. Daugnoraitė, I. Ignatjev, Z. Kuodis, G. Niaura, G. Račiukaitis, Concentric microring structures containing gold nanoparticles for SERS-based applications, Appl. Surf. Sci. 497 (2019) 143752, https://doi.org/10.1016/j.apsusc.2019.143752.

[5] V. Petrikaitė, M. Talaikis, L. Mikoliūnaitė, A.-M. Gkouzi, R. Trusovas, M. Skapas, G. Niaura, E. Stankevičius, Stability and SERS signal strength of laser-generated gold, silver, and bimetallic nanoparticles at different KCl concentrations, Heliyon 10 (2024) e34815, https://doi.org/10.1016/j.heliyon.2024.e34815.

[6] S.A. Jalil, M. Akram, J.A. Bhat, J.J. Hayes, S.C. Singh, M. ElKabbash, C. Guo, Creating superhydrophobic and antibacterial surfaces on gold by femtosecond laser pulses, Appl. Surf. Sci. 506 (2020) 144952, https://doi.org/10.1016/j.apsusc.2019.144952.

[7] S. Kausar, R.M. Munir, T. Iqbal, S. Afsheen, M.S. Mansha, A.M. Elgorban, H.A. Al-Shwaiman, Improving photocatalytic, antimicrobial properties, and enzymatic activity via Ag doping in BiVO4 photocatalysts using a simple co-precipitation technique and verified by theoretical analysis, J. Inorg. Organomet. Polym. Mater. (2024), https://doi.org/10.1007/s10904-024-03236-8.

[8] T. Iqbal, M. Afzal, B.A. Al- Asbahi, S. Afsheen, I. Maryam, A. Mushtaq, S. Kausar, A. Ashraf, Enhancing apple shelf life: a comparative analysis of photocatalytic activity in pure and manganese-doped ZnO nanoparticles, Mater. Sci. Semicond. Process 173 (2024) 108152, https://doi.org/10.1016/j.mssp.2024.108152.

[9] H. Talebi, F. Emami, High performance ultra-thin perovskite solar cell by surface plasmon polaritons and waveguide modes, Opt. Laser Technol. 165 (2023) 109532, https://doi.org/10.1016/j.optlastec.2023.109532.

[10] A. Baba, N. Aoki, K. Shinbo, K. Kato, F. Kaneko, Grating-coupled surface plasmon enhanced short-circuit current in organic thin-film photovoltaic cells, ACS Appl. Mater. Interfaces 3 (2011) 2080–2084, https://doi.org/10.1021/am200304v.

[11] J. Cai, C. Zhang, C. Liang, S. Min, X. Cheng, W.-D. Li, Solution-processed large-area gold nanocheckerboard metasurfaces on flexible plastics for plasmonic biomolecular sensing, Adv. Opt. Mater. 7 (2019) 1900516, https://doi.org/10.1002/adom.201900516.

[12] L. Minati, A. Chiappini, G. Armellini, A. Carpentiero, D. Maniglio, A. Vaccari, L. Zur, A. Lukowiak, M. Ferrari, G. Speranza, Gold nanoparticles 1D array as mechanochromic strain sensor, Mater. Chem. Phys. 192 (2017) 94–99, https://doi.org/10.1016/j.matchemphys.2017.01.073.

[13] A.M. Shrivastav, U. Cvelbar, I. Abdulhalim, A comprehensive review on plasmonic-based biosensors used in viral diagnostics, Commun. Biol. 4 (2021) 70, https://doi.org/10.1038/s42003-020-01615-8.

[14] D.J. Roth, A.V. Kravovin, A.V. Zayats, Nanophotonics with plasmonic nanorod metamaterials, Laser Photonics Rev. 18 (2024) 2300886, https://doi.org/10.1002/lpor.202300886.

[15] T. Lee, G.H. Kim, S.M. Kim, K. Hong, Y. Kim, C. Park, H. Sohn, J. Min, Label-free localized surface plasmon resonance biosensor composed of multi-functional DNA 3 way junction on hollow Au spike-like nanoparticles (HAuSN) for avian influenza virus detection, Colloid Surf. B: Biointerfaces 182 (2019) 110341, https://doi.org/10.1016/j.colsurfb.2019.06.070.

[16] T. He, C. Jiang, J. He, Y. Zhang, G. He, J. Wu, J. Lin, X. Zhou, P. Huang, Manganese-dioxide-coating-instructed plasmonic modulation of gold nanorods for activatable duplex-imaging-guided NIR-II photothermal-chemodynamic therapy, Adv. Mater. 33 (2021) 2008540, https://doi.org/10.1002/adma.202008540.

[17] V. Petrikaite, I. Ignatjev, A. Selskis, G. Niaura, E. Stankevičius, Hybrid gold-silver nanoparticles synthesis on a glass substrate using a nanosecond laser-induced dewetting of thin bimetallic films and their application in SERS, Opt. Laser Technol. 168 (2024) 109956, https://doi.org/10.1016/j.optlastec.2023.109956.

[18] J. Breault-Turcot, J.-F. Masson, Nanostructured substrates for portable and miniature SPR biosensors, Anal. Bioanal.chem. 403 (2012) 1477–1484, https://doi.org/10.1007/s00216-012-5963-1.

[19] P. Berini, I. De Leon, Surface plasmon–polariton amplifiers and lasers, Nat. Photonics 6 (2012) 16–24, https://doi.org/10.1038/nphoton.2011.285.

[20] Y.X. Huang, R. Singh, L.J. Xie, Y.B. Ying, Attenuated total reflection for terahertz modulation, sensing, spectroscopy and imaging applications: a review, Appl. Sci.-Basel 10 (2020) 4688, https://doi.org/10.3390/app10144688.

[21] J. Cao, Y. Sun, Y. Kong, W. Qian, The Sensitivity of grating-based SPR sensors with wavelength interrogation, Sensors 19 (2019) 405, https://doi.org/10.3390/s19020405.

[22] F.F. Mahani, L.A.M. Astorga, H.W. Choi, A. Mekhtari, P. Beriai, Plasmonic slanted slit gratings for efficient through-substrate light-plasmon coupling and sensing, Sci. Rep. 14 (2024) 2084, https://doi.org/10.1038/s41598-024-52564-9.
[23] A. Kanegulla, L.-J. Cheng, Metal assisted focused-ion beam nanopatterning, Nanotechnology 27 (2016) 361T01, https://doi.org/10.1088/0957-4484/27/36/361T01.
[24] F. Romanato, H.K. Kang, K.H. Lee, G. Ruffato, M. Prasciolu, C.C. Wong, Interferential lithography of 1D thin metallic sinusoidal gratings: accurate control of the profile for azimuthal angular dependent plasmonic effects and applications, Microelectron. Eng. 86 (2009) 573–576, https://doi.org/10.1016/j.mee.2009.01.080.
[25] M. Hentschel, J. Karst, H. Giessen, Tailored optical functionality by combining electron-beam and focused gold-ion beam lithography for solid and inverse coupled plasmonic nanostructures, Adv. Opt. Mater. 8 (2020) 2000879, https://doi.org/10.1002/adom.202000879.
[26] L.Y.M. Tobing, A.D. Mueller, J. Tong, D.H. Zhang, Nanobridges formed through electron beam image reversal lithography for plasmonic mid-infrared resonators with high aspect ratio nanogaps, Nanotechnology 30 (2019) 425302, https://doi.org/10.1088/1361-6528/ab32e5.
[27] D.A.B. Therien, N.M. Čulum, D.M. McRae, L. Mazaheri, F. Lagugné-Labarthet, Single-beam inscription of plasmon-induced surface gratings, Opt. Mater. 112 (2021) 110775, https://doi.org/10.1016/j.optmat.2020.110775.
[28] E. Skliutas, M. Lebedevaite, E. Kabouraki, T. Baldacchini, J. Ostrauskaite, M. Vamvakaki, M. Farsari, S. Juodkazis, M. Malinauskas, Polymerization mechanisms initiated by spatio-temporally confined light, Nanophotonics 10 (2021) 1211–1242, https://doi.org/10.1515/nanoph-2020-0551.
[29] E. Sedghamiz, M. Liu, W. Wenzel, Challenges and limits of mechanical stability in 3D direct laser writing, Nat. Commun. 13 (2022) 2115, https://doi.org/10.1038/s41467-022-29740-9.
[30] O. Lyutakov, J. Túma, I. Huttel, V. Prajzler, J. Siegel, V. Švorčík, Polymer surface patterning by laser scanning, Appl. Phys. B 110 (2013) 539–549, https://doi.org/10.1007/s00340-012-5291-3.
[31] J. Bonse, J. Krüger, Structuring of thin films by ultrashort laser pulses, Appl. Phys. A 129 (2022) 14, https://doi.org/10.1007/s00339-022-06229-x.
[32] K. Vilkevičius, A. Selskis, E. Stankevičius, Femtosecond laser Wavelength-Dependent formation of plasmonic gold nanostructures, Appl. Surf. Sci. 617 (2023) 156629, https://doi.org/10.1016/j.apsusc.2023.156629.
[33] F. Korte, S. Adams, A. Egbert, C. Fallnich, A. Ostendorf, S. Nolte, M. Will, J. P. Ruske, B.N. Chichkov, A. Tünnermann, Sub-diffraction limited structuring of solid targets with femtosecond laser pulses, Opt. Express 7 (2000) 41–49, https://doi.org/10.1364/OE.7.000041.
[34] D. Pavlov, S. Syubaev, A. Kuchmizhak, S. Gurbatov, O. Vitrik, E. Modin, S. Kudryashov, X. Wang, S. Juodkazis, M. Lapine, Direct laser printing of tunable IR resonant nanoantenna arrays, Appl. Surf. Sci. 469 (2019) 514–520, https://doi.org/10.1016/j.apsusc.2018.11.069.
[35] E. Stankevičius, K. Vilkevičius, M. Gedvilas, E. Butavaitė-Verteliene, A. Selskis, Z. Balevičius, Direct laser writing for the formation of large-scale gold microbumps arrays generating hybrid lattice plasmon polaritons in Vis–NIR range, Adv. Opt. Mater. 9 (2021) 2100027, https://doi.org/10.1002/adom.202100027.
[36] Y.P. Meshcheryakov, N.M. Bulgakova, Thermoelastic modeling of microbump and nanojet formation on nanosize gold films under femtosecond laser irradiation, Appl. Phys. A 82 (2006) 363–368, https://doi.org/10.1007/s00339-005-3319-9.
[37] A.A. Kuchmizhak, D.V. Pavlov, O.B. Vitrik, Y.N. Kulchin, Laser ablative fabrication of nanocrowns and nanojets on the Cu supported film surface using femtosecond laser pulses, Appl. Surf. Sci. 357 (2015) 2376–2384, https://doi.org/10.1016/j.apsusc.2015.09.235.
[38] A. Kuchmizhak, S. Gurbatov, A. Nepomniaschiy, A. Mayor, Y. Kulchin, O. Vitrik, S. Maharov, S. Kudryashov, A. Ionin, Hydrodynamic instabilities of thin Au/Pd alloy film induced by tightly focused femtosecond laser pulses, Appl. Surf. Sci. 337 (2015) 224–229, https://doi.org/10.1016/j.apsusc.2015.02.090.
[39] V.G. Kravets, A.V. Kabashin, W.L. Barnes, A.N. Grigorenko, Plasmonic surface lattice resonances: a review of properties and applications, Chem. Rev. 118 (2018) 5912–5951, https://doi.org/10.1021/acs.chemrev.8b00243.
[40] Y. Kalachyova, D. Mares, O. Lyutakov, M. Kostejn, L. Lapcak, V. Švorčík, Surface plasmon polaritons on silver gratings for optimal SERS response, J. Phys. Chem. C 119 (2015) 9506–9512, https://doi.org/10.1021/acs.jpcc.5b01793.
[41] H. Su, S. Wu, Y. Yang, Q. Leng, L. Huang, J. Fu, Q. Wang, H. Liu, L. Zhou, Surface plasmon polariton–enhanced photoluminescence of monolayer MoS2 on suspended periodic metallic structures, Nanophotonics 10 (2021) 975–982, https://doi.org/10.1515/nanoph-2020-0545.
[42] S. Kasani, K. Curtin, N. Wu, A review of 2D and 3D plasmonic nanostructure array patterns: fabrication, light management and sensing applications, Nanophotonics 8 (2019) 2065–2089, https://doi.org/10.1515/nanoph-2019-0158.
[43] D. Pavlov, A. Zhizhchenko, L. Pan, A.A. Kuchmizhak, Tuning collective plasmon resonances of femtosecond laser-printed metasurface, Micromachines 15 (2022) 1834, https://doi.org/10.3390/mi15051834.
[44] Y. Hua, A.K. Fumani, T.W. Odom, Tunable lattice plasmon resonances in 1D nanogratings, ACS Photonics 6 (2019) 322–326, https://doi.org/10.1021/acsphotonics.8b01541.
[45] M. Todeschini, A. Bastos da Silva Fanta, F. Jensen, J.B. Wagner, A. Han, Influence of Ti and Cr adhesion layers on ultrathin Au films, ACS Appl. Mater. Interfaces 9 (2017) 37374–37385, https://doi.org/10.1021/acsami.7b10136.
[46] R. Liudvinavičius, A. Selskis, E. Stankevičius, Titanium adhesion layer influence on the formation of hybrid lattice plasmon structures via laser-direct writing, Opt. Laser Technol. 175 (2024) 110807, https://doi.org/10.1016/j.optlastec.2024.110807.
[47] F. Korte, J. Koch, B.N. Chichkov, Formation of microbumps and nanojets on gold targets by femtosecond laser pulses, Appl. Phys. A 79 (2004) 879–881, https://doi.org/10.1007/s00339-004-2590-5.
[48] K. Vilkevičius, G.D. Tsibidis, A. Selskis, E. Stratakis, E. Stankevičius, Formation of highly tunable periodic plasmonic structures on gold films using direct laser writing, Adv. Opt. Mater. 12 (2024) 2400172, https://doi.org/10.1002/adom.202400172.
[49] R. Fang, A. Vorobyev, C. Guo, Direct visualization of the complete evolution of femtosecond laser-induced surface structural dynamics of metals, Light Sci. Appl. 6 (2017) e16256–e, https://doi.org/10.1038/lsa.2016.256.

4th publication / 4 publikacija

K. Vilkevičius, L. A. Letelier, L. Grinevičiūtė, E. Stankevičius,
Grating-Coupled Plasmonic Resonances in Symmetric 2D Gold Nanobump Grating: Theory Meets Experiments,
ACS Applied Materials & Interfaces, 18(23), 33007-33023 (2026).

https://doi.org/10.1021/acsami.6c04043

ACS APPLIED MATERIALS & INTERFACES

Open Access

www.acsami.org

Research Article

Grating-Coupled Plasmonic Resonances in Symmetric 2D Gold Nanobump Grating: Theory Meets Experiments

Kernius Vilkevičius,* Lucciano A. Letelier, Lina Grinevičiūtė, and Evaldas Stankevičius*

Cite This: https://doi.org/10.1021/acsami.6c04043

Read Online

ACCESS | Metrics & More | Article Recommendations | Supporting Information

ABSTRACT: The excitation of hybridized plasmonic modes is induced by periodic, two-dimensional gratings. Hybrid lattice plasmon resonances (HLPRs) emerge from the interaction of surface plasmon polaritons (SPPs), localized surface plasmons (LSPs), and grating-induced light diffraction and scattering. These resonances are characterized by dispersive and narrow line widths, which are particularly relevant for biosensing and surface-enhanced spectroscopies. In this comprehensive investigation, the diffraction-based excitation of HLPR resonances in a symmetric 2D gold nanobump grating is examined with excitation occurring across multiple lattice planes. The resonance tunability with respect to azimuthal and incidence angles, as well as polarization, is experimentally investigated. To identify and validate the origins of the resonant peaks, theoretical calculations of the spectral and near-field responses were conducted, providing a thorough examination of the phenomena. This combined theoretical-experimental study highlights the pivotal role of symmetry and excitation geometry in defining hybrid plasmonic modes, thereby providing guidelines for the engineering of highly tunable plasmonic platforms.

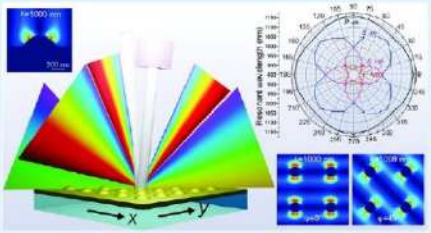

KEYWORDS: *grating-coupled resonance, plasmonics, periodic gold nanostructures, femtosecond laser, direct laser writing, FDTD simulations*

1. INTRODUCTION

Periodic metallic nanostructures support a variety of plasmonic resonances arising from the interaction of fundamental plasmonic modes and incident radiation. One of these hybrid modes arises from the coupling between repetitive localized surface plasmons (LSPs) and diffraction-induced propagating surface plasmon polaritons (SPPs).[1−3] The hybridization of plasmons is obtained in the periodic nanostructure array when the wave is diffracted at the cutoff angle, emanating from the metal surface, and the Rayleigh anomaly condition is fulfilled.[4] When the localized surface plasmons of neighboring individual nanostructures and the scattered field are in phase, plasmonic oscillations and local electromagnetic field are enhanced, resulting in reduced radiative losses and efficient far-field coupling. This interaction between repetitive LSPs and a diffracted ray gives rise to a hybrid mode known as surface lattice resonance (SLR), whose key features are a narrow line width and strong spectral tunability.[5−7] The addition of a gold layer among the periodic nanostructures leads to the excitation of the SPP by the same in-plane diffracted ray at the metal-dielectric interface.[8] Consequently, the coupling of LSP-SPP modes is initiated, and a hybrid lattice plasmon resonance (HLPR) is obtained. Although SPPs can be excited by the presence of a glass prism, the excitation of this HLPR mode is achieved exclusively with a diffraction grating.[9] In two-dimensional gratings, the coexistence of multiple diffraction planes enables the simultaneous excitation of plasmonic modes along orthogonal symmetry axes and diagonals.

The resonant properties of these hybrid plasmonic systems strongly depend on the structural grating parameters and are tunable by tailoring the period and symmetry of the grating,[10−14] as well as the particle geometry and dimensions,[15,16] and the number and arrangement of nanostructures in the array.[17−20] The results are also influenced by sample parameters such as incidence angle and polarization,[21−23] the plasmonic metal, the adhesion layer, and the surrounding medium.[15,24,25] To ensure stable resonant properties, the nanostructures must be uniform in shape, and the metal surface must be chemically stable (nonoxidizing). Hybrid resonance phenomena are widely used for accurate, powerful sensing of biomolecules, protein binding, analyte solu-

Received: February 26, 2026
Revised: May 11, 2026
Accepted: May 12, 2026

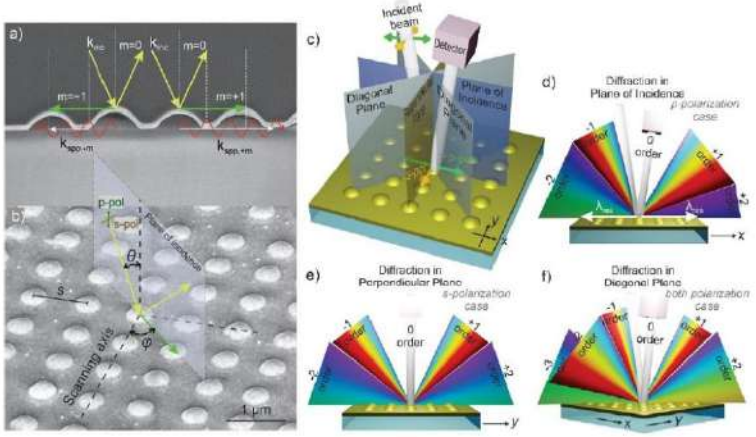

Figure 1. (a) Cross-section of the bumps with grating-coupled excitation of surface plasmons. (b) SEM micrograph of gold bumps grating with marked plane of incidence and angles used in measurements. (c) 3D drawing of the main diffraction planes at an 8° incident angle beam at the fabricated gold nanostructures grating. Diffraction in (d) plane of incidence (PI), (e) perpendicular plane (PP), and (f) diagonal plane (DP). The spectral visualization of diffraction is depicted for the wavelength range of 400−800 nm. White arrow marks resonant wavelength.

tions,[26−28] tumors,[29] and gases,[30] which depend strongly on changes in the surrounding refractive index. The use of resonant structures is also a method of enhancing the Raman scattering signal in the vicinity of nanostructures.[31−34] Plasmonic lattices and hybrid modes have also been investigated for nonlinear optical response and lasing,[35−37] fluorescence,[38] and used for boosting other energy conversions,[39] as well as for fluid flow manipulation,[40] nonradiative cooling,[41] and anticounterfeit labels.[42]

While periodic metallic nanostructures can be manufactured in several ways,[43−45] a single-step large-scale direct laser writing (DLW) technique was implemented in this fabrication. Ultrafast laser processing of the sample, by ablating or modifying the metal layer, enables accurate microprocessing at the focal point of the laser beam.[46−48] By applying a single laser pulse to modify the layer, energy-dependent nanostructures can be obtained from the heated and melted metal layer. Previous studies have shown that the formation of these structures depends strongly on the laser wavelength and pulse energy,[49] the metal used,[50] and its thickness.[32,51] The plasmonic properties of such nanostructures also depend on these parameters, and the most prominent dependence is morphology, as the resonant wavelength redshifts with increasing height and morphological phase of the structure.

The diffraction-based plasmonic excitation can be described using either a fully complex 2D or a simplified 1D periodic-array model. In the literature, the latter 1D case is more commonly investigated because the phenomena are reduced to a single axis, allowing clearer analytical treatment and simpler interpretation of the underlying physics.[52−54] As a result, many plasmonic concepts are typically introduced and analyzed within a 1D framework. However, a 2D grating description is essential when studying systems with hybrid-mode formation, multiaxis diffraction, and multidirectional plasmonic coupling. Symmetric arrays have been widely investigated in the context of SLR excitation and transitional conditions between individual LSP and SLR modes.[55−57] Additionally, grating-coupled SPP mode excitation in two-dimensional lattices under orthogonal incidence conditions, as well as the Bragg mode excitation in hybrid plasmonic-photonic crystal systems, have been explored for practical implementations.[27,58] Despite extensive studies and analysis on 1D gratings and geometries, the full angular dependence of plasmonic resonances in symmetric 2D lattices, particularly the interplay between main-axis and diagonal diffraction orders, remains insufficiently explored. This study aims to experimentally and theoretically investigate grating-coupled plasmonic resonances in symmetric 2D gold hemispherical nanobump gratings fabricated on thin films. By systematically varying polarization, azimuthal orientation, and incidence angle, we resolve the dispersion and hybridization behavior of multiple diffraction-based resonances. Numerical simulations are used to model both the spectral response and near-field distributions, enabling a clear classification of the observed resonances to their origins. This combined experimental-theoretical approach clarifies how diffraction order, propagation direction, and polarization jointly shape the hybrid plasmonic response in 2D gratings.

2. RESULTS AND DISCUSSION

2.1. Grating-Coupled Resonances in 2D Gold Nanobump Arrays

Large-scale periodic symmetrical 2D arrays of gold nanostructures on a 100 nm thin film were fabricated using the DLW technique, when the third-harmonic (343 nm) pulses of 300 fs Yb:KGW-based laser Pharos (Light Conversion Ltd.) were utilized in this study. The focused beam size was 0.8 μm, achieved with a high numerical aperture (NA) objective of NA = 0.5. The fabrication process entailed scanning periodic lines at a constant sample translation speed and pulse repetition rate

https://doi.org/10.1021/acsami.6c04043
ACS Appl. Mater. Interfaces XXXX, XXX, XXX−XXX

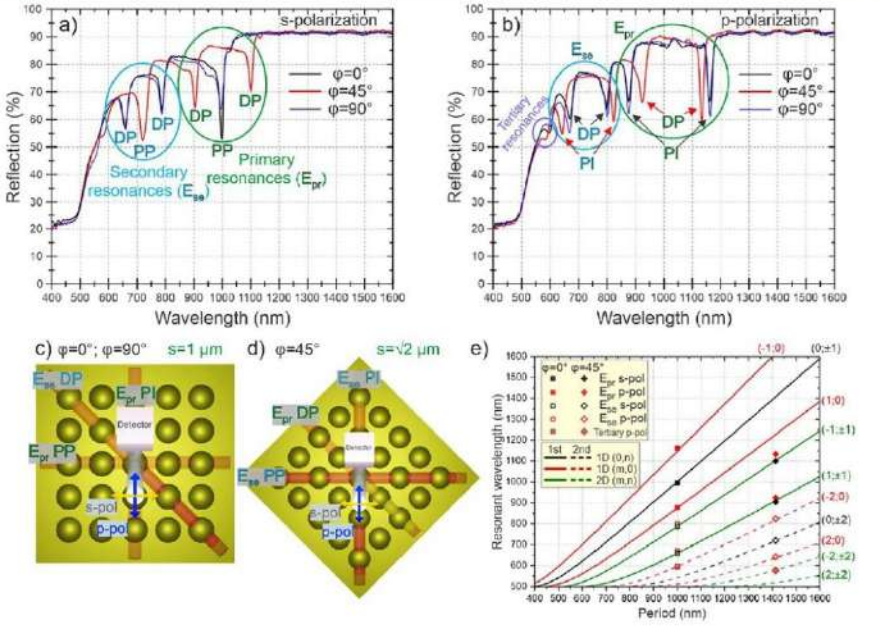

Figure 2. Reflectance spectra of gold nanobumps grating with a period of 1 μm for (a) s- and (b) p-polarization. The sample was measured at three azimuthal angles φ = 0° (black line), φ = 45° (red line), and φ = 90° (blue line). The marked primary resonances (E_{pr}, green) and secondary resonances (E_{se}, cyan), originating in the plane of incidence (PI), perpendicular plane (PP), and diagonal plane (DP) at (c) φ = 0°/90° and (d) φ = 45°. (e) Theoretically calculated resonant wavelength dependence on the grating period at an 8° incident angle for 1D-origin s- (black lines) and p-polarization (red lines), as well as 2D-origin (green lines). The first diffraction order is depicted in solid lines, while the second order is in dashed lines. The symbols mark experimentally measured resonance values from (a) and (b) graphs. Primary (filled symbols), secondary (empty symbols), and tertiary (gray symbols) resonances are marked by squares (φ = 0°) and diamonds (φ = 45°) for s- (black) and p-polarization (red).

(7 kHz) to structurize thin metal films and obtain nanostructures with a period of 1 μm in the scanning lines. In order to produce a symmetric 2D grating, the same period of 1 μm was used between the scanning lines. The structures were produced using a 0.8 nJ single-pulse energy to obtain hemispherical bumps.

The fabricated periodic nanobump arrays excite a hybrid plasmonic mode that propagates along the metal surface. The SPP mode propagation wavevector at the metal-dielectric interface is described as follows:[59]

$$k_{SPP} = \frac{2\pi}{\lambda}\sqrt{\frac{\epsilon_{Au}}{1+\epsilon_{Au}}} \quad (1)$$

where ϵ_{Au} is the permittivity of the gold film. The SPP excitation is based on light diffraction from the grating and Wood's anomaly, when the specific wavelength of the beam diffracts at a grazing angle so that it propagates along the surface (Figure 1a). The periodic grating changes the momentum of the incident light, leading to a matching of photon and SPP wavevectors and a consequent SPP excitation. Nanobump array changes the incident light wavevector k_i = $2\pi/\lambda$ by an integer number of grating wavevectors k_g = $2\pi/s$, where s is the grating period; thus, the resonant wavelength highly depends on the distance between the structures in both axes. For SPP excitation in a 2D array in an air environment, the following diffracted wave condition must be met:[60]

$$k_{SPP} = k_i \sin\theta \pm mk_{g,x} \pm nk_{g,y} \quad (2)$$

where θ is the angle of incidence, $k_{g,x}$ and $k_{g,y}$ correspond to grating wavevectors in the x and y axes of the array, which, in this case of a symmetrical square grating, are identical, and m and n are integers representing diffraction orders in x and y directions. This includes an additional resonant-wavelength control via azimuthal and incidence angles. Therefore, the coupling between a surface plasmon and a diffracted wave is fulfilled when eqs 1 and 2 are matched and can be achieved by different diffraction orders. In addition to the SPP, since the nanostructures are of close proximity to the light wavelength in size, the LSPs are excited on each of the periodic structures. Therefore, the hybridization of LSPs, SPP, and the diffracted ray at a grazing angle occurs in the symmetric 2D gold nanobump grating. During the measurements, the grating period was kept constant, with only polarization, the angle of incidence θ (angle between the incident beam and the surface

https://doi.org/10.1021/acsami.6c04043
ACS Appl. Mater. Interfaces XXXX, XXX, XXX−XXX

normal), and the azimuthal angle φ (angle between the plane of incidence and the laser scanning axis) being investigated (Figure 1b).

The beam impinging to the crossed 2D grating exhibits a conical diffraction, having the four main planes of diffraction (Figure 1c): Plane of incidence (PI, Figure 1d), that is the plane of the incident and the reflected beam, perpendicular plane (PP, Figure 1e), that is perpendicular to the plane of incidence, and 2 diagonal planes (DP, Figure 1f), that are at 45° with both PI and PP. The positive and negative diffraction orders are different in PI and DP ($m = +1$ and -1, $m = +2$ and -2), while in PP, these are similar ($n = \pm 1, \pm 2$) due to the symmetrical diffraction conditions. The p-polarized light has an electric field lying in the PI, while the s-polarized light has an electric field parallel to PP. As mentioned, plasmons are excited when the beam is diffracted at 90° to the normal and is parallel to the surface (the cutoff wavelength). Thus, in such a grating of 1 μm period, the beam diffracted in the first order excites them with the IR spectral part, while the second-order diffracted beam, with a visible or UV range wavelength.

The plasmonic response of the fabricated periodic gratings was measured using a spectrophotometer (Photon RT, Essentoptics). The reflectance spectra of the arrays were analyzed to determine the position of the plasmon resonance, as evidenced by a decrease in reflectance upon absorption of the incident radiation. A light beam with a 2 mm-diameter circular spot was used. The measurements were obtained using both s- and p-polarized radiation, in the spectral range of 400–1600 nm with a step of 4 nm. Most measurements were performed at a single angle of incidence ($\theta = 8°$); however, to assess the effect of angle, measurements were also obtained at 15° and 30°. Additionally, the azimuthal angle φ of the sample was changed by 15° so that $\varphi = 0°$ was considered when the spectrophotometer plane of incidence was parallel to the laser scanning lines, $\varphi = 45°$ when oblique to the scanning lines, and $\varphi = 90°$ perpendicular to them.

Since the presented DLW method enables easy morphological tuning by adjusting the deposited energy, it is possible to produce differently shaped structures within the same grating in a single fabrication step. This allows the production of distinct profiles between adjacent or in each second line in the grating. Spectral comparison of uniform bumps, bump-cone, and bump-jet gratings showed that the sharpest resonant peaks are obtained with bump gratings, and greater morphological variation leads to broader, less-pronounced resonances. This can be attributed to reduced effective resonance coupling and wider height variations for the out-of-plane resonant mode. Although such more complex, mixed-morphology structures are of broader interest, the analysis of grating-coupled excitation described in this work is most clearly distinguished in uniform-bump gratings, which exhibit the sharpest and most distinct resonances.

Figure 2a,b shows the measured reflection spectra for s- and p-polarizations at azimuthal angles $\varphi = 0°$, $\varphi = 45°$, and $\varphi = 90°$ for the bumps grating with a 1 μm period. In the spectra, at $\varphi = 0°$ (Figure 2a,b; black line) and $\varphi = 90°$ (Figure 2a,b; blue line), the first-order diffraction resonance behavior is similar for both polarizations: one resonance in the PP at s-polarization (996 nm), and two resonances in the PI at p-polarization (1162 and 877 nm). In addition to these usual first-order 1D-origin diffraction resonances, other diffraction peaks are observable. To identify their origin, spectra were measured by rotating the sample around its azimuthal axis. The near-identical spectra at $\varphi = 0°$ and $\varphi = 90°$ imply that the grating is uniform along both the scanning and perpendicular axes. Meanwhile, the $\varphi = 45°$ spectra (Figure 2a,b; red line) prove the plasmon excitation not only in the main periodic array of 1 μm period, but also in a diagonal lattice of $\sqrt{2}$ μm effective period. Also, the 2D crossed gratings support multiple diffraction periodicities defined by the in-plane lattice vectors (k_x, k_y). The 1D-related resonances are associated with (1,0) and (0,1) lattice vectors and are excited in PI and PP, while those of 2D origin, with (1,1) or higher-order lattice vectors, are excited in DP. In further analysis, the observed peaks will be separated into two groups: primary resonances (denoted as E_{pr}), excited at longer wavelengths in the 850–1200 nm range, and secondary resonances (E_{se}), excited at shorter wavelengths in the 600–850 nm range. Near the edge of absorption (550–600 nm range), shallow tertiary resonances may also be observed but will not be widely investigated.

For s-polarization (Figure 2a), at $\varphi = 0°/90°$, two secondary E_{se} dips are observed below the single primary peak E_{pr} of the first-order diffraction at PP. These originate from the 2D-type diffraction in DP (788 nm for negative and 658 nm for positive orders). The resonances in the measured spectra at $\varphi = 45°$ change as the single 1D-type E_{pr} resonance originating at PP splits into two (positive and negative) 2D-type resonances, which are excited in the DP of the rotated sample (1100 and 904 nm). Meanwhile, the two secondary E_{se} peaks observed from the DP at $\varphi = 0°$ merge into a single peak (720 nm) at $\varphi = 45°$, as it is now excited at symmetrical PP. The transition from two peaks at $\varphi = 0°$ into one at $\varphi = 45°$ confirms that this secondary resonance in PP is of 1D-type diffraction origin from a diagonal grating.

In p-polarization spectra (Figure 2b), the same resonance origins are observed, with the difference that instead of a single resonance from PP, the two resonances from PI appear. Meanwhile, the resonances originating in DP (E_{se} at $\varphi = 0°$ and E_{pr} at $\varphi = 45°$) occur at rather similar spectral positions in both polarizations (Figure S1), with minor shifts attributed to alignment inaccuracies at $\varphi = 0°$ and $\varphi = 45°$ angles, leading to the coupling in a diagonal plane and 2-dimensional diffraction that is less sensitive to polarization. The two E_{pr} 1D-type resonances at $\varphi = 0°/90°$ originating from PI (1162 and 877 nm) shift closer to each other (1134 and 924 nm) as the azimuthal angle is changed to $\varphi = 45°$, and E_{pr} are then excited in DP. At the shorter-wavelength region, the E_{se} are observable, where the ones originating in PI at $\varphi = 45°$ are in a wider wavelength range (824 and 642 nm) than the ones excited in DP at $\varphi = 0°/90°$ (800 and 670 nm). Finally, the tertiary resonances are observed in the lowest wavelengths (596 nm at $\varphi = 0°/90°$) just before the gold absorption zone. All the components that are visible in Figure 2a,b are visualized in Figure 2c,d with respective directions.

Since the resonant excitation is of diffractional origin, the diffraction grating equation can be employed to theoretically evaluate and compare the experimentally observed resonant wavelengths. For a squared grating, the 2D diffraction formula for plasmonic excitation can be applied to calculate the resonant wavelength:[61]

https://doi.org/10.1021/acsami.6c04043
ACS Appl. Mater. Interfaces XXXX, XXX, XXX−XXX

$$\lambda_{res,2D} = \frac{s}{(m^2+n^2)}\left(-m\sin\theta \pm \sqrt{\frac{\varepsilon_{Au}}{1+\varepsilon_{Au}}(m^2+n^2) - n^2\sin^2\theta}\right) \quad (3)$$

where s is the grating period, m is the diffraction order in direction parallel to the plane of incidence, n is the diffraction order perpendicular to the plane of incidence, θ is the angle of incidence, and ε_{Au} is the dielectric constant of gold. According to this notation, the diffraction of 2D-origin is denoted as $(m;n)$.

As the crossed 2D grating is composed of two orthogonal 1D arrays, the theoretical values can also be calculated using the simplified 1D diffraction grating formulas,[52,62] which represent special cases of the 2D formula. When the electric field oscillations are perpendicular to the 1D grating lines (diffraction in PI, p-polarization case), the grating vector is parallel to PI, while the perpendicular component does not contribute. In this $(m;0)$ case, the resonant wavelength is expressed as

$$\lambda_{res,1D,p-pol} = -\frac{s}{m}\left(\sin\theta \mp \sqrt{\frac{\varepsilon_{Au}}{1+\varepsilon_{Au}}}\right) \quad (4)$$

For the case when the electric field oscillations are parallel to the grating lines (diffraction in PP, s-polarization) and PI does not contribute, the $(0;n)$ case wavelength is given by

$$\lambda_{res,1D,s-pol} = \pm\frac{s}{n}\sqrt{\frac{\varepsilon_{Au}}{1+\varepsilon_{Au}} - \sin^2\theta} \quad (5)$$

The calculated resonant wavelength dependence on the grating period at a constant incidence angle of $\theta = 8°$ is presented in Figure 2e. The results are shown for the first (solid lines) and second (dashed lines) orders of 2D-type (green lines) and 1D-type (black and red lines) diffraction. Black lines correspond to s-polarization $(0;n)$, while red lines correspond to p-polarization $(m;0)$. 2D-type diffraction is observed at lower wavelengths than one-dimensional diffraction, occurring between the first and second orders. The experimental data extracted from the spectra in Figure 2a,b are indicated by discrete symbols: data points at a period of 1 μm for $\varphi = 0°/90°$ are shown as squares, while those at a $\sqrt{2}$ μm period for $\varphi = 45°$ are shown as diamonds. Filled symbols denote the primary resonances (E_{pr}), whereas empty symbols correspond to secondary resonances (E_{sc}), and filled gray symbols mark the tertiary resonant wavelengths. Great agreement between the experimental data and the theoretical curves enables unambiguous identification and assignment of the resonances to their diffraction origins.

At $\varphi = 0°$, the observed E_{pr} resonances are attributed to the first-order 1D-origin diffraction. In s-polarization, the resonance in PP corresponds to the $(0; \pm1)$ diffraction, and in p-polarization, the resonances in PI are $(-1;0)$ and $(1;0)$. Meanwhile, the E_{sc} of both polarizations excited at DP are associated with the first-order 2D-type diffraction. Specifically, the resonances near 800 nm are assigned to $(-1; \pm1)$, and the ones around 650 nm correspond to $(1; \pm1)$. Under p-polarization excitation, a shallow tertiary resonance is observed below 600 nm. It coincides with the $(-2;0)$ curve, indicating that higher-order modes of both repetitive 1D-type and 2D-type diffractions are excited at shorter wavelengths. At $\varphi = 45°$, the excitation occurs in a diagonal grating with $\sqrt{2}$ μm effective period. Here, primary resonances E_{pr} for both polarizations are excited in DP and accurately match the 2D-origin diffraction curves of $(-1; \pm1)$ and $(1; \pm1)$. S-polarization data (black solid diamonds) fit perfectly with the theoretical line, while the p-polarization results (red solid diamonds) exhibit a slight deviation. This discrepancy can be attributed to the oblique excitation and the presence of an out-of-plane component in the p-polarized field, whereas the s-polarized field remains entirely in-plane. Secondary E_{sc} resonances (empty diamonds) coincide with second-order 1D-type diffraction curves: p-polarized resonances excited in PI correspond to $(-2;0)$ and $(2;0)$, and s-polarization in PP matches the $(0; \pm2)$ curve. Again, under p-polarized light, observed tertiary resonance below 600 nm matches the $(-2; \pm2)$ curve, further confirming the repetitive excitation of higher-order modes. In this diagonal case, the first-order 1D-type diffraction at longer wavelengths is not observable, meaning the efficiency of this component is too low for the excitation. Summarizing the observations, azimuthal rotation alters the lattice of excitation, leading to a changed resonance origin. Main grating ($\varphi = 0°/90°$) primarily excites 1D-type diffractional resonances in PI and PP, with the following 2D-type diffraction peaks obtained in DP. In a diagonal grating ($\varphi = 45°$), primary resonances originate from 2D-type diffraction in DP, followed by higher-order 1D-type diffraction in PI and PP. This whole analysis and attribution of the peak origin is summarized in Figure S2.

The obtained plasmonic peaks were characterized by measuring their width and depth and by determining the quality factor (Q-factor), defined as the ratio of the resonant wavelength to the resonance width ($Q = \lambda/\text{fwhm}$). Also, a modified quality factor (MQ-factor) including the depth of the peak h was calculated for the comparison of its intensity:

$$MQ = \frac{\lambda \cdot h}{FWHM \cdot 100\%} \quad (6)$$

The exact evaluation of the peak depth and MQ-factor is described in.[50] The E_{pr} resonance qualities were measured at azimuthal angles of $\varphi = 0°$, $\varphi = 45°$, and $\varphi = 90°$ to compare the values. The results are given in Table 1. The calculated values confirm a previously determined trend:[62] resonance in s-polarization is stronger at $\varphi = 0°$, whereas in p-polarization it is stronger at $\varphi = 90°$. However, the difference in quality is minimal, and both azimuthal angles can be used for measurements. At $\varphi = 45°$, when the diagonal grating becomes dominant, and the origin is changed from 1D to 2D-type, the qualities of shifted E_{pr} resonances increase a bit for negative and decrease for other orders of diffraction. Meanwhile, for the

Table 1. Q-factor and MQ-Factor of the E_{pr} Resonances in the Bump Grating at $\varphi = 0°$, 45°, 90° Azimuthal Angles

	Q-factor		MQ-factor	
azimuthal angle	s-polarization $-m/+m$	p-polarization $-m/+m$	s-polarization $-m/+m$	p-polarization $-m/+m$
$\varphi = 0°$ (1D-type)	76.2	68.8/48.6	19.2	14.2/6.9
$\varphi = 45°$ (2D-type)	83.5/66.8	74.6/44.4	11.5/9.15	21.1/6.2
$\varphi = 90°$ (1D-type)	68.8	73.4/49.5	8.1	19.5/8.9

https://doi.org/10.1021/acsami.6c04043
ACS Appl. Mater. Interfaces XXXX, XXX, XXX−XXX

E_{se} component (Table 2), the qualities are higher at $\varphi = 45°$ for p-polarization peaks when the excitation is 1D-origin. Peaks

Table 2. Q-factor and MQ-Factor of the E_{se} Resonances in the Bump Grating at $\varphi = 0°$, 45°, 90° Azimuthal Angles

	Q-factor		MQ-factor	
azimuthal angle	s-polarization $-m/+m$	p-polarization $-m/+m$	s-polarization $-m/+m$	p-polarization $-m/+m$
φ=0° (2D-type)	58.3/38	36.6/35.3	7/4.4	4.4/3.3
φ=45° (1D-type)	28.45	59.5/36.8	4.9	8.9/3.7
φ=90° (2D-type)	57.1/35	45.9/33.9	7.2/3.7	6.7/3.7

in s-polarization, however, are of higher quality at $\varphi = 0°$, since the one at $\varphi = 45°$ is broader. The Q-factor of the described periodic gold bump reaches up to 70−80 for primary resonances E_{pr}, while it is reduced to around 60 for secondary E_{se} resonances. The Q-factor is influenced by the variations in the structure size, shape, and periodicity, as well as diffractive coupling into several lattices simultaneously, which can reduce the coupling efficiency, broaden the peaks, and reduce this parameter. In the literature, the described Q-factor of self-assembled lattices reaches up to 20,[10] higher resonance qualities (over 300) are achieved using isolated periodic nanoparticles that excite SLR,[24] while similar periodic structures with a gold layer in between reach around 70−140,[63] depending on the structure size.

2.2. Rotational Plasmonic Properties in the Azimuthal Angle

To gain a deeper understanding of resonance spectral manipulation, reflection spectra were measured at azimuthal angles from $\varphi = 0°$ to $\varphi = 90°$ in 15° steps. By changing this angle at a constant $\theta = 8°$ angle of incidence, a clearer resonance shift from $\varphi = 0°$ to $\varphi = 45°$, and back is observed, as represented in Figure 3a,b. Each curve exhibits several reflection minima corresponding to plasmonic resonances excited at different diffraction orders and planes. Here, the primary E_{pr} resonances in the near-IR (850−1200 nm range) are circled in blue, and the secondary E_{se} resonances (650−850 nm range) are circled in green. The exact resonant wavelength value tendencies are depicted in Figure 3c,d, with blue lines showing E_{pr} and green lines marking E_{se}. Upon rotation, the E_{pr} resonances split into two, reaching maximum separation at $\varphi = 45°$ in s-polarization and at $\varphi = 0°$ in p-polarization, whereas the E_{se} resonances show the opposite behavior. This periodic splitting-merging with φ is a consequence of the conical diffraction behavior occurring in the crossed grating. The excitational component of the incident wavevector is projected differently onto various lattices of the sample as it is rotated, and the change between 1D-type and 2D-type diffraction is happening.

At the intermediate angles (15°, 30°, 60°, 75°), several shallow resonant peaks can be observed close to each other, with several of these attributed to the shifting resonance of either E_{pr} or E_{se} with the changed excitation and coupling lattice. At such angles, the incident wavevector is projected onto several lattices, and neither the main nor the diagonal

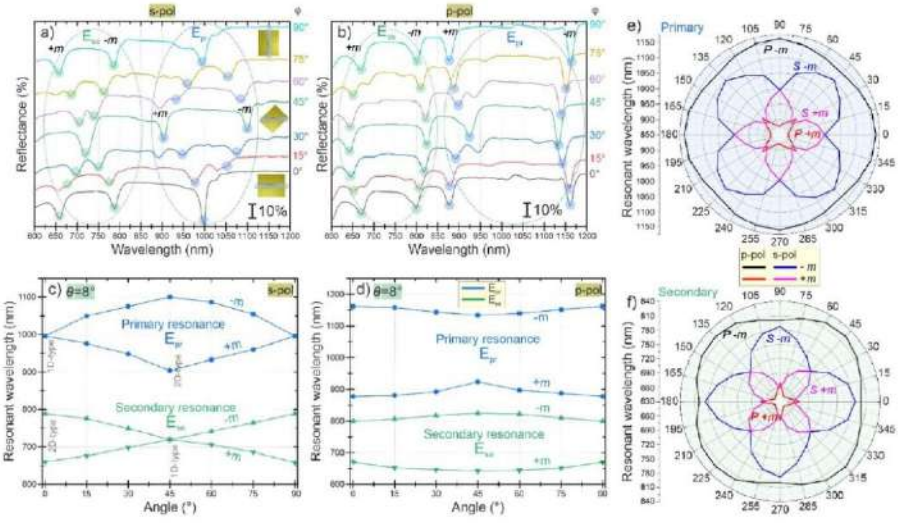

Figure 3. Reflectance spectra of gold nanobumps grating with a period of 1 μm at different azimuthal angles from $\varphi = 0°$ to $\varphi = 90°$ with a step of 15° for (a) s- and (b) p-polarization. Blue circles indicate the primary resonances, while green circles indicate the secondary resonances. Resonant wavelength shift with the change of azimuthal angle at a fixed $\theta = 8°$ angle of incidence for (c) s- and (d) p-polarization. Resonant wavelength change of (e) primary E_{pr} and (f) secondary E_{se} resonances in the polar coordinate system.

https://doi.org/10.1021/acsami.6c04043
ACS Appl. Mater. Interfaces XXXX, XXX, XXX−XXX

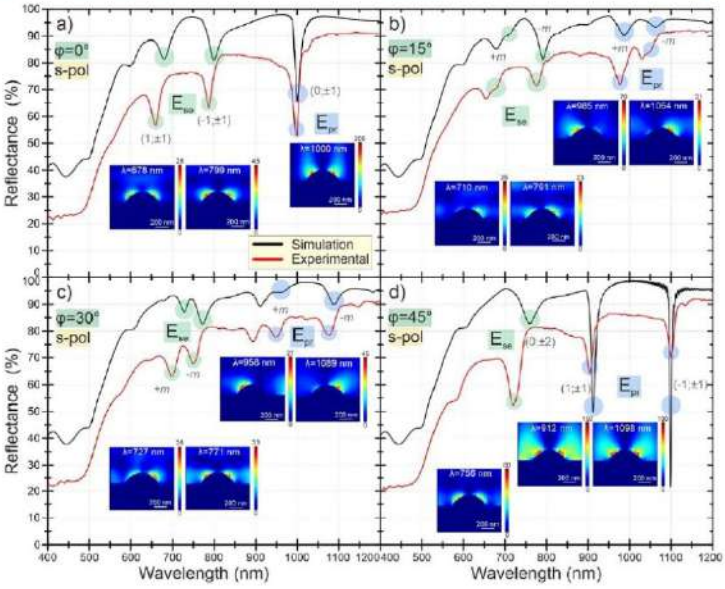

Figure 4. FDTD simulated (black line) and experimental (red line) reflectance spectra of s-polarized light response from gold nanobumps with a period of 1 μm at $\theta = 8°$. The spectra are shown for azimuthal (a) $\varphi = 0°$, (b) $\varphi = 15°$, (c) $\varphi = 30°$, and (d) $\varphi = 45°$. Blue circles indicate the primary E_{pr} resonances, while green circles indicate the secondary E_{se} resonances. Insets show the side-view profiles of the simulated near-field enhancement on the structures at the corresponding resonant wavelengths.

grating diffraction condition is strictly satisfied. This leads to excitation coupling across several planes and to reduced coupling strength for each in-plane mode. For example, at $\varphi = 15°$ in s-polarization, two shallow overlapping peaks are observed at 1050 and 1029 nm, which may arise from coupling to several lattices with similar effective periods. Also, some of the additional dips can be explained by the influence of another polarization, as denoted in Figure S3. At angles $\varphi = 15°$ and $\varphi = 75°$, two E_{se} peaks at 652 and 678 nm, and at 651 and 684 nm, respectively, are observed in both polarizations, differing only in intensity. The same is observed for E_{pr} at $\varphi = 30°$ and $\varphi = 60°$, the resonances being at 892 and 948 nm, and at 897 and 933 nm, respectively. Other resonant peaks are observed in both polarizations, albeit with lower intensities. Such a tendency illustrates the coupling between the two polarizations into main or diagonal gratings at nonperpendicular azimuthal angles. The depth and width of the resonant peaks are indicative of the coupling rate through the specific diffraction plane and of the metal's intrinsic losses. Sharp and deep dips indicate efficient diffractive momentum matching, whereas broad, shallow features indicate weak coupling. The observed peak narrowing and broadening with φ indicate angle-dependent coupling, which was most effective for the (1,0) and (1,1) lattices at 0° and 45°, whereas at intermediate angles the peaks were shallow with modest diffractive coupling.

The polar plots in Figure 3e,f provide a visualization of the angular evolution of the resonant wavelength for the E_{pr} and E_{se} modes in the main and diagonal gratings. The resonances produce a four-lobed pattern aligned with either principal grating axis or along the diagonals, demonstrating a consistent pattern across the entire azimuthal rotation. The alignment of the lobes along the main axes demarcates the blueshifting peaks, while the lobes along the diagonals denote the redshifting resonances as the excitation plane undergoes a transition from main to diagonal grating (from $\varphi = 0°$ to $\varphi = 45°$). A general trend emerges that is consistent across all resonances. The modes exhibit minimal splitting and merge upon excitation by 1D-type diffraction in PP. An intermediate interpeak distance is observed with 2D-type diffraction at DP, and the largest splitting is attained at 1D-type PI excitation.

To complement the experimental observations and verify the origin of the observed resonances, the optical response of the 2D periodic gold-bump grating was modeled using the Lumerical FDTD solver. To model the 3D structure (2D grating), we defined a unit cell with Bloch boundary conditions, based on Bloch−Floquet theory,[64,65] in the direction perpendicular to the grating, and with perfectly matched layers (PMLs) in the light-propagation direction. This configuration enables the simulation of a periodic structure with a precise mesh. The unit cell, with a periodicity of 1 μm, consists of a dielectric material with refractive index $n = 1.51$ at 900 nm (Soda-Lime Glass[66]) and is topped by a 100 nm-thick gold layer. As illustrated in Figure 1a, the bump is modeled with a height of 270 nm and a diameter of 550 nm. The bump consists of a 65 nm-thick shell, and its interior is filled with a medium of refractive index $n = 1$. The gold material is

https://doi.org/10.1021/acsami.6c04043
ACS Appl. Mater. Interfaces XXXX, XXX, XXX−XXX

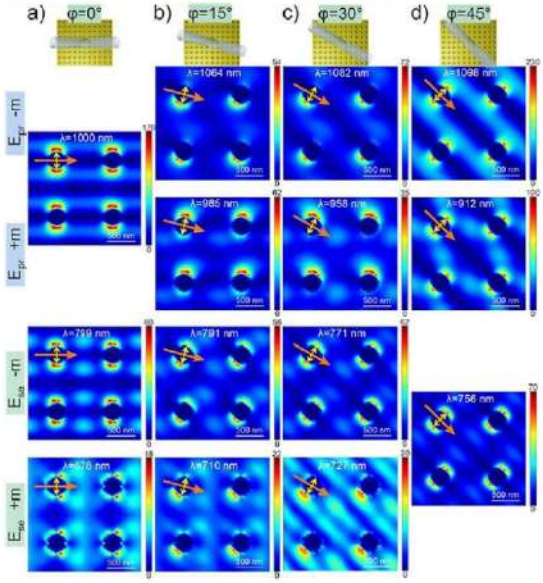

Figure 5. Top-view FDTD simulations of s-polarization near-field enhancement on gold nanobumps with a period of 1 μm at the resonant wavelengths for (a) $\varphi = 0°$, (b) $\varphi = 15°$, (c) $\varphi = 30°$, and (d) $\varphi = 45°$ azimuthal angles. The first and second rows depict the primary E_{pr} resonances for negative and positive diffraction orders, respectively, while the third and fourth rows depict the secondary E_{sw} resonances for negative and positive diffraction orders, respectively. Orange arrows indicate the light incidence direction, and yellow arrows denote the electric field oscillation direction. Graphs obtained at 87.5% of the structure's height.

described using the optical constants from Johnson and Christy.[67] To account for the oblique incidence used in the experiment, the simulation employs Lumerical's Broadband Fixed Angle Source Technique (BFAST), which enables oblique illumination by correcting the phase according to the incidence angle.[68] The 3D simulation provides the transmission and reflection spectra and the electric-field distribution parallel to the surface, evaluated at different heights. In addition, the 3D model enables the extraction of the electric-field distribution along an oblique vertical cross-section, which cannot be obtained from standard two-dimensional simulations, by slicing the full 3D tensor field. Since the source is planar and normalized, the local E_{pr} and E_{sw} fields represent an increment attributable to plasmonic resonances.

The simulated reflection spectra and near-field distributions provide direct insight into the diffraction-based plasmonic mode excitation and its dependence on polarization and azimuthal orientation. Figure 4 presents the spectra of s-polarized light, with black lines representing the simulated response and red lines representing the experimentally measured reflectance. Peaks marked in blue are attributed to E_{pr} resonances, while those marked in green are E_{sw}. A comparison of the simulated and experimental spectra and resonances reveals a strong coincidence in both spectral positions and overall peak behavior across the shifted azimuthal angle. There is only a slight shift of the simulated peaks toward longer wavelengths relative to the experimental peaks, which may arise from nonideal grating fabrication and the use of ideal hemispherical structures in the simulation. Consistent with the experimental observations, the strongest peaks, with the largest intensity drops, are observed at $\varphi = 0°$ and $\varphi = 45°$ for the E_{pr} resonances. Meanwhile, the peaks at intermediate azimuthal angles are low in intensity because the incident direction is not matched to the grating and is not optimally aligned with the dominant grating. Since the resonances at $\varphi = 0°$ and $\varphi = 45°$ are already identified, their origin is labeled, while for intermediate angles, peaks are not uniquely attributable to a single diffraction lattice and are therefore distinguished only by their positive $(+m)$ and negative $(-m)$ diffraction orders.

The cross sections of the insets in Figure 4 are obtained at the plane of electric field oscillations according to the azimuth. All plasmonic excitations obtained with s-polarization are in-plane modes, with near-field enhancements along the sides of the structure. The field is distributed uniformly, with two lobes at angles where the incident plane aligns with the main or diagonal grating (Figure 4a,d), thereby enabling efficient coupling and deep resonances. Azimuthal changes to $\varphi = 15°$ and $\varphi = 30°$ result in asymmetric field localization on either side of the structure. This phenomenon may coincide with positive and negative diffraction orders, as observed for E_{pr} resonances, and appears due to the coupling not confined to the single lattice.

https://doi.org/10.1021/acsami.6c04043
ACS Appl. Mater. Interfaces XXXX, XXX, XXX−XXX

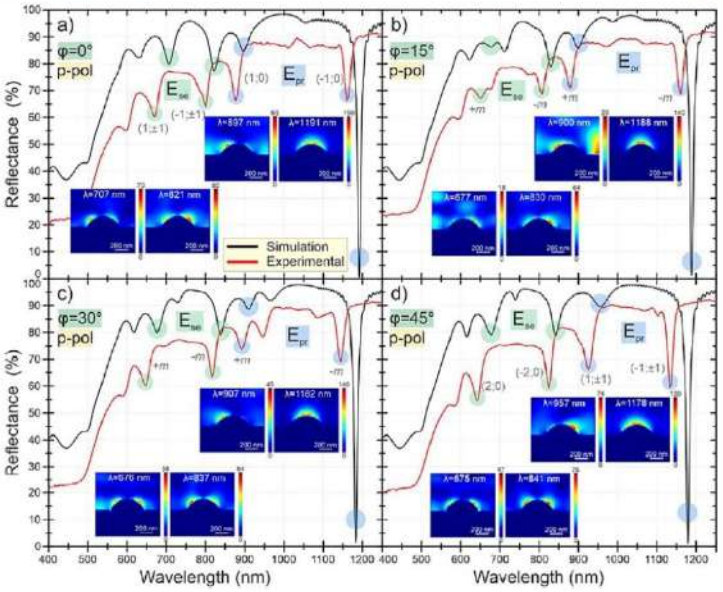

Figure 6. FDTD simulated (black line) and experimental (red line) reflectance spectra of p-polarized light response from gold nanobumps with a period of 1 μm at $\theta = 8°$. The spectra are shown for azimuthal (a) $\varphi = 0°$, (b) $\varphi = 15°$, (c) $\varphi = 30°$, and (d) $\varphi = 45°$. Blue circles indicate the primary E_{pr} resonances, while green circles indicate the secondary E_{se} resonances. Insets show the side-view profiles of the simulated near-field enhancement on the structures at the corresponding resonant wavelengths.

These simulations also enable the demonstration of the hybrid origin of the resonances (HLPRs) and their distinction from SLRs. Typical SLR systems are composed of isolated metallic nanostructures, and their LSPs are coupled via in-plane photonic diffraction modes, whereas the structures in this work are connected by a continuous gold film and coupled by surface waves (SPPs). Similar hybrid excitation in metallic structures with a thin film was observed in other publications.[1,69−71] The simulation of the response spectra of our periodic bumps (HLPR excitation) and identical structures without the film (theoretical SLR excitation) revealed a significant difference (Figure S4a−c). Since our structures are covered with a highly reflective gold film, the resonances can be characterized by reflectance measurements. Meanwhile, bumps without film between the structures result in a low reflection response, as transmission through those regions increases. A direct comparison was performed using the extinction calculation (Figure S4c), eliminating transmittance and reflectance (100%-R-T). Although resonant peaks are observed in the bump without gold film arrays at similar positions, they are much less pronounced, indicating that a continuous gold film enhances coupling efficiency by involving SPP modes. Additionally, insight into the near-field side-view profiles of the primary E_{pr} resonances at $\varphi = 0°$ was performed (Figure S4d,e). It revealed that the field is not confined to the individual structure and its sides but extends along the metal surface and penetrates into the thin gold film with a characteristic decay length. This observation proves SPP excitation in the metal layer, thereby confirming coupling via surface waves and HLPR origin.

Top-view simulations of the near-field at the periodic nanobumps provide deeper insight into plasmonic mode excitation. Figure 5 presents the spatial localization of plasmonic modes excited under s-polarization, where each column corresponds to a different azimuthal angle, and each row shows a different diffractional order of E_{pr} and E_{se}. At $\varphi = 0°$ (Figure 5a), where the plane of incidence (orange arrow) is aligned with the main grating axis, a strong field localization is observed at the edges of the nanobumps along the direction of electric field oscillation (yellow arrow). Both E_{pr} and E_{se} resonances exhibit similar field alignment along the main lattice, indicating that this plane is superior in that configuration. It is noteworthy that the E_{se} resonances at 799 and 678 nm exhibit lobes oriented at the corners, indicating diagonal 2D-type excitation. When the azimuthal angle is increased (Figure 5b,c), the near-field profiles exhibit a noticeable asymmetry and a rotation of lobes. This rotation reflects changes in the in-plane component of the wavevector that contribute to plasmonic excitation. At E_{pr} resonances, a stronger lobe is observed, with hotspot localization maintained along the main axis in PP, with a contribution from the rotated electric field at an angle. Meanwhile, at E_{se} resonances, a moderate angular electric-field contribution is also observed; in this case, the lobes are oriented, and the field is more

https://doi.org/10.1021/acsami.6c04043
ACS Appl. Mater. Interfaces XXXX, XXX, XXX−XXX

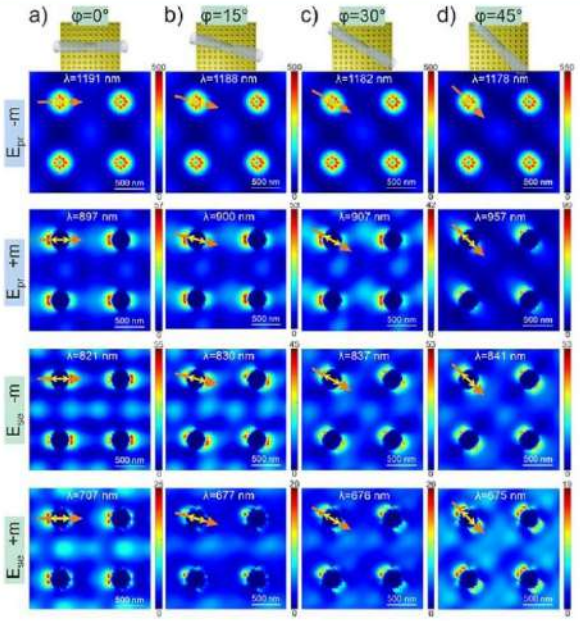

Figure 7. Top-view FDTD simulations of p-polarization near-field enhancement on gold nanobumps with a period of 1 μm at the resonant wavelengths for (a) $\varphi = 0°$, (b) $\varphi = 15°$, (c) $\varphi = 30°$, and (d) $\varphi = 45°$ azimuthal angles. The first and second rows depict the primary E_{pr} resonances for negative and positive diffraction orders, respectively, while the third and fourth rows depict the secondary E_{si} resonances for negative and positive diffraction orders, respectively. Orange arrows indicate the light incidence direction, and yellow arrows denote the electric field oscillation direction. First row graphs were obtained at 100% height, while others—at 87.5% height of the structure.

concentrated along the diagonal axis. In both cases, there is a noticeable 15° and 30° azimuthal influence determining lobe orientation. Finally, at $\varphi = 45°$ (Figure 5d), the incident beam is aligned with the diagonal grating direction, and the near-field hot spots across all resonances are distributed along the diagonal lattice axis, indicating efficient coupling into this grating configuration.

Comparing experimental peaks and their quality led to the conclusion that s-polarization resonant peaks at $\varphi = 0°$ are narrower than those at $\varphi = 45°$. Meanwhile, the FDTD-calculated graph comparison in Figure 4a,d shows the opposite trend, with much narrower, deeper peaks at $\varphi = 45°$. Such a theoretical discrepancy can be explained by analyzing the top-view near-field enhancements of the E_{pr} peaks in the structures (Figure 5a,d). At $\varphi = 0°$, the coupling is governed by diffraction and plasmonic excitation along a principal lattice, leading to interaction between neighboring structures only in this axis, and coupling being defined by the lattice period. In contrast, at $\varphi = 45°$ (Figure 5d), the excitation involves a 2D-type diffraction condition, where near-field maps reveal that the coupling is not based on direct longer-period ($\sqrt{2}$ μm) interaction. Instead, the stronger coupling in the diagonal is achieved through the interaction of shorter effective coupling pathways through the neighboring structures. Such shorter interaction length leads to smaller damping and more pronounced resonant peaks. However, the experimental gratings suffer from irregularities in the period, which are more significant in the diagonal lattice, thus leading to reduced coupling efficiency and shallower peaks.

The simulated reflectance spectra for p-polarization are depicted in Figure 6. Similar to s-polarization, the simulated resonances are slightly red-shifted relative to the experimental resonances. From all angles, the E_{pr} negative peak retains its depth and is the most intense resonance. Near-field simulations (insets of Figure 6) prove that this resonance (at ~1180−1190 nm) is an out-of-plane mode with the field localization at the top of the structure. Unlike other resonances, this resonance depends strongly on the structure's shape and height.[51] The remaining spectral peaks are caused by the in-plane modes, characterized by the field localization at the lateral boundaries of the nanobump. While in the s-polarization case, the E_{pr} positive resonance manifests as two lobes at $\varphi = 0°$ and $\varphi = 45°$ angles. Under p-polarization, this resonant mode exhibits field localization only at a single side of the structure across all azimuthal angles, and the field is positioned at the side of the incident beam. This indicates the nonuniform excitation conditions of the positive and negative order plasmonic modes under p-polarization at zero azimuth. Meanwhile, at s-polarization, the excitation conditions are uniform since the field is perpendicular to the plane of

https://doi.org/10.1021/acsami.6c04043
ACS Appl. Mater. Interfaces XXXX, XXX, XXX−XXX

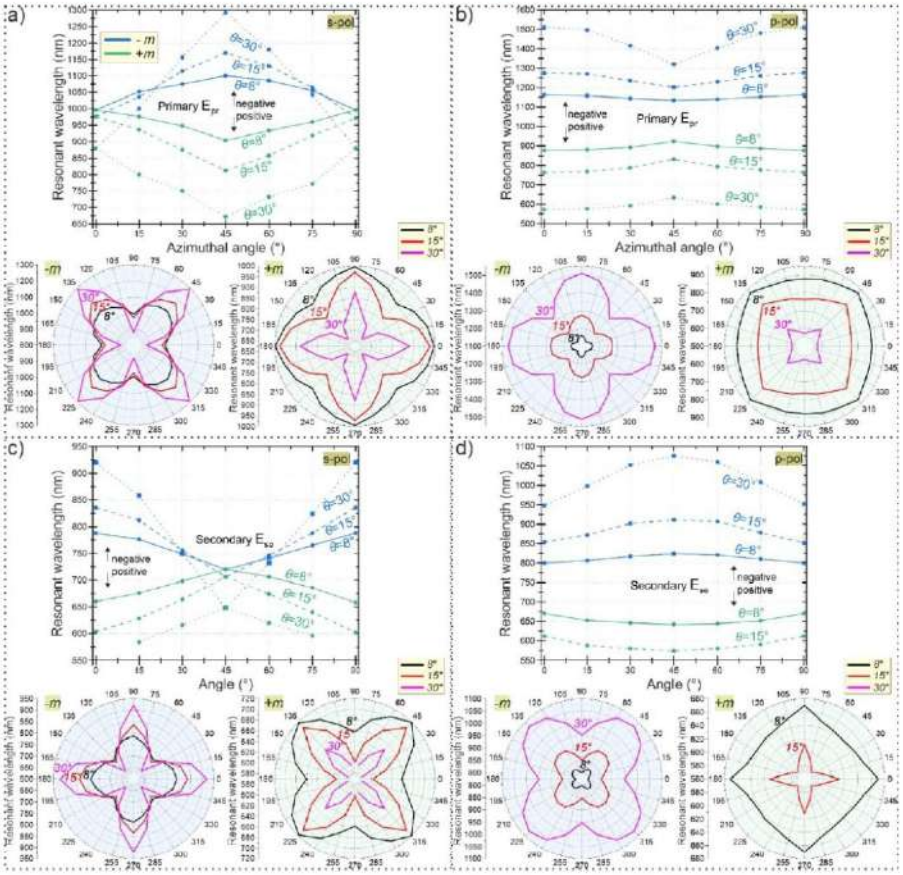

Figure 8. Experimental (a,b) primary E_{pr} and (c,d) secondary E_{se} resonant wavelength dependence on azimuthal angle, with incident angle influence for (a,c) s- and (b,d) p-polarization. Blue lines mark the positive-order diffraction resonances, and green lines the negative-order resonances, at incident angles of 8° (solid lines), 15° (dashed lines), and 30° (dotted lines). The insets show polar plots of the same resonant peaks, with negative-order displayed in a blue background and positive-order in a green background.

incidence. Similar to the experimental results, near the attributed E_{pr} and E_{so} resonances, some additional peaks are visible (Figure 6b,c) that are due to coupling into several lattices excited with both polarizations (similar to Figure S3).

The top-view graphs of the near-field at the resonant wavelengths under p-polarization are presented in Figure 7. The first row evidently illustrates the out-of-plane mode, with excitation located at the apex of the structure and a uniform field surrounding the bump across all angles. As in the s-polarization case, at $\varphi = 0°$ (Figure 7a), the plane of incidence is aligned with the main grating axis, resulting in field localization along the sides of the nanobumps in this direction. In the case of p-polarization, the positive diffraction orders of both E_{pr} and E_{se} resonances experience enhanced field on the incidence side of the structure, whereas the negative order of the in-plane E_{so} mode is more pronounced on the propagation side. This single-sided field asymmetry at positive diffraction orders persists through all azimuthal rotations examined. The change in the φ angle further confirms the primary governing grating for the resonant modes. At $\varphi = 15°$ and $\varphi = 30°$, the near-field of E_{pr} is maintained along the main grating axis, exhibiting a slight influence from the shifted excitation angle. Concurrently, the E_{se} undergoes a shift in respect to the azimuth, with the most significant enhancement occurring within the plane of incidence, while a portion of the field is oriented along the diagonal axis. When at $\varphi = 45°$, the diagonal

https://doi.org/10.1021/acsami.6c04043
ACS Appl. Mater. Interfaces XXXX, XXX, XXX−XXX

plane becomes dominant (Figure 7d), the field becomes exclusively localized along the diagonal axis for all in-plane resonances.

The simulated Figure S4 graphs also give insight into the polarization mode origin. For the isolated bump array (without the gold film), which corresponds to a conventional SLR system, a weak resonance is observed only in s-polarization at 1000 nm, indicating lattice-diffraction-coupled LSPs. For bumps with a Au film, the resonance persists at a similar position but with higher intensity, suggesting that this mode is SLR-mediated and greatly enhanced by interactions with SPPs in the metal film. Meanwhile, for p-polarization, strong resonances appear only in the presence of the gold film, indicating that the mode origin is more closely related to the grating-excited SPPs when the electric field component is normal to the metal surface.

Summarizing, a more pronounced directional asymmetry is observed under p-polarization excitation, originating from the electric field vector and its coupling to the SPP modes. Given the excitation's oblique angle and the electric field's component parallel to the plane of incidence, the diffraction-based excitation of the SPPs modifies the wavevector in opposite ways for positive and negative orders. This imbalance in momentum matching manifests as a single lobe in the near-field for p-polarization resonances. Conversely, under s-polarization, the electric field is perpendicular to the incidence plane, resulting in a symmetric coupling to both propagation directions.

One of the advantages of the DLW method is the flexibility in fabricating freely chosen lattice geometries. For further azimuthal grating-coupling exploration, bump gratings with rectangular symmetry were fabricated by reducing the in-line period along the scanning direction (0.865 and 0.75 μm), while maintaining a constant 1 μm perpendicular periodicity. The comparison of the reflectance spectra is given in Figure S5. The square lattice (Figure S5a) exhibits smooth, symmetric resonance shifts with azimuthal angle (marked with dashed lines), with similar responses at $\varphi = 0°$ and $\varphi = 90°$ due to the continuous coupling transition from the principal 1 μm-period lattice to the diagonal lattice and back to the 1 μm-lattice. Since the in-plane component of the incident wavevector is perfectly aligned with either principal or diagonal lattices at the azimuthal angles of $\varphi = 0/90°$ and $\varphi = 45°$ (Figure S5a(iii)), the most efficient coupling and thus the sharpest resonant peaks are observed at these high-symmetry angles, with the reduced coupling efficiency at intermediate angles.

In contrast, the rectangular arrays (Figure S5b,c) exhibit more complex and fragmented spectral behavior due to symmetry breaking and changes in diffraction-mode excitation conditions along the two principal lattice directions. Such anisotropic excitation conditions affect not only the mismatch in resonant wavelengths at $\varphi = 0°$ and $\varphi = 90°$ but also the coupling to different lattices at intermediate azimuthal angles. At 0.865 μm in-line period, the additional effective coupling to oblique lattices is achieved at $\varphi = 30°$ (lattice vector of (2,1)) and $\varphi = 60°$ (lattice vector of (2,3)). This makes the resonant peaks at these angles more pronounced than at other intermediate angles. In contrast, at 0.75 μm in-line period, the effective diffraction-based coupling is achieved at $\varphi = 15°$ (lattice vector of (5,1)) and $\varphi = 45°$ (lattice vector of (4,3)). In such a rectangular alignment, the resonance shift does not follow a continuous trend but instead exhibits a nonuniform, fragmented shift, with discontinuities (around $\varphi = 45°$) corresponding to transitions in coupling between the perpendicular principal lattices. A further reduction of the in-line period leads to the formation of anisotropic gratings that approach quasi-1D and 1D behavior, in which isolated resonant peaks dominate.[72] These results show that while rectangular lattices provide increased flexibility and access to a richer k-space, they also introduce complexity in resonance behavior due to anisotropic coupling conditions. Therefore, the following research will focus solely on the symmetric grating, which offers more intuitive and more easily defined resonance control.

2.3. Double-Angular Control of Resonant Wavelengths

To further explore the angular dependence of diffractively coupled plasmonic excitation, the azimuthal rotation study was extended to different angles of incidence. This approach enables double-angular manipulation of the resonances. The sample was measured at incident angles $\theta = 8°$, 15°, and 30°, at the same φ as previously, with a 15° step. Figure 8 presents the experimentally determined dependence of wavelength on azimuthal angle, accounting for the angle of incidence. The measured reflectance spectra at $\theta = 15°$ and 30°, with resonances attributed to primary or secondary, are shown in Figure S6. Since θ impacts the diffraction condition, the plasmonic excitation highly depends on this parameter as well. An increase in the angle leads to an increasing separation of the diffractively coupled resonances at PI and DP (p-polarization and s-polarization), and a redshift of the single resonance at PP (s-polarization). Angular shift leads to a redshift of negative and a blueshift of positive order of diffraction resonance in p-polarization (Figure 8b,d). Meanwhile, the s-polarization (Figure 8a,c) response depends on the azimuthal angle: a blueshift of resonances is observed at azimuthal orientations close to the 1D-type excitation in PP ($\varphi = 0°/90°$ and 15°/75° for the E_{pp}, and $\varphi = 45°$ and 30°/60° for the E_{ss}). At other φ angles, the same tendency as in p-polarization is maintained, with a redshift of negative order resonance. This indicates that polarization also plays an important role in determining the diffraction-induced plasmonic excitation, and which angular shift, azimuthal or excitational, has a greater effect on the resonant spectral position. It has been demonstrated that a larger incident angle yields steeper dependence curves, indicating more sensitive resonance control with an azimuthal shift. The overall spectral dispersion with incident angle is weaker for the secondary modes (Figure 8c,d). At higher incidence angles (Figure S6d), the separation of the resonant modes becomes pronounced, shifting the positive diffraction order into the metal absorption zone, where it is no longer observable. Meanwhile, additional unassigned resonances (Figure S6b,d) emerge in the spectra. These originate from higher-order diffractions that redshift out of the gold absorption zone as the incident angle increases. Figure 8 insets of the polar plots demonstrate that peak shifts exhibit a similar tendency across all incident angles, emphasizing the rotational symmetry of the resonances. Such double-angle control enables continuous tuning of the plasmonic excitation conditions without altering the grating geometry.

By implementing eqs 3−5, the tendency for resonant wavelength dependence on the incidence angle was calculated and presented in Figure S7. The results are depicted for the special case of 1D diffraction (Figure S7a), calculated using 4) and (5) formulas, as well as for the 2D diffraction (Figure S7b). Marked symbols, representing experimental values, are in

https://doi.org/10.1021/acsami.6c04043
ACS Appl. Mater. Interfaces XXXX, XXX, XXX−XXX

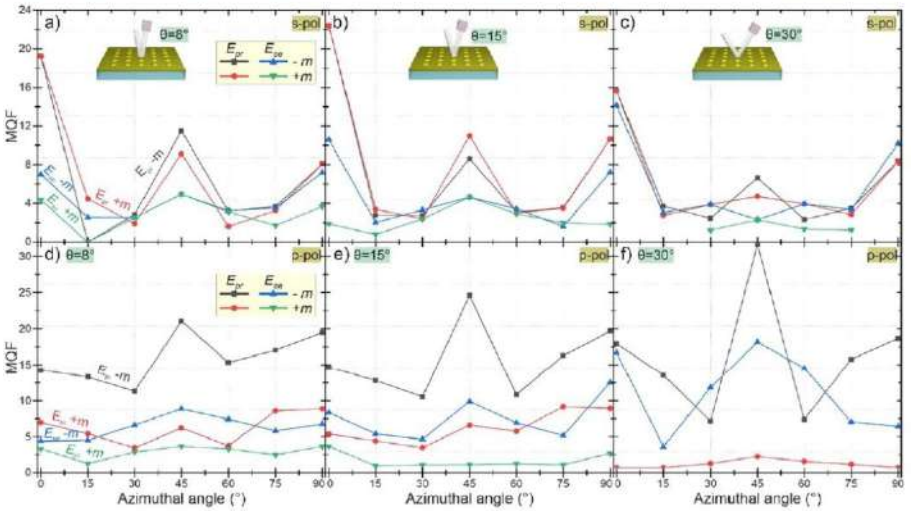

Figure 9. Modified quality factor dependence on the azimuthal angle for the experimental resonances obtained under (a–c) s-polarization and (d–f) p-polarization at (a,d) 8°, (d,e) 15°, and (c,f) 30° incident angles. Black lines denote E_{pr} negative, red lines E_{pr} positive, blue lines E_{se} negative, and green lines E_{se} positive resonances.

consistent agreement with the curves at all three angles of incidence: 8°, 15°, and 30°. For diagonal 2D-type diffraction excitation, s-polarization results exhibit better agreement with the calculations than p-polarization data, which can be attributed to the purely in-plane component in s-polarization.

Finally, the qualitative assessment of the resonances has been performed by evaluating the modified quality factor of each peak. The tendency for azimuthal rotation with respect to the incidence angle and polarization is provided in Figure 9. Unlike the conventional Q-factor, the MQ-factor, as described in eq 6, in this case, provides a more reliable basis for comparing resonances across all azimuthal orientations. Narrow but shallow resonances, obtained at φ = 15° and φ = 30°, may artificially increase and distort the Q-factor tendency, whereas the MQ-factor simultaneously accounts for line width and depth, yielding a physically meaningful measure for comparison. Under s-polarization, the resonance quality is generally poorer than under p-polarization, as reflected in lower MQ-factor values. The dominant are primary E_{pr} resonances with higher qualities, while E_{se} peaks remain comparatively weaker. All resonances exhibit a pronounced maximum at azimuthal angles aligned with the main and diagonal lattice axes (φ = 0° and 45°). Such a methodology, incorporating azimuthal rotation and quality measurements, could be used to experimentally determine the dominant diffraction axes of the fabricated grating. Under s-polarization, for θ = 8° (Figure 9a), the highest MQ values occur at φ = 0°, followed by a sharp decrease at intermediate angles, indicating that these resonances are tightly confined to the excitation along the main symmetry direction of the grating. A moderate secondary maximum at φ = 45° corresponds to coupling into the diagonal lattice, although with lower efficiency. Increasing the incidence angle to 15° and 30° (Figure 9b,c) enhances the angular selectivity of the peaks, maintaining similar quality along the main grating and reducing the quality of the diagonal-coupled resonances. At all incident angles, consistent with the tendencies observed in Tables 1 and 2, the s-polarization resonances exhibit higher quality at φ = 0° than at φ = 90°, showing stronger coupling when the plane of incidence is parallel, and the electric field is perpendicular to the scanning lines.

Using p-polarization, the out-of-plane mode (primary negative E_{pr}, $-m$) dominates across all azimuthal angles, with a particularly large MQ-factor. At all investigated angles of incidence, the quality is higher at the φ = 90° configuration (MQ around 20) compared to φ = 0° (MQ around 15), indicating that p-polarization plasmonic excitation is more efficient when the plane of incidence and the electric field are perpendicular to the scanning lines. However, the highest-quality resonances are achieved at φ = 45° angles, demonstrating that coupling to a diagonal grating provides the most favorable conditions. Increasing the incidence angle improves the peak quality, from MQ = 20 at 8° to MQ = 32 at 30°. Other resonances, though weaker, follow a similar azimuthal tendency. Overall, a general trend emerges: the highest-quality peaks are obtained at excitation angles aligned with either the main or the azimuthal lattice direction, with a sharp drop in quality at intermediate angles. This behavior reflects the symmetry of the 2D grating and a directional dependence of the diffraction-coupled resonances.

3. CONCLUSIONS

In this paper, we have insightfully studied the diffraction-based excitation of the hybrid plasmonic resonances in a 2D periodic nanobump grating. The resonances, arising from the hybrid-

https://doi.org/10.1021/acsami.6c04043
ACS Appl. Mater. Interfaces XXXX, XXX, XXX−XXX

ization of grating-induced surface plasmon polaritons, localized surface plasmons, and diffracted light at the lattice, were identified and assigned to their origins. The experimentally observed spectral features are well described by hybrid lattice plasmon resonances, whose behavior is governed by coupling to the array's main or diagonal axes. The results were fully supported by combining angle-resolved reflection measurements with theoretical grating-diffraction formulas, FDTD simulations, and near-field mappings. The azimuthal-angle study revealed strong directional selectivity in the modes, thereby providing additional spectral tunability of the resonant peaks. The wavelength positions systematically shift with azimuthal variation due to the varying in-plane components of the diffracted wavevectors. Near-field simulations demonstrated that s-polarization generates more symmetric in-plane field distributions, whereas under p-polarization, asymmetric single-lobe patterns are obtained due to oblique excitation. A thorough analysis of the modified quality factor indicated that the high-quality resonances are obtained when the excitation is aligned with the high-symmetry directions of the lattice — either along the main grating (φ = 0°, 90°) or along the diagonal axes (φ = 45°). Finally, the novelty of this work lies in the demonstration and investigation of dual-angular control of both azimuthal and incidence angles, further expanding the resonance control region across the entire Vis-NIR range. Overall, the combined experimental-theoretical approach provides a comprehensive understanding of the excitation and tunability of diffraction-based plasmonic resonances in symmetric 2D arrays.

4. EXPERIMENTAL SECTION

4.1. Materials

A 100 nm-thick gold film was deposited on 1 mm-thick soda-lime optical glass using a magnetron sputter coater (Quorum Q150T) at a deposition rate of ~0.26 nm/s.

4.2. Nanostructures Array Formation

Gold nanostructures were fabricated on the thin gold film using direct laser writing (DLW) using third-harmonic (343 nm) of 300 fs laser pulses generated by a Yb:KGW-based fs-laser (Pharos, Light Conversion). Structures were fabricated using a tightly focused (~800 nm) femtosecond laser beam with 0.8 nJ pulse energy to produce the hemispherical bumps on the surface. The structures were produced by scanning a laser pulse along a line at a specified speed and frequency, so that individual pulses could be distinguished by the required period. The period along the perpendicular axis was determined by the spacing between the scanning lines. The period of the uniform 2D grating was chosen to be 1 μm. The size of the produced symmetrical 2D array was 3 × 3 mm^2.

4.3. Characterization

The periodic array was characterized using a spectrophotometer (Photon RT, Essentoptics) and a scanning electron microscope (Helios NanoLab650). The reflectance spectra in the wavelength range from 0.4 to 1.6 μm were measured at different light polarizations (s- and p-polarization) at several incidence angles θ (8°, 15°, 30°). The azimuthal angle φ was varied from 0° to 180° in 15° increments by manually rotating the sample on the angular scale. Angle φ = 0° corresponds to the case when the plane of incidence is parallel to the laser scanning lines, and at φ = 90°, the plane of incidence is perpendicular to the scanning lines. The spot size of the impinging light was a 2 mm diameter circle. SEM characterization of the bump array was performed after reflectance spectrum measurements.

4.4. Theoretical Calculations

Resonant wavelengths for plasmonic excitations were computed using the 2D diffraction grating formula, with gold dispersion taken from Johnson and Christy.

4.5. Numerical Modeling

Numerical simulations were performed using the Lumerical FDTD solver. A single unit cell of the 2D periodic gold-bump grating (period Δx = 1 μm) was modeled in 3D using Bloch boundary conditions along the periodic axis and PML in the propagation direction. The substrate (n = 1.51 at 900 nm), the 100 nm gold layer, and the bump geometry (from SEM measurements) were defined as in the experiment, with the bump interior assigned n = 1. Gold dispersion was taken from Johnson and Christy. Oblique illumination was implemented using BFAST, with a broadband source from 400 to 1600 nm and 1 nm spectral resolution. A uniform mesh was used, obtained by discretizing the unit-cell period into 32 points (mesh size $d_x = \Delta x/32$). A time-step multiplier of 0.9 was applied to avoid instabilities arising from dispersive materials under oblique incidence. Simulations were performed for the same incidence angles as in the experiment (θ = 8°, 15°, 30°) and for both s- and p-polarizations. Due to symmetry, azimuthal angles were simulated only from 0° to 45° in 15° steps.

0th-order reflection spectra were obtained using 2D frequency-domain FDTD power monitors positioned above the gold structure. Electric-field distributions were computed using a full 3D monitor covering the entire unit cell, enabling the evaluation of in-plane fields at different heights and vertical oblique field cuts to visualize resonance profiles to extract a field cross-section at an arbitrary angle θ from a 2D field matrix. The coordinate system is recentered so that the origin coincides with the center of the matrix.

For a matrix $A(i, j, k)$ of size $N_x \times N_y \times N_z$, the centered coordinates are defined as

$$i_0 = \frac{N_x - 1}{2}, \quad j_0 = \frac{N_y - 1}{2}$$

A linear cut at an angle θ is parametrized by the line passing through the origin,

$$i(r) = \frac{r}{d_x}\cos\theta - i_0, \quad j(r) = \frac{r}{d_x}\sin\theta - j_0$$

where $r \in [-d_x\sqrt{i_0^2 + j_0^2}, d_x\sqrt{i_0^2 + j_0^2}]$, with step of d_x, the field value along the cut is obtained from $A(i, j, k)$ using nearest-neighbor or bilinear interpolation for noninteger indices. Within the limits of the matrix, this procedure yields a one-dimensional field profile corresponding to a slice through the structure at the specified angle; here, the plane is

$$E(r, z) = A\left(\frac{r}{d_x}\cos\theta - i_0, \frac{r}{d_x}\sin\theta - j_0, k\right)$$

Each reflectance spectrum simulation required ~2 min per angle, while near-field calculations at resonance wavelengths required ~14 min per resonant wavelength.

■ ASSOCIATED CONTENT

Supporting Information

The Supporting Information is available free of charge at https://pubs.acs.org/doi/10.1021/acsami.6c04043.

Reflectance spectra comparison of DP resonance excitation with both polarizations; main and diagonal lattices resonance attribution; resonance at intermediate azimuthal angles comparison; reflectance spectra azimuthal shift for higher AOIs; and theoretically calculated resonance dependence on AOI (PDF)

https://doi.org/10.1021/acsami.6c04043
ACS Appl. Mater. Interfaces XXXX, XXX, XXX−XXX

AUTHOR INFORMATION

Corresponding Authors

Kernius Vilkevičius – *Plasmonics and Nanophotonics Laboratory, Department of Laser Technologies, Center for Physical Sciences and Technology (FTMC), LT-02300 Vilnius, Lithuania;* orcid.org/0000-0001-8109-7286; Email: kernius.vilkevicius@ftmc.lt

Evaldas Stankevičius – *Plasmonics and Nanophotonics Laboratory, Department of Laser Technologies, Center for Physical Sciences and Technology (FTMC), LT-02300 Vilnius, Lithuania;* orcid.org/0000-0003-3783-5506; Email: evaldas.stankevicius@ftmc.lt

Authors

Lucciano A. Letelier – *Optical Coatings Laboratory, Department of Laser Technologies, Center for Physical Sciences and Technology (FTMC), LT-02300 Vilnius, Lithuania;* orcid.org/0000-0002-5818-4020

Lina Grinevičiūtė – *Optical Coatings Laboratory, Department of Laser Technologies, Center for Physical Sciences and Technology (FTMC), LT-02300 Vilnius, Lithuania*

Complete contact information is available at: https://pubs.acs.org/10.1021/acsami.6c04043

Notes

The authors declare no competing financial interest.

ACKNOWLEDGMENTS

K.V. and E.S. have received funding from the Research Council of Lithuania (LMTLT), agreement No. S-LT-TW-25-3. We would like to thank Prof. Algirdas Selskis for the SEM analysis.

REFERENCES

(1) Hidayat, R.; Pradana, J. S.; Fariz, A.; Komalasari, S.; Chalimah, S.; Bahar, H. Dual Plasmonic Modes in the Visible Light Region in Rectangular Wave-Shaped Surface Relief Plasmonic Gratings. *Sci. Rep.* **2023**, *13*, 5274.

(2) Yang, J.; Sun, Q.; Ueno, K.; Shi, X.; Oshikiri, T.; Misawa, H.; Gong, Q. Manipulation of the Dephasing Time by Strong Coupling between Localized and Propagating Surface Plasmon Modes. *Nat. Commun.* **2018**, *9*, 4858.

(3) Sarkar, S.; König, T. A. F. Engineering Plasmonic Hybridization toward Advanced Optical Sensors. *Adv. Sens. Res.* **2024**, *3*, No. 2300054.

(4) Maradudin, A. A.; Simonsen, I.; Polanco, J.; Fitzgerald, R. M. Rayleigh and Wood Anomalies in the Diffraction of Light from a Perfectly Conducting Reflection Grating. *J. Opt.* **2016**, *18*, No. 024004.

(5) Wang, D.; Guan, J.; Hu, J.; Bourgeois, M. R.; Odom, T. W. Manipulating Light–Matter Interactions in Plasmonic Nanoparticle Lattices. *Acc. Chem. Res.* **2019**, *52*, 2997–3007.

(6) Cherqui, C.; Bourgeois, M. R.; Wang, D.; Schatz, G. C. Plasmonic Surface Lattice Resonances: Theory and Computation. *Acc. Chem. Res.* **2019**, *52*, 2548–2558.

(7) Liu, S.-D.; Yue, P.; Zhang, S.; Wang, M.; Dai, H.; Chen, Y.; Nie, Z.-Q.; Cui, Y.; Han, J.-B.; Duan, H. Metasurfaces Composed of Plasmonic Molecules: Hybridization between Parallel and Orthogonal Surface Lattice Resonances. *Adv. Opt. Mater.* **2020**, *8*, No. 1901109.

(8) Bai, Y.; Zheng, H.; Zhang, Q.; Yu, Y.; Liu, S.-d. Perfect Absorption and Phase Singularities Induced by Surface Lattice Resonances for Plasmonic Nanoparticle Array on a Metallic Film. *Opt. Express* **2022**, *30*, 45400–45412.

(9) Homola, J.; Koudela, I.; Yee, S. S. Surface Plasmon Resonance Sensors Based on Diffraction Gratings and Prism Couplers: Sensitivity Comparison. *Sens. Actuators, B* **1999**, *54*, 16–24.

(10) Ponomareva, E.; Volk, K.; Mulvaney, P.; Karg, M. Surface Lattice Resonances in Self-Assembled Gold Nanoparticle Arrays: Impact of Lattice Period, Structural Disorder, and Refractive Index on Resonance Quality. *Langmuir* **2020**, *36*, 13601–13612.

(11) Freire-Fernández, F.; Kataja, M.; Dijken, S. v. Surface-Plasmon-Polariton-Driven Narrow-Linewidth Magneto-Optics in Ni Nanodisk Arrays. *Nanophotonics* **2020**, *9*, 113–121.

(12) Auguié, B.; Barnes, W. L. Collective Resonances in Gold Nanoparticle Arrays. *Phys. Rev. Lett.* **2008**, *101*, No. 143902.

(13) Lim, T.-L.; Vaddi, Y.; Bin-Alam, M. S.; Cheng, L.; Alaee, R.; Upham, J.; Huttunen, M. J.; Dolgaleva, K.; Reshef, O.; Boyd, R. W. Fourier-Engineered Plasmonic Lattice Resonances. *ACS Nano* **2022**, *16*, 5696–5703.

(14) Abid, I.; Safar, W.; Edely, M.; Felidj, N.; Lamy de la Chapelle, M.; Shen, H. Symmetry Breaking in Gold Nanocylinder Grating: Influence on Plasmonic Properties and on Surface Enhanced Raman Scattering Performances. *J. Phys. Chem. C* **2022**, *126*, 8676–8683.

(15) Huang, X.; Zhang, B.; Yu, B.; Zhang, H.; Shao, G. Figures of Merit of Plasmon Lattice Resonance Sensors: Shape and Material Matters. *Nanotechnology* **2022**, *33*, 225206.

(16) Mu, S.; Chen, H.; Shi, C.; Zhang, J.; Yang, B. Au Nanoring Arrays with Tunable Morphological Features and Plasmonic Resonances. *Nano Res.* **2021**, *14*, 4674–4679.

(17) Cuartero-González, A.; Sanders, S.; Zundel, L.; Fernández-Domínguez, A. I.; Manjavacas, A. Super- and Subradiant Lattice Resonances in Bipartite Nanoparticle Arrays. *ACS Nano* **2020**, *14*, 11876–11887.

(18) Zundel, L.; Deop-Ruano, J. R.; Martinez-Herrero, R.; Manjavacas, A. Lattice Resonances Excited by Finite-Width Light Beams. *ACS Omega* **2022**, *7*, 31431–31441.

(19) Braik, M.; Geronimi-Jourdain, T.; Lau-Truong, S.; Belkhir, A.; Gam-Derouich, S.; Chevillot-Biraud, A.; Mangeney, C.; Félidj, N. Hybridization of Surface Lattice Modes: Towards Plasmonic Metasurfaces with High Flexible Tunability. *Nanophotonics* **2023**, *12*, 2179–2188.

(20) Baur, S.; Sanders, S.; Manjavacas, A. Hybridization of Lattice Resonances. *ACS Nano* **2018**, *12*, 1618–1629.

(21) Marae-Djouda, J.; Caputo, R.; Mahi, N.; Lévêque, G.; Akjouj, A.; Adam, P.-M.; Maurer, T. Angular Plasmon Response of Gold Nanoparticles Arrays: Approaching the Rayleigh Limit. *Nanophotonics* **2017**, *6*, 279–288.

(22) Jeong, I.; Yun, S.; Yoon, S. Polarization-Dependent Plasmon Coupling between Au Nanorods and Au Nanospheres in Core–Satellite Nanoassemblies. *J. Mater. Chem. C* **2024**, *12*, 18683–18690.

(23) Borah, R.; Ninakanti, R.; Bals, S.; Verbruggen, S. W. Plasmon Resonance of Gold and Silver Nanoparticle Arrays in the Kretschmann (Attenuated Total Reflectance) Vs. Direct Incidence Configuration. *Sci. Rep.* **2022**, *12*, 15738.

(24) Le-Van, Q.; Zoethout, E.; Geluk, E.-J.; Ramezani, M.; Berghuis, M.; Gómez Rivas, J. Enhanced Quality Factors of Surface Lattice Resonances in Plasmonic Arrays of Nanoparticles. *Adv. Opt. Mater.* **2019**, *7*, No. 1801451.

(25) Kelavuori, J.; Vanyukov, V.; Stolt, T.; Karvinen, P.; Rekola, H.; Hakala, T. K.; Huttunen, M. J. Thermal Control of Plasmonic Surface Lattice Resonances. *Nano Lett.* **2022**, *22*, 3879–3883.

(26) Liu, B.; Chen, S.; Zhang, J.; Yao, X.; Zhong, J.; Lin, H.; Huang, T.; Yang, Z.; Zhu, J.; Liu, S.; Lienau, C.; Wang, L.; Ren, B. A Plasmonic Sensor Array with Ultrahigh Figures of Merit and Resonance Linewidths Down to 3 Nm. *Adv. Mater.* **2018**, *30*, No. 1706031.

(27) Kim, R. M.; Lee, S. M.; Han, J. H.; Cho, S. H.; Lv, J.; Im, S. W.; Ha, I. H.; Lee, Y. H.; Lim, D.; Kim, H.; Cho, N. H.; Lee, H.-E.; Namgung, S. D.; Nam, K. T. Helicoid Grating-Coupled Surface Plasmon Resonance Sensor. *Nano Lett.* **2024**, *24*, 15668–15675.

(28) Vilkevičius, K.; Rakickas, T.; Stankevičius, E. High-Quality Plasmonic Ag—Au Bilayer Nanobump Grating Sensor. *Adv. Mater. Technol.* **2025**, *10*, No. e01199.
(29) Franco, A.; Vidal, V.; Gómez, M.; Gutiérrez, O.; Martino, M.; González, F.; Moreno, F.; Fernández-Luna, J. L. A Label-Free Optical System with a Nanohole Array Biosensor for Discriminating Live Single Cancer Cells from Normal Cells. *Nanophotonics* **2022**, *11*, 315−328.
(30) Nugroho, F. A. A.; Bai, P.; Darmadi, I.; Castellanos, G. W.; Fritzsche, J.; Langhammer, C.; Gómez Rivas, J.; Baldi, A. Inverse Designed Plasmonic Metasurface with Parts Per Billion Optical Hydrogen Detection. *Nat. Commun.* **2022**, *13*, 5737.
(31) Seo, S.; Chang, T.-W.; Liu, G. L. 3d Plasmon Coupling Assisted Sers on Nanoparticle-Nanocup Array Hybrids. *Sci. Rep.* **2018**, *8*, 3002.
(32) Vilkevičius, K.; Ignatjev, I.; Selskis, A.; Niaura, G.; Stankevičius, E. Tuning Sers Performance through the Laser-Induced Morphology Changes of Gold Nanostructures. *Appl. Surf. Sci.* **2024**, *660*, No. 160003.
(33) Pérez-Jiménez, A. I.; Lyu, D.; Lu, Z.; Liu, G.; Ren, B. Surface-Enhanced Raman Spectroscopy: Benefits, Trade-Offs and Future Developments. *Chem. Sci.* **2020**, *11*, 4563−4577.
(34) Alam, K.; Kabusure, K. M.; Asamoah, B. O.; Nuutinen, T.; Baah, M.; Mohamed, S.; Matikainen, A.; Heikkinen, J.; Rekola, H.; Roussey, M.; Kuittinen, M.; Hakala, T. K. Double Resonant Plasmonic Lattices for Raman Studies. *Nanoscale* **2020**, *12*, 23166−23172.
(35) Beer, S.; Gour, J.; Alberucci, A.; David, C.; Nolte, S.; Zeitner, U. D. Second Harmonic Generation under Doubly Resonant Lattice Plasmon Excitation. *Opt. Express* **2022**, *30*, 40884−40896.
(36) Michaeli, L.; Keren-Zur, S.; Avayu, O.; Suchowski, H.; Ellenbogen, T. Nonlinear Surface Lattice Resonance in Plasmonic Nanoparticle Arrays. *Phys. Rev. Lett.* **2017**, *118*, No. 243904.
(37) Hong, C.; Zheng, Z.; Patel, S. K.; Odom, T. W. High-Chirality Polariton Lasing from Symmetry-Broken Plasmonic Lattices. *ACS Nano* **2025**, *19*, 18824−18832.
(38) Anulytė, J.; Žičkus, V.; Bužavaitė-Vertelienė, E.; Faccio, D.; Balevičius, Z. Strongly Coupled Plasmon-Exciton Polaritons for Photobleaching Suppression. *Nanophotonics* **2024**, *13*, 4091−4099.
(39) Cortés, E.; Wendisch, F. J.; Sortino, L.; Mancini, A.; Ezendam, S.; Saris, S.; de S Menezes, L.; Tittl, A.; Ren, H.; Maier, S. A. Optical Metasurfaces for Energy Conversion. *Chem. Rev.* **2022**, *122*, 15082−15176.
(40) Jing, Z.; Yu, P.; Movsesyan, A.; Ma, C.; Li, P.; Zhu, Y.; Govorov, A. O.; Neogi, A.; Wang, Z. Manipulation of Fluid Convection by Surface Lattice Resonance. *Adv. Opt. Mater.* **2022**, *10*, No. 2201066.
(41) Kawamura, N.; Tanaka, T.; Kubo, W. Nonradiative Cooling. *ACS Photonics* **2024**, *11*, 1221−1227.
(42) Lapidas, V.; Zhizhchenko, A.; Pustovalov, E.; Storozhenko, D.; Kuchmizhak, A. Direct Laser Printing of High-Resolution Physically Unclonable Function Anti-Counterfeit Labels. *Appl. Phys. Lett.* **2022**, *120*, 261104.
(43) Yang, Y.; Jeon, Y.; Dong, Z.; Yang, J. K. W.; Haddadi Moghaddam, M.; Kim, D.-S.; Oh, D. K.; Lee, J.; Hentschel, M.; Giessen, H.; Kang, D.; Kim, G.; Tanaka, T.; Zhao, Y.; Bürger, J.; Maier, S. A.; Ren, H.; Jung, W.; Choi, M.; Bae, G.; Chen, H.; Jeon, S.; Kim, J.; Lee, E.; Kang, H.; Park, Y.; Du Nguyen, D.; Kim, I.; Cencillo-Abad, P.; Chanda, D.; Jing, X.; Liu, N.; Martynenko, I. V.; Liedl, T.; Kwak, Y.; Nam, J.-M.; Park, S.-M.; Odom, T. W.; Lee, H.-E.; Kim, R. M.; Nam, K. T.; Kwon, H.; Jeong, H.-H.; Fischer, P.; Yoon, J.; Kim, S.-H.; Shim, S.; Lee, D.; Pérez, L. A.; Qi, X.; Mihi, A.; Keum, H.; Shim, M.; Kim, S.; Jang, H.; Jung, Y. S.; Rossner, C.; König, T. A. F.; Fery, A.; Li, Z.; Aydin, K.; Mirkin, C. A.; Seong, J.; Jeon, N.; Xu, Z.; Gu, T.; Hu, J.; Kwon, H.; Jung, H.; Alijani, H.; Aharonovich, I.; Kim, J.; Rho, J. Nanofabrication for Nanophotonics. *ACS Nano* **2025**, *19*, 12491−12605.
(44) Vinnacombe-Willson, G. A.; Conti, Y.; Jonas, S. J.; Weiss, P. S.; Mihi, A.; Scarabelli, L. Surface Lattice Plasmon Resonances by Direct in Situ Substrate Growth of Gold Nanoparticles in Ordered Arrays. *Adv. Mater.* **2022**, *34*, No. 2205330.
(45) Fraggelakis, F.; Lingos, P.; Tsibidis, G. D.; Cusworth, E.; Kay, N.; Fumagalli, L.; Kravets, V. G.; Grigorenko, A. N.; Kabashin, A. V.; Stratakis, E. Double-Pulse Femtosecond Laser Fabrication of Highly Ordered Periodic Structures on Au Thin Films Enabling Low-Cost Plasmonic Applications. *ACS Nano* **2025**, *19*, 23258−23275.
(46) Yang, L.; Wei, J.; Ma, Z.; Song, P.; Ma, J.; Zhao, Y.; Huang, Z.; Zhang, M.; Yang, F.; Wang, X. The Fabrication of Micro/Nano Structures by Laser Machining. *Nanomaterials* **2019**, *9*, 1789.
(47) Yuan, Y.; Wang, W.; Li, D.; Zhao, T.; Han, W. Controllable Large-Area Fabrication of Illumination Angle-Sensitive Metasurfaces Using Femtosecond Laser. *Plasmonics* **2025**, *20*, 7001−7010.
(48) Zhu, H.; Wu, B.; Gao, M.; Ren, F.; Qin, W.; Juodkazis, S.; Chen, F. Femtosecond Laser Direct-Write Plasmonic Nanolithography in Dielectrics. *Small Sci.* **2022**, *2*, No. 2200038.
(49) Vilkevičius, K.; Selskis, A.; Stankevičius, E. Femtosecond Laser Wavelength-Dependent Formation of Plasmonic Gold Nanostructures. *Appl. Surf. Sci.* **2023**, *617*, No. 156629.
(50) Liudvinavičius, R.; Vilkevičius, K.; Stankevičius, E. High-Quality Grating-Coupled Surface Plasmon Resonances in Silver and Gold Bumps Arrays Fabricated in Thin Metallic Films Using the Third Harmonic of Femtosecond Laser. *Appl. Surf. Sci.* **2025**, *711*, No. 164127.
(51) Vilkevičius, K.; Tsibidis, G. D.; Selskis, A.; Stratakis, E.; Stankevičius, E. Formation of Highly Tunable Periodic Plasmonic Structures on Gold Films Using Direct Laser Writing. *Adv. Opt. Mater.* **2024**, *12*, No. 2400172.
(52) Seo, M.; Lee, J.; Lee, M. Grating-Coupled Surface Plasmon Resonance on Bulk Stainless Steel. *Opt. Express* **2017**, *25*, 26939−26949.
(53) Joseph, S.; Sarkar, S.; Joseph, J. Grating-Coupled Surface Plasmon-Polariton Sensing at a Flat Metal−Analyte Interface in a Hybrid-Configuration. *ACS Appl. Mater. Interfaces* **2020**, *12*, 46519−46529.
(54) Joseph, S.; Sarkar, S.; Khan, S.; Joseph, J. Exploring the Optical Bound State in the Continuum in a Dielectric Grating Coupled Plasmonic Hybrid System. *Adv. Opt. Mater.* **2021**, *9*, No. 2001895.
(55) Hamdad, S.; Diallo, A. T.; Chakaroun, M.; Boudrioua, A. The Role of Rayleigh Anomalies in the Coupling Process of Plasmonic Gratings and the Control of the Emission Properties of Organic Molecules. *Sci. Rep.* **2022**, *12*, 3218.
(56) Trinh, Q. T.; Nguyen, S. K.; Nguyen, D. H.; Tran, G. K.; Le, V. H.; Nguyen, H.-S.; Le-Van, Q. Coexistence of Surface Lattice Resonances and Bound States in the Continuum in a Plasmonic Lattice. *Opt. Lett.* **2022**, *47*, 1510−1513.
(57) Roggero, U. F. S.; Rojas-Bejarano, C. J.; Herreño-Fierro, C. A.; Seifert, A.; Garcia-Etxarri, A.; Hernández-Figueroa, H. E.; Zapata-Herrera, M. Surface Lattice Resonances for High-Performance Sensing: A Study on Gold Nanoparticle Arrays. *Opt. Express* **2025**, *33*, 30328−30341.
(58) Ge, D.; Shi, J.; Rezk, A.; Ma, C.; Zhang, L.; Yang, P.; Zhu, S. Two-Dimensional Hole-Array Grating-Coupling-Based Excitation of Bloch Surface Waves for Highly Sensitive Biosensing. *Nanoscale Res. Lett.* **2019**, *14*, 319.
(59) Murugan, D.; Tintelott, M.; Narayanan, M. S.; Vu, X.-T.; Kurkina, T.; Rodriguez-Emmenegger, C.; Schwaneberg, U.; Dostalek, J.; Ingebrandt, S.; Pachauri, V. Recent Advances in Grating Coupled Surface Plasmon Resonance Technology. *Adv. Opt. Mater.* **2024**, *12*, No. 2401862.
(60) Yang, K.; Yao, X.; Liu, B.; Ren, B. Metallic Plasmonic Array Structures: Principles, Fabrications, Properties, and Applications. *Adv. Mater.* **2021**, *33*, No. 2007988.
(61) Seo, M.; Lee, M. Surface Plasmon Resonance and Coloration in Stainless Steel with a 2d Periodic Texture. *Appl. Phys. A: Mater. Sci. Process.* **2019**, *125*, 624.
(62) Stankevičius, E.; Vilkevičius, K.; Gedvilas, M.; Bužavaitė-Vertelienė, E.; Selskis, A.; Balevičius, Z. Direct Laser Writing for the Formation of Large-Scale Gold Microbumps Arrays Generating

https://doi.org/10.1021/acsami.6c04043
ACS Appl. Mater. Interfaces XXXX, XXX, XXX−XXX

Hybrid Lattice Plasmon Polaritons in Vis–Nir Range. *Adv. Opt. Mater.* **2021**, *9*, No. 2100027.
(63) Yang, Y.; Ding, Q.; Wei, Y.; Du, Y.; Wang, W.; Chen, Z.; Liu, B. A Flexible Plasmonic Array with Both High Q-Factor and Strong near-Field. *Adv. Opt. Mater.* **2025**, *13*, No. 2402274.
(64) Bloch, F. Über Die Quantenmechanik Der Elektronen in Kristallgittern. *Z. Angew. Phys.* **1929**, *52*, 555–600.
(65) Floquet, G. Sur Les Équations Différentielles Linéaires À Coefficients Périodiques. *Ann. Sci. Ec. Norm. Super.* **1883**, *12*, 47–88.
(66) Rubin, M. Optical Properties of Soda Lime Silica Glasses. *Sol. Energy Mater.* **1985**, *12*, 275–288.
(67) Johnson, P. B.; Christy, R. W. Optical Constants of the Noble Metals. *Phys. Rev. B* **1972**, *6*, 4370–4379.
(68) Liang, B.; Bai, M.; Ma, H.; Ou, N.; Miao, J. Wideband Analysis of Periodic Structures at Oblique Incidence by Material Independent Fdtd Algorithm. *IEEE Trans. Antennas Propag.* **2014**, *62*, 354–360.
(69) Cai, H.; Wang, M.; Liu, J.; Wang, X. Theoretical and Experimental Study of a Highly Sensitive Spr Biosensor Based on Au Grating and Au Film Coupling Structure. *Opt. Express* **2022**, *30*, 26136–26148.
(70) Kohandani, R.; Saini, S. Self-Referencing Surface Plasmon Sensor for Resolution Enhancement. *Sci. Rep.* **2025**, *15*, 7960.
(71) Ghosh, A. K.; Sarkar, S.; Nebel, L. J.; Aftenieva, O.; Gupta, V.; Sander, O.; Das, A.; Joseph, J.; Wießner, S.; König, T. A. F.; Fery, A. Exploring Plasmonic Resonances toward "Large-Scale" Flexible Optical Sensors with Deformation Stability. *Adv. Funct. Mater.* **2021**, *31*, No. 2101959.
(72) Vilkevičius, K.; Čepaitis, K.; Selskis, A.; Stankevičius, E. Ultrafast Laser Ablation and Modification of Thin Metal Film for Quasi-1d Array Formation. *Opt. Laser Technol.* **2025**, *183*, No. 112330.

https://doi.org/10.1021/acsami.6c04043
ACS Appl. Mater. Interfaces XXXX, XXX, XXX−XXX

Supporting Information

Grating-Coupled Plasmonic Resonances in Symmetric 2D Gold Nanobump Grating: Theory Meets Experiments

Kernius Vilkevičius,[*,†] *Lucciano A. Letelier,*[‡] *Lina Grinevičiūtė,*[‡] *and Evaldas Stankevičius*[*,†]

[†] Plasmonics and Nanophotonics Laboratory, Department of Laser Technologies, Center for Physical Sciences and Technology (FTMC), Savanoriu Ave. 231, LT-02300, Vilnius, Lithuania

[‡] Optical Coatings Laboratory, Department of Laser Technologies, Center for Physical Sciences and Technology (FTMC), Savanoriu Ave. 231, LT-02300, Vilnius, Lithuania

Corresponding authors' email: kernius.vilkevicius@ftmc.lt; evaldas.stankevicius@ftmc.lt

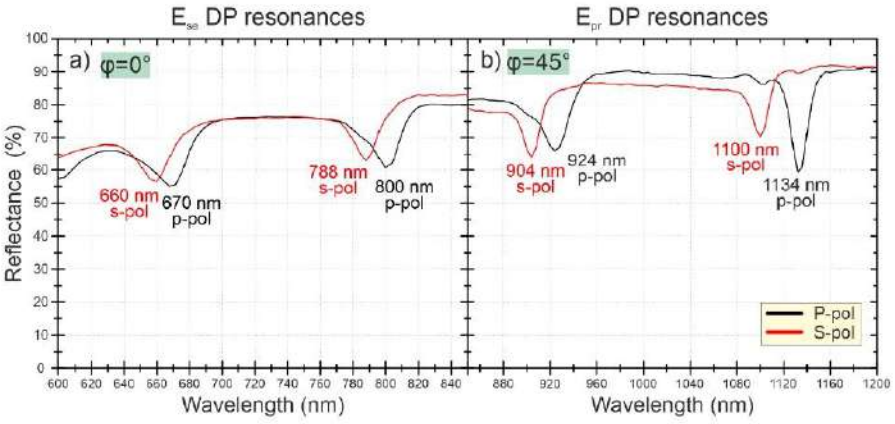

Figure S1. Reflectance spectra of 2D-origin diffraction (a) secondary resonances at $\varphi = 0°$ and (b) primary resonances at $\varphi = 45°$, both being excited in the diagonal plane. The black line marks the spectra for p-polarized light and the red line for s-polarized light.

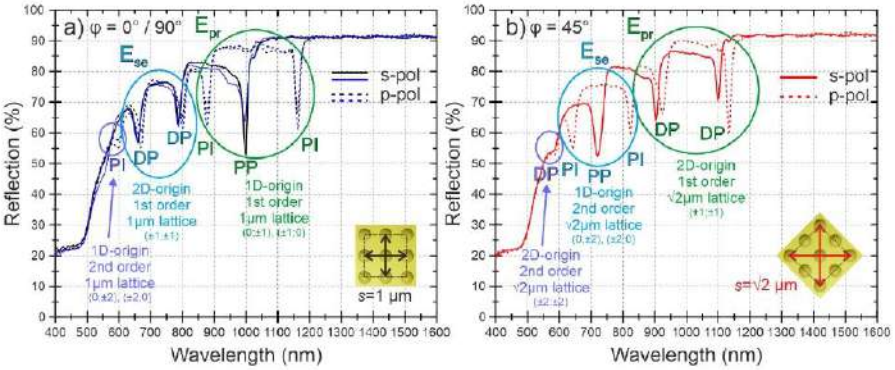

Figure S2. Reflectance spectra of (a) main 1 μm lattice resonances at $\varphi = 0° / 90°$ and (b) diagonal √2 μm lattice resonances at $\varphi = 45°$, with attributed origins of the peaks. Solid lines mark s-polarization response, while dashed lines are for p-polarization.

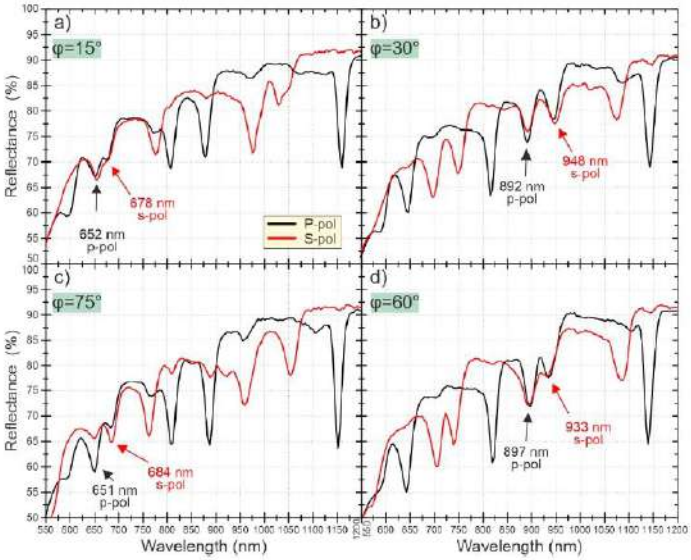

Figure S3. Comparison of the resonances, excited in both s- (red line) and p-polarizations (black line) at (a) $\varphi = 15°$, (b) $\varphi = 30°$, (c) $\varphi = 75°$, and (d) $\varphi = 60°$ azimuthal angles. The response is shown for an angle of incidence of 8°.

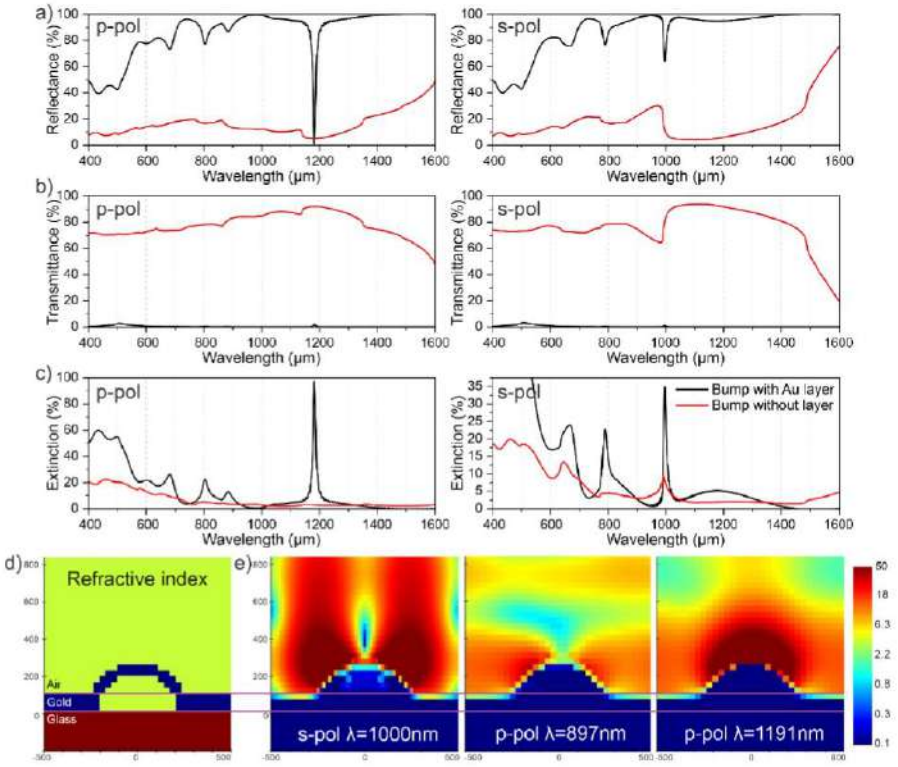

Figure S4. Simulated (a) reflectance, (b) transmittance, and calculated (c) extinction spectra of periodic bumps with gold film (black line) and isolated bumps without gold film (red line). The results are simulated at $\theta = 8°$ and $\varphi = 0°$. (d) Refractive index distribution in the simulated structure using FDTD, and (e) near-field enhancement of the s-polarization response at 1000 nm and p-polarization response at 897 nm and 1191 nm resonances. The violet line marks the Au film-air and film-glass interfaces.

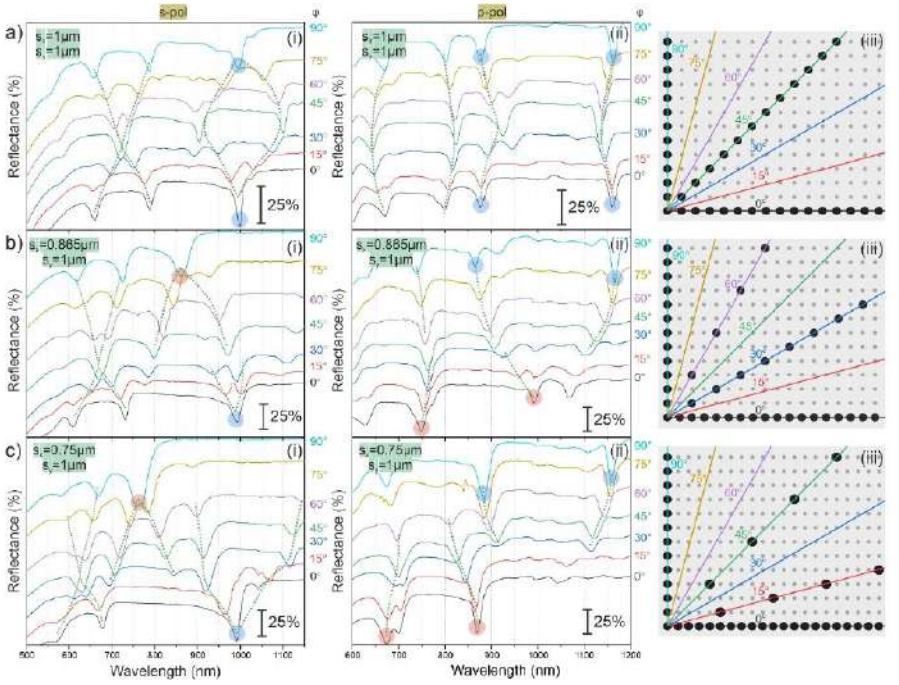

Figure S5. Reflectance spectra dependence on azimuthal angle of (a) a squared 1 μm period array, (b) a rectangular with 0.865 μm in-line period array, and (c) a rectangular with 0.75 μm in-line period array. The reflectance is for s-polarization (i) and p-polarization (ii), with blue circles marking resonances of a larger-period (1 μm) lattice and red circles marking resonances of a smaller-period lattice. Dashed lines mark the resonance shift. Azimuthal rotation coupling into different lattices of the gratings (iii), where black dots mark the aligned lattice.

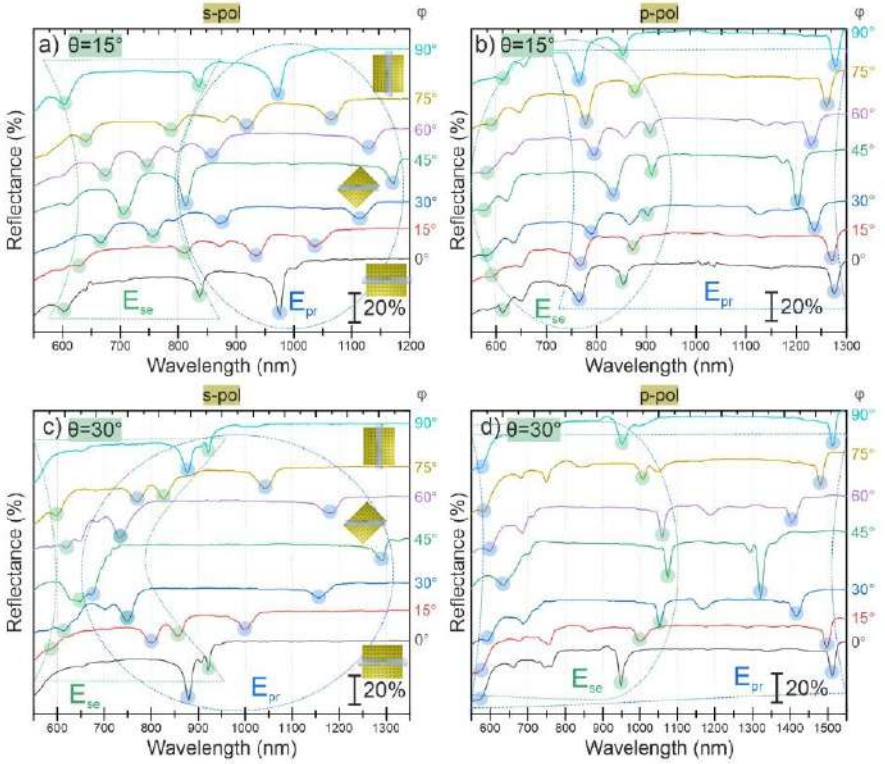

Figure S6. Reflectance spectra of gold nanobumps grating with a period of 1 μm at different azimuthal angles from $\varphi = 0°$ to $\varphi = 90°$ with a step of 15° for (a,c) s- and (b,d) p-polarization at (a,b) $\theta = 15°$ and (c,d) $\theta = 30°$ angles of incidence. Blue circles mark the primary E_{pr} resonances, while green ones mark secondary E_{se} resonances.

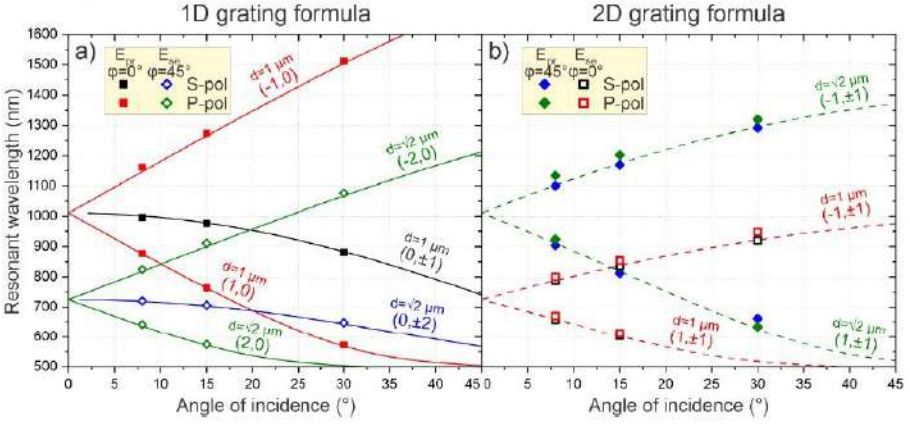

Figure S7. Theoretically calculated wavelength dependence on the incident angle using (a) 1D and (b) 2D diffraction formula. Curves are calculated for the main 1 μm grating at $\varphi = 0°$ (black, red) and the diagonal √2 μm grating at $\varphi = 45°$ (blue, green). Experimentally measured primary E_{pr} (solid symbols) and secondary E_{se} (empty symbols) resonance values are marked in squares ($\varphi = 0°$) and diamonds ($\varphi = 45°$) for s- (black, blue) and p-polarization (red and green).

5th publication / 5 publikacija

K. Vilkevičius, I. Ignatjev, A. Selskis, G. Niaura, E. Stankevičius,
Tuning SERS Performance Through the Laser-induced Morphology Changes of Gold Nanostructures,
Applied Surface Science, 660, 160003 (2024).

https://doi.org/10.1016/j.apsusc.2024.160003

Applied Surface Science 660 (2024) 160003

Contents lists available at ScienceDirect

Applied Surface Science

journal homepage: www.elsevier.com/locate/apsusc

Full Length Article

Tuning SERS performance through the laser-induced morphology changes of gold nanostructures

Kernius Vilkevičius [a,*], Ilja Ignatjev [b], Algirdas Selskis [c], Gediminas Niaura [b], Evaldas Stankevičius [a]

[a] Department of Laser Technologies, Center for Physical Sciences and Technology, Savanoriu av. 231, LT-02300 Vilnius, Lithuania
[b] Department of Organic Chemistry, Center for Physical Sciences and Technology, Sauletekio av. 3, LT-10257 Vilnius, Lithuania
[c] Department of Characterisation of Materials Structure, Center for Physical Sciences and Technology, Sauletekio av. 3, LT-10257 Vilnius, Lithuania

ARTICLE INFO

Keywords:
Plasmon resonance
Direct laser writing
Periodic nanostructures
SERS
Gold nanostructure morphology

ABSTRACT

Differently shaped periodic gold nanostructures on the surface of a thin metal film are fabricated utilizing the direct laser writing technique. The variations in the energy of single femtosecond pulses lead to the formation of morphologically distinct hollow nanostructures. The arrays that excite hybridized plasmonic modes are characterized by electron microscopy and assessed for surface-enhanced Raman spectroscopy (SERS). Plasmonic properties are investigated through SERS using the adsorbed 4-mercaptobenzoic acid (4-MBA) molecules. The development of sharp tips in the nanostructures is initiated by the higher-energy laser pulses, while the structure formation principle itself is altered by the thickening of the film. The change in the structure shape and gold layer thickness tune the SERS signal and the enhancement factor (EF), leading to an EF of 10^9. Such a factor enables the future prospects of the arrays to be applied for single-molecule detection.

1. Introduction

Raman spectroscopy is a non-invasive analytical technique to determine the chemical fingerprint of the molecules based on the non-elastic Raman scattering. During this phenomenon a photon of a certain frequency incident on a molecule is absorbed, excites vibrations, and emits back a photon of a different frequency, which differs from the absorbed through the vibrational frequency. Traditional scattering from the molecules is usually quite weak and the signal is hardly detected, thus requiring strong illumination or high molecule concentrations [1]. A way to enhance the results is to exploit the surface plasmons excited at the metal-dielectric interface and implement surface-enhanced Raman spectroscopy. The locally enhanced electromagnetic field at the metallic surface firmly improves the non-elastic scattering of the molecules in close proximity or directly at a surface. The overall near-field enhancement is due to the electromagnetic enhancement associated with the excitation of localized surface plasmons (LSP) in nanoparticles and the chemical enhancement associated with the charge transfer between the analyzed molecules and metallic particles. In terms of SERS performance, the electromagnetic effect plays a key role in contributing to the significant increase in Raman signal compared to the chemical effect [1–5]. The plasmonic approach has been widely explored and investigated with the potential to achieve high scattering intensities enabling a single molecule level detection. If the metal particles have sharp tips or are spaced several nanometers apart, the plasmons can couple, and the hot spots are created, leading to an extreme signal enhancement of the molecule inside such spot (up to 10 orders of magnitude) [2,4,6,7]. The use of resonant structure is one way to generate enhanced Raman scattering. Absorption is directly proportional to the intensity of the molecule's local electric field, which can be drastically amplified by plasmons, thus the strongest SERS signal is obtained when the excitation wavelength is close to the resonant wavelength, as more photons are involved in the excitation of the molecular vibrations [8,9]. Wavelength-scanned surface-enhanced Raman excitation spectroscopy experiments with well-characterized Ag nanoparticle arrays have demonstrated that the maximum SERS EF takes place at an excitation wavelength slightly blue-shifted with respect to the peak of the plasmons absorption band [10].

While high electric field enhancement is already achieved in single nanoparticles, the coupled nanoparticle-nanoparticle or nanoparticles-substrate structures, as well as the use of periodic arrays can additionally enhance the signal [11–13]. The latter exhibit either hybrid

* Corresponding author.
E-mail address: kernius.vilkevicius@ftmc.lt (K. Vilkevičius).

https://doi.org/10.1016/j.apsusc.2024.160003
Received 3 January 2024; Received in revised form 3 March 2024; Accepted 27 March 2024
Available online 28 March 2024

plasmonic mode with hybridized LSPs and propagating plasmon polariton along the metal surface, or surface lattice plasmons with periodically excited LSPs without the metal layer in between [14,15]. In arrays of nanoparticles, whether arranged in an orderly fashion or distributed randomly, the desired position of the resonance can be adjusted by altering either the particle size or the ordered grating period [16–18]. SERS improvement by structure coupling and overlapping of dipole fields takes advantage of the molecule trapping into the hot spot. The highly-enhanced small spacing between metallic structures for the analyte trapping can be achieved in several ways. The most common is nanoparticles set out close to one another (creating dimers) or at the surface of the metal [19–21]. Another way is to modify the already fabricated structures – for example, by creating gaps in the particles themselves and utilizing intra-particle coupling or taking advantage of the tilting phenomenon in a liquid due to capillary forces and bringing several structures, such as the rods, into close proximity with each other [22,23]. Finally, the plasmonic gap mode is used to achieve efficient amplification by creating SiO_2 gaps between metal layers or nanoparticles, which alter the efficiency [24–26].

Conventional SERS substrates are based on plasmonic nanostructures produced by chemical synthesis [27–30], electron beam lithography [9,31,32], or nanolithography [3,33–35]. Good reproducibility, homogeneity, and uniformity of properties of the nanoparticles are required to achieve SERS results suitable for practical applications (e.g., chemical analysis). The size and shape of the nanostructures, the distance and gap size between them, the substrate, and the surrounding media contribute to the SERS signal intensity [1,5,36]. Colloidal nanoparticles are most commonly used in this field and their easily scalable shape and size make them suitable for a wide range of wavelengths [37]. Also, the core-shell and magneto-plasmonic nanoparticles are of high interest due to the magnetic field homogeneous arrangement of the particles for a higher signal [38–40]. The widely used spherical nanoparticles have moderate, while the aggregates have high Raman enhancement. However, the highest interest these days is for anisotropic nanoparticles with reduced symmetry (nanostars, nanorods), where very intense SERS enhancement is observed at the edges and sharp tips [5,41,42].

Laser is one of the most promising techniques and a versatile tool for nanostructure formation. It is implemented for nanoparticle synthesis and formation using laser ablation [43–45], laser interference lithography [46,47], laser-induced transfer [48], or direct laser writing (DLW) [49,50]. DLW offers the fast ablation-free fabrication of hollow parabola-shaped nanostructures on the surface of the thin metal film [51,52]. Femtosecond pulses induce rapid phase transitions when the locally melted layer quickly solidifies. The morphology and dimensions of the structures are determined by the pulse energy [53–55]. DLW methodology enables the free-form and large-scale periodical arrangement of the structures, leading to the fabrication of a substrate for the excitation of hybrid plasmonic modes.

Here, we present the SERS performance improvement by the laser-induced morphology changes of periodically positioned metallic nanostructures on thin metal film. The energy-dependent morphological states that additionally depend on the gold film thickness enhance the scattering differently, enabling the tunability of the signal intensity. The key factor in the different enhancements is the shape change and the development of sharp tips with hot spots. The strongly improved Raman scattering shows future perspectives for large-scale and effective SERS substrates with single-molecule detection ability.

2. Materials and methods

2.1. Material deposition and array formation

The thin gold films on the soda lime glass were deposited using a magnetron sputter coater (Quorum Q150T) with a deposition rate of 0.266 nm/s. The thickness of the coating was controlled by varying the sputtering time from 188 to 752 s, corresponding to the thickness from 50 to 200 nm with the step of 25 nm.

The nanostructure arrays in thin gold films were produced using a direct laser writing technique with third-harmonic (343 nm) of 300-fs laser pulses generated by Yb:KGW-based laser (Pharos, Light Conversion Ltd.). The femtosecond beam was tightly focused into approximately 0.8 μm spot using an objective with a numerical aperture of 0.5. The structures in periodic alignment were arranged by the specific selection of the sample translation speed and pulse repetition rate so that the distance between two adjacent structures in the scanning axis would be equal to the required period. The energy of the pulses varied from 0.6 nJ in the thinnest layer for the bump formation to 4.0 nJ in the thickest layer for the jet formation. The size of the fabricated gratings was 100 × 100 μm^2.

The nanostructures were characterized using a scanning electron microscope (Helios NanoLab650). The pictures were taken with a magnification of 80,000 at a 52° angle. The structures were measured by processing the SEM images with the ImageJ program.

2.2. SERS experiments

The 4-mercaptobenzoic acid (4-MBA) monolayer was used as the Raman reporter to evaluate the performance of the SERS substrates. The fabricated periodic structures were immersed in 1 mM 4-MBA of isopropanol solution for 6 h. After that, they were rinsed with isopropanol solution and dried under N_2 gas.

The SERS measurements on 4-MBA molecules were done using an inVia Raman spectrometer (Renishaw, Wotton-under Edge) with a thermoelectrically cooled (-70 °C) charge-coupled device camera and a long working distance 50x objective having 0.5NA. The Raman measurements were carried out using a 5x/0.12NA objective with a 14 mm working distance. The diode laser was used as the excitation source with an average power of 0.8 mW at 785 nm. The 1200 lines/mm grating was used to record Raman spectra. The accumulation time was 9 s. The spectra were registered in the optical focus of the integrated confocal microscope (Leica). The Raman wavenumber axis was calibrated by the 520.7 cm^{-1} Si-Si vibrational mode. The mapping was carried out in the 5

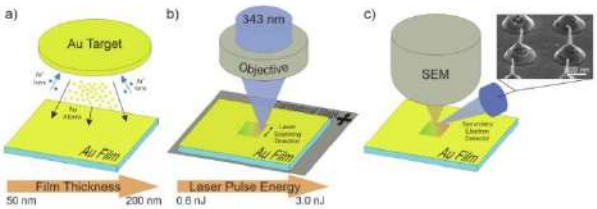

Fig. 1. Preparation steps for gold nanostructure arrays. a) Magnetron sputtering of thin gold film with varying sputtering times to achieve different thicknesses. b) DLW of periodic structures with different pulse energies to obtain distinct morphologies. c) Analysis of the resulting structures using a SEM.

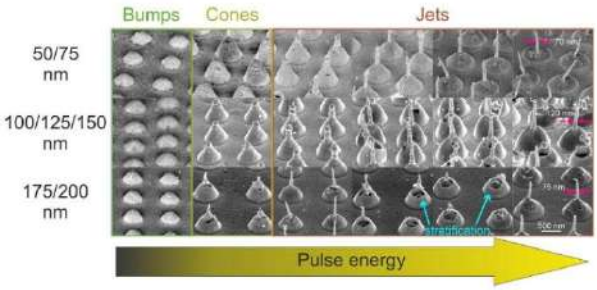

Fig. 2. SEM images of different structures (bumps, cones, jets) on the various thicknesses of the gold film. The jet thickness is marked by magenta arrows, while the stratification in the thickest layers is marked by cyan arrows.

μm × 5 μm surface area with a step of 1 μm and a spot size of 1.2 μm.

2.3. Numerical simulation

The electromagnetic field distributions of the plasmonic structures were calculated using the finite element method (FEM) implemented in a commercially available solver (COMSOL Multiphysics). In simulations, a linearly polarized plane-wave light (785 nm wavelength) was used to excite the structure at normal incidence. The rectangular domain consisting of a single nanostructure was used with a periodic boundary condition. Also, two perfectly matched layers (PML) were adopted above and below the simulation domain to avoid boundary reflections. The dielectric function of gold was extracted from Johnson and Christy's data [56]. The structures were shaped as hollow ellipsoids and cones, with an additional solid antenna. The structure was surrounded by air and located on a soda-lime glass substrate deposited with a thin gold film. The size of the structures was taken from measurements of SEM images.

3. Results and discussion

3.1. Preparation of the periodic gold nanostructure arrays

The present study utilized the swift single-pulse DLW technique to fabricate periodic gold nanostructures. The preparation of the sample before the measurements is shown in Fig. 1. Initially, a thin gold film was deposited on a soda-lime glass using magnetron sputtering. The sputtering time was varied in different samples to achieve film thickness ranging from 50 nm to 200 nm with intervals of 25 nm. Periodic arrays of differently shaped nanostructures on thin gold films were fabricated using the DLW. The formation was achieved by tightly focusing (into approximately 700 nm diameter spot) single 343 nm wavelength pulses from a 300–fs pulse duration Yb:KGW laser Pharos (Light Conversion Ltd.). The pulse energy varied in the sample to create the arrays consisting of diverse morphological structures. Finally, the characterization using a scanning electron microscope (SEM) was applied to determine the exact morphology and the dimensions of the structures in each grating (Fig. 1c).

The thicker the metal film was, the higher pulse energy was required to achieve the same morphology of the structures. Specifically, in the 50 nm gold layer, the bumps were fabricated using 0.6 nJ pulse energy, while the jets required 1.2 nJ. In contrast, to obtain the similar morphology in the 200 nm layer, 3.0 nJ pulses were necessary. Fig. 2 displays images of the resulting structures in three gold layer thickness groups. The diameters of these structures range from approximately 550 nm up to 1 μm. The thinnest layers (50, 75 nm) feature bumps that are 350 nm tall and 550 nm wide, cones with a maximum height of 760 nm and a width of 790 nm, and jets reaching as high as 1320 nm with a needle diameter of 70 nm and a base diameter of 930 nm. In thicker films (100, 125, 150 nm), the cones have a height of up to 770 nm and a width of 760 nm, while the jets are 1250 nm, with 120 nm in needle diameter and a base diameter of 910 nm. In these thicker films, the needle formation occurs at the apex of the cone. Finally, the cones in the thickest layers (175, 200 nm) measure 670 nm in height and 720 nm in base width, while the jet height can reach up to 1 μm, with the diameter of the base and needle measuring 850 nm and 70 nm, respectively.

When analyzing the structures, it is observed that as the film thickness increases, the structures' height and base diameter decrease. This is

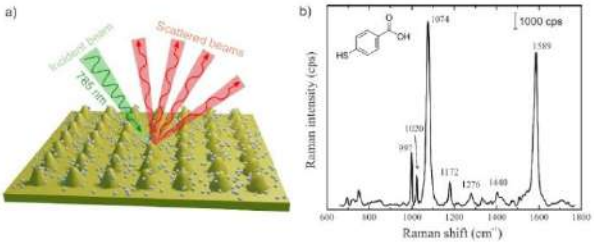

Fig. 3. a) An illustration of the scattering from the grating with 4-MBA molecules. b) Raman scattering spectra obtained from the nanostructures on a 100 nm thick gold film with signal response per 1 s.

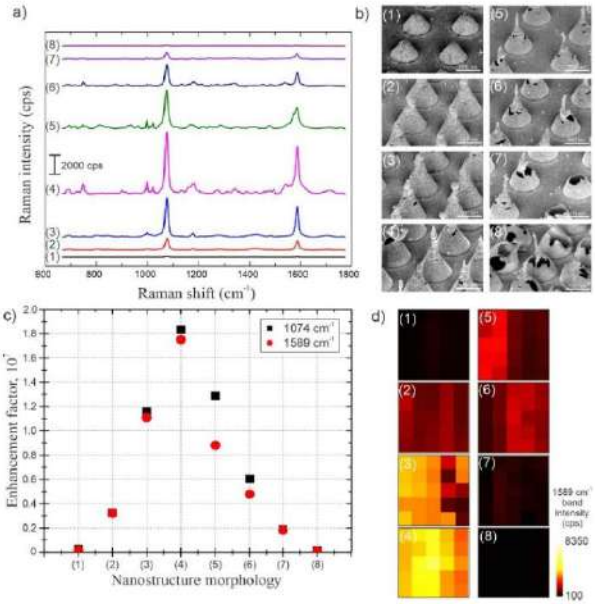

Fig. 4. a) Raman intensity spectra, where differently colored lines correspond to the distinct structure morphology. b) The morphologies of the nanostructures used for SERS measurements. The structures are fabricated on 100 nm thick gold with 1 μm inter-structural distance. c) The SERS enhancement factors of the different morphology nanostructure arrays with MBA molecules at 1074 cm^{-1} (black dots) and 1589 cm^{-1} (red) bands. d) The intensity mapping of the 1589 cm^{-1} mode.

caused by the thickening of the affected layer and the consequent heat distribution. In the thinnest layers, the needle has a narrow diameter of 70 nm, and it becomes thicker, over 100 nm, with increasing layer thickness (Fig. 2 magenta arrows). This phenomenon can be explained by the larger portion of the melt flowing towards the center and producing the needle. Alas in the 175 nm and 200 nm layers, the jet narrows once again because of an observed alteration in the structure formation within these layers. The film undergoes stratification resulting in the appearance of recurring morphologies. As the film is layered, jet formation initially occurs in the upper layer. At higher energies, this part of the layer is removed, leaving the layer below intact (see Fig. 2, indicated by cyan arrows). This process initiates the formation of cones and jets in the lower layer, ultimately resulting in the formation of a jet structure protruding from the torn layer. These multilayers have a lower thickness compared to the entire film, thereby producing thinner needles.

3.2. SERS properties of the periodic gold nanostructure arrays

The plasmonic properties were characterized by measuring the SERS activity. The periodic structures were immersed in a 1 mM solution of 4-mercaptobenzoic acid (4-MBA) in isopropanol for 6 h. After rinsing thoroughly with isopropanol solution, they were dried under N_2 gas. A self-assembled monolayer of 4-MBA molecules formed on the surface of the grating and the enhanced Raman scattering signal was registered (see Fig. 3). Although the structures were arranged in a periodic manner, we did not investigate their periodicity's impact on the results. The incident beam only covered a single structure; therefore, the neighboring structures were used solely for repeatability mapping.

The intense signals were obtained with the two most prominent Raman shift lines at 1074 cm^{-1} and 1589 cm^{-1}, which are the characteristic 4-MBA bands associated with breathing vibration of aromatic ring coupled with C–S stretching ($\nu(12) + \nu(C–S)$) and aromatic ring stretching mode $\nu(8a)$, respectively [57–59]. The low-intensity bands near 1276 cm^{-1} and 1705 cm^{-1} correspond to $\nu(C–OH)$ and $\nu(C=O)$ stretching vibrations of a protonated carboxyl group, respectively, while the low-intensity feature near is associated with symmetric stretching vibration of the unbound carboxylate group, $\nu_s(COO^-)$ [58]. The sharp band near 1172 cm^{-1} belongs to the in-plane CH bending vibration of the aromatic ring $\nu(9a)$ [24]. In some SERS spectra, low-intensity narrow bands are visible at 997 cm^{-1} and 1020 cm^{-1}. These bands were previously assigned to thiophenol [57,60]. Appearance of these bands in the spectra indicates the decarboxylation of some adsorbed 4-MBA molecules. It was demonstrated that the process is related with the involvement of the carboxylate group with interaction with the surface and is catalyzed by the roughness of the surface; no new bands were observed in SERS spectra of 4-MBA at smooth Au and Ag surfaces [57]. In order to compare the relative intensities of the bands we have recorded SERS spectra of complete monolayers of thiophenol and 4-MBA at the same conditions (Figure S1). We have estimated the ratio of intensity of 1074 cm^{-1} band from 4-MBA and 1023 cm^{-1} band from thiophenol [I(1074)/I(1023)]=1.01. Based on the relative intensities of these bands observed in spectra with the most intense thiophenol features we found that the amount of decarboxylized compound in the studied monolayers varies from 0 to 17 %.

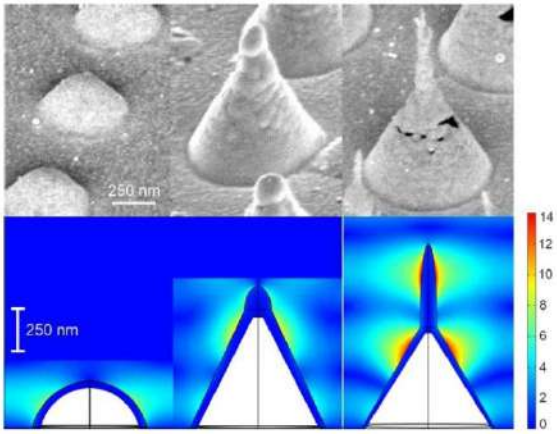

Fig. 5. SEM images of bump (left), cone (center), and jet (right) with corresponding electric field intensity enhancement calculated using COMSOL Multiphysics.

3.2.1. Effect of the morphology

In order to assess how morphology affects the amplification of the SERS signal, the arrays of variously shaped structures were fabricated on a 100 nm thick gold layer using different pulse energies. The SERS spectra are depicted in Fig. 4a, where differently colored lines correspond to specific morphologies shown in Fig. 4b with the numbers indicating the response spectra.

The enhancement of SERS is strongly affected by the structure shape and the generated hot spots. The measured spectra reveal an optimal shape that results in the highest enhancement of the SERS signal. In the bump array (Fig. 4a black line) the intensity is significantly lower due to the round structure lacking sharp corners where the hot spots can be formed. As the cones are obtained (red and blue lines), the Raman enhancement increases and the two main characteristic lines become evident. Furthermore, in addition to the two main lines, other weaker characteristic 4-MBA lines are present in the jet-like structures when a small antenna spike is formed at the apex of the cone (pink line). It can be assumed that both the antenna spikes and the cone tip are forming hot spots, amplifying the signal. As the pulse energy is further increased, the enhancement of the jets deteriorates (green, violet lines), as the structures begin to fracture and eventually become ablated.

The enhancement factor (EF) for the two most intense MBA vibrational modes at 1074 cm^{-1} and 1589 cm^{-1} was calculated using formula:

$$EF = (I_{SERS} \bullet N_R)/(I_R \bullet N_{SERS}) \quad (1)$$

where I_{SERS} and I_R correspond to the intensities of SERS and Raman spectral bands, while N_{SERS} and N_R correspond to the average number of excited molecules in SERS and Raman experiments, respectively. The detailed calculations of EF are described in the reference [61]. The intensity of the non-enhanced Raman spectrum of the 4-MBA is $I_R = 0.90$ cps (counts per second) at 1074 cm^{-1}, and $I_R = 0.72$ cps at 1589 cm^{-1}. For Raman measurements, a 5x/0.12NA objective with a working distance of 14 mm was used to analyze 0.25 M or 250 mol/m^3 MBA in isopropanol solution. For the number of excited molecules in solution, the following formula is used:

$$N_R = V_R \bullet C_R \bullet N_A \quad (2)$$

where V_R – Raman probe volume, C_R – concentration of analyte, N_A – Avagadro constant.

For Raman probe volume calculation were used $\lambda = 7.85\times10^{-7}$ m, $d = 7.70\times10^{-3}$ m, $f = 1.75\times10^{-3}$ m, where λ – laser wavelength, d – diameter of the unfocused laser beam, f – focal length. The calculated probe volume was 8.38×10^{-17} m^3 [61]. It has been established by (2) equation that $N_R = 1.26\times10^{10}$.

For SERS measurements was used 50x/0.75NA objective which projected 785 nm laser light to 1.13×10^{-12} m^2 spot size area on a surface (1.2 μm diameter spot). The gold surface covered with 4-MBA by 5.0×10^{-6} mol/m^2 [62]. Multiplying those means by each other and the Avogadro constant we got the number of 4-MBA molecules with no respect to surface roughness $N_{SERS} = 3.404\times10^{6}\times R$. The roughness factor R was calculated:

$$R = S_{real}/S_{geom} \quad (3)$$

where S_{real} is the actual illuminated area of the surface (1.13×10^{-12} m^2), and S_{geom} is the area of the laser spot focused onto the flat surface. S_{real} is calculated from the SEM images, by using the formulas for calculating the areas of the hemisphere (area of the bump), cone, cylinder (area of the jet spike), and circle (area of the structure base). The exact calculation of the real irradiated area is depicted in Figure S2. The values of nanostructure geometrical evaluation and the roughness factor for Fig. 4 samples are described in Table S1, while the SERS spectrum intensity and the calculated EF are reported in Table S2. The enhancement factor values, calculated using equations (1) and (3), for the Fig. 4b structures are depicted in Fig. 4c.

The bumps and fractured jets exhibit an enhancement factor of 10^6, while the cones and solid jets reach up to 10^7 orders of magnitude, with the largest EF at shape number 4 (Fig. 4b) being 1.83×10^7 at 1074 cm^{-1} and 1.75×10^7 at 1589 cm^{-1}. It is noticeable that the EF is slightly greater in 1074 cm^{-1} mode. Nevertheless, the 1589 cm^{-1} mode is more inert to solvent interactions obtaining the Raman spectrum of MBA in an isopropanol solution, and to metal interactions after developing a self-assembled monolayer of MBA by recording the Raman signal. Thus, the intensities of this 1589 cm^{-1} vibrational mode can be utilized to determine the EF of the prepared substrates [63]. The measured EF values are comparable to the SERS EF for high-quality periodic arrays reported in the literature [16,64–66]. The Raman response was analyzed

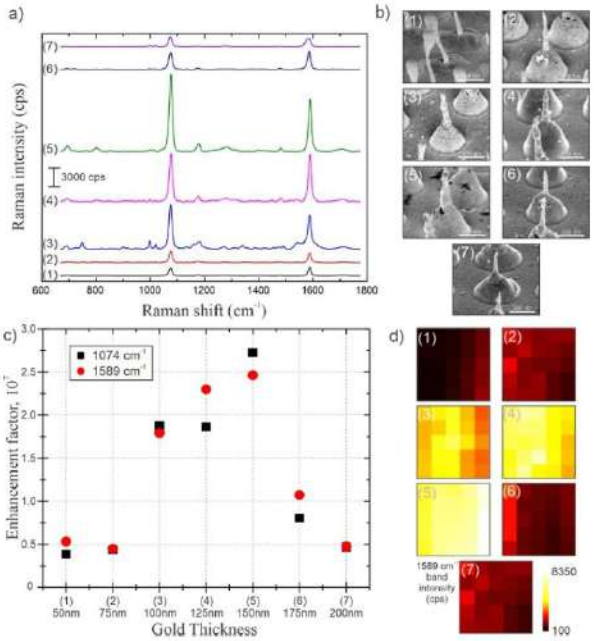

Fig. 6. a) Raman intensity spectra, where differently colored lines correspond to the jets on different film thicknesses. b) The morphologies of the nanostructures used for SERS measurements. The structures are fabricated with a 1 μm inter-structural distance. c) The SERS enhancement factors of the jet arrays on different thickness gold films with MBA molecules at 1074 cm^{-1} (black dots) and 1589 cm^{-1} (red) bands. d) The intensity mapping of 1589 cm^{-1} mode.

via mapping, and Fig. 4d showcases the intensity maps of the gratings at 1589 cm^{-1} mode. The mapped area was 5 μm × 5 μm, with a spot size of 1.2 μm in diameter at the surface using 1 μm step. The intensity mappings demonstrate that the enhancement is recurring in the periodic grating and appears in each nanostructure.

To investigate the influence of shape on the electric field intensity enhancement, we implemented COMSOL Multiphysics modeling to examine near-field plasmonic enhancements in bump, cone, and jet structures. Fig. 5 presents the calculated data (the ratio between the incident and the calculated field intensity), with structure dimensions obtained from SEM images of 1, 3, and 4 shapes in Fig. 4b. The electromagnetic wave impinging on the bump slightly amplifies the field surrounding its middle part. In the cones, the field enhancement occurs near the peak, and the intensified zone merges into a larger one. The jet-like structures have hot spots both at the elongated jet and at the top of the cone where the sharp protrusion combines with the cone. According to the modeling, the electric field enhancement in the jets is double that of cones, and 2.5 times greater than in bumps.

3.2.2. *Effect of the metal thickness*

After determining the optimal shape, we investigated the effect of thin gold film thickness on the enhancement of the needles. The jet-like structures were fabricated on 50, 75, 100, 125, 150, 175, and 200 nm thick layers. Fig. 6a displays the SERS spectra for each layer, with line 1 corresponding to 50 nm and line 7 representing 200 nm. Their shapes are shown respectively in Fig. 6b. The highest Raman intensities are attained in films with thicknesses of 125 nm and 150 nm, with signal levels reaching up to 11,811 cps at the $\nu(12) + \nu(C\text{–}S)$ stretching mode. The rise in the intensity with the growth of the thickness from 50 nm to 125 nm, and the subsequent decrease with further increase to 200 nm, are also conditioned by the structure's shape. In the thinnest layers, the jets are narrower and even without the cone-like base, so the hot spots do not interact. Meanwhile, in the thickest layers, the mechanism for forming the structure undergoes a change, as previously noted. The film layers out and the upper part is ablated, resulting in the formation of a jet from the second layer and a needle protruding from the ruptured layer. Because of the non-continuous nature of these structures, the stratification reduces the Raman intensity.

Using the intensity spectra from Fig. 6a, the enhancement factor for the two strongest modes at different film thicknesses was also calculated and depicted in Fig. 6c. The values of structure geometrical evaluation, the roughness factor, the SERS signal, and the EF for Fig. 6 samples are described in Tables S3-S4. The strongest SERS bands were observed at 100 nm, 125 nm, and 150 nm film thickness, and the EF in the latter thickness reaches as high as 10^7 orders of magnitude (2.72×10^7 at 1074 cm^{-1} and 2.46×10^7 at 1589 cm^{-1}). This enhancement brings the application of such arrays closer to single-molecule detection. The mappings of signal intensity for the 1589 cm^{-1} mode are displayed in Fig. 6d, and the signal in these structures is also recurring periodically.

To further investigate the film thickness-induced variations in the jet and its needle shape, and determine their impact on the enhancement, we employed COMSOL Multiphysics modeling of the near-field

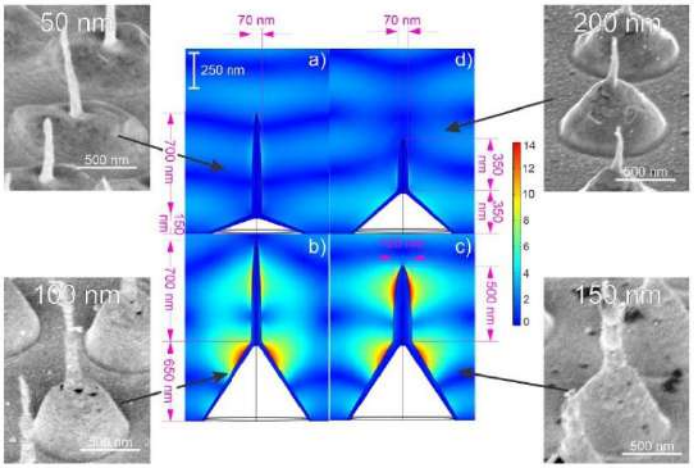

Fig. 7. Modeled electric field enhancement at the nanojets with different needle thicknesses (70 nm (a,b,d) and 120 nm (c)), heights (700 nm (a,b), 500 nm (c) and 350 nm (d)), and cone heights (150 nm (a), 350 nm (d) and 650 nm (b,c)).

enhancements. The study evaluated alterations in the diameter of the needle, its height, and conical base height to match the jets obtained in different thicknesses. The resulting calculations are presented in Fig. 7. The structures with a smaller cone base and narrower needles can be attributed to those obtained in the thinnest (50–75 nm, Fig. 7a) and thickest (175–200 nm, Fig. 7d) layers. In those cases, the enhancement is marginal since the conical base is small and the opposing walls of the conical hollow structure do not interact with each other and with the needle apex. The jets having a higher cone (Fig. 7b-c) correspond to thicknesses of 100–150 nm, where a much stronger electric field is present near the cone junction with the antenna as well as the tip itself. Upon comparing the corresponding 100 nm and 150 nm structures, the one having a thicker needle exhibits stronger excitation near the tip, resulting in the strongest enhancement. The modeled structures reveal that the jets with the most remarkable SERS signal are those developed on the top of a high cone, continuous and having a wider needle. According to the simulations, the signal can be further amplified by increasing the height of the conical base, so that the side walls of the same cone would be closer and sense each other, and the width of the antenna.

4. Conclusions

In this work, differently shaped periodic gold nanostructures were fabricated and investigated for their use in surface-enhanced Raman spectroscopy. Variations in the energy of a single laser pulse and thin gold film thickness result in miscellaneous morphological states. The change in parameters initiates the formation of sharp tips having hot spots in the arranged structures. Our study has demonstrated that the morphological changes induce the refinement of the SERS performance. The nanojets with sharp needle-like tips demonstrate the greatest local electric field enhancement in comparison with other shapes like bumps and cones. This is due to the existence of several interacting hot spots within the structure, resulting in the strongest SERS signal and the highest enhancement factor at this particular shape. Our research investigated the jet formation at different film thicknesses and estimated the corresponding SERS enhancement factors, with the highest peaks of 2.72×10^{7} ($1074\ cm^{-1}$) and 2.46×10^{7} ($1589\ cm^{-1}$) achieved at a 150 nm thickness. The subsequent increase in the thickness resulted in film stratification and reduction of the signal intensity. This approach of fabricating high-EF SERS substrates has good reproducibility and property uniformity, thereby offering the potential for the development of fast and cost-effective single-molecule detectors.

CRediT authorship contribution statement

Kernius Vilkevičius: Writing – review & editing, Writing – original draft, Visualization, Software, Methodology, Investigation, Formal analysis, Data curation, Conceptualization. **Ilja Ignatjev:** Writing – review & editing, Writing – original draft, Validation, Methodology, Investigation, Formal analysis, Conceptualization. **Algirdas Selskis:** Writing – review & editing, Writing – original draft, Methodology, Investigation. **Gediminas Niaura:** Writing – review & editing, Writing – original draft, Supervision, Methodology, Conceptualization. **Evaldas Stankevičius:** Writing – review & editing, Writing – original draft, Supervision, Project administration, Methodology, Funding acquisition, Data curation, Conceptualization.

Declaration of competing interest

The authors declare that they have no known competing financial interests or personal relationships that could have appeared to influence the work reported in this paper.

Data availability

Data will be made available on request.

Acknowledgments

This research has received funding from the Research Council of Lithuania (LMT, Lithuania) under the project No. S-MIP-23-32.

Appendix A. Supplementary data

Supplementary data to this article can be found online at https://doi.org/10.1016/j.apsusc.2024.160003.

References

[1] J. Langer, D. Jimenez de Aberasturi, J. Aizpurua, R.A. Alvarez-Puebla, B. Auguié, J. J. Baumberg, G.C. Bazan, S.E.J. Bell, A. Boisen, A.G. Brolo, J. Choo, D. Cialla-May, V. Deckert, L. Fabris, K. Faulds, F.J. García de Abajo, R. Goodacre, D. Graham, A. J. Haes, C.L. Haynes, C. Huck, T. Itoh, M. Käll, J. Kneipp, N.A. Kotov, H. Kuang, E. C. Le Ru, H.K. Lee, J.-F. Li, X.Y. Ling, S.A. Maier, T. Mayerhöfer, M. Moskovits, K. Murakoshi, J.-M. Nam, S. Nie, Y. Ozaki, I. Pastoriza-Santos, J. Perez-Juste, J. Popp, A. Pucci, S. Reich, B. Ren, G.C. Schatz, T. Shegai, S. Schlücker, L.-L. Tay, K. G. Thomas, Z.-Q. Tian, R.P. Van Duyne, T. Vo-Dinh, Y. Wang, K.A. Willets, C. Xu, H. Xu, Y. Xu, Y.S. Yamamoto, B. Zhao, L.M. Liz-Marzán, Present and future of Surface-enhanced raman scattering, ACS Nano 14 (2020) 28–117, https://doi.org/10.1021/acsnano.9b04224.

[2] A.I. Pérez-Jiménez, D. Lyu, Z. Lu, G. Liu, B. Ren, Surface-enhanced raman spectroscopy: benefits, trade-offs and future developments, Chem. Sci. 11 (2020) 4563–4577, https://doi.org/10.1039/D0SC00809E.

[3] X.X. Han, R.S. Rodriguez, C.L. Haynes, Y. Ozaki, B. Zhao, Surface-enhanced raman spectroscopy, Nat. Rev. Methods Primers 1 (2022) 87, https://doi.org/10.1038/s43586-021-00083-6.

[4] S.-Y. Ding, J. Yi, J.-F. Li, B. Ren, D.-Y. Wu, R. Panneerselvam, Z.-Q. Tian, Nanostructure-based plasmon-enhanced raman spectroscopy for surface analysis of materials, Nat. Rev. Mater. 1 (2016) 16021, https://doi.org/10.1038/natrevmats.2016.21.

[5] O. Guselnikova, H. Lim, H.-J. Kim, S.H. Kim, A. Gorbunova, M. Eguchi, P. Postnikov, T. Nakanishi, T. Asahi, J. Na, Y. Yamauchi, New trends in Nanoarchitectured SERS substrates: nanospaces, 2D materials, and organic heterostructures, Small 18 (2022) 2107182, https://doi.org/10.1002/smll.202107182.

[6] Z.-Y. Li, Mesoscopic and microscopic strategies for engineering plasmon-enhanced raman scattering, Adv. Opt. Mater. 6 (2018) 1701097, https://doi.org/10.1002/adom.201701097.

[7] J.-M. Nam, J.-W. Oh, H. Lee, Y.D. Suh, Plasmonic nanogap-enhanced raman scattering with Nanoparticles, Acc. Chem. Res. 49 (2016) 2746–2755, https://doi.org/10.1021/acs.accounts.6b00409.

[8] N. Khlevich, M. Juodenas, A. Tamulevičienė, T. Tamulevičius, M. Talaikis, G. Niaura, S. Tamulevičius, Wavelength-tailored enhancement of raman scattering on a resonant plasmonic lattice, Sens. Actuators, B 394 (2023) 134418, https://doi.org/10.1016/j.snb.2023.134418.

[9] X. Wang, J. Zhu, Y. Wu, Y. Xu, Y. Su, L. Zhang, Y. Qi, X. Wen, H. Yang, Hybrid surface plasmon effect and SERS characterization in a heterogeneous composite structure of Au nano-array and Ag film, Results Phys. 17 (2020) 103175, https://doi.org/10.1016/j.rinp.2020.103175.

[10] A.D. McFarland, M.A. Young, J.A. Dieringer, R.P. Van Duyne, Wavelength-scanned surface-enhanced raman excitation spectroscopy, J. Phys. Chem. B 109 (2005) 11279–11285, https://doi.org/10.1021/jp050560u.

[11] H.-L. Wang, E.-M. You, R. Panneerselvam, S.-Y. Ding, Z.-Q. Tian, Advances of surface-enhanced raman and IR spectroscopies: from nano/microstructures to macro-optical design, Light Sci. Appl. 10 (2021) 161, https://doi.org/10.1038/s41377-021-00599-2.

[12] Y. Liu, M. Kim, S.H. Cho, Y.S. Jung, Vertically aligned nanostructures for a reliable and ultrasensitive SERS-active platform: fabrication and engineering strategies, Nano Today 37 (2021) 101069, https://doi.org/10.1016/j.nantod.2020.101069.

[13] B. Yan, A. Thubagere, W.R. Premasiri, L.D. Ziegler, L. Dal Negro, B.M. Reinhard, Engineered SERS substrates with multiscale signal enhancement: nanoparticle cluster arrays, ACS Nano 3 (2009) 1190–1202, https://doi.org/10.1021/nn800836f.

[14] S. Kasani, K. Curtin, N. Wu, A review of 2D and 3D plasmonic nanostructure array patterns: fabrication, light management and sensing applications, Nanophotonics 8 (2019) 2065–2089, https://doi.org/10.1515/nanoph-2019-0158.

[15] M. Juodenas, T. Tamulevičius, J. Henzie, D. Erts, S. Tamulevičius, Surface lattice resonances in self-assembled arrays of monodisperse Ag cuboctahedra, ACS Nano 13 (2019) 9038–9047, https://doi.org/10.1021/acsnano.9b03191.

[16] L. Long, W. Ju, H.-Y. Yang, Z. Li, Dimensional design for surface-enhanced raman spectroscopy, ACS Mater. Au 2 (2022) 552–575, https://doi.org/10.1021/acsmaterialsau.2c00005.

[17] C.L. Haynes, A.D. McFarland, L. Zhao, R.P. Van Duyne, G.C. Schatz, L. Gunnarsson, J. Prikulis, B. Kasemo, M. Käll, Nanoparticle optics: the importance of radiative dipole coupling in two-dimensional Nanoparticle arrays, J. Phys. Chem. B 107 (2003) 7337–7342, https://doi.org/10.1021/jp034234x.

[18] V. Petrikaite, I. Ignatjev, A. Selskis, G. Niaura, E. Stankevičius, Hybrid gold-silver nanoparticles synthesis on a glass substrate using a nanosecond laser-induced dewetting of thin bimetallic films and their application in SERS, Opt. Laser Technol. 168 (2024) 109956, https://doi.org/10.1016/j.optlastec.2023.109956.

[19] N.H. Kim, W. Hwang, K. Baek, M.R. Rohman, J. Kim, H.W. Kim, J. Mun, S.Y. Lee, G. Yun, J. Murray, J.W. Ha, J. Rho, M. Moskovits, K. Kim, Smart SERS hot spots: single molecules can be positioned in a plasmonic nanojunction using host-guest chemistry, J. Am. Chem. Soc. 140 (2018) 4705–4711, https://doi.org/10.1021/jacs.8b01501.

[20] D. Radziuk, H. Moehwald, Prospects for plasmonic hot spots in single molecule SERS towards the chemical imaging of live cells, Phys. Chem. Chem. Phys. 17 (2015) 21072–21093, https://doi.org/10.1039/C4CP04946B.

[21] S. Sergiienko, K. Moor, K. Gudun, Z. Yelemessova, R. Bukasov, Nanoparticle–nanoparticle vs. nanoparticle–substrate hot spot contributions to the SERS signal: studying raman labelled monomers, dimers and trimers, Phys. Chem. Chem. Phys. 19 (2017) 4478–4487, https://doi.org/10.1039/C6CP08254H.

[22] M.S. Schmidt, J. Hübner, A. Boisen, Large area fabrication of leaning silicon Nanopillars for Surface enhanced raman spectroscopy, Adv. Mater. 24 (2012) OP11–OP18, https://doi.org/10.1002/adma.201103496.

[23] Q. Zhao, H. Hilal, J. Kim, W. Park, M. Haddadnezhad, J. Lee, W. Park, J.-W. Lee, S. Lee, I. Jung, S. Park, All-hot-spot bulk Surface-enhanced raman scattering (SERS) substrates: Attomolar detection of adsorbates with designer plasmonic nanoparticles, J. Am. Chem. Soc. 144 (2022) 13285–13293, https://doi.org/10.1021/jacs.2c04514.

[24] T. Chung, T. Koker, F. Pinaud, Split-GFP: SERS enhancers in plasmonic nanocluster probes, Small 12 (2016) 5891–5901, https://doi.org/10.1002/smll.201601631.

[25] L. Ma, Y.-L. Chen, D.-J. Yang, S.-J. Ding, L. Xiong, P.-L. Qin, X.-B. Chen, Gap-dependent plasmon coupling in Au/AgAu hybrids for improved SERS performance, J. Phys. Chem. C 124 (2020) 25473–25479, https://doi.org/10.1021/acs.jpcc.0c07701.

[26] Y. Gu, S. Xu, H. Li, S. Wang, M. Cong, J.R. Lombardi, W. Xu, Waveguide-enhanced Surface plasmons for ultrasensitive SERS detection, J. Phys. Chem. Lett. 4 (2013) 3153–3157, https://doi.org/10.1021/jz401512h.

[27] C.-W. Lee, Z.C. Chia, Y.-T. Hsieh, H.-C. Tani, Y. Tai, T.-T. Yu, C.-C. Huang, A facile wet-chemistry approach to engineer an au-based SERS substrate and enhance sensitivity down to ppb-level detection, Nanoscale 13 (2021) 3991–3999, https://doi.org/10.1039/D0NR06637D.

[28] H. Li, P. Merkl, J. Sommertune, T. Thersleff, G.A. Sotiriou, SERS hotspot engineering by aerosol self-assembly of plasmonic ag nanoaggregates with tunable interparticle distance, Adv. Sci. 9 (2022) 2201133, https://doi.org/10.1002/advs.202201133.

[29] L. Chen, H. Sun, Y. Zhao, Y. Zhang, Y. Wang, Y. Liu, X. Zhang, Y. Jiang, Z. Hua, J. Yang, Plasmonic-induced SERS enhancement of shell-dependent Ag@Cu2O core–shell nanoparticles, RSC Adv. 7 (2017) 16553–16560, https://doi.org/10.1039/C7RA01187C.

[30] M.E. Navarro-Segura, R.D. Rivera-Rangel, A. Arizmendi-Morquecho, I. Lopez, J. Alvarez-Quintana, M. Sanchez-Dominguez, Ultra-high sensitivity Surface-enhanced raman spectroscopy (SERS) substrates based on au nanostructured hollow octahedra, Appl. Mater. Today 29 (2022) 101598, https://doi.org/10.1016/j.apmt.2022.101598.

[31] A. Gopinath, S.V. Boriskina, B.M. Reinhard, L.D. Negro, Deterministic aperiodic arrays of metal nanoparticles for surface-enhanced raman scattering (SERS), Opt. Express 17 (2009) 3741–3753, https://doi.org/10.1364/OE.17.003741.

[32] T. Wu, Y.-W. Lin, Surface-enhanced raman scattering active gold nanoparticle/nanohole arrays fabricated through electron beam lithography, Appl. Surf. Sci. 435 (2018) 1143–1149, https://doi.org/10.1016/j.apsusc.2017.11.213.

[33] S. Seo, T.-W. Chang, G.L. Liu, 3D plasmon coupling assisted sers on nanoparticle-nanocup Array hybrids, Sci. Rep. 8 (2018) 3002, https://doi.org/10.1038/s41598-018-19256-7.

[34] Y. Wang, H. Ni, H. Li, J. Chen, D. Zhang, L. Fu, Plasmonic microneedle arrays for rapid extraction, SERS detection, and inactivation of bacteria, Chem. Eng. J. 442 (2022) 136140, https://doi.org/10.1016/j.cej.2022.136140.

[35] V. Suresh, L. Ding, A.B. Chew, F.L. Yap, Fabrication of Large-area flexible SERS substrates by nanoimprint lithography, ACS Appl. Nano Mater. 1 (2018) 886–899, https://doi.org/10.1021/acsanm.7b00295.

[36] Z. Fusco, R. Bo, Y. Wang, N. Motta, H. Chen, A. Tricoli, Self-assembly of au nanoislands with tuneable organized disorder for highly sensitive SERS, J. Mater. Chem. C 7 (2019) 6308–6316, https://doi.org/10.1039/C9TC01231A.

[37] F. Benz, R. Chikkaraddy, A. Salmon, H. Ohadi, B. de Nijs, J. Mertens, C. Carnegie, R.W. Bowman, J.J. Baumberg, SERS of individual Nanoparticles on a Mirror: size does matter, but so does shape, J. Phys. Chem. Lett. 7 (2016) 2264–2269, https://doi.org/10.1021/acs.jpclett.6b00986.

[38] L. Mikoliunaite, M. Talaikis, A. Michalowska, J. Dobilas, V. Stankevic, A. Kudelski, G. Niaura, Thermally stable magneto-plasmonic nanoparticles for SERS with tunable plasmon resonance, Nanomater. 12 (2022) 2860, https://doi.org/10.3390/nano12162860.

[39] L. Mikoliunaite, E. Stankevičius, S. Ademovičiūtė-Grabuovė, V. Petrikaite, R. Trusovas, M. Talaikis, M. Skapas, A. Zdaniauskienė, A. Selskis, V. Sablinskas, G. Niaura, Magneto-plasmonic nanoparticles generated by laser ablation of layered Fe/Au and Fe/Au/Fe composite films for SERS application, Coatings 13 (2023) 1523, https://doi.org/10.3390/coatings13091523.

[40] A. Guadagnini, S. Agnoli, D. Badocco, P. Pastore, D. Coral, M.B. Fernández van Raap, D. Fourez, V. Amendola, Facile synthesis by laser ablation in liquid of nonequilibrium cobalt-silver nanoparticles with magnetic and plasmonic properties, J. Colloid Interface Sci. 585 (2021) 267–275, https://doi.org/10.1016/j.jcis.2020.11.089.

[41] D.M. Solís, J.M. Taboada, F. Obelleiro, L.M. Liz-Marzán, F.J. García de Abajo, Optimization of Nanoparticle-based SERS substrates through Large-scale realistic simulations, ACS Photonics 4 (2017) 329–337, https://doi.org/10.1021/acsphotonics.6b00786.

[42] M. Chirumamilla, A. Chirumamilla, A.S. Roberts, R.P. Zaccaria, F. De Angelis, P. Kjær Kristensen, R. Krahne, S.I. Bozhevolnyi, K. Pedersen, A. Toma, Hot-spot engineering in 3D multi-branched nanostructures: ultrasensitive substrates for surface-enhanced raman spectroscopy, Adv. Opt. Mater. 5 (2017) 1600836, https://doi.org/10.1002/adom.201600836.

[43] E. Stankevičius, I. Ignatjev, V. Petrikaitė, A. Selskis, G. Niaura, Gold nanoparticles generated using the nanosecond laser treatment of multilayer films and their use for SERS applications, ACS Omega 6 (2021) 33889–33898, https://doi.org/10.1021/acsomega.1c05165.
[44] D. Goncharova, M. Salaev, A. Volokitina, O. Magaev, V. Svetlichnyi, O. Vodyankina, Gold-based catalysts prepared by pulsed laser ablation: a review of recent advances, Mater. Today Chem. 33 (2023) 101709, https://doi.org/10.1016/j.mtchem.2023.101709.
[45] E. Fazio, B. Gökce, A. De Giacomo, M. Meneghetti, G. Compagnini, M. Tommasini, F. Waag, A. Lucotti, C.G. Zanchi, P.M. Ossi, M. Dell'Aglio, L. D'Urso, M. Condorelli, V. Scardaci, F. Biscaglia, L. Litti, M. Gobbo, G. Gallo, M. Santoro, S. Trusso, F. Neri, Nanoparticles engineering by pulsed laser ablation in liquids: concepts and applications, Nanomater. 10 (2020) 2317, https://doi.org/10.3390/nano10112317.
[46] N. Gisbert Quilis, M. Lequeux, P. Venugopalan, I. Khan, W. Knoll, S. Boujday, M. Lamy de la Chapelle, J. Dostalek, Tunable laser interference lithography preparation of plasmonic nanoparticle arrays tailored for SERS, Nanoscale 10 (2018) 10268–10276, https://doi.org/10.1039/C7NR09905H.
[47] E. Stankevicius, M. Garliauskas, M. Gedvilas, N. Tarasenko, G. Raciukaitis, Structuring of surfaces with gold nanoparticles by using bessel-like beams, Annalen der Physik 529 (2017) 1700174, https://doi.org/10.1002/andp.201700174.
[48] A.I. Kuznetsov, A.B. Evlyukhin, M.R. Gonçalves, C. Reinhardt, A. Koroleva, M. L. Arnedillo, R. Kiyan, O. Marti, B.N. Chichkov, Laser fabrication of Large-scale nanoparticle arrays for sensing applications, ACS Nano 5 (2011) 4843–4849, https://doi.org/10.1021/nn2009112.
[49] K. Vilkevičius, A. Selskis, E. Stankevicius, Femtosecond laser wavelength-dependent formation of plasmonic gold nanostructures, Appl. Surf. Sci. 617 (2023) 156629, https://doi.org/10.1016/j.apsusc.2023.156629.
[50] D. Pavlov, S. Syubaev, A. Kuchmizhak, S. Gurbatov, O. Vitrik, E. Modin, S. Kudryashov, X. Wang, S. Juodkazis, M. Lapine, Direct laser printing of tunable IR resonant nanoantenna arrays, Appl. Surf. Sci. 469 (2019) 514–520, https://doi.org/10.1016/j.apsusc.2018.11.069.
[51] E. Stankevičius, K. Vilkevičius, M. Gedvilas, E. Buzavaitė-Vertelienė, A. Selskis, Z. Balevičius, Direct laser writing for the formation of Large-scale gold microbumps arrays generating hybrid lattice plasmon polaritons in vis-NIR range, Adv. Opt. Mater. 9 (2021) 2100027, https://doi.org/10.1002/adom.202100027.
[52] D.V. Lebedev, N.A. Solomonov, L.N. Dvoretckaia, V.A. Shkoldin, D.V. Permyakov, A.V. Arkhipov, A.M. Mozharov, D.V. Pavlov, A.A. Kuchmizhak, I.S. Mukhin, Femtosecond laser-printed gold nanoantennas for electrically driven and bias-tuned nanoscale light sources operating in visible and infrared spectral ranges, J. Phys. Chem. Lett. 14 (2023) 5134–5140, https://doi.org/10.1021/acs.jpclett.3c00650.
[53] D. Pavlov, A. Zhizhchenko, L. Pan, A.A. Kuchmizhak, Tuning collective plasmon resonances of femtosecond laser-printed metasurface, Micromachines 15 (2022) 1834, https://doi.org/10.3390/ma15051834.
[54] A.I. Kuznetsov, C. Unger, J. Koch, B.N. Chichkov, Laser-induced jet formation and droplet ejection from thin metal films, Appl. Phys. A 106 (2012) 479–487, https://doi.org/10.1007/s00339-011-6747-8.
[55] J. Koch, F. Korte, T. Bauer, C. Fallnich, A. Ostendorf, B.N. Chichkov, Nanotexturing of gold films by femtosecond laser-induced melt dynamics, Appl. Phys. A 81 (2005) 325–328, https://doi.org/10.1007/s00339-005-3212-6.
[56] P.B. Johnson, R.W. Christy, Optical constants of the noble metals, Phys. Rev. B 6 (1972) 4370–4379, https://doi.org/10.1103/PhysRevB.6.4370.
[57] A. Michota, J. Bukowska, Surface-enhanced raman scattering (SERS) of 4-mercaptobenzoic acid on silver and gold substrates, J. Raman Spectrosc. 34 (2003) 21–25, https://doi.org/10.1002/jrs.920.
[58] W.K.H. Ho, Z.Y. Bao, X. Gan, K.-Y. Wong, J. Dai, D. Lei, Probing conformation change and binding mode of metal ion-carboxyl coordination complex through resonant surface-enhanced raman spectroscopy and density functional theory, J. Phys. Chem. Lett. 10 (2019) 4692–4698, https://doi.org/10.1021/acs.jpclett.9b01435.
[59] G. Sirgedaite, M. Talaikis, G. Niaura, L. Mikoliunaite, Magneto-plasmonic nanostructures for SERS: magnetite decorated by silver and gold nanoparticles, New J. Chem. 47 (2023) 402–411, https://doi.org/10.1039/D2NJ04368H.
[60] R.L. Aggarwal, L.W. Farrar, S.K. Saikin, Increase of SERS signal upon heating or exposure to a high-intensity laser field: benzenethiol on an AgFON substrate, J. Phys. Chem. C 116 (2012) 16656–16659, https://doi.org/10.1021/jp305944h.
[61] I. Aleknavičienė, E. Pabreža, M. Talaikis, M. Jankunec, G. Raciukaitis, Low-cost SERS substrate featuring laser-ablated amorphous nanostructure, Appl. Surf. Sci. 571 (2022) 151248, https://doi.org/10.1016/j.apsusc.2021.151248.
[62] P.N. Sisco, C.J. Murphy, Surface-coverage dependence of Surface-enhanced raman scattering from gold nanocubes on self-assembled monolayers of analyte, J. Phys. Chem. A 113 (2009) 3973–3978, https://doi.org/10.1021/jp810329j.
[63] C.-H. Ho, S. Lee, SERS and DFT investigation of the adsorption behavior of 4-mercaptobenzoic acid on silver colloids, Colloids Surf A 474 (2015) 29–35, https://doi.org/10.1016/j.colsurfa.2015.03.004.
[64] K. Jung, J. Hahn, S. In, Y. Bae, H. Lee, P.V. Pikhitsa, K. Ahn, K. Ha, J.-K. Lee, N. Park, M. Choi, Hotspot-engineered 3D multipetal flower assemblies for surface-enhanced raman spectroscopy, Adv. Mater. 26 (2014) 5924–5929, https://doi.org/10.1002/adma.201401004.
[65] Q. Fu, Z. Zhan, J. Dou, X. Zheng, R. Xu, M. Wu, Y. Lei, Highly reproducible and sensitive SERS substrates with ag inter-nanoparticle gaps of 5 nm fabricated by ultrathin aluminum mask technique, ACS Appl. Mater. Interfaces 7 (2015) 13322–13328, https://doi.org/10.1021/acsami.5b01524.
[66] J.-F. Bryche, R. Gillibert, G. Barbillon, M. Sarkar, A.-L. Coutrot, F. Hamouda, A. Aassime, J. Moreau, M. Lamy de la Chapelle, B. Bartenlian, M. Canva, Density effect of gold nanodisks on the SERS intensity for a highly sensitive detection of chemical molecules, J. Mater. Sci. 50 (2015) 6601–6607, https://doi.org/10.1007/s10853-015-9203-x.

Supplementary material

Tuning SERS Performance Through the Laser-Induced Morphology Changes of Gold Nanostructures

Kernius Vilkevičius[a,*], Ilja Ignatjev[b], Algirdas Selskis[c], Gediminas Niaura[b], Evaldas Stankevičius[a]

[a] *Department of Laser Technologies, Center for Physical Sciences and Technology, Savanoriu av. 231, LT-02300 Vilnius, Lithuania*
[b] *Department of Organic Chemistry, Center for Physical Sciences and Technology, Sauletekio av. 3, LT-10257 Vilnius, Lithuania*
[c] *Department of Characterization of Materials Structure, Center for Physical Sciences and Technology, Sauletekio av. 3, LT-10257 Vilnius, Lithuania*

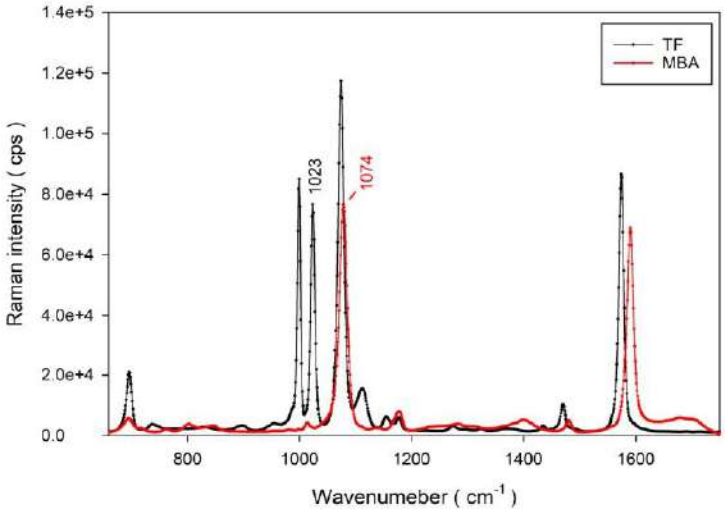

Figure S1. SERS spectra of self-assembled monolayers of 4-MBA (4-mercaptobenzoic acid) and TF (thiophenol) on an electrochemically rough Au surface.

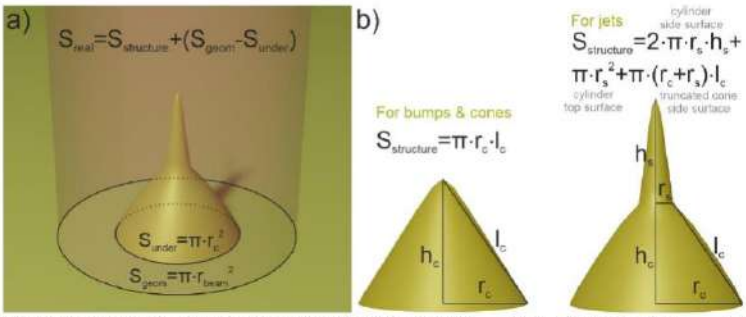

Figure S2. a) Calculation of real irradiated surface area S_{real}. Geometrical area S_{geom} is the spot size into which the beam is focused. S_{under} is the area under the structure (basis area), while $S_{structure}$ is the surface area of the structure. b) Calculation of structure surface area. The bump and cone surface area was approximated using a cone, while for the jet – the spike surface area was approximated using a cylinder and a conical base was approximated using a truncated cone. The subscript c marks the height, radius, and slant height for the cone/conical basis, while subscript s marks the height and radius for the spike.

Table S1. Geometrical parameters of the structures and the calculated roughness for the samples of shape influence investigation (Figure 4).

No.	r_c (nm)	h_c (nm)	l_c (nm)	r_s (nm)	h_s (nm)	$S_{structure}$ ($\times 10^{-12}$ m^2)	S_{real} ($\times 10^{-12}$ m^2)	R
(1)	316	380	495	-	-	0.492	1.308	1.157
(2)	366	868	942	-	-	1.085	1.794	1.586
(3)	345	865	931	-	-	1.011	1.767	1.562
(4)	368	704	780	33	284	1.044	1.750	1.547
(5)	366	640	721	40	402	1.022	1.732	1.532
(6)	375	660	735	53	501	1.161	1.850	1.635
(7)	388	610	694	57	637	1.211	1.869	1.652
(8)	420	558	610	180	-	1.250	1.827	1.612

Table S2. The intensity of SERS signal and calculated enhancement factor for the samples of shape influence investigation (Figure 4).

No.	I_{SERS} (cps)		EF	
	1074 cm^{-1}	**1589 cm^{-1}**	**1074 cm^{-1}**	**1589 cm^{-1}**
(1)	84	42	2.99×10^5	1.87×10^5
(2)	1256	999	3.26×10^6	3.24×10^6
(3)	4397	3369	1.16×10^7	1.11×10^7
(4)	6891	5265	1.83×10^7	1.75×10^7
(5)	4768	2504	1.28×10^7	8.41×10^6
(6)	2406	1527	6.06×10^6	4.80×10^6
(7)	762	593	1.90×10^6	1.85×10^6
(8)	56	34	1.43×10^5	1.09×10^5

Table S3. Geometrical parameters of the structures and the calculated roughness for the samples of gold thickness influence investigation (Figure 6).

No.	r_c (nm)	h_c (nm)	l_c (nm)	r_s (nm)	h_s (nm)	$S_{structure}$ ($\times 10^{-12}$ m^2)	S_{real} ($\times 10^{-12}$ m^2)	R
(1)	528	150	516	34	1332	1.201	1.45	1.286
(2)	411	548	652	57	878	1.284	1.88	1.666
(3)	339	542	617	44	700	0.941	1.71	1.511
(4)	400	639	730	46	635	1.211	1.84	1.626
(5)	459	654	761	70	604	1.55	2.02	1.784
(6)	402	414	553	36	596	0.9	1.52	1.346
(7)	450	441	608	31	447	1.01	1.5	1.328

Table S4. The intensity of SERS signal and calculated enhancement factor for the samples of gold thickness influence investigation (Figure 6).

No.	I_{SERS} (cps)		EF	
	1074 cm^{-1}	**1589 cm^{-1}**	**1074 cm^{-1}**	**1589 cm^{-1}**
(1)	1171	1293	3.58×10^6	5.32×10^6
(2)	1765	1452	4.36×10^6	4.48×10^6
(3)	6891	5265	1.83×10^7	1.75×10^7
(4)	7363	7266	1.86×10^7	2.30×10^7
(5)	11811	8531	2.73×10^7	2.46×10^7
(6)	2630	2810	8.04×10^6	1.07×10^7
(7)	1502	1225	4.66×10^6	4.75×10^6

6th publication / 6 publikacija
K. Vilkevičius, T. Rakickas, E. Stankevičius,
High-quality plasmonic Ag-Au bilayer nanobump grating sensor,
Advanced Materials Technologies, 10(20), e01199 (2025).

https://doi.org/10.1002/admt.202501199

ADVANCED MATERIALS TECHNOLOGIES
www.advmattechnol.de

High-Quality Plasmonic Ag—Au Bilayer Nanobump Grating Sensor

Kernius Vilkevičius, Tomas Rakickas, and Evaldas Stankevičius*

A novel plasmonic sensing platform based on bimetallic silver–gold nanobump grating fabricated via a single-step direct laser writing process is presented. The plasmonic modes excited at the surface of the grating are sensitive to the local refractive index and its changes, resulting in a spectral shift of the resonant peak. Comprehensive optical measurements reveal a linear redshift of the resonance with increasing refractive index, achieving a sensitivity of up to 933 nm/RIU and a figure of merit of up to 57 RIU^{-1}. The choice in resonant peak and optimization in operating conditions, such as the angle of incidence, allow us to achieve these values by enhancing plasmon coupling efficiency and reducing the resonance linewidth. The suggested method offers a free-form design for the platform, maintaining high-quality resonances while exhibiting great stability, repeatability, and durability.

1. Introduction

Micro- and nanofabrication of metallic films is a widely discussed topic and rapidly evolving area of research since the structures produced exhibit unique plasmonic properties with their extensive applications in nanophotonics – including sensing, imaging, lasing, and more.[1] Advances in fabrication techniques have enabled the production of precisely controlled nanostructures with diverse shapes and arrangements. From individual structures, such as metallic nanowires and nanorods or nanospheres[2] to 2D both periodic and aperiodic metallic gratings of nanoholes, nanorings, or nanodisks[3] – all kinds of nanostructures are utilized for plasmonic applications.

Such highly applicable nanostructures require appropriate equipment and methods for fabrication. The most accurate techniques, such as electron-beam and focused ion-beam lithography, offer extremely high resolution and are capable of producing structures with features on the order of a few nanometers.[4] However, these are limited by low throughput and high cost, restricting the scalability. These challenges are circumvented by implementing alternative chemical[5] and lithographical approaches such as nanosphere lithography or photoreduction.[6] Also, the replication and molding techniques are becoming more pronounced for the rapid production of 2D and even quasi-3D metallic structures.[7] Laser implementation is another promising and versatile method, which can be used in subtractive, additive, and transformative manners to produce free-form metallic structures.[8] The ablative technique offers precise removal of the material, while laser sintering and agglomeration have been used to produce plasmonic nanostructures directly within crystals.[9] A transformative method has also emerged as a promising way, of modifying the surface so that new structures are produced. In direct laser writing (DLW) technique, the use of highly focused single ultrashort laser pulses leads to the formation of energy-dependent metal nanostructures with shapes ranging from hemispherical bumps to tip-based jets.[10] Since only a deposition of material and its modification using a direct laser beam is required, such a method could be called single-step and in this aspect has a significant benefit over multi-step lithographic techniques. Depending on the fabrication speed, repetition rate, and pulse energy, this modification method allows the fabrication of 1D, quasi-1D, and 2D arrays with varying and easily tunable optical properties.[11]

Single nanostructure and nanoparticle applications highly rely on the localized surface plasmon (LSP) mode mainly impacted by the nanoparticle's size and geometry. Other plasmonic devices based on a continuous metallic film are governed by the excitation of the propagating surface plasmon (PSP) mode, which necessitates additional optical or structural coupling elements to overcome momentum mismatch. Diffraction-based plasmonic excitation offers a versatile way to excite one of two hybrid plasmonic modes.[12] In the absence of an underlying metal film, the surface lattice resonance (SLR) is achieved by periodic coupling of the LSPs of individual nanostructures with the diffractive photonic modes.[13] This resonance features a sharp spectral response, lower losses, and enhanced plasmon coupling, and is already applied in nanolasers and biosensing.[14] An additional metal film along the structures induces additional Ohmic losses and the coupling of LSP-PSP mode, leading to hybridization and resulting in the so-called hybrid lattice plasmon resonance (HLPR).[15] The latter mode is specifically obtained in the gratings of nanostructures created by single-pulse DLW on the

K. Vilkevičius, E. Stankevičius
Department of Laser Technologies
Center for Physical Sciences and Technology
Savanoriu Ave. 231, Vilnius LT-02300, Lithuania
E-mail: kernius.vilkevicius@ftmc.lt
T. Rakickas
Department of Nanoengineering
Center for Physical Sciences and Technology
Savanoriu Ave. 231, Vilnius LT-02300, Lithuania
The ORCID identification number(s) for the author(s) of this article can be found under https://doi.org/10.1002/admt.202501199

DOI: 10.1002/admt.202501199

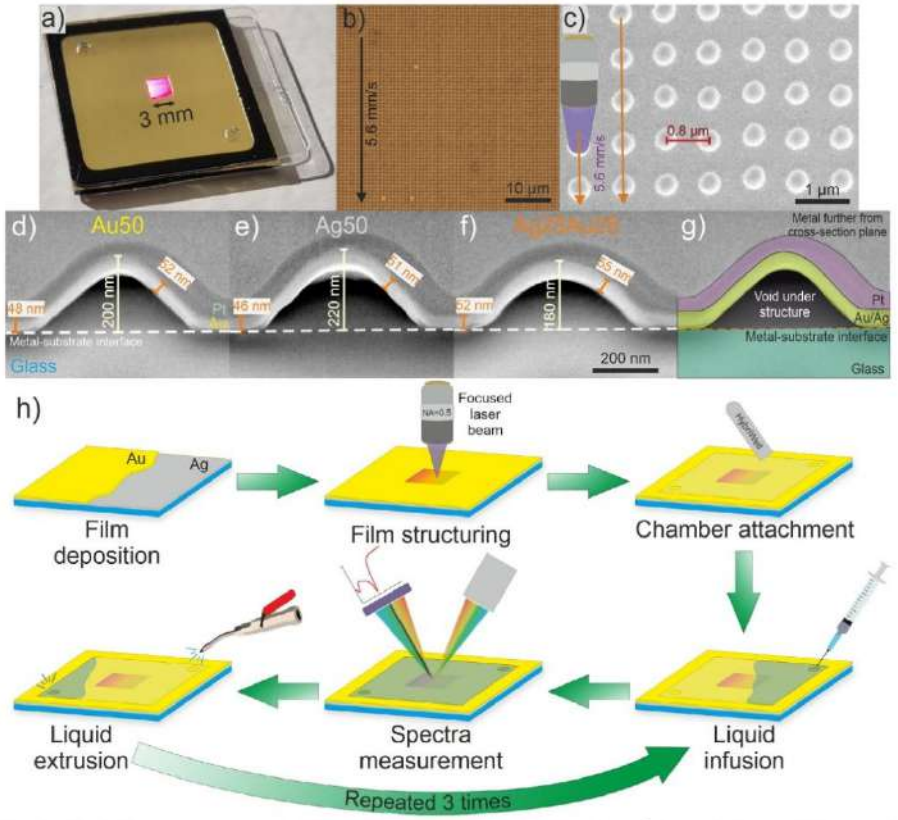

Figure 1. a) Ag—Au bilayer nanostructured sample with an adhesive chamber. b) Optical microscope image of a large-scale 2D array with 0.8 µm period. c) Top-view SEM image of 0.8 µm grating, with the laser scanning direction indicated. SEM images of fabricated bumps cross-sections on 50 nm of d) Au, e) Ag, and f) Ag—Au bilayer taken at a 54° angle. g) Bump structure with distinguished zones of materials. A thin platinum layer was coated on top of the structures for a better contrast of cross-sections. h) Sample preparation and measurement scheme.

surface of thin metal films. Here, the resonant peaks depend on the period, structure size, polarization, and angle of incidence, and can be determined according to the diffraction along the surface and its order.[16]

Plasmonic devices have already gained attraction in biological and health sciences, offering a powerful methodology for optical sensing. Researchers continue to improve sensitivity and detection limit through improved plasmon coupling, exploited anisotropy, or controlling nanoparticle size.[17] Also, not only pure metals but alloys and multilayered structures are currently being investigated for the enhanced performance of plasmonic devices.[18] The locally enhanced electromagnetic field around the nanostructures greatly improves the signals from the molecules within the area. This phenomenon is widely applicable in surface-enhanced Raman spectroscopy since the Raman signal can be greatly strengthened and distinguished from the noise, leading to determining a unique molecular fingerprint. The strongest signals are obtained by exploiting structures with narrow gaps (exploiting gap mode) or sharp tips and edges like nanojets.[19]

Another field is optical refractive-index sensing based on the surface plasmon resonance (SPR) sensitivity to changes in the local refractive index (RI). The real-time detection of changes in RI through the spectral shifts in plasmon resonance wavelength

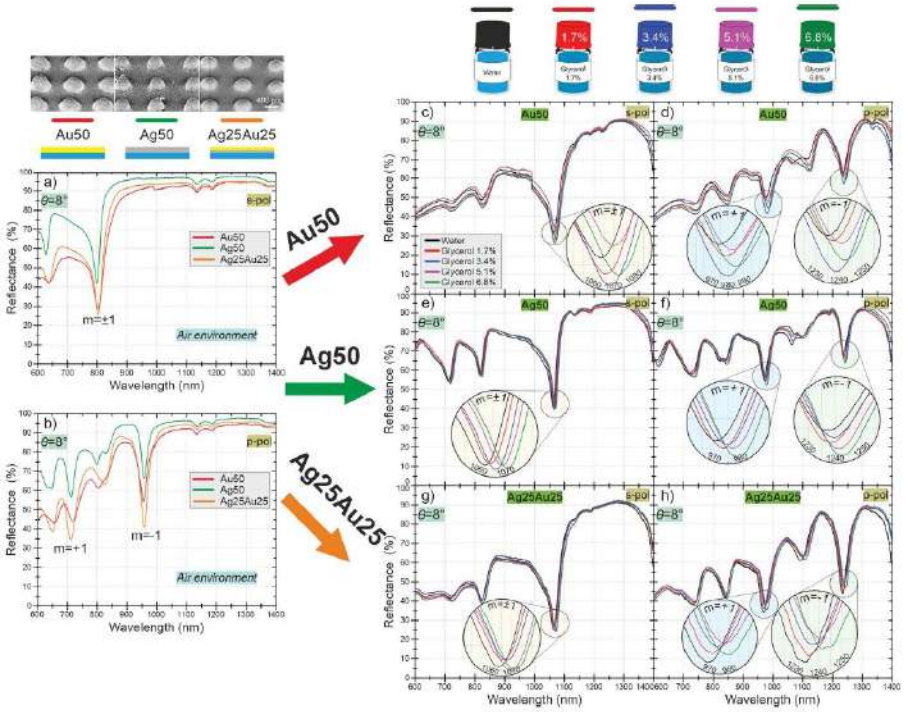

Figure 2. Au, Ag, and Ag–Au sample spectra comparison. Reflectance in the air for a) s- and b) p-polarization at an 8° angle, where the red line is Au50, green line Ag50, and the orange line Ag25Au25 samples. Gold (c, d), silver (e, f), and bilayer (g, h) reflectance in water (black line) and different concentrations of glycerol (red, blue, magenta, green lines) for s- (c, e, g) and p-polarization (d, f, h).

has paved the way for the label-free detection of biomolecules, analytes, and other pathogens and chemical agents. Herein, the molecular adsorption onto the metallic structures leads to the transition of RI and spectral shift. However, the process is not selective for the analytes and investigated molecules, therefore surface functionalization with antibodies or other analyte-sensitive receptors is compulsory for the selective measurements.[20] Alternatively, resonance-shift sensors are applied for gas and liquid RI sensing, as the pollutants and investigated concentrations are accurately determined without surface functionalization.[21]

The performance of a sensing platform is typically evaluated in terms of its sensitivity, which marks the peak shift per refractive index unit (RIU), and the figure of merit (FOM) where the sensitivity is divided by the peak width (FWHM). Since sensor efficiency depends not only on its intrinsic parameters but also on plasmon coupling efficiency, ways for resonance linewidth reduction are in search to enhance the results.[22] Higher quality factors are indicative of higher sensor efficiency. Conventional prism-based sensors,[23] while effective, require additional bulk optical components that increase the overall size and complexity of the device, leading to a search for new more compact sensing platforms. Implementation of the grating-excitation offers a promising alternative by reducing the size and increasing the excitation area since surface gratings can be produced in a free-form and large-scale manner.[24] Additionally, fiber RI sensors are in attention due to their design flexibility and high sensitivity.[25] Therefore, the solutions for fast and simply produced, easily scalable, and repetitive sensing platforms are in demand.

Here, we present a single-step fabrication of an easily scalable bimetallic HLPR-based sensing platform for liquid detection. In this study, a glycerol solution in water of various concentrations is used as a reporter to determine and characterize the sensing platform's performance and parameters. The DLW-produced gratings, combined with an additional adhesion chamber, can be easily incorporated into any standard spectrophotometers, enabling a fast measurement and response of spectral shift of the fluid of interest. The proposed platform offers high sensitivity, stability

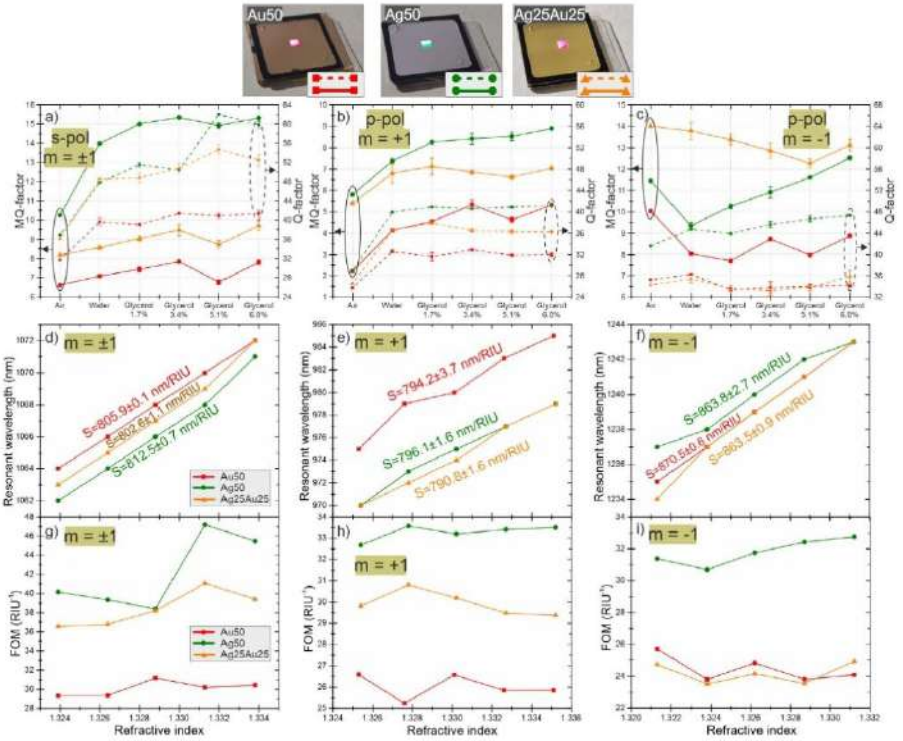

Figure 3. Au, Ag, and Ag—Au bilayer sample quality, resonant wavelength, sensitivity, and figure of merit (FOM) comparison. Resonant peak quality (a-c) with MQ-factor (solid line, left-side axis) and Q-factor (dashed line, right-side axis), resonant wavelength (d-f), and FOM (g-i) dependence on RI for the main resonant peaks: $m = \pm 1$ at s-polarization (a, d, g), $m = +1$ at p-polarization (b, e, h), and $m = -1$ at p-polarization (c, f, i). For all graphs, red line marks Au50, green line – Ag50, and orange line – Ag25Au25 samples. The angle of incidence is 8°.

and repeatability, making it a promising candidate for practical sensing applications.

2. Experimental Section

2.1. Material Deposition and Array Formation

The sensing platforms were produced on silver-gold bilayer and pure metal (Ag and Au) films. Thin films on the microscopic glass were deposited using a magnetron sputter coater (Quorum Q150T). The deposition rate for Au was 0.26 nm/s, while for Ag it was 0.59 nm/s. The thicknesses of the coatings were controlled by varying the sputtering time. Ag—Au bilayer film was produced by depositing Ag for 42 s (to get a 25 nm layer) and then Au for 94 s. Pure Ag film was sputtered for 84 s, while pure Au film - for 188 s. The overall thickness of the deposited layers was 50 nm. Before the metal deposition, an additional adhesive layer of Ti (3 nm) was deposited on the substrate.

The periodic arrays of nanobumps were produced by a direct laser writing (DLW) technique. The 343 nm wavelength (third-harmonic of Yb:KGW-based 249 fs laser (Pharos, Light Conversion Ltd.)) was used. The beam was tightly focused onto the metal surface into a ≈0.8 µm spot using a 0.5 numerical aperture (NA) objective. The formation of the structures was applied using a single pulse per area. The 2D periodic alignment of the bumps was achieved by performing a unidirectional scanning of the laser beam. The sample translation speed and pulse repetition rate were carefully selected so that the distance between the structures in the scanning line would equal the grating period – 0.8 µm. In this case, the sample translation speed was 5.6 mm/s and the pulse repetition rate was 7 kHz. The required period in a perpendicular direction was achieved by selecting a distance between

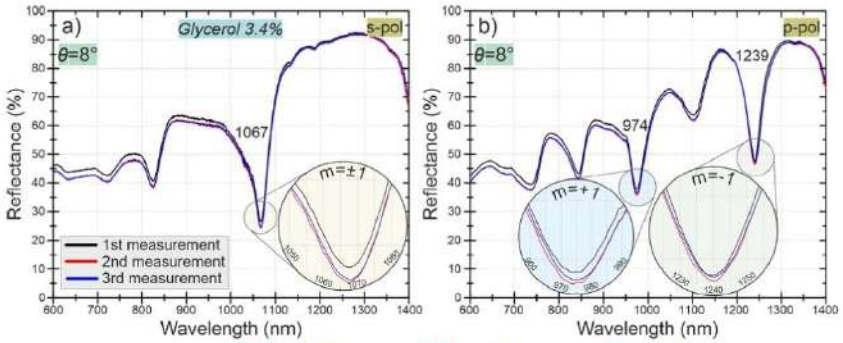

	1st	2nd	3rd	1st	2nd	3rd	1st	2nd	3rd
QF	51.4	51	51.3	37.4	37.2	37	34.6	34.9	34.5
MQF	9.4	9.9	9.7	6.8	6.9	6.6	13.3	12.9	12.9
FOM	38.7	38.4	38.5	30.3	30.2	30	24.1	24.3	24
	m = ±1			m = +1			m = -1		

Figure 4. Stability measurements (3 consecutive measurements) of Ag–Au sample at 8° angle. Reflection spectra in glycerol 3.4% environment for a) s-polarization and b) p-polarization. Legend is the same for both graphs.

the scanning lines. The used pulse energy was in the range of 0.46–0.55 nJ for different layer configurations. The size of the fabricated gratings was 3 × 3 mm^2, and the fabrication time was ≈60 min. For the repeatability measurements, 3 samples using each film layout were produced.

The shape of the fabricated structures was characterized using a scanning electron microscope (Helios NanoLab650). The pictures were taken at a 52° angle. Also, the bumps were cut using focused Ga ions to obtain the cross-section images. A thin platinum layer was coated on top for a better contrast.

2.2. Sensing Liquid Preparation

The sensing experiment was performed with 5 liquids: ultrapure water and 4 different concentration glycerol solutions in water. Ultrapure water (resistivity of 18.2 MΩ×cm at 25 °C) was taken from a Synergy UV water purification system (Merck, USA), glycerol (86 weight%) was obtained from Carl Roth GmbH, Germany.

The solution refractive indexes were measured with an imaging null ellipsometer Accurion Nanofilm EP3, using a Kinetics/SPR cell with BK7 glass prism, at 658 nm wavelength. First of all, the total internal reflection angle was found with ultrapure water, injected into the cell, and the glass refractive index was calculated, assuming that the water refractive index is well known and it was taken from Kedenburg et al.[26] Then, glycerol in ultrapure water solutions were sequentially injected into the cell and total internal reflection angles were found. Water and glycerol refractive index dispersions were calculated using the Sellmeier equation, taking constants from the literature[26,27] in the 400-2000 nm wavelength range (Figure S1, Supporting Information). Solution concentrations were calculated using the linear effective media approximation. The measured concentrations of glycerol solutions were 1.7%, 3.4%, 5.1%, and 6.8%. For an additional limit of detection measurements, glycerol solutions of 0.84%, 0.41%, and 0.2% were used.

2.3. Sensing Platform Preparation and Reflection Measurements

For sensing experiments, the adhesive chamber (HybriWell-FL) was attached to the surface of the metal. The reflection measurements were applied using a spectrophotometer (EssentOptics PHOTON RT) mainly in the wavelength range of 600-1400 nm with a step of 1 nm. The results were obtained using both s- and p-polarized radiation with a light incidence angle of 8°. Additional experiments of angle influence on the results were performed at 15°, 30°, 45°, and 60° in the wavelength range of 600-2000 nm with a step of 1 nm. The measurements with liquids were performed using the following steps. First, the reference spectrum of air response was measured with only an adhesive chamber on the surface. Then the liquid was infused inside the chamber using a syringe and the reflection spectrum with the liquid inside the chamber was measured. Finally, the liquid was blown out of the chamber and the measurement cycle repeated. For each investigated liquid these steps were repeated 3 times to investigate the stability of the sensing platform. The results of each liquid were obtained by averaging all 3 measurements.

2.4. Sensing Platform Evaluation

Resonant peaks of the sensing platform were evaluated by measuring their quality, sensitivity, and figure of merit. The quality

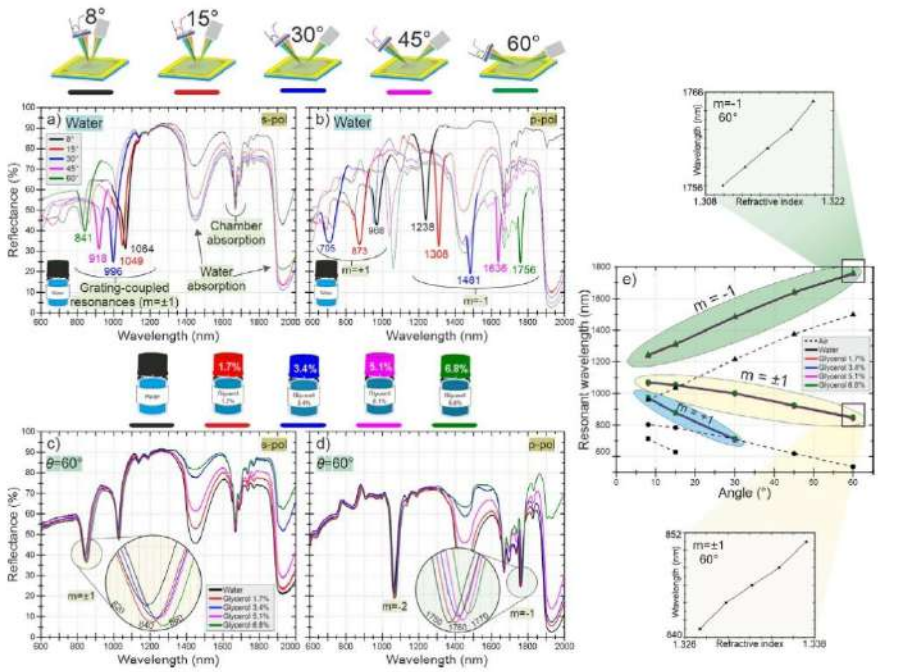

Figure 5. Reflectance spectra dependence on the angle of incidence. Reflectance spectra in water at angles of 8° (black line), 15° (red), 30° (blue), 45° (magenta), and 60° (green) for a) s- and b) p-polarization. Reflectance spectra at a 60° angle in water (black line) and different glycerol concentrations (red, blue, magenta, green lines) for c) s- and d) p-polarization. e) Resonant wavelength changes with angle in air (dashed line) and liquids (solid lines). The insets show the specific peak wavelength dependence on the liquid refractive index at a 60° angle.

was determined by the Q-factor ($Q = \lambda_{res}/FWHM$) and MQ-factor ($MQ = Q \cdot h/100\%$) with the peak height included. The resonance baseline was chosen to be on the left side of the peak, where the reflection drop begins. The resonant wavelength, peak width, and depth were determined using the Origin function Peak Analyzer.

While the Q-factor is the usual metric parameter, our introduced MQ-factor additionally accounts for the depth of the resonance peak, suggesting more efficient coupling between the plasmonic modes and stronger plasmonic interactions. In wavelength interrogation sensors, the MQ-factor is less critical, as only the spectral shift is measured, and a sufficient signal-to-noise ratio is typically adequate. However, for intensity interrogation-based sensors, the change in signal intensity is the main registered parameter,[28] therefore, deeper resonance peaks lead to higher RI resolution and more accurate results. Such sensing platforms would benefit more from the MQ-factor rather than the conventional Q-factor.

Sensitivity and FOM were determined using the following formulas: $S = \Delta\lambda_m/\Delta n$ and $FOM = S/FWHM$. To determine the change in refractive index, the exact RIs at the specific resonant wavelengths were taken from the dispersion curves of each liquid (Figure S1, Supporting Information). The sensitivity was averaged from the values of all investigated liquids. The FOM was averaged for each specific liquid from different consecutive measurements.

For durability measurements, the samples were stored in a non-hermetically sealed plastic Petri dishes, in a dry and dark box at room temperature (20–22 °C) for 6 months, and then remeasured again. In this period, the relative humidity was in range of 20–50%. The adhesive chamber was left attached to the sample, which acted as a protective layer.

3. Results and Discussion

3.1. Plasmonic Au, Ag, and Ag—Au Bilayer Sensor

The periodic nanostructures on the metal surface for the sensing experiments were produced using single pulses of a fs-laser (343 nm) with a DLW technique. Using a high-NA objective,

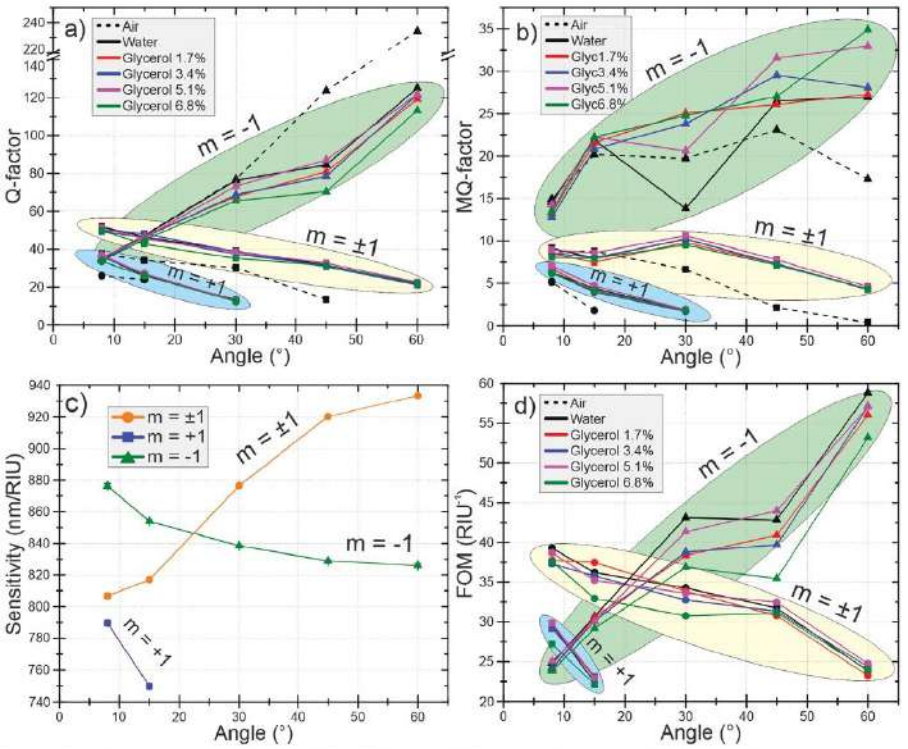

Figure 6. Angle influence on quality, sensitivity, and FOM. a) Q-factor and b) MQ-factor at different angles of incidence in air (dashed line), water (solid black line), and various concentrations of glycerol (red, blue, magenta, green lines). c) The sensitivity of the peaks $m = \pm 1$ (orange), $m = +1$ (blue), and $m = -1$ (green) at different angles of incidence. d) FOM of the main investigated peaks for water (black line) and glycerol (red, blue, magenta, green lines) at various angles.

the beam was focused on a surface into a ≈0.8 μm diameter spot. The vertical laser scanning was implemented for a fast fabrication of the large-scale square arrays (3 × 3 mm^2) consisting of bumps with a period of 0.8 μm (**Figure 1a–c**). Structures are well-aligned and evenly spaced in the scanning direction. However, a small deviation from an ideal 2D periodic lattice is observed in the axis perpendicular to the scanning, as seen in Figure 1c. This lateral displacement is due to vibrations in the positioning system. Although this might broaden the resonances, the quality of the plasmonic resonances excited by large-scale arrays remains sufficiently high. Hemispherical nanostructure arrays were produced on Au (sample Au50), Ag (sample Ag50), and Ag—Au bilayer (sample Ag25Au25) films of 50 nm thickness. To improve metal adhesion to the substrate, an additional Ti layer of 3 nm was deposited directly on the substrate, so that the structured area would not be removed under contact with liquid.[29] Pulse energies for different material films were chosen so that the fabricated structures would be of similar size and dimensions (0.46 nJ for Au, 0.55 nJ for Ag, and 0.5nJ for Ag—Au). The SEM images of fabricated structure cross-sections on the Ag, Au, and Ag—Au bilayer taken at a 54° angle are depicted in Figure 1d–f. The diameter of the bumps is 440–450 nm, while the height is 220 nm for Ag, 200 nm for Au, and 180 nm for Ag—Au samples. As determined in our previous research, the formation of hemispherical hollow bumps is based on the metal film detachment from the substrate and mass displacement of the molten layer, without impacting the glass substrate, thus producing a void between the uplifted structure and substrate.[10] Each structural zone is distinguished in Figure 1g.

The investigation of sensing of the liquid was performed by using an adhesive chamber (HybriWell) that was attached to the surface of the metal (Figure 1a). With the help of the needle, the test

Table 1. Comparison of 2D plasmonic array sensing platforms parameters.

Structure	Fabrication method	Plasmonic mode	Sensitivity [nm/RIU]	FOM [RIU^{-1}]	Refs.
Au nanoholes	Focused ion beam milling	HLPR	463	–	[36]
Au nanodiscs	Photolithography	HLPR	600	46	[32a]
Au nanopillars	Electron beam & metal deposition	HLPR	675	112.5	[32b]
Au nanocylinders	Nanoimprinting & plasma etching	HLPR	454.4	–	[37]
Au columns	Direct laser writing lithography	HLPR	478-617	24	[33]
Ag–Au bilayer nanobumps	Direct laser writing	HLPR (Coupled LSP-PSP) $m = \pm 1$	810-930	24-38	This work
		HLPR (Coupled LSP-PSP) $m = -1$	830-880	24-57	

liquid was infused into the chamber so that it covered the entire structured zone. The reflectance spectra were measured using a spectrophotometer (Essentoptics Photon TR UV-VIS-NIR) in the 600–1400 nm wavelength range with a step of 1 nm. A circularly shaped beam with a diameter of 2 mm was used to irradiate the sample and the response of both *s*- and *p*-polarized light at 8° and 15° angle of incidence was captured. After the measurement, the liquid was blown out using high-pressure air. This infusion, measurement, and extrusion procedure was repeated 3 times for each liquid. Figure 1h shows the full preparation scheme.

The investigation and reflection measurement were performed with 5 different liquids: ultrapure water and glycerol of 4 different concentrations. The refractive indexes of water (n = 1.3314) and the solutions were determined with an ellipsometer using a 658 nm wavelength source (n = 1.3339, n = 1.3364, n = 1.3389, and n = 1.3414 respectively for 1.7%, 3.4%, 5.1%, and 6.8%). First, the spectrum of the structured area on the thin film was measured without the adhesive chamber, and later – with an attached chamber in the air environment. The use of such a chamber reduces the intensity of the resonant peak while not affecting the resonant wavelength and peak width (Figure S2, Supporting Information). The decrease in intensity is about 6–10%. However, since further measurements with liquids were carried out using this adhesive chamber, this decrease did not affect the comparative results.

During the research, the quality of the resonant peaks was determined using the parameter Q-factor with the ratio of wavelength and width of the peak. Additionally, the modified MQ-factor including the peak depth was more commonly used in this study. For sensitivity calculations, the refractive indexes (RI) of water and glycerol at the specific resonant wavelengths had to be used. These were found from the dispersion curves of each concentration using the Sellmeier dispersion equation and coefficients for water[26] and glycerol[27] solutions. The dispersion curves are given in Figure S1 (Supporting Information).

Silver has the strongest plasmonic properties owing to its low damping losses, while gold has weaker plasmonic properties but is chemically stable and resistant to the environment, as silver is more prone to degradation by oxidation. Thus, three different configurations of silver, gold, and silver-gold bilayer were analyzed and the reflectance spectra of these were compared to determine the optimal sample configuration and material composition. The fabricated arrays support grating-coupled HLPR modes, enabling highly tunable resonant behavior. The resonant peak spectral positions vary with the polarization of the incident light, as s- and p-polarized light excite different resonant wavelengths. Further tunability is achieved by adjusting the grating period (an increase results in a redshift) and the angle of incidence (an increase causes a redshift of the $m = -1$ mode and a blueshift of the $m = +1$ and $m = \pm 1$ modes), whose influence and resonant wavelength can be theoretically estimated using the 1D diffraction grating equation.[16,31] Additionally, the geometry of the nanostructures affects the resonances – specifically, increasing the nanobump height leads to a redshift of the $m = -1$ mode, which is associated with an out-of-plane resonance origin.[30] The results obtained for the 8° angle of incidence are shown in **Figure 2**. The main 3 resonant peaks were investigated throughout the study: $m = \pm 1$ in the s-polarization response (Figure 2a), $m = +1$ and $m = -1$ in the p-polarization response (Figure 2b). Since the resonance peaks depend not only on the period of the grating but also on the size and shape of the nanostructure, the arrays were fabricated with bumps of similar heights so that the height-dependent out-of-plane resonances ($m = -1$ in p-polarization) of different samples would be close together.

In the air environment, resonances appear at 799 nm for Ag50 and at 803 nm for Au50 and Ag25Au25 samples in s-polarization. By comparing the MQ-factors of $m = \pm 1$ resonances (**Figure 3a**), it is observed that silver has the highest factor MQ = 10.25 since this metal exhibits stronger plasmonic properties, with silver-gold bilayer being in the middle (MQ = 8.18) and gold array having the lowest quality of MQ = 6.62. Meanwhile, in p-polarization, the $m = +1$ resonance is observed at 718 nm, 712 nm, and 713 nm for Au50, Ag50, and Ag25Au25 samples respectively, while for $m = -1$ peaks the wavelengths are corresponding: 955 nm, 958 nm, and 957 nm. The non-identical grating of the bumps, as any deviation in height and diameter slightly affects the resonance, might explain the differences in wavelength. Despite that, the wavelength mismatch is not critical and the results can be compared. The modified quality factor for p-polarization $m = +1$ peak (Figure 3b) also maintains the tendency with MQ = 5.8 for Ag50, MQ = 5.4 for Ag25Au25, and MQ = 2.2 for Au50. Meanwhile, the m = −1 peak (Figure 3c) offers a slightly different trend with the silver-gold bilayer having the highest MQ-factor of 14, silver being 11.4, and gold having an MQ-factor of 10.

Furthermore, the reflectance spectra measurements using different liquids were performed for each sample and depicted in Figure 2c–h for both distinguished polarizations. The resonance shift to longer wavelengths by more than 250 nm is evident as the environment changes from air to liquid. It denotes that the

active zone of our samples is sensitive to the ambient refractive index and its changes. First, the ultrapure water was used as a sensor reporter. The shifts for $m = \pm1$, $m = +1$, and $m = -1$ peaks are around 260, 256, and 280 nm, respectively. Across different material configurations, these values remained almost similar, showing a deviation of only 2 nm. With the substitution of the liquid from water to glycerol of varying concentrations (1.7%, 3.4%, 5.1%, and 6.8%), a redshift of the peaks by 2–3 nm was obtained with each increasing concentration. In the case of Ag25Au25 sample $m = \pm1$ peak, the shift was from 1063 nm to 1072 nm due to a change in the RI from $n = 1.3239$ to $n = 1.3338$. The wavelength dependence on the liquid refractive index is provided in Figure 3d–f. As the increase in concentration is linear, the wavelength change is almost linear as well. However, there is a small deviation from a perfect linear trend, which might imply the measurement errors resulting from the positioning of the grating. For each measurement, the sample was taken out of the spectrophotometer, and after changing liquids inserted again. Manual insertion of the sample results in inaccuracy in the positioning of the azimuthal angle and measurement area. Therefore, this might result in small shifts in the resonant wavelength or its broadening. For more accurate results during the real sensing applications, a fixed and stable plasmonic platform should be used with measurements in the same zone. To reduce the influence of this, several successive measurements were conducted, and the results were averaged to enhance accuracy and minimize the measurement uncertainty. A 1.7% change in glycerol concentration results in a wavelength shift of ≈2 nm. Therefore, the periodic bump gratings on gold layer, silver layer, and silver-gold bilayer are sensitive to changes in concentration and RI and can be effectively utilized as sensors.

Using liquids, the MQ-factor (Figure 3a–c) itself maintains the trend for $m = \pm1$ and $m = +1$ peaks, that the silver array has the highest quality (MQ >14 for s-polarization peak and MQ > 7 for $m = +1$ peak). The silver-gold bilayer sample has intermediate quality (MQ ≈ 9 for s-polarization and MQ ≈ 7 for $m = +1$ peak), while the gold sample demonstrates the worst features (MQ-factor ≈ 7 for s-polarization and ≈ 5 for $m = +1$ peak). The trend is also similar to that obtained in the air for $m = -1$ peak, where the Ag25Au25 sample has the highest MQ-factor, the Ag50 sample falls in the middle and the Au50 array shows the lowest quality.

To determine the parameters of sensing platforms, the sensitivity and figure of merit were calculated. For these calculations, the RI shift was determined for each liquid in comparison to the air ($n = 1$) environment. The resonant wavelength of each peak was taken from the averaged value of 3 consecutive measurements for each liquid. Since the sensitivity is a constant parameter of the sensing platform and a specific peak, the calculated values of S at each liquid were averaged. Each resonant peak demonstrates different dispersive properties with distinct shifts. The $m = \pm1$ peak by changing the medium from air to water shifts by ≈260 nm (261 nm for Au, 263 nm for Ag, and 260 nm for Ag—Au) and increasing with glycerol solution concentration, resulting in a platform sensitivity of ≈ 800 nm/RIU, to be exact $S = 805.9$ nm/RIU for the gold array, $S = 812.5$ nm/RIU for the silver array, and $S = 802.6$ nm/RIU for the silver-gold bilayer array. The smaller-wavelength resonance at p-polarization ($m = +1$) demonstrates an air-water shift of ≈257 nm (258 nm for Au, 258 nm for Ag, 257 nm for Ag—Au) with the averaged peak sensitivities of $S = 794.2$ nm/RIU for Au, $S = 796.1$ nm/RIU for Ag, and $S = 790.8$ nm/RIU for Ag—Au. In contrast, the $m = -1$ peak exhibits a larger air-to-water shift of ≈280 nm (280 nm for Au, 279 nm for Ag, 277 nm for Ag—Au) yielding a higher sensitivity of $S = 870.5$ nm/RIU (Au50), $S = 863.8$ nm/RIU (Ag50), and $S = 863.5$ nm/RIU (Ag25Au25). While all three resonant peaks are sensitive to changes in the RI, the $m = -1$ peak appearing at p-polarization is of the highest sensitivity. However, no clear tendency is observed regarding sensitivity dependence on the used material, as gold, silver, and bilayer samples maintain similar results. Additionally, the FOM values were analyzed for a more accurate assessment of sensor performance and comparison of different materials. In this case, the material impact and its tendency are more apparent, as illustrated in Figure 3g–i. The FOM was calculated for each liquid, as the peak widths varied, and was calculated as the average of 3 consecutive measurements in a specific solution. Among the investigated samples, silver exhibits the largest FOM for all peaks, exceeding 30 RIU^{-1}, since the metal possesses the strongest plasmonic properties influencing the appearance of narrow resonances. While the silver-gold bilayer sample demonstrates the lowest sensitivity among others, its FOM shows intermediate values for $m = \pm1$ (≈ 38 RIU^{-1}) and $m = -1$ (≈ 30 RIU^{-1}), with FOM at $m = +1$ being similar to that of the gold sample at 24 RIU^{-1}. Other gold sample FOM values are 30 RIU^{-1} and 26 RIU^{-1} for $m = \pm1$ and $m = -1$, respectively, making it the least effective of investigated samples and proving that although the sensitivity is relatively high, the resonances are wide as well, resulting in a lower FOM and inferior performance as a sensor configuration. The specific values of sensitivity, FOM, Q-factor, and MQ-factor for Au, Ag, and Ag—Au samples for the $m = \pm1$, $m = +1$, and $m = -1$ resonant peaks are summarized in Supporting Information, Tables S1–S3 (Supporting Information), respectively. The given values were obtained at an 8° angle of incidence.

A thorough comparison of a few metal configurations suitable for plasmon-based liquid sensors has shown that although silver demonstrates the strongest sensing properties, the most practical configuration is to use a silver-gold bilayer. It combines intermediate plasmonic properties (better than gold but lower than silver) with the advantage of a top gold layer serving as an oxidation protector, preventing the degradation of the properties commonly observed in pure silver samples. Henceforth, further investigation will be focused on the Ag25Au25 silver-gold bilayer samples.

3.2. Stability of the Sensing Platform

During the investigation, spectral measurements before and after the liquid infusion were repeated three times for each liquid to determine the error margins and evaluate the stability of the platform. Here, **Figure 4** illustrates the stability measurements for the Ag25Au25 sample using glycerol of 3.4% concentration. The resonant wavelength during several measurements maintains its place in the spectrum at 1067 nm ($m = \pm1$), 974 nm ($m = +1$), and 1239 nm ($m = -1$) confirming the reliability of the results. Only small deviations in peak width and depth were observed, leading to small variations in quality factors and FOM with the

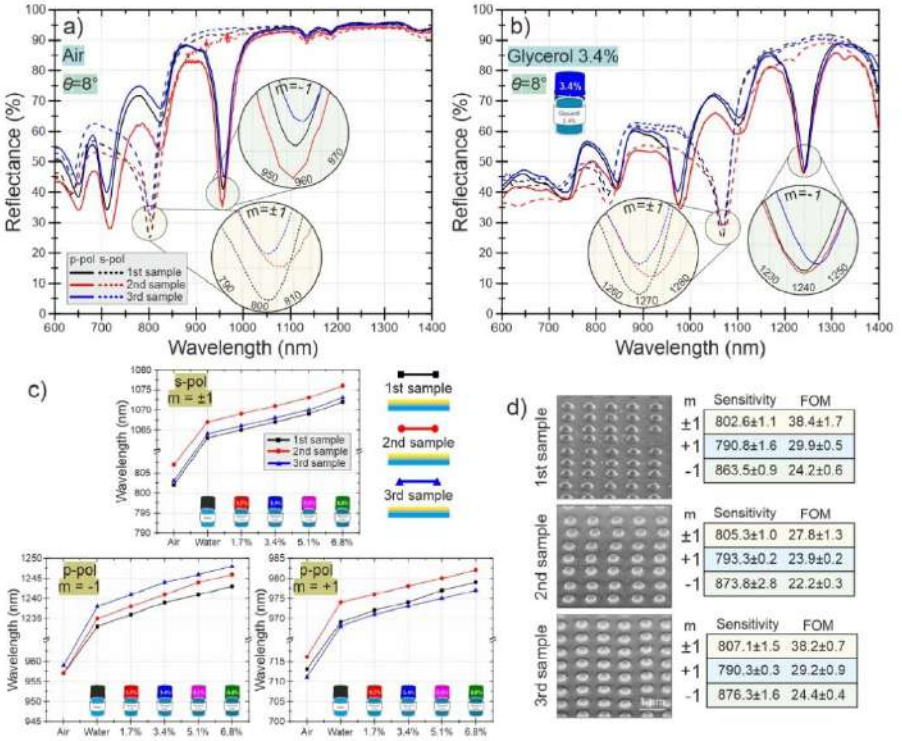

Figure 7. Repeatability measurements of 3 different Ag–Au samples. Reflection spectra in a) air and b) glycerol 3.4% environment at 8° angle of incidence. The solid line depicts the response of p-polarization, while the dashed line – s-polarization. c) Resonant wavelength dependence on the environment (air, water, glycerol 1.7%/3.4%/5.1%/6.8%) of the main resonant peaks for 3 different Ag–Au samples. d) SEM images of bump gratings of 3 samples and their sensitivity and averaged FOM values.

values provided in the same figure. The errors both in Q-factor and FOM are 0.3%, 0.4%, and 0.5% for $m = \pm 1$, $m = +1$, and $m = -1$, respectively, while the MQ-factor errors are 2.2%, 1.8%, and 1.5%. These errors include measurement inaccuracy since the manual selection of the peak baseline might introduce some deviations in height and width. Nonetheless, the low percentages highlight the high stability of the sample and obtained results. Similar results were obtained for all investigated liquids.

3.3. Angle Influence on the Platform Response

Previous measurements were conducted using only an 8° angle of incidence. Therefore, another Ag25Au25 sample was measured additionally at 15°, 30°, 45°, and 60° angles to evaluate the sensor's performance at various angles and examine the sensitivity and FOM changes with light incidence angle. Reflectance spectra for two orthogonal polarizations in a water environment are presented in **Figure 5a,b**. A noticeable shift in the peak wavelengths is observed as the angle increases. The behavior of the resonant peaks is similar to the previous findings in air for similar gratings.[16] For s-polarized light, the $m = \pm 1$ resonance blueshifts from 1064 nm at 8° to 841 nm at 60°. A stronger blueshift is observed for $m = +1$ peak from 968 nm at 8° to 705 nm at 30°, before entering the absorption zone at larger angles. In contrast, a shift to the opposite side of the spectra is obtained for $m = -1$ peak from 1238 nm at 8° to 1756 nm at 60°. In the latter case, not all resonances are equally usable for the sensing measurements, since certain resonances overlap with absorption zones. The resonance at 30° coincides with the water absorption zone (1481 nm), limiting the intensity of the peak, and the one obtained at 45° is near the absorption peak of the adhesion

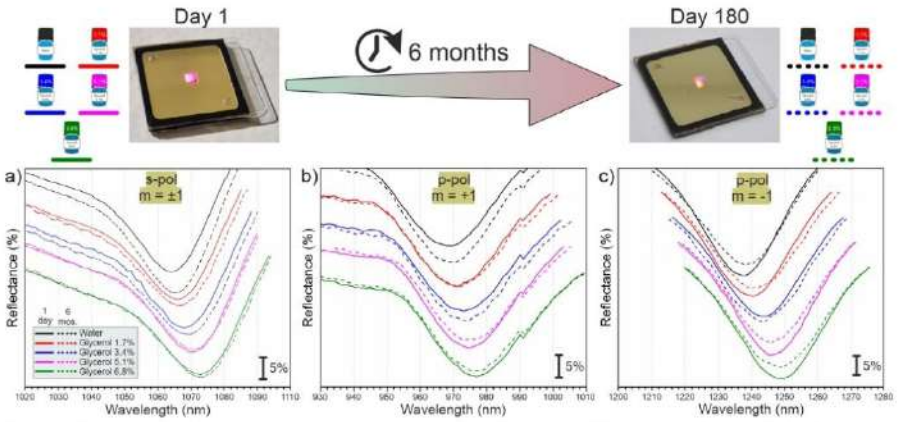

Figure 8. Reflectance at peaks a) $m = \pm 1$, b) $m = +1$, and c) $m = -1$ at the day of fabrication (solid lines) and after 6 months (dashed line) for water (black line) and glycerol of 1.7%, 3.4%, 5.1%, and 6.8% concentrations (red, blue, magenta, and green lines). The reflectance scale bar is 5%.

chamber (1636 nm). These findings highlight the importance of optimizing the angle of incidence based on the liquid and materials used to avoid spectral overlap.

To ensure the performance of the sensing platform even at large angles, additional measurements with different liquids were performed at 60°, and the corresponding spectra are represented in Figure 5c,d. At this angle, the $m = +1$ peak already falls within the metal absorption zone and is therefore not observable, leaving only the $m = \pm 1$ and $m = -1$ resonance for analysis. A change in the liquid, and consequently the RI, results in a redshift of the resonant peaks. Similar to measurements at 8°, here the change in resonant wavelength with each liquid is also approximately 2 nm. The $m = \pm 1$ peak, initially located at 536 nm in the air, shifted to 841 nm in water and further shifted from 844 nm to 851 nm by 2–3 nm in various concentrations of glycerol. Similarly, the peak of $m = -1$ resonance appeared at 1500 nm in air, at 1756 nm in water and showed incremental shifts from 1758 nm to 1765 nm across different samples of glycerol. Such a consistent shift demonstrates the reliability of the platform at various angles of incidence, from small ones (close to normal incidence) to large ones approaching the glancing angle. The resonant wavelength for each peak is depicted in Figure 5e, while the wavelength shifts for each liquid are presented in Figure S3 (Supporting Information). All investigated peaks maintain the same tendency across all angles, exhibiting a linear increase in wavelength with the increment of RI, as illustrated in the insets of Figure 5e for the $m = -1$ and $m = \pm 1$ peaks at a 60° angle. The limit of detection (LOD) was additionally determined by measuring glycerol solutions of lower concentrations (0.2%, 0.41%, 0.84%, and 1.68%) and analyzing the smallest detectable shift in resonance wavelength (Figure S4, Supporting Information). Based on this analysis, the calculated LOD is approximately 0.84% glycerol (relative to deionized water), corresponding to a refractive index change of 0.0013. The RI change was determined from the dispersion curves in Figure S4g (Supporting Information). This limit is constrained by the spectrophotometer's wavelength step of 1 nm; however, smaller shifts may still be visually detected at sub-nanometer resolution. By improving the spectral resolution of the spectrophotometer, the LOD could potentially be reduced to 0.41% of glycerol, corresponding to a RI change of 0.0006.

The calculated Q-factor and MQ-factor (**Figure 6a,b**) provide some insights into the sensor's performance at different angles and the applicability of each peak. Both factors show a similar trend, with $m = \pm 1$ and $m = +1$ slightly decreasing and $m = -1$ significantly rising with the increasing angle. This might imply that the blueshifting peaks broaden with an increment in angle while the redshifting peak maintains or even reduces its width. Although the Q-factor at 60° of $m = -1$ peak in the air reaches up to $QF = 235$, it drops to ≈ 120 in liquids. Such a behavior can be explained by the MQ-factor, which for those specific conditions in the air ($MQF = 17.3$) is lower compared to that in liquid ($MQF \approx 57$), indicating that although the resonance obtained in the air is narrower, it is of lower intensity than in liquids. Another aspect observed in the MQ-factor graph is a drop at 30° for the $m = -1$ when the resonant peak falls within the water absorption zone, reducing its intensity. Among all, the latter $m = -1$ resonance provides the highest qualities ($MQF > 15$), exhibiting narrow and intense peaks, particularly at 8°, 15°, and 60° which do not coincide with absorption zones.

A distinct trend is observed in the wavelength shift (Figure S3, Supporting Information) and sensitivity (Figure 6c) dependence on the angle, since at larger angles both p-polarization resonances decrease in sensitivity (from $S = 876$ nm/RIU at 8° to $S = 826$ nm/RIU at 60° for $m = -1$) and exhibit smaller shifts in spectra. Conversely, the shift of $m = \pm 1$ resonance at s-polarization increases with angle, enhancing the sensitivity of such platform from $S = 807$ nm/RIU at 8° up to $S = 933$ nm/RIU at 60°. Despite

the increasing sensitivity of the s-polarization peak, the FOM (Figure 6d) for the same $m = \pm 1$ peak maintains a decreasing tendency as it broadens while blueshifting, dropping from FOM of ≈ 38 RIU^{-1} at 8° to 24 RIU^{-1} at 60°. Since $m = -1$ retains its narrow resonances with the angle, the FOM significantly rises at large angles from 24 RIU^{-1} at 8° to ≈ 57 RIU^{-1} at 60°. Overall, while the angular increment improves the sensitivity of the s-polarization peak and lowers it for p-polarization peaks, the angle-associated blueshift broadens the peaks whereas the redshift preserves narrow resonances, thus changing the overall trend for FOM and sensor's functionality. Therefore, a choice of a usable peak depends on the angle: at lower angles, the s-polarization is preferable due to its higher FOM, while for angles above 20° the $m = -1$ becomes more advantageous, excluding the overlapping with absorption zones.

The Ag—Au nanobumps presented here are comparable to other plasmonic structures used for sensing applications. While some nanostructures may outperform others in specific performance metrics, it is uncommon for one to excel in all aspects. In **Table 1**, we compare several HLPR-exciting nanostructure gratings fabricated using various techniques. The sensitivity comparison reveals that our nanobumps achieve the highest value among the compared gratings, exceeding 800 nm/RIU, and thus provide a robust response to low RI changes. Gold nanodiscs produced with photolithography show a similar FOM to nanobumps presented here, while gold nanopillars demonstrate an exceptional FOM of 112 RIU^{-1} outperforming DLW bumps.[32] However, these nanopillars are manufactured using slow and hardly scalable electron beam production. In contrast, a clear advantage of the Ag—Au nanobumps lies in the rapid production rate and scalability of a comparatively high-performance plasmonic sensing platform. A comparable DLW lithography approach has also been applied to fabricate gold columns, providing similarly fast sensor production and comparable FOM values, though with lower sensitivity characteristics.[33] Despite using a similar technique, our approach offers the formation of periodic structure straight out of metal, without the need for any use of polymers. In addition, since SPR sensing is already widely applied in commercial sensing systems, it is worth noting the standards used in industry. Many commercial SPR instruments (Biacore) are prism-based devices relying on angular interrogation.[34] There are also LSPR-based instruments (Nicoya OpenSPR) that implement nanoparticles for wavelength interrogation.[35] However, grating-coupled sensing platforms are still not widely adopted in industry. Despite this, grating-coupled devices offer significant advantages: they eliminate the need for bulky prisms, enabling more compact and integrable sensor designs, while still achieving comparable sensing parameters. Furthermore, free-form design allows for a flexible and easily scalable sensing area, which could be tailored for specific application needs.

3.4. Repeatability of the Sensing Platform

The repeatability of the sensing platform was explored by producing three Ag25Au25 samples with identical parameters and evaluating their sensing parameters. Measurements in air and glycerol of 3.4% concentration at an 8° angle are presented in **Figure 7a,b**, where different-colored lines correspond to different samples, allowing a direct comparison of their spectral responses. All investigated gratings exhibit diffractive resonances at similar wavelengths in air, with only minor deviations attributed to slight variations in the grating fabrication process. In liquids, a larger wavelength distribution of 10 nm is observed, which marks slight differences in the sensitivity of the gratings. Despite that, a resonant increasing shift is constant and linear for each sample (Figure 7c), confirming the stability of the sensor's response. While small differences in the initial positions in air and resonant shifts lead to slight variations in sensitivity and resonance quality among the samples, the overall trends remain reproducible.

The comparison of different samples reveals a high similarity in the resonance quality. For the $m = \pm 1$ peak, the MQ-factor is approximately 9, 7.8, and 8.6 for the three samples, respectively, while for the $m = +1$ peak, it is around 6.9, 5.4, and 6.5. The highest values are observed for the $m = -1$ resonance, with MQ-factors of 13.1, 11.5, and 13.7. Although the second example exhibits slightly lower quality, its values remain comparable to the other two samples. These minor deviations could be attributed to inaccuracies in sample fabrication, like energy fluctuations. However, the main aspect is the repeatability of the platform's sensitivity and FOM, demonstrating its reliability.

The calculated sensitivities (Figure 7d) remain consistent among the samples with only a minor deviation. The values are close to 804 nm/RIU for the s-polarization peak, around 790 nm/RIU for the $m = +1$ peak, and reach 870 nm/RIU for the $m = -1$ peak. The FOM values for p-polarization peaks remain stable through all three samples. The only notable difference is observed in the s-polarization resonance, where a bit lower FOM is obtained due to the peak's reduced intensity. These results further confirm the reliability of the sensor and the ability to reproduce the sensor of required parameters accurately.

3.5. Durability and Reusability of the Sensing Platform

Finally, the durability and reusability of the sensing platform were investigated by remeasuring the sample spectra after 6 months to determine any potential degradation in performance. The samples were stored in a dry and dark box at a room temperature (20–22 °C) with a relative humidity in the range of 20–50%. Since the chamber is attached to the sample, it serves as a protective layer, preventing surface contamination, oxidation, and mechanical damage to the silver-gold layer and grating. The reflectance spectra, shown in **Figure 8**, present measurements taken on the day of fabrication (solid lines) and after 6 months (dashed lines). Despite long-term storage, the resonant wavelengths for all three peaks ($m = \pm 1$, $m = +1$, and $m = -1$) remain unchanged, proving the stability of the grating and the preservation of the plasmonic properties. Although minor variations in peak intensities are observed, which could be attributed to slight changes in sample positioning, the resonance positions and their shift in response to liquid RIs remain consistent. The calculated sensitivity values are maintained, while only a small error is observed for FOM, as the peak intensity and width vary minimally. Such long-term stability confirms the robustness of the platform, making it suitable for practical applications where durability and prolonged measurements are required.

4. Conclusion

In this work, periodic nanobump arrays were fabricated on gold, silver, and silver-gold bilayer, and their application as refractive index sensors was investigated. Due to the grating coupling of plasmonic modes, prominent resonant peaks were observed in reflectance spectra across all metal configurations. The peaks were determined to be highly sensitive to environmental changes, exhibiting a redshift with an increasing refractive index of the liquid. Among the tested metals, the silver-gold bilayer turned out to be the optimal sensor design, as it effectively combines the advantageous properties of both metals. Our study has demonstrated that each diffractive peak reacts uniquely to changes in refractive index, with different sensitivities and figures of merit. The resonance dependence not only on the liquid RI but also on the angle of incidence has been explored, leading to a sensitivity of $S = 933$ nm/RIU and FOM of 57 RIU^{-1}. Additionally, the sensing platform demonstrated high stability with great repeatability and durability throughout the measurements in time, as confirmed by performed measurements. Overall, the presented approach offers an easily scalable and rapid fabrication method for high-performance plasmonic sensing platforms, with a promising way for practical applications in environmental monitoring and biochemical detection.

Supporting Information

Supporting Information is available from the Wiley Online Library or from the author.

Acknowledgements

This project has received funding from the Research Council of Lithuania (LMTLT), agreement No. S-TPP-23-14. The authors would like to thank prof. Algirdas Selskis for SEM analysis.

Conflict of Interest

The authors declare no conflict of interest.

Data Availability Statement

The data that support the findings of this study are available from the corresponding author upon reasonable request.

Declaration of generative AI and AI-assisted technologies in the writing process

During the preparation of this work the authors used DeepL Write in order to improve clarity and style of the English language. After using this tool/service, the authors reviewed and edited the content as needed and take full responsibility for the content of the publication.

Keywords

direct laser writing, grating-coupled resonance, periodic nanostructures, plasmonic sensor, silver-gold bilayer

Received: June 5, 2025
Revised: August 6, 2025
Published online: August 29, 2025

[1] a) K. Yang, X. Yao, B. Liu, B. Ren, *Adv. Mater.* **2021**, *33*, 2007988; b) J. Jiang, X. Wang, S. Li, F. Ding, N. Li, S. Meng, R. Li, J. Qi, Q. Liu, G. L. Liu, *Nanophotonics* **2018**, *7*, 1517; c) K. A. Sergeeva, D. V. Pavlov, A. A. Seredin, E. V. Mitsai, A. A. Sergeev, E. B. Modin, A. V. Sokolova, T. C. Lau, K. V. Baryshnikova, M. I. Petrov, S. V. Kershaw, A. A. Kuchmizhak, K. S. Wong, A. L. Rogach, *Adv. Funct. Mater.* **2023**, *33*, 2307660; d) A. A. Sergeev, D. V. Pavlov, A. A. Kuchmizhak, M. V. Lapine, W. K. Yiu, Y. Dong, N. Ke, S. Juodkazis, N. Zhao, S. V. Kershaw, A. L. Rogach, *Light Sci. Appl.* **2020**, *9*, 16.

[2] a) J. Zheng, X. Cheng, H. Zhang, X. Bai, R. Ai, L. Shao, J. Wang, *Chem. Rev.* **2021**, *121*, 13342; b) T. An, B. Zhu, Y. Ling, S. Gong, W. Cheng, *J. Mater. Chem. A* **2019**, *7*, 14233; c) V. Petrikaitė, I. Ignatjev, A. Selskis, G. Niaura, E. Stankevičius, *Opt. Laser Technol.* **2024**, *168*, 109956.

[3] a) C. Ruiz de Galarreta, N. Casquero, E. Humphreys, J. Bertolotti, J. Solis, C. D. Wright, J. Siegel, *ACS Appl. Mater. Interfaces* **2022**, *14*, 3446; b) T. H. Chow, Y. Lai, X. Cui, W. Lu, X. Zhuo, J. Wang, *Small* **2019**, *15*, 1902608; c) J. Pang, I. G. Theodorou, A. Centeno, P. K. Petrov, N. M. Alford, M. P. Ryan, F. Xie, *J. Mater. Chem. C* **2017**, *5*, 917.

[4] M. Hentschel, J. Karst, H. Giessen, *Adv. Opt. Mater.* **2020**, *8*, 2000879.

[5] K. Volk, J. P. S. Fitzgerald, P. Ruckdeschel, M. Retsch, T. A. F. König, M. Karg, *Adv. Opt. Mater.* **2017**, *5*, 1600971.

[6] a) Y. Zhang, Z. Liang, A. P. Zhang, H.-Y. Tam, *Adv. Opt. Mater.* **2021**, *9*, 2001368; b) X. Zhao, J. Wen, M. Zhang, D. Wang, Y. Wang, L. Chen, Y. Zhang, J. Yang, Y. Du, *ACS Appl. Mater. Interfaces* **2017**, *9*, 7710.

[7] J. Hwang, Y. Zhang, B. Kim, J. Jeong, J. Yi, D. R. Kim, Y. L. Kim, A. Urbas, G. Ariyawansa, B. Xu, Z. Ku, C. H. Lee, *Adv. Sci.* **2024**, *11*, 2404870.

[8] T. Pinheiro, M. Morais, S. Silvestre, E. Carlos, J. Coelho, H. V. Almeida, P. Barquinha, E. Fortunato, R. Martins, *Adv. Mater.* **2024**, *36*, 2402014.

[9] a) E. H. Waller, S. Duran, G. v. Freymann, *Nanophotonics* **2023**, *12*, 1549; b) H. Zhu, L. Chu, H. Lv, Q. Ye, S. Juodkazis, F. Chen, *Adv. Sci.* **2024**, *11*, 2402840.

[10] a) K. Vilkevičius, A. Selskis, E. Stankevičius, *Appl. Surf. Sci.* **2023**, *617*, 156629; b) Y. Nakata, T. Okada, M. Maeda, *Jpn. J. Appl. Phys.* **2003**, *42*, L1452; c) S. Gao, X. Li, Y. Lian, S. Zhou, X. Zhang, Z. Fu, J. Huang, *Opt. Laser Technol.* **2022**, *151*, 108035; d) D. Pavlov, S. Syubaev, A. Kuchmizhak, S. Gurbatov, O. Vitrik, E. Modin, S. Kudryashov, X. Wang, S. Juodkazis, M. Lapine, *Appl. Surf. Sci.* **2019**, *469*, 514.

[11] K. Vilkevičius, K. Čepaitis, A. Selskis, E. Stankevičius, *Opt. Laser Technol.* **2025**, *183*, 112330.

[12] D. Murugan, M. Tintelott, M. S. Narayanan, X.-T. Vu, T. Kurkina, C. Rodriguez-Emmenegger, U. Schwaneberg, J. Dostalek, S. Ingebrandt, V. Pachauri, *Adv. Opt. Mater.* **2024**, *12*, 2401862.

[13] a) V. G. Kravets, A. V. Kabashin, W. L. Barnes, A. N. Grigorenko, *Chem. Rev.* **2018**, *118*, 5912; b) A. D. Utyushev, V. I. Zakomirnyi, I. L. Rasskazov, *Rev. Phys.* **2021**, *6*, 100051.

[14] a) M. Juodėnas, N. Khinevich, G. Klyvis, J. Henzie, T. Tamulevičius, S. Tamulevičius, *Nanoscale Horiz.* **2025**, *10*, 142; b) A. Danilov, G. Tselikov, F. Wu, V. G. Kravets, I. Ozerov, F. Bedu, A. N. Grigorenko, A. V. Kabashin, *Biosens. Bioelectron.* **2018**, *104*, 102; c) B. Wang, P. Yu, W. Wang, X. Zhang, H.-C. Kuo, H. Xu, Z. M. Wang, *Adv. Opt. Mater.* **2021**, *9*, 2001520; d) Z.-T. Huang, C.-W. Yin, Y.-H. Hong, H. Li, K.-B. Hong, T. S. Kao, M.-H. Shih, T.-C. Lu, *Adv. Opt. Mater.* **2021**, *9*, 2100299.

[15] a) T. Maurer, P.-M. Adam, G. Lévêque, *Nanophotonics* **2015**, *4*, 363; b) R. Liudvinavičius, K. Vilkevičius, E. Stankevičius, *Appl. Surf. Sci.* **2025**, *711*, 164127.

[16] E. Stankevičius, K. Vilkevičius, M. Gedvilas, E. Bužavaitė-Vertelienė, A. Selskis, Z. Balevičius, *Adv. Opt. Mater.* **2021**, *9*, 2100027.

[17] a) L. Guo, J. A. Jackman, H.-H. Yang, P. Chen, N.-J. Cho, D.-H. Kim, *Nano Today* **2015**, *10*, 213; b) J. Zeng, Y. Zhang, T. Zeng, R. Aleisa, Z. Qiu, Y. Chen, J. Huang, D. Wang, Z. Yan, Y. Yin, *Nano Today* **2020**, *32*, 100855.

[18] a) V. Coviello, D. Badocco, P. Pastore, M. Fracchia, P. Ghigna, A. Martucci, D. Forrer, V. Amendola, *Nat. Commun.* **2024**, *15*, 834; b) I.

Darmadi, S. Z. Khairunnisa, D. Tomeček, C. Langhammer, *ACS Appl. Nano Mater* **2021**, *4*, 8716; c) N. Li, A. Tittl, S. Yue, H. Giessen, C. Song, B. Ding, N. Liu, *Light Sci. Appl.* **2014**, *3*, 226.

[19] a) K. Vilkevičius, I. Ignatjev, A. Selskis, G. Niaura, E. Stankevičius, *Appl. Surf. Sci.* **2024**, *660*, 160003; b) J.-M. Kim, C. Lee, Y. Lee, J. Lee, S.-J. Park, S. Park, J.-M. Nam, *Adv. Mater.* **2021**, *33*, 2006966.

[20] a) O. Tokel, U. H. Yildiz, F. Inci, N. G. Durmus, O. O. Ekiz, B. Turker, C. Cetin, S. Rao, K. Sridhar, N. Natarajan, H. Shafiee, A. Dana, U. Demirci, *Sci. Rep.* **2015**, *5*, 9152; b) F. Inci, Y. Saylan, A. M. Kojouri, M. G. Ogut, A. Denizli, U. Demirci, *Appl. Mater. Today* **2020**, *18*, 100478; c) A. Vázquez-Guardado, F. Mehta, B. Jimenez, A. Biswas, K. Ray, A. Baksh, S. Lee, N. Saraf, S. Seal, D. Chanda, *Nano Lett.* **2021**, *21*, 7505; d) D. Kotlarek, M. Vorobii, W. Ogieglo, W. Knoll, C. Rodriguez-Emmenegger, J. Dostálek, *ACS Sens.* **2019**, *4*, 2109; e) M. Couture, S. S. Zhao, J.-F. Masson, *Phys. Chem. Chem. Phys.* **2013**, *15*, 11190; f) B. Špačková, P. Wrobel, M. Bocková, J. Homola, *Proc. IEEE* **2016**, *104*, 2380.

[21] a) F. A. Sayed, H. A. Elsayed, M. Al-Dossari, M. F. Eissa, A. Mehaney, A. H. Aly, *Sci. Rep.* **2023**, *13*, 21793; b) K. Lodewijks, J. Ryken, W. Van Roy, G. Borghs, L. Lagae, P. Van Dorpe, *Plasmonics* **2013**, *8*, 1379; c) C. Zhang, Z. Liu, C. Cai, Z. Yang, Z.-M. Qi, *Opt. Lett.* **2022**, *47*, 4155; d) H. Altug, S.-H. Oh, S. A. Maier, J. Homola, *Nat. Nanotechnol.* **2022**, *17*, 5.

[22] a) M. Gao, W. Yang, Z. Wang, S. Lin, J. Zhu, Z. Yang, *Photon. Res.* **2020**, *8*, 1226; b) Y. Xu, P. Bai, X. Zhou, Y. Akimov, C. E. Png, L.-K. Ang, W. Knoll, L. Wu, *Adv. Opt. Mater.* **2019**, *7*, 1801433; c) D. Wang, A. Yang, A. J. Hryn, G. C. Schatz, T. W. Odom, *ACS Photonics* **2015**, *2*, 1789; d) B. Liu, S. Chen, J. Zhang, X. Yao, J. Zhong, H. Lin, T. Huang, Z. Yang, J. Zhu, S. Liu, C. Lienau, L. Wang, B. Ren, *Adv. Mater.* **2018**, *30*, 1706031.

[23] a) S. Aşır, B. Uğur, M. Jalilzadeh, I. Göktürk, D. Türkmen, *ACS Omega* **2023**, *8*, 492; b) F. B. Kamal Eddin, Y. W. Fen, N. A. S. Omar, J. Y. C. Liew, W. M. E. M. M. Daniyal, *Spectrochim. Acta, Part A* **2021**, *263*, 120202.

[24] a) S. Rossi, E. Gazzola, P. Capaldo, G. Borile, F. Romanato, *Sensors* **2018**, *18*, 1621; b) D. Le, A. Ranta-Lassila, T. Sipola, M. Karppinen, J. Petäjä, M. Kehusmaa, S. Aikio, T.-L. Guo, M. Roussey, J. Hiltunen, A. Popov, *Photon. Res.* **2024**, *12*, 947; c) S. Sarkar, T. A. F. König, *Adv. Sens. Res.* **2024**, *3*, 2300054; d) C. Valsecchi, A. G. Brolo, *Langmuir* **2013**, *29*, 5638; e) S. Saxena, Y. Rastogi, N. K. Sharma, *Plasmonics* **2025**, https://doi.org/10.1007/s11468-025-02799-7.

[25] a) S. Cao, X. Shang, H. Yu, L. Shi, L. Zhang, N. Wang, M. Qiu, *Opt. Express* **2022**, *30*, 25536; b) H.-L. Du, N. Kari, B. Li, Q. Wang, *Opt. Laser Technol.* **2025**, *181*, 111697; c) R. Huang, L. Long, Q. Deng, Z.-Y. Li, *Opt. Laser Technol.* **2023**, *167*, 109796.

[26] S. Kedenburg, M. Vieweg, T. Gissibl, H. Giessen, *Opt. Mater. Express* **2012**, *2*, 1588.

[27] a) D. Jakubczyk, G. Derkachov, K. Nyandey, S. Alikhanzadeh-Arani, A. Derkachova, *Sci. Data* **2023**, *10*, 894; b) J. E. Saunders, C. Sanders, H. Chen, H.-P. Loock, *Appl. Opt.* **2016**, *55*, 947.

[28] a) X. Yuan, Z. Niu, L. Liu, Y. Zeng, L. Ma, Z. Nie, Z. Tian, D. Kai, F. Zhang, G. Liu, S. Li, Z. Yuan, *Biosensors* **2023**, *13*, 946; b) Y. Zeng, J. Zhou, W. Sang, W. Kong, J. Qu, H. P. Ho, K. Zhou, B. Z. Gao, J. Chen, Y. Shao, *Front. Chem.* **2021**, *9*, 801355; c) S. Celiksoy, W. Ye, K. Wandner, K. Kaefer, C. Sönnichsen, *Nano Lett.* **2021**, *21*, 2053; d) Z. Huo, Y. Li, B. Chen, W. Zhang, X. Yang, X. Yang, *Talanta* **2023**, *255*, 124213.

[29] R. Liudvinavičius, A. Selskis, E. Stankevičius, *Opt. Laser Technol.* **2024**, *175*, 110807.

[30] K. Vilkevičius, G. D. Tsibidis, A. Selskis, E. Stratakis, E. Stankevičius, *Adv. Opt. Mater.* **2024**, *12*, 2400172.

[31] M. Seo, J. Lee, M. Lee, *Opt. Express* **2017**, *25*, 26939.

[32] a) M. Couture, T. Brulé, S. Laing, W. Cui, M. Sarkar, B. Charron, K. Faulds, W. Peng, M. Canva, J.-F. Masson, *Small* **2017**, *13*, 1700908; b) A. E. Çetin, A. A. Yanik, C. Yilmaz, S. Somu, A. Busnaina, H. Altug, *Appl. Phys. Lett.* **2011**, *98*, 111110.

[33] P. Urbancova, D. Pudis, M. Goraus, J. Kovac, *Nanomaterials* **2021**, *11*, 1163.

[34] a) S. C. B. Gopinath, *Sens. Actuators, B* **2010**, *150*, 722; b) N. Khansili, G. Rattu, P. M. Krishna, *Sens. Actuators, B* **2018**, *265*, 35; c) J. Ryken, J. Li, T. Steylaerts, R. Vos, J. Loo, K. Jans, W. Van Roy, T. Stakenborg, P. Van Dorpe, J. Lammertyn, L. Lagae, *Sens. Actuators, B* **2014**, *200*, 167.

[35] a) E. K. Hanson, R. J. Whelan, *Sensors* **2023**, *23*, 4831; b) E. K. Hanson, C.-W. Wang, L. Minkoff, R. J. Whelan, *Sensors* **2023**, *23*, 6703.

[36] J. P. Monteiro, L. B. Carneiro, M. M. Rahman, A. G. Brolo, M. J. L. Santos, J. Ferreira, E. M. Girotto, *Sens. Actuators, B* **2013**, *178*, 366.

[37] J. Zhu, Z. Wang, S. Lin, S. Jiang, X. Liu, S. Guo, *Biosens. Bioelectron.* **2020**, *150*, 111905.

High-quality plasmonic Ag-Au bilayer nanobump grating sensor

Kernius Vilkevičius, Tomas Rakickas, and Evaldas Stankevičius*

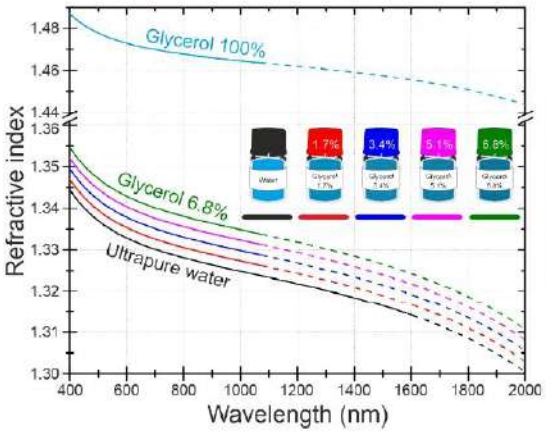

Sellmeier dispersion equation

$n^2(\lambda)=A+(B_1\lambda^2)/(\lambda^2-C_1)+(B_2\lambda^2)/(\lambda^2-C_2)$

	Water	Glycerol
A	1	1.6062±3E-5
B_1	0.75832±0.00082	0.0622±4E-4
C_1	0.01007±0.00027	7.99±0.05
B_2	0.08495±0.001912	0.53803±3E-5
C_2	8.91377±1.35076	0.0181±1E-5

Figure S1. Dispersion curves of ultrapure water (black line) and glycerol of 1.7% (red), 3.4% (blue), 5.1% (magenta), 6.8% (green), and 100% (cyan) concentrations. The coefficients in the table are given for the Sellmeier dispersion equation of deionized water and glycerol according to Kedenburg et al.[26] and Jakubczyk et al.[27a] Solid lines depict the experimentally obtained values and dashed lines mark the values calculated according to the dispersion formula.

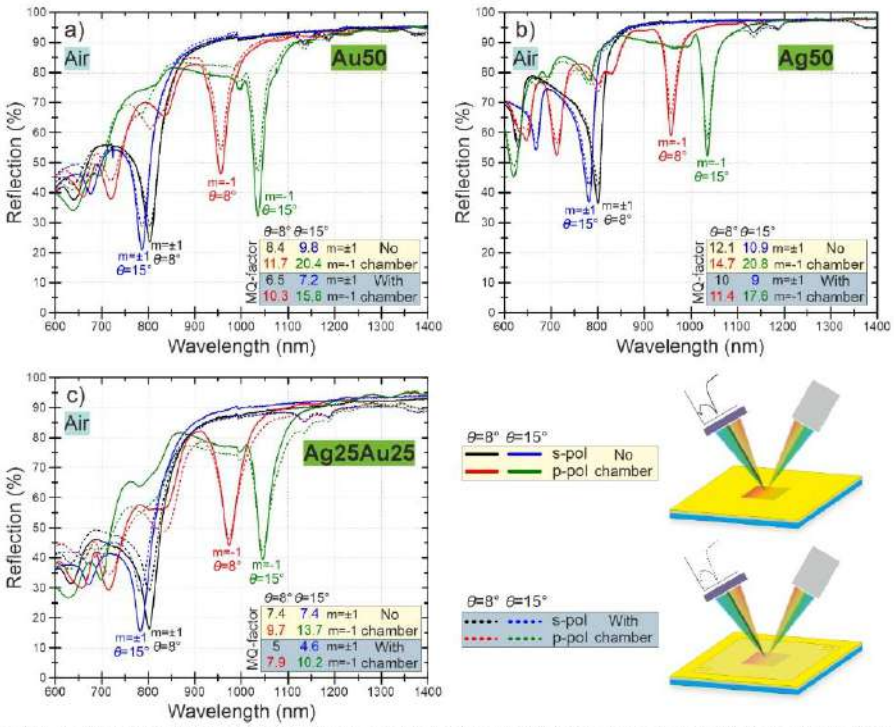

Figure S2. Reflectance spectra in air environment with (dashed line) and without (solid line) chamber for Au (a), Ag (b), and AgAu (c) samples. The response is shown for 8° (black and red) and 15° (blue and green) angles for both s- (black and blue) and p-polarization (red and green).

Table S1. 2D bump grating sensing parameters for m=±1 resonance at an 8° angle of incidence.

Sample	Environment	S [nm/RIU]	FOM [RIU^{-1}]	Q-factor	MQ-factor
Au	Air	805.9 ± 0.1	-	31.8 ± 0	6.6 ± 0
	Water		29.3	39.6 ± 0.7	7.1 ± 0.1
	Glycerol 1.7%		29.4	39.1 ± 0.2	7.4 ± 0.1
	Glycerol 3.4%		31.2	41.4 ± 0.05	7.8 ± 0.03
	Glycerol 5.1%		30.2	40.9 ± 0.5	6.8 ± 0.1
	Glycerol 6.8%		30.4	41.4 ± 0.7	7.8 ± 0.1
Ag	Air	812.5 ± 0.7	-	36.9 ± 0	10.3 ± 0
	Water		40.2	47.8 ± 0.04	14 ± 0.06
	Glycerol 1.7%		39.3	51.6 ± 0.5	15 ± 0.02
	Glycerol 3.4%		38.4	50.4 ± 0.02	15.3 ± 0.1
	Glycerol 5.1%		47.2	62 ± 0.2	14.9 ± 0.1
	Glycerol 6.8%		45.5	59.8 ± 0.7	15.3 ± 0.05
Ag-Au	Air	802.6 ± 1.1	-	36.2 ± 0	8.2 ± 0
	Water		36.6	48.5 ± 0.2	8.6 ± 0.1
	Glycerol 1.7%		36.8	48.8 ± 0.9	9 ± 0.1
	Glycerol 3.4%		38.2	50.8 ± 1	9.5 ± 0.3
	Glycerol 5.1%		41.1	54.7 ± 0.9	8.7 ± 0.2
	Glycerol 6.8%		39.4	52.5 ± 1.1	9.7 ± 0.3

Table S2. 2D bump grating sensing parameters for m=+1 resonance at an 8° angle of incidence.

Sample	Environment	S [nm/RIU]	FOM [RIU^{-1}]	Q-factor	MQ-factor
Au	Air	794.2 ± 3.7	-	25.8 ± 0	2.2 ± 0
	Water		25.7	32.6 ± 0.2	4.1 ± 0.1
	Glycerol 1.7%		23.8	31.7 ± 0.7	4.5 ± 0.05
	Glycerol 3.4%		24.8	32.9 ± 0.09	5.3 ± 0.2
	Glycerol 5.1%		23.8	31.9 ± 0.06	4.6 ± 0.1
	Glycerol 6.8%		24.1	32 ± 0.3	5.3 ± 0.03
Ag	Air	796.1 ± 1.6	-	29 ± 0	5.8 ± 0
	Water		31.4	40 ± 0.02	7.4 ± 0.1
	Glycerol 1.7%		30.7	41 ± 0.02	8.3 ± 0.03
	Glycerol 3.4%		31.7	40.6 ± 0.2	8.4 ± 0.3
	Glycerol 5.1%		32.4	40.9 ± 0.1	8.5 ± 0.2
	Glycerol 6.8%		32.7	41.2 ± 0.08	8.9 ± 0.04
Ag-Au	Air	790.8 ± 1.6	-	26.2 ± 0	5.4 ± 0
	Water		24.7	36.6 ± 0.2	6.8 ± 0.5
	Glycerol 1.7%		23.5	37.9 ± 0.2	7.1 ± 0.4
	Glycerol 3.4%		24.2	36.5 ± 0.2	6.9 ± 0.1
	Glycerol 5.1%		23.5	36.3 ± 0.3	6.6 ± 0.08
	Glycerol 6.8%		24.9	36.3 ± 0.1	7 ± 0.04

Table S3. 2D bump grating sensing parameters for m=−1 resonance at an 8° angle of incidence.

Sample	Environment	S [nm/RIU]	FOM [RIU^{-1}]	Q-factor	MQ-factor
Au	Air	870.5 ± 0.6	-	35.2 ± 0	10 ± 0
	Water		26.6	36.2 ± 0.1	8 ± 0.04
	Glycerol 1.7%		25.2	33.4 ± 0.3	7.7 ± 0.1
	Glycerol 3.4%		26.6	33.8 ± 1	8.7 ± 0.06
	Glycerol 5.1%		25.8	34 ± 0.4	8 ± 0.04
	Glycerol 6.8%		25.8	34.1 ± 0.2	8.9 ± 0.03
Ag	Air	863.8 ± 2.7	-	41.6 ± 0	11.5 ± 0
	Water		32.7	44.7 ± 0.02	9.3 ± 0.2
	Glycerol 1.7%		33.6	43.9 ± 0.2	10.2 ± 0.1
	Glycerol 3.4%		33.2	45.6 ± 0.5	10.9 ± 0.3
	Glycerol 5.1%		33.4	46.7 ± 0.6	11.6 ± 0.02
	Glycerol 6.8%		33.5	47.3 ± 0.06	12.5 ± 0.08
Ag-Au	Air	863.5 ± 0.9	-	34.3 ± 0	14 ± 0
	Water		29.8	35.4 ± 0.6	13.8 ± 0.4
	Glycerol 1.7%		30.8	33.6 ± 0.4	13.4 ± 0.2
	Glycerol 3.4%		30.2	33.3 ± 0.9	12.9 ± 0.3
	Glycerol 5.1%		29.5	33.8 ± 0.6	12.3 ± 0.2
	Glycerol 6.8%		29.4	35.9 ± 1.1	13.1 ± 0.2

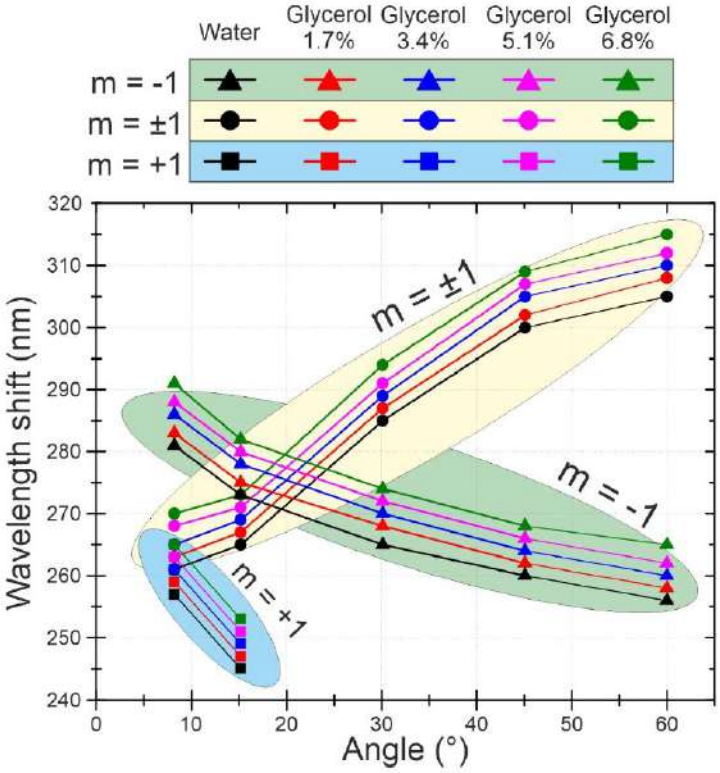

Figure S3. Resonant wavelength shift dependence on the angle of incidence in water (black line), and glycerol of 1.7% (red line), 3.4% (blue line), 5.1% (magenta line), and 6.8% (green line) concentrations.

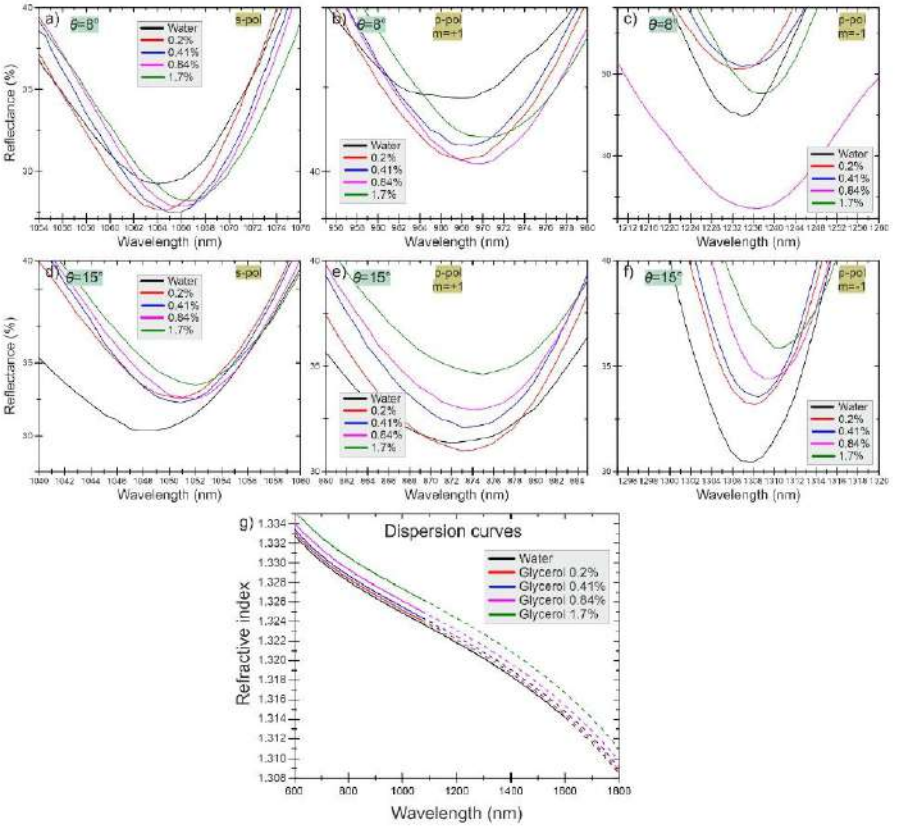

Figure S4. Resonant wavelength shift at the low-concentration of glycerol for m=±1 (a,d), m=+1 (b,e), and m=−1 (c,f) resonances at 8° (a-c) and 15° (d-f) angles of incidence. Used liquids are deionized water (black line), and glycerol of 0.2% (red line), 0.41% (blue line), 0.84% (magenta line), and 1.7% (green line) concentrations. g) Dispersion curves of the same liquids.

NOTES

NOTES

NOTES

Vilniaus universiteto leidykla
Saulėtekio al. 9, III rūmai, LT-10222 Vilnius
El. p. info@leidykla.vu.lt, www.leidykla.vu.lt
bookshop.vu.lt, journals.vu.lt
Tiražas 30 egz.